University of Technology Sydney (UTS)

Faculty of Engineering and Information Technology (FEIT)

School of Biomedical Engineering

Centre for Health Technologies

Theories and Applications of Non-Contact Sleep Monitoring using Microwave Doppler Radar

by

Vinh Phuc Tran

under the principle supervision of

Associate Professor Dr. Adel Ali Al-Jumaily

and co-supervision of

Dr. Jeff Armitstead

Thesis submitted as a requirement for the degree of

Doctor of Philosophy

February 2020

Certificate of Original Authorship

I, Vinh Phuc Tran declare that this thesis, is submitted in fulfilment of the requirements for the award of Doctor of Philosophy (PhD), in the Faculty of Engineering and Information Technology (FEIT), School of Biomedical Engineering at the University of Technology Sydney (UTS).

This thesis is wholly my own work unless otherwise reference or acknowledged. In addition, I certify that all information sources and literature used are indicated in the thesis.

This document has not been submitted for qualifications at any other academic institution.

This research is supported by the Australian Government Research Training Program scholarship.

Signature: Production Note:
Signature removed prior to publication.

Date: 21 February 2020

Acknowledgement

My deepest gratitude first and foremost to the God Almighty, Who has endowed me with the strength and perseverance to complete the Thesis. Without His Grace and Mercy, this achievement would not have been possible.

My sincere thank you to my parents, for their continuous prayers, encouragement, advice and love. They are a great source of motivation and without their support, I would not be able to successfully complete work on the Thesis. Thank you also to my two wonderful sisters for their understanding, encouragement and counsel throughout my academic journey.

Thank you to my principle supervisor, Associate Professor Dr. Adel Ali Al-Jumaily, for his guidance, support, patience, and valuable insights into my research. Dr. Al-Jumaily has been very supportive as a mentor and I am very thankful for his time and friendship. A special thank you to my industry co-supervisor Dr. Jeff Armistead, Vice President of Medical, Clinical Science and Innovation at ResMed Asia Pacific Ltd. for his valuable opinions, time, effort and support during my research.

I would like to express my appreciation to Dr. Julian Magarey, Patent Attorney at ResMed Asia Pacific Ltd., for his time and assistance in reviewing documents and handling all my research IPs and patents at ResMed. I would also like to thank Professor Dr. Klaus Schindhelm, Adjunct Professor Dr. Steven Farrugia and Lecturer Dr. Syed Mohammed Shamsul Islam for their constructive feedbacks on the research.

Thank you ResMed Asia Pacific Ltd. for providing the SleepMinder^{TM} biosensor and patients' database for my research.

Finally, thank you the Australian Government Research Training Program for the scholarship and the University of Technology Sydney (UTS) for the opportunity and a great learning experience.

Thesis Structure

The structure of the Thesis is the "Conventional Thesis", adhering to the "2019 UTS Graduate Research Candidature Management, Thesis Preparation and Submission Procedures". The structure of Thesis is as follows:

- **Publications** – this is a list of published academic conference and journal papers, as well as journal paper submitted and under peer-review at the time of Thesis submission.

- **Patents** – this is a list of published patents, including world international patent (WIPO), US patent and filed provisional Australian IP (AusPat) applications.

- **Statement of Contribution** – this is a summary section documenting the contributions of the Thesis to the knowledge of the non-contact sleep monitoring field.

- **List of Tables** – this section provides a list of tables in the Thesis.

- **List of Figures** – this section provides a list of figures in the Thesis.

- **Acronyms and Abbreviations** – this section provides a list of acronyms and abbreviations in the Thesis.

- **Abstract** – this is a summary of the research works in the Thesis.

- **Chapter 1: Literature Review (*Thesis Contribution 1 – Knowledge*)** – Chapter 1 provides a comprehensive review of the current state of the non-contact microwave Doppler radar sleep monitoring technology. It also

outlines the current challenges and recommendations for future research directions.

- **Chapter 2: Sleep Disorders (*Thesis Contribution 1 – Knowledge*)** – Chapter 2 provides an overview of the sleep disorders and focuses on obstructive sleep apnea (OSA). The purpose of chapter 2 is to outline the basic fundamentals of sleep disorders and to provide the background knowledge for the research work in the Thesis.

- **Chapter 3: Relative Demodulation (*Thesis Contribution 2 – Novel Theory 1*)** – Chapter 3 presents a novel real-time demodulation theory and technique for the non-contact microwave Doppler radar system. Included in this chapter, is a novel respiratory and heart rates estimation algorithm, using the non-contact microwave Doppler radar.

- **Chapter 4: Pulmonary Ventilation Mathematical Model (*Thesis Contribution 3 – Novel Theory 2*)** – Chapter 4 presents a novel pulmonary ventilation mathematical model that defines the relationship between the intrapulmonary pressure and the chest displacement. Included is this chapter, is a novel tidal volume estimation algorithm, using the non-contact microwave Doppler radar.

- **Chapter 5: External Ventilation Mathematical Model (*Thesis Contribution 4 – Novel Theory 3*)** – Chapter 5 presents a novel mathematical model that quantitatively defines the relationships between the arterial oxygen saturation (SaO_2), the arterial partial pressure of oxygen (PaO_2) and the arterial partial pressure of carbon dioxide ($PaCO_2$). Included in this chapter is a novel non-contact algorithm that utilizes the mathematical model, multilayer perceptron (MLP) artificial neural network (ANN) and the non-contact microwave Doppler radar, to translate the human periodic chest displacements caused by respiratory efforts into peripheral capillary oxygen saturation (SpO_2) measurements.

- **Chapter 6: 3-Dimensional Feature Representation and Extraction Technique (*Thesis Contribution 5 – Novel Theory 4*)** – Chapter 6 presents a novel 3-dimensional feature representation and extraction technique, consisting of two methods, Spatial Dimensions Transform (SDT) and Spatial Dimensions Decomposition (SDD). SDT and SDD when combined can achieve data transformation, augmentation, normalization, scaling, and feature extraction in a single process.

- **Chapter 7: Novel Real-life Applications and Results of Non-Contact Sleep Monitoring (*Thesis Contribution 6 – Novel Real-Life Applications and Results*)** – Chapter 7 presents the real-life non-contact sleep monitoring applications of the novel contributions theories and techniques presented in chapters 3, 4, 5 and 6. The applications demonstrate the non-contact monitoring of the following sleep parameters:

    1. Respiratory rate.
    2. Heart rate.
    3. Tidal volume.
    4. Body orientations, i.e., “Prone”, “Upright”, “Supine”, “Right” and “Left” sleep orientations.
    5. Oxygen saturation.

- **Conclusion** – this section includes the “Statement of Conclusion” for the research presented in the Thesis.

- **Appendix I** – this section includes the descriptions of the non-contact microwave Doppler radar biosensor used in the research and presented in the Thesis.

- **Appendix II** – this section includes the descriptions of the patients’ databases, including ethics approval used in the research and presented in the Thesis. Additionally, this section also includes the justifications for the data exclusions, selections and partitions.

- **Appendix III** – this section includes the descriptions of common hyperparameters utilized in the artificial neural networks (ANN) and covered in the Thesis.

- **References** – this section includes a list of references utilized in the Thesis.

Publications

Published Conference Papers

1. V. P. Tran, and A. A. Al-Jumaily, "Non-Contact Dual Pulse Doppler System based Respiratory and Heart Rates Estimation for CHF Patients," in 37th Annual International Conference of the IEEE Engineering in Medicine and Biology Society, MiCo – Milano Conference Center – Milan, Italy, 2015, pp. 4202-4205.

2. V. P. Tran, and A. A. Al-Jumaily, "Non-Contact Real-Time Estimation of Intrapulmonary Pressure and Tidal Volume for Chronic Heart Failure Patients," in 38th Annual International Conference of the IEEE Engineering in Medicine and Biology Society, Orlando, Florida USA, 2016, pp. 3564-3567.

3. V. P. Tran, and A. A. Al-Jumaily, "Non-Contact Doppler Radar Based Prediction of Nocturnal Body Orientations Using Deep Neural Network for Chronic Heart Failure Patients," in 2017 International Conference on Electrical and Computing Technologies and Applications (ICECTA), American University of Ras Al Khaimah, Ras Al Khaimah, United Arab Emirates (UAE), 2017.

Published Journal Papers

4. V. P. Tran, and A. A. Al-Jumaily, "Non-Contact Dual Pulse Doppler System Based Real-Time Relative Demodulation and Respiratory & Heart Rates Estimations for Chronic Heart Failure Patients," *Procedia Computer Science*, vol. 76, no. 2015, pp. 47–52, 2015.
   (Best paper awarded at IEEE-IRIS conference in 2015)

5. V. P. Tran, A. A. Al-Jumaily, and S. M. S. Islam, “Doppler Radar-Based Non-Contact Health Monitoring for Obstructive Sleep Apnea Diagnosis: A Comprehensive Review,” *Big Data and Cognitive Computing*, vol. 3, no. 3, pp. 1-21, 2019.

6. V. P. Tran, and A. A. Al-Jumaily, “A Novel Oxygen-Hemoglobin Model for Non-Contact Sleep Monitoring of Oxygen Saturation,” *IEEE Sensors Journal*, vol. 19, no. 24, pp. 12325-12332, 2019.

Submitted Journal Paper

7. V. P. Tran, and A. A. Al-Jumaily, “A Novel 3-Dimensional Feature Representation and Extraction Technique with Non-Contact Sleep Monitoring Applications,” *IEEE Sensors Journal, 2020*.

Patents

Published World International Patent (WIPO)

1. (WO2019079855) DETECTION AND MONITORING OF BODY ORIENTATION
   https://patentscope.wipo.int/search/en/detail.jsf?docId=WO2019079855
   Publication date: 02-May-2019

2. (WO2016205891) DIAGNOSIS AND MONITORING OF CARDIO-RESPIRATORY DISORDERS
   https://patentscope.wipo.int/search/en/detail.jsf?docId=WO2016205891
   Publication date: 29-Dec-2016

Published US Patent

3. (US20180153427) DIAGNOSIS AND MONITORING OF CARDIO-RESPIRATORY DISORDERS
   https://patentscope.wipo.int/search/en/detail.jsf?docId=US219626659
   Publication date: 07-Jun-2018

Filed Australian Provisional IP (AusPat) Applications

4. Non-contact monitoring of nocturnal body position
   http://pericles.ipaustralia.gov.au/ols/auspat/applicationDetails.do?applicationNo=2018900724
   Filed date: 06-Mar-2018

5. Non-contact monitoring of nocturnal body position
http://pericles.ipaustralia.gov.au/ols/auspat/applicationDetails.do?applicationNo=2017904337
Filed date: 26-Oct-2017

6. Non-contact monitoring of nocturnal oxygen saturation in the arterial blood
http://pericles.ipaustralia.gov.au/ols/auspat/applicationDetails.do?applicationNo=2016903946
Filed date: 28-Sep-2016

7. Estimation of Pulmonary Ventilation Quantities Based On Non-Contact Sensor Data
http://pericles.ipaustralia.gov.au/ols/auspat/applicationDetails.do?applicationNo=2016900897
Filed date: 10-Mar-2016

8. Heart and respiratory rate estimation from non-contact sensor data
https://pericles.ipaustralia.gov.au/ols/auspat/applicationDetails.do?applicationNo=2015902494
Filed date: 26-Jun-2015

Statement of Contribution

The Thesis is a response to the demands for non-contact sleep monitoring systems. The demands arise due to the limitations of the polysomnography (PSG) system, the importance of early screening for obstructive sleep apnea (OSA), the need for long-term continuous monitoring and the concern with respect to patient discomfort when using the current gold-standard PSG system.

The Thesis presents novel theories, real-life applications and the results of the non-contact sleep monitoring using the microwave Doppler radar, including the "non-stationary" and the "non-direct facing" subjects' measurements in the complex sleep environment.

The Thesis includes six contributions to the knowledge of the non-contact sleep monitoring field. The six contributions in its entirety, are my own work.

1. Contribution 1: Knowledge

Chapter 1: Literature Review – Chapter 1 adds to the knowledge and understanding of non-contact sleep monitoring field by presenting a comprehensive review of the current state of the non-contact Doppler radar sleep monitoring technology. This chapter includes an outline of the current challenges and recommendations on future research directions.

Chapter 2: Sleep Disorders – Chapter 2 adds to the knowledge and understanding of the non-contact sleep monitoring field and the research work by presenting an overview of the sleep disorders with the focus on obstructive sleep apnea (OSA). The overview includes the epidemiology, pathophysiology, comorbidities and cardiovascular comorbidities associated with OSA.

2. *Contribution 2: Novel Theory 1*

Chapter 3: Relative Demodulation – Chapter 3 contributes to the field of non-contact sleep monitoring by introducing "Relative Demodulation", a novel real-time demodulation theory and technique for the non-contact microwave Doppler radar system. The novelty of the "Relative Demodulation" technique is that it pivots from conventional displacements analysis to introduce derivatives analysis. Included in this chapter, is a novel respiratory and heart rates estimation algorithm that utilizes the "Relative Demodulation" technique and the non-contact microwave Doppler radar.

3. *Contribution 3: Novel Theory 2*

Chapter 4: Pulmonary Ventilation Mathematical Model – Chapter 4 contributes to the field of non-contact sleep monitoring by introducing a novel pulmonary ventilation mathematical model that defines the relationship between the intrapulmonary pressure and the chest displacement. The novelty of the mathematical model is that it enables the capability to estimate tidal volume using the non-contact microwave Doppler radar. Included in this chapter, is a novel tidal volume estimation algorithm that utilizes the mathematical model and the non-contact microwave Doppler radar.

4. *Contribution 4: Novel Theory 3*

Chapter 5: External Ventilation Mathematical Model – Chapter 5 contributes to the field of non-contact sleep monitoring by introducing a novel oxygen-hemoglobin dissociation mathematical model that quantitatively defines the relationships between the arterial oxygen saturation (SaO_2), the arterial partial pressure of oxygen (PaO_2) and the arterial partial pressure of carbon dioxide ($PaCO_2$). The novelty of the mathematical model is that it enables the capability to estimate oxygen saturation using non-contact microwave Doppler radar. Included in this chapter, is a novel non-contact algorithm that utilizes the mathematical model, multilayer perceptron (MLP) artificial neural network (ANN) and non-contact microwave Doppler radar to translate the human periodic chest

displacements caused by respiratory efforts into peripheral capillary oxygen saturation (SpO_2) measurements.

5. Contribution 5: Novel Theory 4

Chapter 6: 3-Dimensional Feature Representation and Extraction Technique – Chapter 6 contributes to the field of non-contact sleep monitoring by introducing a novel 3-dimensional feature representation and extraction technique, consisting of two methods, Spatial Dimensions Transform (SDT) and Spatial Dimensions Decomposition (SDD). The SDT and SDD when combined can achieve data transformation, augmentation, normalization, scaling, and feature extraction in a single process. The novelty of SDT and SDD is that the feature engineering process is not required. The preprocessing of signals, DC-offsets removal, signals filtering, expert domain knowledge, wavelet packet decomposition and/or time-frequency domain analysis are not required in the process of feature extraction. This technique is applicable to both classification and dynamic time-series regression applications.

6. Contribution 6: Novel Real-Life Applications and Results

Chapter 7: Novel Real-Life Applications and Results of Non-Contact Sleep Monitoring – Chapter 7 contributes to the field of non-contact sleep monitoring by presenting the real-life non-contact sleep monitoring applications and the results of the contributions presented in chapters 3, 4, 5 and 6. The contributions of chapter 7 include the novel high accuracy non-contact estimations/predictions of the following sleep monitoring parameters:

1. Respiratory rate.
2. Heart rate.
3. Tidal volume.
4. Body orientations, i.e., “Prone”, “Upright”, “Supine”, “Right” and “Left” sleep orientations.
5. Oxygen saturation.

Table of Contents

INTRODUCTION 1

Research Aim 2

Research Objectives 2

Research Methodologies 3

CHAPTER 1: LITERATURE REVIEW 4

ABSTRACT 4

INTRODUCTION 5

1.1 RADAR Overview 7

1.1.1 Radar – Definition 7

1.1.2 Radar – Architecture 8

1.1.3 Radar – A Brief Historical Journey 10

1.2 Non-Contact Doppler Radar Architecture 11

1.2.1 Heterodyne versus Homodyne Topology 11

1.2.2 Continuous-Wave versus Pulsed-Wave Architecture 13

1.2.3 Single versus Quadrature Architecture 14

1.3 Non-Contact Doppler Radar Principle 15

1.3.1 Theoretically Analysis 15

1.4 Sources of Noise in Non-Contact Doppler Radar 22

1.4.1 Clutter and DC Offset 22

1.4.2 Phase-Nulling or Null-Point 22

1.4.3 Others Sources of Noise 22

1.5 Non-Contact Doppler Radar Signal Processing 23

1.5.1 Clutter and DC Offset Cancellation 24

1.5.2 Phase-Nulling Cancellation 24

1.5.3 Multi-Targets and Motions Artefacts Cancellation 26

1.6 Categories of Non-Contact Doppler Radar Signal Processing Techniques 29

1.6.1 Time-Frequency Analysis 30

1.6.2 Numerical Analysis 31

1.6.3 Classification and Training 33

1.6.4 Other Methodologies 34

1.7 Ultra-Wide Band Doppler Radar 35

1.8 Challenges and Future Research Directions 37

1.8.1 Current Achievements 37
1.8.2 Challenges and Future Research Directions 38
1.9 Conclusion 39
CHAPTER 2: SLEEP DISORDERS 40
INTRODUCTION 40
2.1 Sleep Disorders 40
2.1.1 Sleep Disorders – Classification 40
2.1.2 Sleep Disordered Breathing – Definition 41
2.2 Obstructive Sleep Apnea 42
2.2.1 Epidemiology 42
2.2.2 Pathophysiology 43
2.2.3 Comorbidities 47
2.2.4 Obstructive Sleep Apnea & Cardiovascular Comorbidities 48
2.3 Conclusion 49
CHAPTER 3: RELATIVE DEMODULATION 50
INTRODUCTION 50
3.1 Theory of Relative Demodulation 50
3.1.1 Continuous Time Domain 50
3.1.2 Discretized Time Domain 54
3.2 Respiratory and Heart Rates Estimation Algorithm 56
3.2.1 Algorithm Block Diagram 56
3.2.2 DC Offsets and Amplitude Gain Constants 57
3.2.3 Band-Pass Filter Type and Frequency Bandwidth 57
3.2.4 Inspiration and Expiration Detection Algorithm 58
3.2.5 Systole and Diastole Detection Algorithm 59
3.2.6 Respiratory and Heart Rate Estimation Algorithm 59
3.3 Conclusion 60
CHAPTER 4: PULMONARY VENTILATION MATHEMATICAL MODEL 61
INTRODUCTION 61
4.1 Pulmonary Ventilation Model 61
4.1.1 Theoretical Analysis and Modeling 61
4.2 Tidal Volume Estimation Algorithm 67
4.2.1 Algorithm Block Diagram 67
4.3 Conclusion 69
CHAPTER 5: EXTERNAL VENTILATION MATHEMATICAL MODEL 70
INTRODUCTION 70

5.1 Oxygen-Hemoglobin Dissociation Model 70
5.1.1 Theoretical Analysis and Modeling 71
5.1.2 Case 1 – Overdamped Solution ($\zeta > 1$) 74
5.1.3 Case 2 – Critically Damped Solution ($\zeta = 1$) 75
5.1.4 Case 3 – Underdamped Solution ($0 < \zeta < 1$) 76
5.1.5 Generalized SaO_2 Equation 76
5.2 Relationships of the Alveolar Partial Pressures 77
5.2.1 Alveolar Ventilation Relationship to Subject's Height 78
5.2.2 Carbon Dioxide Production Relationships to Subject's Heart Rate and Respiratory Quotient 79
5.2.3 Arterial Partial Pressure of Carbon Dioxide Relationships to Alveolar Ventilation and Carbon Dioxide Production 80
5.2.4 Arterial Partial Pressure of Oxygen Relationship to Arterial Partial Pressure Carbon Dioxide 81
5.3 Non-Contact Prediction of Oxygen Saturation Algorithm 82
5.3.1 Algorithm Block Diagram 83
5.3.2 Feature Extraction Process 86
5.3.3 SpO_2 Multilayer Perceptron Artificial Neural Network Architecture 86
5.4 Conclusion 87
CHAPTER 6: 3-DIMENSIONAL FEATURE REPRESENTATION AND EXTRACTION TECHNIQUE 89
INTRODUCTION 89
6.1 Spatial Dimensions Transform 90
6.1.1 SDT Rules 90
6.1.2 SDT Methodology 91
6.1.3 Inverse SDT 99
6.2 Spatial Dimensions Decomposition 99
6.2.1 SDD Methodology 100
6.2.2 SDD Decomposition Tree 100
6.2.3 SDD Algorithm 101
6.2.4 SDD Approach on Data Transformation 101
6.2.5 SDD Approach on Data Augmentation 101
6.2.6 SDD Approach on Feature Extraction 101
6.3 Conclusion 103
CHAPTER 7: NOVEL REAL-LIFE APPLICATIONS AND RESULTS OF NON-CONTACT SLEEP MONITORING 104

INTRODUCTION 104
7.1 Non-Contact Respiratory and Heart Rates Estimation 106
7.1.1 Patients' Dataset for Respiratory and Heart Rates Estimation 107
7.1.2 Respiratory and Heart Rates Estimations using Automated Estimation Algorithm 107
7.1.2.1 Signal Separation & Reconstruction Component 108
7.1.2.2 Signal Demodulation Component 109
7.1.2.3 Respiratory and Heart Rates Estimation Component 110
7.1.2.4 Performance Measures 110
7.1.2.5 Results and Discussions 111
7.1.2.6 Conclusion 114
7.1.3 Respiratory and Heart Rates Estimations using Relative Demodulation and Respiratory and Heart Rates Estimation Algorithm 114
7.1.3.1 Results and Discussions 114
7.1.3.2 Conclusion 118
7.1.4 Remarks 118
7.2 Non-Contact Tidal Volume Estimation 120
7.2.1 Patients' Dataset for Tidal Volume Estimation 120
7.2.2 Tidal Volume Estimations using Pulmonary Ventilation Model and Tidal Volume Estimation Algorithm 120
7.2.2.1 Results and Discussions 120
7.2.2.2 Conclusion 122
7.3 Non-Contact Body Orientations Prediction 123
7.3.1 Patients' Dataset Partitions for Body Orientations Prediction 124
7.3.2 Body Orientations Prediction using Wavelet Packet Decomposition and Deep Neural Network 124
7.3.2.1 Wavelet Packet Decomposition Process 124
7.3.2.2 Feature Extraction Process 126
7.3.2.3 Deep Artificial Neural Network Architecture 127
7.3.2.4 Deep Artificial Neural Network Training Characteristics 128
7.3.2.5 Results and Discussions 129
7.3.2.6 Conclusion 133
7.3.3 Body Orientations Prediction using SDT, SDD and Multilayer Perceptron 134
7.3.3.1 Feature Extraction using SDT and SDD 134
7.3.3.2 Multilayer Perceptron Artificial Neural Network Architecture 134
7.3.3.3 Multilayer Perceptron Artificial Neural Network Training Characteristics 135

7.3.3.4 Results and Discussions 135
7.3.3.5 Conclusion 138
7.3.4 Remarks 138
7.4 Non-Contact Oxygen Saturation Prediction 140
7.4.1 Patients' Database for Oxygen Saturation Estimation 141
7.4.1.1 Adjusted Patients' Database and Patients' Data Partitions for External Ventilation Mathematical Model 141
7.4.1.2 Adjusted Patients' Database and Patients' Data Partitions for SDD and SDT 141
7.4.2 Oxygen Saturation Estimation using External Ventilation Mathematical Model 141
7.4.2.1 Results and Discussions 141
7.4.2.2 Conclusion 150
7.4.3 Oxygen Saturation Estimation using SDT, SDD and Multilayer Perceptron ... 151
7.4.3.1 Feature Extraction using SDT and SDD 151
7.4.3.2 Multilayer Perceptron Artificial Neural Network Architecture 152
7.4.3.3 Multilayer Perceptron Artificial Neural Network Training Characteristics.. 153
7.4.3.4 Results and Discussions 153
7.4.3.5 Conclusion 159
7.4.4 Remarks 160
7.5 Conclusion 161
CHAPTER 8: SUMMARY, FUTURE RESEARCH, and CONCLUSION 163
INTRODUCTION 163
8.1 Thesis Summary 164
8.2 Recommendations for Future Research 167
8.3 Conclusion 168
APPENDIX I 170
A.I Biosensor 170
A.I.I SleepMinder™ 170
APPENDIX II 172
A.II Patients' Database 172
A.II.I Total Patients 172
A.II.II Patients Exclusions 173
A.II.III Selected Patients' Database 176
A.II.IV Adjusted Patients' Database for Respiratory and Heart Rates Estimations 177

A.II.V Adjusted Patients' Database for Tidal Volume and Oxygen Saturation Estimations by External Ventilation Mathematical Models 178
A.II.VI Patients' Database Partitions for Body Orientations Prediction 180
A.II.VII Patients' Database Partitions for Oxygen Saturation Prediction by SDT and SDD 181
APPENDIX III 183
A.III Common Neural Network Training Characteristics 183
A.III.I Hyperparameters 183
REFERENCES 184

List of Tables

Table 1.3.1.1 – Parameters That Can Be Estimated Using Non-Contact Doppler Radar 21
Table 1.8.1.1 – Sleep Monitoring Using Non-Contact Doppler Radar Achievements 38
Table 2.2.1.1 – OSA Prevalence Statistics World-Wide 43
Table 5.1.1.1 – Empirical Estimates of Zeta and W_n 73
Table 5.3.2.1 – Time-Domain Statistical Features 86
Table 5.3.3.1 – SpO_2 MLP Artificial Neural Network Architecture Characteristics 87
Table 7.1.4.1 – Respiratory and Heart Rates Accuracy Comparison 119
Table 7.3.2.1 – Time-Domain Statistical Features 127
Table 7.3.2.2 – Frequency-Domain Features 127
Table 7.3.2.3 – Deep Artificial Neural Network Architecture Characteristics 128
Table 7.3.3.1 – MLP Artificial Neural Network Architecture Characteristics 135
Table 7.3.4.1 – Body Orientations Prediction Performance and Accuracy Comparison 139
Table 7.4.2.1 – SpO_2 MLP Artificial Neural Network Mean Squared Error (MSE) 144
Table 7.4.3.1 – SpO_2 MLP Artificial Neural Network Architecture Characteristics 152
Table 7.4.3.2 – SpO_2 MLP Artificial Neural Network Mean Squared Error (MSE) 154
Table 7.4.4.1 – SpO_2 Prediction Performance and Accuracy Comparison 161
Table II.1 – Patients' Demographics and Recorded Sleep Duration 176
Table III.1 – Selected Patients' Database Summary 177
Table IV.1 – Adjusted Patients' Database Summary for Respiratory and Heart Rates 178
Table V.1 – Adjusted Patients' Database Summary for Tidal Volume & Oxygen Saturation by Mathematical Models 179
Table V.2 – Selected Patients' Database Partitions for Saturation Oxygen 180
Table VI.1 – Selected Patients' Database Partitions for Body Orientations 181
Table VII.1 – Selected Patients' Database Partitions for Saturation Oxygen 182
Table I.1 – Artificial Neural Network Training Characteristics 183

List of Figures

Figure 1.1.2.1 – Radar Architecture 8
Figure 1.2.1.1 – Heterodyne Transceiver Topology 12
Figure 1.2.1.2 – Homodyne Transceiver Topology 13
Figure 1.2.3.1 – Single-Channel Architecture 14
Figure 1.2.3.2 – Quadrature Architecture 15
Figure 1.3.1.1 – Non-Contact Doppler Radar Setup in a Sleep Laboratory or at Home 20
Figure 2.2.2.1 – Pharynx Anatomy 44
Figure 2.2.2.2 – Airway Obstruction During Sleep and Adenoids & Tonsil 45
Figure 2.2.2.3 – Central Nervous System: Automatic Nervous System Activity 46
Figure 2.2.3.1 – Obstructive Sleep Apnea and Comorbidities Statistics 48
Figure 3.1.1.1 – Relative Demodulation Concept Diagram 52
Figure 3.2.1.1 – Respiratory and Heart Rates Estimation Algorithm Block Diagram 56
Figure 4.1.1.1 – Pulmonary Ventilation Model 62
Figure 4.2.1.1 – Tidal Volume Estimation Algorithm 68
Figure 5.1.1.1 – Bohr's Oxygen-Hemoglobin Dissociation Curve (ODC) 71
Figure 5.1.1.2 – Simulated Step Responses of Second-Order Transfer Functions 72
Figure 5.3.1.1 – Non-Contact Prediction of SpO_2 Algorithm Block Diagram 84
Figure 5.3.3.1 – SpO_2 MLP Artificial Neural Network Architecture 87
Figure 6.1.1.1 – Spatial Dimensions Transform Theory Graphical Representation 91
Figure 6.1.2.1 – Spatial Dimensions Directional Cosines 92
Figure 6.1.2.2 – Spatial Dimensions Theta Transposition 93
Figure 6.1.2.3 – Spatial Dimensions Transform of Simulated Time-Series Signal 97
Figure 6.1.2.4 – Spatial Dimensions Transform of An Image 98
Figure 6.2.2.1 – Spatial Dimensions Decomposition Tree 100
Figure 7.1.2.1 – Automated Estimation Algorithm Block Diagram 108
Figure 7.1.2.2 – SleepMinder™ versus PSG Estimated Respiratory and Heart Rates 112
Figure 7.1.2.3 – SleepMinder™ Estimated Respiratory Rate Mean Accuracy and Error 113
Figure 7.1.2.4 – SleepMinder™ Estimated Heart Rate Mean Accuracy and Error 113
Figure 7.1.3.1 – SleepMinder™ Demodulated Respiratory and Heart Displacements 115
Figure 7.1.3.2 – SleepMinder™ versus PSG Estimated Respiratory and Heart Rates 116
Figure 7.1.3.3 – SleepMinder™ Estimated Respiratory Rate Mean Accuracy and Error 117
Figure 7.1.3.4 – SleepMinder™ Estimated Heart Rate Mean Accuracy and Error 118
Figure 7.2.2.1 – SleepMinder™ Estimated Tidal Volume Median Accuracy and Error 122

Figure 7.3.2.1 – Wavelets Extraction Process Block Diagram 125
Figure 7.3.2.2 – Deep Artificial Neural Network Architecture For Body Orientations Prediction 128
Figure 7.3.2.3 – Deep Artificial Neural Network Training Performance 129
Figure 7.3.2.4 – Deep Artificial Neural Network Confusion Matrix 130
Figure 7.3.2.5 – Nocturnal Body Orientations Prediction For "Test" Dataset 131
Figure 7.3.2.6 – Nocturnal Body Orientations Prediction for a CHF Patient 132
Figure 7.3.2.7 – Time-series Illustration Of The Features For A CHF Patient 133
Figure 7.3.3.1 – Body Orientations MLP Artificial Neural Network Architecture 134
Figure 7.3.3.2 – Body Orientations MLP Artificial Neural Network Training Performance 136
Figure 7.3.3.3 – Body Orientations MLP Artificial Neural Network Confusion Matrix 136
Figure 7.3.3.4 – Nocturnal Body Orientations Prediction For "Test" Dataset 137
Figure 7.3.3.5 – Nocturnal Body Orientations Prediction For A CHF Patient 138
Figure 7.4.2.1 – Bland-Altman Plot of Bohr's Measured SO_2 and Model's SaO_2 142
Figure 7.4.2.2 – Bohr and Model Oxygen-Hemoglobin Dissociation Curve 143
Figure 7.4.2.3 – SpO_2 MLP Artificial Neural Network Training Performance 144
Figure 7.4.2.4 – SpO_2 MLP Artificial Neural Network Regression Performance 145
Figure 7.4.2.5 – Nocturnal SpO2 Prediction for "Test" Dataset 146
Figure 7.4.2.6 – Bland-Altman (B&A) Plot for "Training" 147
Figure 7.4.2.7 – Bland-Altman (B&A) Plot for "Validation" 147
Figure 7.4.2.8– Bland-Altman (B&A) Plot for "Test" 148
Figure 7.4.2.9 – Bland-Altman (B&A) Plot for "All" 148
Figure 7.4.2.10 – SleepMinder™ Estimated SaO_2, PaO_2 and $PaCO_2$ 149
Figure 7.4.2.11 – SleepMinder™ Estimated V_A, CO and VCO_2 150
Figure 7.4.3.1 – SpO_2 MLP Artificial Neural Network Architecture 152
Figure 7.4.3.2 – SpO_2 MLP Artificial Neural Network Training Performance 153
Figure 7.4.3.3 – SpO_2 MLP Artificial Neural Network Regression Performance 154
Figure 7.4.3.4 – Nocturnal SpO2 Prediction for "Test" Dataset 155
Figure 7.4.3.5 – Bland-Altman (B&A) Plot for "Training" 156
Figure 7.4.3.6 – Bland-Altman (B&A) Plot for "Validation" 157
Figure 7.4.3.7– Bland-Altman (B&A) Plot for "Test" 157
Figure 7.4.3.8 – Bland-Altman (B&A) Plot for "All" 158
Figure 7.4.3.9 – Nocturnal SpO_2 Prediction for a CHF Patient 159
Figure I.1 – SleepMinder™ by BiancaMed 171
Figure I.2 – S+ by ResMed 171
Figure I.1 – SleepMinder™ Setup in a Sleep Laboratory or at Home 173

Acronyms and Abbreviations

AASM	–	American Academy of Sleep Medicine
ADC	–	Analogue-to-Digital Converter
AF	–	Atrial Fibrillation
AHI	–	Apnea Hypopnea Index
AI	–	Apnea Index
ANN	–	Artificial Neural Network
ANS	–	Autonomic Nervous System
BMI	–	Body Mass Index
BP	–	Blood Pressure (sometimes referred to as Arterial Blood Pressure)
CCD	–	Charge-Coupled Device
CHF	–	Congestive Heart Failure
CO_2	–	Carbon Dioxide
CSA	–	Central Sleep Apnea
CSAS	–	Central Sleep Apnea Syndrome
CSR	–	Cheyne-Stokes Respiration
CW	–	Continuous-Wave
DC	–	Direct Current
ECG	–	Electrocardiography
EM	–	Electromagnetic
FFT	–	Fast Fourier Transform
FIR	–	Finite Impulse Response
FM	–	Frequency Modulated
FMCW	–	Frequency-Modulated Continuous-Wave
FT	–	Fourier Transform
FRC	–	Functional Residual Capacity
HBPF	–	Heart Band-Pass Filter
HF	–	High Frequency
HI	–	Hypopnea Index
HR	–	Heart Rate

HRV – Heart Rate Variability
ICSD – International Classification of Sleep Disorders
ICU – Intensive Care Unit
IP – Intellectual Property
LDV – Laser Doppler Vibrometry
LF – Low Frequency
MHz – Mega Hertz
MLP – Multilayer Perceptron
MTI – Moving Target Indicator
OSA – Obstructive Sleep Apnea
OSAS – Obstructive Sleep Apnea Syndrome
$PaCO_2$ – Arterial Partial Pressure of Carbon Dioxide
PaO_2 – Arterial Partial Pressure of Oxygen
PCO_2 – Partial Pressure of Carbon Dioxide
PSG – Polysomnography
PW – Pulsed-Wave
Radar – Radio Detection and Ranging
RBPF – Respiratory Band-Pass Filter
Rf – Respiration Frequency
RIP – Respiratory Inductive Plethysmography
SaO_2 – Arterial Oxygen Saturation
SD – Sleep Disorders
SDB – Sleep Disordered Breathing
SpO_2 – Peripheral Capillary Oxygen Saturation
SSG – Seismosomnography
STFT – Short Time Fourier Transform
TLC – Total Lung Capacity
UHF – Ultra-High Frequency
UWB – Ultra-Wave Band
Vf – Ventilation Frequency
WPD – Wavelet Packet Decomposition

ABSTRACT

Obstructive sleep apnea (OSA) is a common and potentially lethal sleep disorder affecting at least 4% of adult males and 2% of adult females worldwide. Early detection, treatment and continuous monitoring of OSA are extremely important as it may reduce the risks associated with cardiovascular comorbidities. Polysomnography (PSG) is the gold-standard to diagnose OSA, however there are limitations, such as its unsuitability for long-term continuous monitoring.

The Thesis is a response to the demands for the non-contact sleep monitoring systems. The demands arise due to the limitations of the PSG system, the importance of early screening for OSA, the need for long-term continuous monitoring and the concern with respect to patient discomfort when using the gold-standard PSG system. The research presented in the Thesis are the novel theories, real-life applications and the results of the non-contact sleep monitoring using the non-contact microwave Doppler radar, including the "non-stationary" and "non-direct facing" subjects' measurements in the complex sleep environment.

The novel theories that the Thesis contributes to the field of non-contact sleep monitoring are:

1. Relative Demodulation – a novel theory and technique for real-time demodulation of the subject's chest or abdomen periodic motions using non-contact microwave Doppler radar.

2. Pulmonary Ventilation Mathematical Model – a novel mathematical model of the physiological pulmonary ventilation that enables the estimation of tidal volume using non-contact microwave Doppler radar.

3. External Ventilation Mathematical Model – a novel mathematical model of the physiological external ventilation that enables the estimation of oxygen

saturation using non-contact microwave Doppler radar.

4. 3-Dimensional Feature Representation and Extraction – a novel theory and technique that represents and extracts features in 3-dimensional space. This technique, when combine with the artificial neural networks (ANN) will enable the predictions of body orientations and oxygen saturation using non-contact microwave Doppler radar.

The novel non-contact sleep monitoring real-life applications and results that the Thesis contributes to the field of non-contact sleep monitoring are:

1. Respiratory rate – achieves 91.53% accuracy with median error of ±1.30 breaths/min.

2. Heart rate – achieves 91.28% accuracy with median error of ±6.20 beats/min.

3. Tidal volume – achieves 83.13% accuracy with median error of 57.32 milliliters.

4. Body orientations – achieve high correct classification rate of 99.9%. The misclassification is at a negligible rate of 0.1%.

5. Oxygen saturation – achieves correlation coefficient of 0.92 and the 95% limits of agreement is ±2.7 (% oxygen saturation).

The contributions of the novel theories, real-life applications and the results presented in the Thesis demonstrated a good level of accuracies. The potential applications include non-contact sleep early screening and/or continuous monitoring of the respiratory and heart rates, tidal volume, body orientations and saturation oxygen during sleep. This can be use in homes, hospitals, primary care sectors, nursing home facilities and/or sleep laboratories.

INTRODUCTION

Obstructive sleep apnea (OSA) is a common and potentially lethal sleep disorder affecting at least 4% of adult males and 2% of adult females world-wide [1]. OSA is define as the cessation of airflow for at least 10 seconds due to the collapse of the upper airway during sleep. This can occur at any age from infancy to old age [2]. OSA is recognized as an important cause of medical morbidity and mortality [3] and is an independent risk factor for a number of other disorders [4]. The treatment of severe and moderate OSA is associated with a 64% reduction in cardiovascular risk independent of age, comorbidities and the preexisting cardiovascular disease [5]. It is therefore extremely important for OSA patients with associated comorbidities to be diagnosed through early screening, to have treatments and be continuously monitored.

The gold-standard for OSA diagnosis is the use of polysomnography (PSG) to monitor the patient's overnight sleep activities. However, the PSG is not well suited for long-term continuous monitoring [6] due to limited mobility and discomfort to the patient during the monitoring process [7]. These limitations have led to stronger demands for non-contact sleep monitoring systems.

The non-contact biosensor such as microwave Doppler radar, used for physiological vital signs monitoring, had been discovered in the 1970's. There are evidences documented in literatures that showed the "stationary" and "direct-facing" subject's measurements using the Doppler radar for physiological vital signs estimations, such as respiratory and heart rates are feasible and can achieve good level of accuracy. However, "stationary" and "direct-facing" subject measurements are not an ideal scenario for sleep monitoring. There are also documented evidences that the "non-stationary" and "non-direct facing" subject's measurements can pose a greater challenge in the signal processing of the non-contact Doppler radar system [8, 9].

The Thesis is a response to the demands for a non-contact sleep monitoring systems, recognizing the limitations of the PSG system, the importance of early screening for

obstructive sleep apnea (OSA), the need for long-term continuous monitoring and the concern with respect to patient discomfort when using the PSG system. The aim, objectives and methodologies of the research are documented in the subsequent subsections.

Research Aim

The principle aim of the Thesis is to develop novel theories, demonstrate real-life applications and record the tested results of non-contact sleep monitoring using the non-contact microwave Doppler radar, including the "non-stationary" and "non-direct facing" subjects' measurements in the complex of sleep environment.

Research Objectives

The research objectives are:

1. Develop novel theories that enable the utilization of non-contact microwave Doppler radar to continuously monitor the physiological vital signs and sleep body orientations in the complex sleep environment.

2. Develop novel "non-stationary" and "non-direct facing" subjects' measurements applications that will achieve good level of accuracy in the estimation of the following sleep monitoring parameters:

    1. Respiratory rate.
    2. Heart rate.
    3. Tidal volume.
    4. Body orientations, i.e., "Prone", "Upright", "Supine", "Right" and "Left" sleep orientations.
    5. Oxygen saturation.

Research Methodologies

The research methodologies include

1. Utilizing mathematics, physiology and anatomy knowledge and understanding to develop the novel physiological mathematical models.

2. Utilizing machine learning methodologies and artificial neural network (ANN) models to achieve classifications and dynamic time-series regressions applications.

3. Obtaining real patients' measurements in the complex sleep environment with the "non-stationary" and "non-direct facing" criteria.

4. Using real patients' database in the developments and verifications of the non-contact sleep monitoring when non-contact microwave Doppler radar applications is utilized.

CHAPTER 1

LITERATURE REVIEW

Thesis Contribution 1: Knowledge

ABSTRACT

Today's rapid growth of elderly populations, aging problems and the prevalence of obstructive sleep apnea (OSA) and other health related issues have affected many aspects of society. This has led to high demands for a more robust healthcare monitoring, diagnosing and treatments facilities. In Sleep Medicine, sleep has a key role to play in both physical and mental health. The quality and duration of sleep have a direct and significant impact on people's learning, memory, metabolism, weight, safety, mood, cardio-vascular health, diseases, and immune system function. The gold-standard for OSA diagnosis is the overnight sleep monitoring system, using polysomnography (PSG). However, despite the quality and reliability of the PSG system, it is not well suited for long-term continuous usage due to limited mobility as well as causing possible irritation, distress, and discomfort to patients during the monitoring process. These limitations have led to stronger demands for the non-contact sleep monitoring systems. The aim of chapter 1 is to provide a comprehensive review of the current state of the non-contact Doppler radar sleep monitoring technology, provide an outline of current challenges and make recommendations on future research directions to practically realize and commercialize the technology for everyday usage.

INTRODUCTION

Obstructive sleep apnea (OSA) is a common and potentially lethal sleep disorder affecting at least 4% of adult males and 2% of adult females world-wide [1]. The statistics published in 2013 reported that the prevalence of OSA had increased between 10–17% for adult males and 3–9% for adult females in the United States of America (USA) [10].

OSA is the cessation of airflow due to the collapse of the upper airway during sleep and can occur at any age from infancy to old age. The statistics shown that the male to female ratio is about 2:1 and probably affects prepubertal males and females at equal rate [11]. There is evidence that OSA is associated with ischemic heart disease, increase prevalence of stroke, coronary artery disease, atrial fibrillation (AF), chronic heart failure (CHF), and cardiac sudden death [12]. In addition, OSA may also be associated with increase in cholesterol, hypertension [13], type 2 diabetes [14, 15], and cancer mortality [16]. OSA can also lead to oxygen desaturations, oxidative stress, blood pressure, heart rate changes, and interrupted sleep [17, 18].

The gold-standard for OSA diagnosis is the overnight sleep monitoring system using polysomnography (PSG). This records the electric potentials of the brain, heart, eye movement, muscle activity, respiratory effort, airflow, oxygen saturation and leg movements throughout the night [19]. Despite the quality and reliability of the PSG system, it is not well suited for long-term continuous monitoring usage [6] due to limited mobility as well as causing possible irritation, distress, and discomfort to patients during the monitoring process [7]. These limitations have led to stronger demands for the non-contact sleep monitoring systems.

Non-contact biosensor such as microwave Doppler radar for physiological vital signs monitoring had been discovered in the 1970s and there are published literatures regarding the non-contact assessments of respiratory and heart rates. However, the

reported achievements were based on “stationary” and “direct-facing” subject measurements, which is not an ideal scenario for the complex sleep environment.

As documented in literatures, the issue with getting an accurate reading from a non-contact monitoring device is due to background clutter, phase-nulling or null point, DC offsets, motion artefacts and electromagnetic interferences [7]. In addition, for continuous sleep monitoring in particular, the challenges are in the complex sleep environment, the noises associated with the unpredictability of body movements, body orientations, the changes in sleeping posture, multi-subjects cancellation, undesired harmonics and intermodulation [8, 9].

There had been numerous reviews, comparison studies [20-23], and smart systems designs [24, 25] regarding unobtrusive [26], nonintrusive [27] and non-contact physiological vital signs monitoring for sleep monitoring. However, a comprehensive review of the non-contact Doppler radar for health monitoring for OSA diagnosis has been limited. This is the primary motivation of chapter 1.

The aim of chapter 1 is to provide a comprehensive review on the current state of the non-contact Doppler radar for sleep monitoring technology. This includes a review of the system theoretical fundamentals, signal processing methodologies, techniques, achievements and challenges. In addition, chapter 1 also discussed the potential future research directions, as well as, potential applications of this technology in the daily life.

The searched topic used for the research is “sleep monitoring using non-contact Doppler radar”. The searched for relevant literatures was done across multiple databases and online journals; including the University of Technology Sydney (UTS, Ultimo NSW 2007, Australia) databases, PubMed, ScienceDirect, IEEE Xplore, and many more. The inclusions and/or exclusions of articles were based on its relevance to the field of non-contact Doppler radar physiological vital signs estimations and sleep indices predictions.

1.1 RADAR Overview

1.1.1 Radar – Definition

Radar is an acronym for **RA**dio **D**etection **A**nd **R**anging. Radar is an object-detection system that transmits electromagnetic signal towards an object. The transmitted signal can be in the form of continuous-wave (CW), frequency-modulated continuous-wave (FMCW) or pulsed-wave (PW). The echo signal from an object is then used to determine the range, altitude, direction, and/or speed of the object [28]. The object's information can be derived from the following radar characteristics:

- Phase-shift – the time delay between the transmitted signal and the echo signal indicates the distance to the object.

- Frequency-shift – the frequency shifts between the transmitted signal and the echo signal enables calculation of the object's velocity.

- Signal-strengths – the strength of the echo signal reveals the object's radar cross section, providing information regarding the object's size, geometry, and composition.

Radar system operates at microwave frequencies and depending on its application, the frequencies can vary from a few megahertz (MHz) to well beyond optical frequencies. A major advantage of microwave frequencies is in its ability to penetrate through objects and allowing the detection of concealed objects.

Radar was initially developed for military purposes such as surveillance and weapon control. However, radar is presently use in many significant civil applications such as aircraft, ships, spacecraft, environment remote sensing especially weather, law enforcement, physiological monitoring and many other applications.

1.1.2 Radar – Architecture

Radar architecture typically consists of a transmitter, a duplexer, an antenna, a receiver and a signal processing component. The signal processing component can be implemented as hardware and/or software. An illustration of the radar architecture is in Fig. 1.1.2.1.

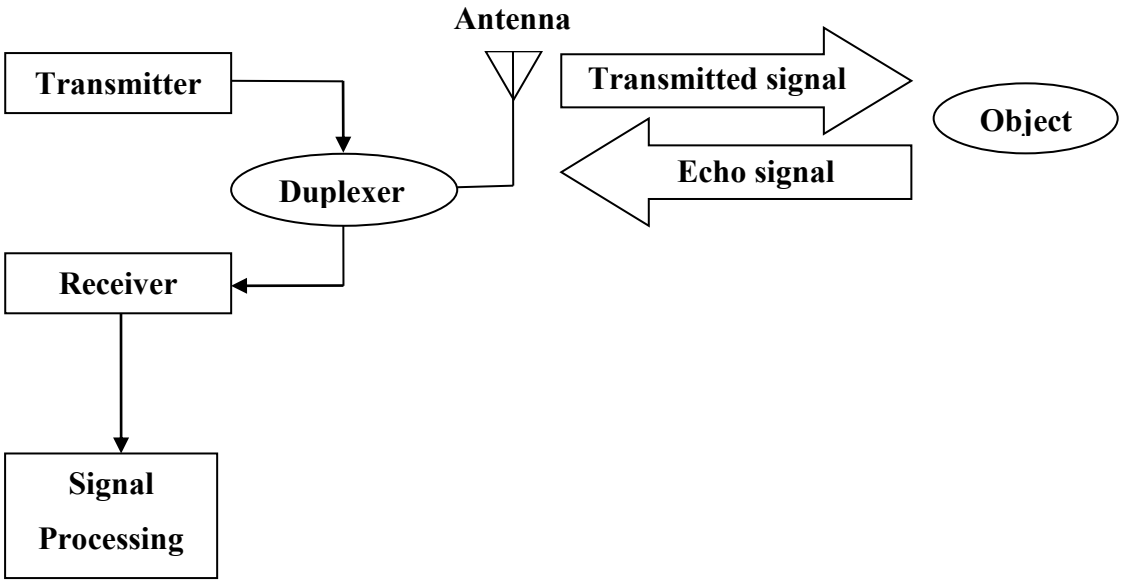

Figure 1.1.2.1 – Radar Architecture

- Transmitter – generates waveform at operating frequency, amplify the signal to the required transmission power and stabilize the signal for transmission.

- Duplexer – is the "Protector" of the radar, which acts as a rapid switch to protect the "Receiver" when the "Transmitter" is active. When the "Transmitter" is inactive, the "Duplexer" redirects the weak echo signal to the "Receiver" rather than to the "Transmitter".

- Antenna – radiates the transmitter power into space and concentrates the energy into a narrow beam towards an object. The antenna size will depend in part, on the operating frequency of the radar system.

- Receiver – serve two purposes: (1) perform filtering to eliminate noise and other interfering signals from the desired signal and (2) amplify the desired signal sufficiently to enable the signal processing process to follow.

- Signal Processing – there has been no general agreement about the signal-processing function, however it is usually use to reject clutter and out-of-band noise, while passing the desired signal and to derive information from the signal.

Depending on the radar system configuration and the type of the transmitted signal, the detection of the range and/or angle to the target, the size and shape of the target and the linear and/or rotational velocity of the target can be obtained [28]. In addition, depending on which of these parameters are consider important to capture, as well as the range and the nature of the targeted object, different radar topologies may be adopted. Here are some of the radar topologies:

1. Continuous-wave (CW) – detects moving targets via the Doppler shift of the received signal, however, this system cannot detect the range. CW systems are commonly use when the rotational velocity of the target needs to be detected. Police radar systems typically sense the speed of cars with pure CW radar systems because they are difficult to detect and interfere with [29].

2. Frequency-modulated continuous-wave (FMCW) – detects both the range to and the velocity of the target. Altimeters and Doppler navigation devices use FMCW radar systems [29].

3. Pulsed-wave (PW) – enables the transmitting and receiving to occur at different times. This topology is use when there is difficulty in sensing the received signal in the presence of the transmitted signal because the echo signal is much smaller than the transmitted signal. PW radar is also useful when the peak power of the transmitted signal needs to be much higher than the average power [28]. There are three major groups of PW radar: (1)

pulse compression radar, (2) moving target indicator (MTI) radar, and (3) pulsed Doppler radar.

1.1.3 Radar – A Brief Historical Journey

In 1842, Christian Andreas Doppler, an Austrian physicist, was the first to observe and describe the frequency of light and sound waves that were affected by the relative motion of the source and the detector [30]. This phenomenon was latter known as the "Doppler Effect". In 1864, James Clerk Maxwell, a Scottish mathematical physicist, pioneered the use of electromagnetic waves and developed the equations governing the electromagnetic waves. In 1886, Heinrich Hertz, a German physicist, expanded Maxwell's work and demonstrated the transmission and reflection of radio waves [31]. The use of reflected electromagnetic waves to detect objects was not explored until the 1920s when the "Doppler Effect" was used to detect moving objects.

In 1924, Sir Edward Victor Appleton, an English physicist, used what is now refer to as the FMCW radar to prove the existence of and measure the distance to the ionosphere. The ionosphere is consider to be the first object detected by radar [31]. In 1937, Dr. Albert Hoyt Taylor, a radio engineer of the Naval Research Laboratory, known as the "Father of Naval Radar", developed a radar system for ship tracking purpose and his invention was the first to successfully install on a ship [28]. In 1916, Sir Robert Alexander Watson-Watt of Britain developed a radar system to detect storms while working at the British Meteorological Office. Latter in 1935, Sir Watson-Watt joined British Air Ministry, Bawdsey Research Station, located in Bawdsey Manor near Felixstowe, Suffolk, and developed a radar system for detecting enemy aircrafts before they were visible. His invention patented as the first pulsed radar system. By 1939, Britain had a chain of radar stations along its coasts to detect enemy arrivals by air and by sea, which was instrumental in the World War II [31]. Additionally, imaging radars and sweep displays were also developed during World War II [28].

After the end of World War II, the use of radar by civilians began to proliferate. In the 1950s, the first weather imaging radar systems were developed. In the 1960s, a network of Doppler weather radar systems, known as NexRad, was installed to observe rainfall

rate, mean radial velocity and the spread in wind speed. In the 1960s, the Federal Aviation Administration began to build radar systems for air route surveillance. Progressing through to the second millennium, airborne weather avoidance radar used the Doppler information to indicate turbulence, windshear and downbursts to commercial airline pilots. FMCW radar is also use in wind profiling to detect both the velocity and the location of the wind shifts [32].

In contrast, the use of the continuous-wave (CW) radar systems are limited because it is only effective in detecting moving objects and not effective in detecting stationary or slow-moving clutter. The CW radar is predominately use in detecting low-flying aircrafts that are lost in clutter with pulsed radar systems. The low-altitude Hawk radar system, first developed in the 1960s, uses CW radar to detect moving targets amidst clutter. The CW radar systems are commonly use in target illumination, such as in semi-active radar-homing air-to-air missiles. Additionally, CW radar has a low probability of detection since it has a very narrow bandwidth [29].

1.2 Non-Contact Doppler Radar Architecture

1.2.1 Heterodyne versus Homodyne Topology

Heterodyning is a radio signal processing technique used to create new frequencies by combining or mixing two frequencies, these new frequencies are called “Heterodynes”. Heterodyne transceiver usually contains a separate local oscillator (LO) oscillating at the radar’s operating frequency (RF) to radiate and transmit signal (Tx). The received signal (Rx), filtered by a band-pass filter (BPF) and is mixed with another separate LO oscillating at different frequency compared to the RF. This means that the mixed signal is modulated on a non-zero intermediate frequency (IF) rather than being converted directly to baseband. The mixed signal is also filtered by another BPF, followed by a low noise amplifier (LNA), and demodulated directly or mixed down to baseband

before demodulation [7, 22, 33]. An illustration of the heterodyne transceiver topology is shown in Fig. 1.2.1.1.

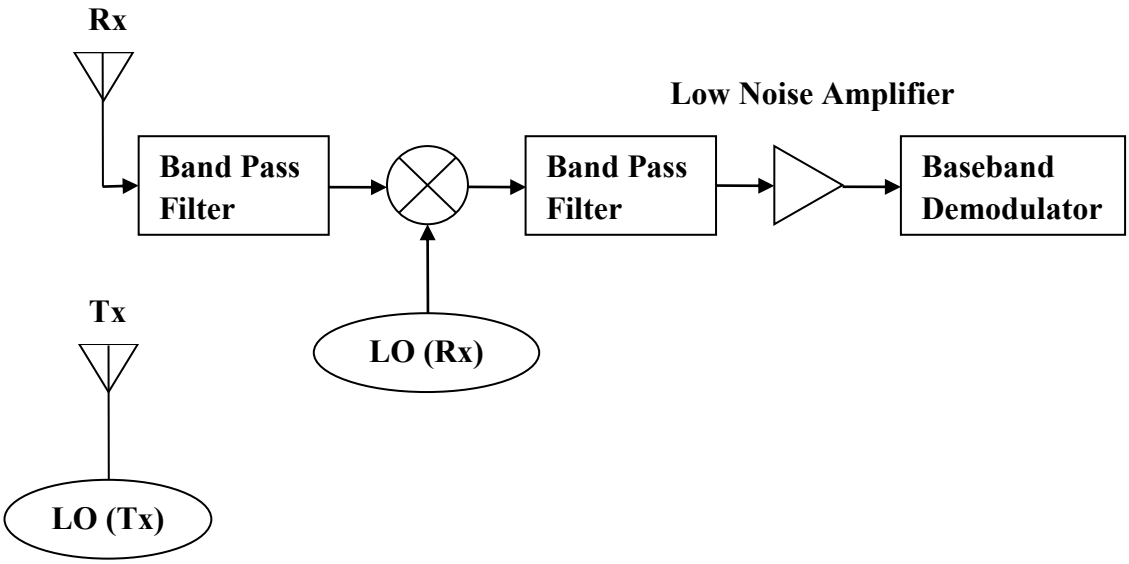

Figure 1.2.1.1 – Heterodyne Transceiver Topology

The advantage of heterodyne topology is that the different received frequencies can be converted to the same IF prior to the amplification or filtering processes and the IF is also at a considerably lower frequency than the RF. However, a major disadvantage of the heterodyne topology is the high number of circuitry components and passives [7, 22, 33].

Homodyne is often referring to as direct-conversion receiver (DCR), synchrodyne or zero-IF receiver. The received signal is mixed with a LO at the RF, i.e., the same frequency as its carrier, which converts the signal to baseband. The baseband signal is filtered using baseband BPF and is amplified using baseband LNA prior to baseband demodulator process or digitizer [7, 22, 33]. An illustration of the homodyne transceiver topology is shown in Fig. 1.2.1.2.

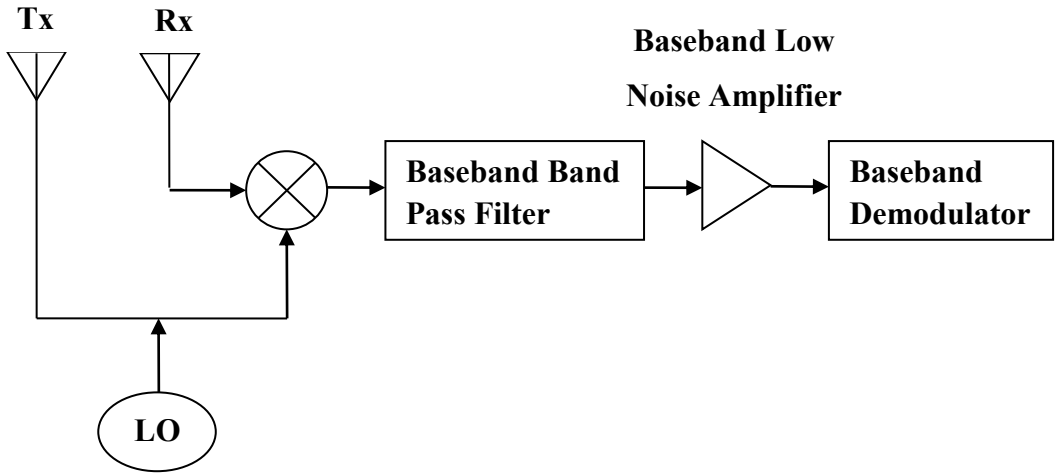

Figure 1.2.1.2 – Homodyne Transceiver Topology

The advantage of homodyne topology is the simplification of the basic circuit complexity. However, a major disadvantage of homodyne topology is the amount of DC offsets introduced by the system, which can cause saturation for digitizer process [7, 22, 33].

1.2.2 Continuous-Wave versus Pulsed-Wave Architecture

The continuous-wave (CW) radar system continuously transmits and receives narrow bandwidth signal. The CW radar consists of a signal source that can be used for both transmitting and receiving. Either heterodyne or homodyne topology can be used in CW radar system. However, homodyne topology is more commonly use in CW. This radar system has the advantages of simplicity, potential of minimal spread in the transmitted spectrum and can unambiguously measure velocity of targets. In addition, CW radar simplifies the filters at each stage of the receiver, and the signal processing is seemingly straightforward if the velocity or displacement information is target. However, a disadvantage of the CW radar system is the inability to separate reflections temporally, causing DC offsets and low-frequency noises to be introduced in the received signal [34].

A pulsed-wave (PW) radar system requires a switch to pulse the transmitting and receiving signals and has a wider bandwidth. The advantage of the PW radar is in its

ability to instantaneously measure the target range, temporally separate transmitter leakages, and strong short-range echoes from the weaker echoes of long-range targets. However, a disadvantage of the PW radar system is the ambiguity in both the range and velocity measurements. In non-contact physiological vital signs monitoring, the target is typically at the same or shorter range than the nearest clutter therefore, the PW radar advantage is limited to the elimination of leakage. Since range measurements does not aid the physiological motions monitoring, the increased in complexity of the PW radar over the CW radar does not result in a commensurate increase in benefits [34].

1.2.3 Single versus Quadrature Architecture

The Doppler radar transceivers can be build based on a single-channel or a quadrature design. The performance of single-channel, known to be sensitive to the position of the targets and in the worst case of null-point, produced virtually no phase-modulated signal for the estimation of physiological motions. The quadrature transceiver is mainly use to mitigate the null-point issue in single-channel transceiver by selecting the better of the quadrature, i.e., I-channel (in-phase) or Q-channel (90° out-of-phases) for optimum signal demodulation [7, 33, 35]. The illustrations of the single-channel and quadrature designs are in Figure 1.2.3.1 and Fig. 1.2.3.2.

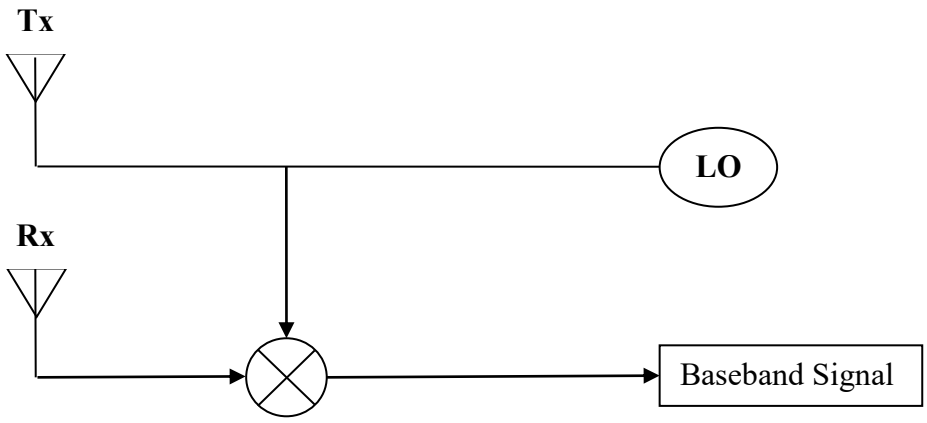

Figure 1.2.3.1 – Single-Channel Architecture

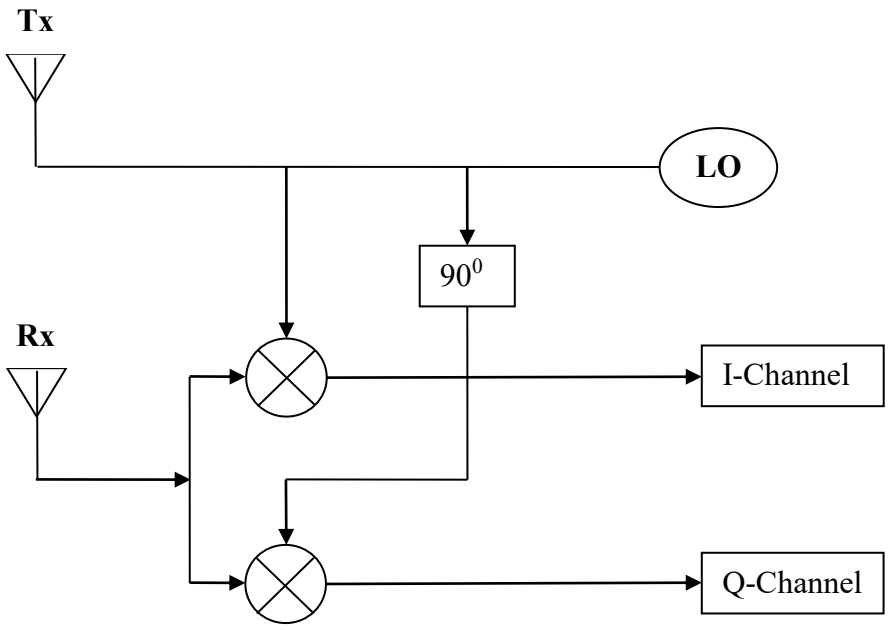

Figure 1.2.3.2 – Quadrature Architecture

1.3 Non-Contact Doppler Radar Principle

1.3.1 Theoretically Analysis

The Doppler radar for physiological vital signs monitoring was discovered in the 1970s. The use of the Doppler radar was demonstrated for detection of respiratory rate in 1975 and heart rate in 1979. Since the 1980s, the use of pulsed-wave (PW), continuous-wave (CW), frequency-modulated continuous-wave (FMCW), linear-frequency-modulated continuous-wave (LFMCW), and ultra-wide band (UWB) radars have also been explored for physiological sensing [34, 36-40].

The basic principle of Doppler radar is to transmit a microwave signal towards a target. The transmitted frequency of the microwave signal is usually within the unlicensed, not unregulated Industrial, Scientific, and Medical (ISM) radio bands, e.g., 5.8 GHz, 10 GHz, or 24 GHz. The phase-modulated of the backscattered signal is then measure to

estimate the periodic motions between the target and the source of transmission. This technology utilized the principle known as the “Doppler Effect”.

The “Doppler Effect” occurs when there is a shift in the frequency of the signal, either in the transmitted or echo signal, due to relative motion between the transmitter and the receiver. In other words, when the target has a time-varying position with a net zero velocity, the echo signal is phase-modulated proportionally to the target variation [36, 41, 42].

In a general case, the Doppler shift in frequency can be expressed as [29] [43] [44]:

$$f_d(t) = \frac{2f}{c} v(t) = \frac{2v(t)}{\lambda} \tag{1}$$

The time-varying phase shift proportional to the displacement “x(t)” can be expressed as [45] [44] [46]:

$$\Phi_r(t) = \frac{2f}{c} 2\pi x(t) = \frac{4\pi x(t)}{\lambda} \tag{2}$$

Let’s assume that a continuous-wave Doppler radar transmit a single-tone signal called “T(t)”, the equation representing the transmitting signal can be expressed as [43] [47] [48] [49] [50]:

$$T(t) = A_T cos\big(2\pi f t + \emptyset(t)\big) \tag{3}$$

Where:

- A_T – the amplitude of the transmitted signal in voltage (V).
- f – the oscillation frequency in Hertz (Hz).
- t – the elapsed time in second (sec).
- $\emptyset(t)$ – the phase noise of the oscillation in radian (rad).

Let the distance from the target to the continuous-wave Doppler radar transmitter be denoted as "d_0", and the time-varying position with a net zero velocity of the echo signal be denoted as "x(t)". The equation representing the distance travelled by the echo signal between the transmitter source and the target can be expressed as [43]:

$$d(t) = d_0 + x(t) \tag{4}$$

As the human chest-wall has a time-varying displacement, the distance travelled by the signal at the time of reflection is given as [43]:

$$d(t_{rf}) = d\left(t - \frac{d(t)}{c}\right) \tag{5}$$

The time delay by the time the signal is received can be expressed as [43]:

$$t_d = \frac{2d\left(t - \frac{d(t)}{c}\right)}{c} = \frac{2\left(d_0 + x\left(t - \frac{d(t)}{c}\right)\right)}{c} \tag{6}$$

Let the echo signal received by the receiver be denoted as "R(t)", which is the time-delayed version of the transmitted signal given in equation (3). The representing equation for "R(t)" can be expressed as [43]:

$$R(t) = A_R cos[(2\pi f(t - t_d) + \emptyset(t - t_d) + \theta)] \tag{7}$$

Substituting for "t_d" from equation (6) in equation (7), "R(t)" becomes:

$$R(t) = A_R cos\left[2\pi f\left(t - \frac{2\left(d_0 + x\left(t - \frac{d(t)}{c}\right)\right)}{c}\right) + \emptyset\left(t - \frac{2\left(d_0 + x\left(t - \frac{d(t)}{c}\right)\right)}{c}\right) + \theta\right] \tag{8}$$

The wavelength "λ" in meter (m) is define as the velocity of the wave "c" divided by the frequency "f" and can be expressed as:

$$\lambda = \frac{c}{f} \tag{9}$$

Equation (8) can now be represented as:

$$R(t) = A_R cos\left[2\pi ft - \frac{4\pi d_0}{\lambda} - \frac{4\pi x\left(t - \frac{d(t)}{c}\right)}{\lambda} + \emptyset\left(t - \frac{2d_0}{c} - \frac{2x\left(t - \frac{d(t)}{c}\right)}{c}\right) + \theta\right] \tag{10}$$

There are two components in equation (10) that can be neglected:

- $4\pi x\left(\frac{d(t)}{c}\right)$ – this is because the period of the chest movement for both respiratory and heart rates has a time period much greater than "d_0 / c" [43].

- $\emptyset\left(\frac{2x\left(t-\frac{d(t)}{c}\right)}{c}\right)$ – this is because the displacement of the chest movement generally in the order of 1 centimeter, which is much smaller compared to the distance between the transmitter and the target ranging from 50 centimeters to 2 meters [43].

Finally, the echo signal received by the receiver denoted as "*R(t)*" can be represented as [43] [47] [48] [49] [50]:

$$R(t) \approx A_R cos\left[2\pi ft - \frac{4\pi d_0}{\lambda} - \frac{4\pi x(t)}{\lambda} + \emptyset\left(t - \frac{2d_0}{c}\right) + \theta\right] \tag{11}$$

$$\theta = \frac{4\pi d_0}{\lambda} + \theta_0 \tag{12}$$

Where:

- A_R – the amplitude of the received signal in voltage (V).
- f – the oscillation frequency in Hertz (Hz).
- t – the elapsed time in second (sec).

- d_0 – the distance from the target to the continuous wave Doppler radar transmitter in meter (m).
- λ – the wave length of the signal in meter (m)
- c – the signal propagation velocity in meter per second (ms^{-1}).
- $\emptyset(t)$ – the phase noise of the oscillation in radian (rad).
- θ – the constant phase-shift determined by the distance to the target in radian (rad).
- θ_0 – the contributing phase-shift of the mixer and the antenna.

In the case of physiological vital signs monitoring, the target object is usually the subject's chest or abdominal region. The echo signal is then demodulate in the receiver to obtain information regarding the subject's chest or abdominal movements. Typically, the movements contain information for both respiratory and heart rates [36, 41, 42]. It has also been reported that abdominal movements cause stronger Doppler shift due to higher amplitude and deeper displacement compared to chest movements [41].

The demodulated baseband quadrature outputs I and Q channels are generally expressed as:

$$I(t) = V_I + A_I cos\left(\theta_0 + \frac{4\pi d_0}{\lambda} + \frac{4\pi x(t)}{\lambda} + \frac{4\pi y(t)}{\lambda} + \Delta\phi(t)\right) \quad (13)$$

$$Q(t) = V_Q + A_Q sin\left(\theta_0 + \frac{4\pi d_0}{\lambda} + \frac{4\pi x(t)}{\lambda} + \frac{4\pi y(t)}{\lambda} + \Delta\phi(t)\right) \quad (14)$$

$$\Delta\phi(t) = \phi(t) - \phi\left(t - \frac{2d_0}{c}\right) \quad (15)$$

Where:

- V_I & V_Q – the DC offsets of the channels in volt (V).
- A_I & A_Q – are the amplitude gain constants of the channels in volt (V).
- θ_0 – the initial constant phase-shift of the system in radian (rad).

- λ – the wave length of the signal in meter (m), which equal the signal propagation velocity "c" (ms^{-1}) divided by the radar operating frequency in Hertz (Hz).
- c – the signal propagation velocity in meter per second (ms^{-1}), which in this case is equivalent to the speed of light, i.e., 299,792,458 ms^{-1}.
- d_0 – the initial distant between the radar and the subject's chest or abdomen in meter (m).
- $\emptyset(t)$ – the phase noise of the system oscillation in radian (rad).
- x(t) – the function of respiratory that causes change in the chest displacement in meter (m).
- y(t) – the function of heart that causes change in the chest displacement in meter (m).

Typically, Doppler radar is design for measuring velocity of moving targets and therefore the scope of its applications are more restricted. However, it is not limited to respiratory and/or cardiac activity monitoring in a single subject [51]. The information for both respiratory and heart rates can be extracted from the phase-modulated by the time varying physiological periodic movement of the chest-wall. Nevertheless, such physiological motions are elastic, deformable with clothing which can create significant noise issue and will adversely affect the sensitivity of the system [41]. An illustration of the non-contact Doppler radar setup in a sleep laboratory or at home is in Figure 1.3.1.1.

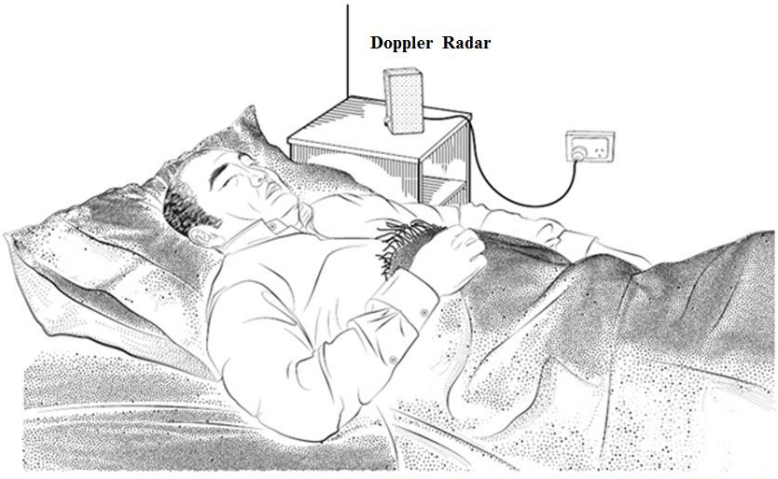

Figure 1.3.1.1 – Non-Contact Doppler Radar Setup in a Sleep Laboratory or at Home

The physiological parameters and sleep indices that are feasible for estimation and/or prediction using non-contact microwave Doppler radar is in Table 1.3.1.1.

Physiological Parameters	***Reference***	***Comment***
Respiratory rate	[9, 52-57]	*Ref. [56] and [57] are the author's published works presented in chapter 3 and chapter 7 of the Thesis.*
Heart rate	[8, 9, 55-57]	
Heart rate variability	[60]	
Pulse pressure	[61]	
Intrapulmonary pressure	[58]	
Tidal volume	[58, 62, 63]	*Ref. [58] is the author's published work presented in chapter 4 and chapter 7 of the Thesis.*
Sleep/wake pattern	[6, 64]	
Apnea-hypopnea index	[21, 65, 66]	
Cheyne-Stokes Respiration	[67]	
Body orientations	[59, 68]	*Ref. [59] is the author's published work presented in chapter 7 of the Thesis.*

Table 1.3.1.1 – Parameters That Can Be Estimated Using Non-Contact Doppler Radar

The applications of the Ultra-Wide Band (UWB) radars, utilizing the "Doppler Effect" principle for sensing physiological vital signs, reported in literatures mainly focus on through-wall life-signs detection targeting respiratory and heart rates. The most challenging task is the registration of respiration activity of an unconscious person. The other focus is aimed at sensing some key physiological bio-markers of astronauts during intra-vehicular and extra-vehicular activities [69, 70].

1.4 Sources of Noise in Non-Contact Doppler Radar

1.4.1 Clutter and DC Offset

In a radar system, clutters are generally echoes from all objects other than the target. Clutter detected at the receiver is commonly in the form of a single-tone component of the same frequency as the local oscillator (LO), however, with a different phase offset. The constant phase-shift is the function of the surface reflectivity and the size of the stationary portion of the target. When clutters are mixed with the LO, it will result in a DC offset in the baseband signal, and it is therefore difficult to separate in the frequency domain. If there is a significant DC component present at the signal output, the output is no longer linearly proportional to the displacement [71, 72]. As a result, the DC offset can saturate and desensitize the receiver in conventional CW radar system and this is a critical issue [73].

1.4.2 Phase-Nulling or Null-Point

In a Doppler radar system, the most important limitation in measuring periodic motions such as the respiratory and the heart rate, is the presence of phase-nulling or null-point. The null-point occurs when the received signal is either in-phase or 180° out-of-phases compared to the local oscillator [42]. The null-point occurs at the target's distance with every quarter of the radar transmitted signal wave-length ($\lambda/4$), and in the worst case produced virtually no phase-modulated signal for the estimation of physiological motions [35, 42, 73].

1.4.3 Others Sources of Noise

Beside clutters, other issues such as DC offsets, phase-nulling contributions, motions artefacts and electromagnetic interferences are also posing as a challenge to the signal processing of the Doppler radar signals [7, 74]. Another major challenge in sleep

monitoring application is the noise associated with the unpredictable body movements, body orientations, changes in sleeping posture, multi-subjects cancellation, undesired harmonics and intermodulation [8, 9, 56].

1.5 Non-Contact Doppler Radar Signal Processing

It has been decades since the first observation of non-contact Doppler radar in measuring physiological motions such as respiratory and heart rates. However, to date, a complete understanding of the mechanism and causes of the observed modulations, frequency penetrations and body electromagnetic radiation absorptions are not yet fully achieved.

There had been numerous attempts made either in the form of experimental or simulation to investigate the contributions of blood perfusion, internal body organ movements, body surface movement, and black-body radiation (due to temperature variations) to the phase-modulated of the received signal [75]. However, the most dominating theory on the cause of the observed modulations is still believe to be the small periodic movements of the chest wall (due to respiratory and heart motions) resulting in a small phase changes in the received signal.

The single and multiple Doppler radar systems were explored in the estimation of the physiological vital signs. Advances in the hardware circuitry design, antenna exploratory, signal processing techniques, and the classification algorithms had also been considered. However, the main challenge in using the Doppler radar systems for physiological measurement is still in the analysis and processing of the received signal data [76].

1.5.1 Clutter and DC Offset Cancellation

Earlier work on the Doppler radar system used a single antenna with a circulator to isolate the transmitting and receiving paths [60], however a major disadvantage in using a circular was self-mixing, which translate to DC offsets on the output signal [55]. The dual-antennas with separated transmit and receive paths had also been explored with the advantage of reduced DC offsets [35, 77].

Low-pass filters, high-pass filters, notch filters, and complex digital signal processing algorithms had also been considered for noise filtering and DC offsets elimination [35, 36, 42, 77-79]. The reported filters are types of Sallen-Key [77, 80-82], Elliptic [78, 83], Butterworth and RC passive filters [42, 72, 76, 84]. The Phase and Self-Injection-Locked (PSIL) oscillator with dual-tuning voltage-controlled oscillator were reported as achieving high signal-to-noise ratio [73]. The filtering at the signal processing level, including Finite Impulse Response (FIR) with Kaiser window [53, 77, 85], Infinite Impulse Response (IIR) [38] and Savitzky-Golay Polynomial Least Squares (SG) [41] filters had also been proposed.

There were other phase-modulation methods proposed to address the DC offset. These include using arctangent demodulation technique with DC offset calibrated through empty-room measurements [72], or at predetermined displacement range and periodic motions measurements [86]. However, these methods may not be valid because the DC offset value will depend on the surface reflectivity, the size of the stationary portion of the target and it cannot be calibrated other than the subject under test [72]. Complex signal demodulation method using Bessel's functions were explored to remove DC offset; however, it is still affected by the even order harmonics that are present in the baseband signal [87].

1.5.2 Phase-Nulling Cancellation

The main limitation in the Doppler radar measurement of periodic motions is the presence of phase-nulling or null-point. The most prevailing solution is the quadrature (I/Q) architecture, where at least one of the outputs I/Q is not at null-point. Channel

selection is then required to select the most optimum channel for processing at any given point in time [36, 41, 73]. However, the I/Q output channels are not always in quadrature because of the inherent amplitude and phase imbalance due to the imperfect system components [86]. The contribution of extra flicker noise caused by the mixers also contribute to the degradation of the detection accuracy [73].

The arctangent demodulation method combines the in-phase and quadrature (i.e., ±90° out-of-phases) baseband signals into a single channel to eliminate null-point. The equation that governs the extraction of angle/phase from *I* and *Q* channels is provided in (16), where $\Phi_r(t)$ is the demodulated Doppler angle/phase in radians.

$$\Phi_r(t) = tan^{-1}\left(\frac{Q(t)}{I(t)}\right) \tag{16}$$

The successful arctangent demodulation depends on the correction of channel imbalances and the removal of undesired DC offsets [88]. Channel imbalances can be corrected by using Gram-Schmidt procedure [88], however complex calibrations on the DC offsets are required for accurate demodulation [36, 73].

The Self-Injection-Locked (PSIL) oscillator with dual-tuning, voltage-controlled oscillator and single-channel receiver topology, using path-diversity transmission (where one path is 90° out-of-phases) was proposed to address the null-point issue. The path-diversity proposal is the periodic switching, to ensure at least one path is at optimal point while other experienced a null-point. The reported advantage of path-diversity transmission is the reduced average transmitted power. In other words, PSIL with path-diversity is more similar to the pulsed-wave radar topology [73].

There are several other radar topologies explored to overcome the phase-nulling issue. Topologies such as phase-diversity using phase-shifted two-channel receiver, two-channel receiver with displaced antennas, single-channel receiver with variable phase-shifter, and frequency-diversity (e.g., double sideband) transmission (to ensure at least one of the sidebands is not at null-point) were reported [42].

A "Relative Demodulation[1]" technique had also been proposed to address the phase-nulling and DC offsets issues in quadrature (I/Q) architecture demodulation. This technique pivoted from the conventional displacement and/or phase-shift analysis to introduce derivatives analysis. The "Relative Demodulation" technique provides real-time DC offsets, clutters, and null-points automatic elimination. The technique also approximates the instantaneous derivatives of the subject's chest periodic motions with the separation of the instantaneous subject's respiratory and heart periodic displacements [57]. The "Relative Demodulation" equation that governs the extraction of the chest motions velocity (v(t)) is in (17) and (18).

$$v(t) = \frac{\lambda}{8\pi}\left(\frac{kQ'(t)}{(I(t) - V_I)} - \frac{I'(t)}{k\big(Q(t) - V_Q\big)}\right) \quad (ms^{-1}) \tag{17}$$

$$k = \frac{A_I}{A_Q} \tag{18}$$

Where: "A_I" and "A_Q" are the amplitude gain constants of I and Q channels.

1.5.3 Multi-Targets and Motions Artefacts Cancellation

Even through the literatures that are reported to have addressed noises associated with the Doppler radar for physiological measurements in a single-subject, the focus on addressing multi-targets cancellation methodologies has rather been limited.

One of the limitations of a non-contact Doppler radar system when measuring physiological vital signs is in its sensitivity to non-physiological motions of the subject, such as any background motions, body movements, body orientations, and multi-targets motions. For these types of interference, once occurred at the same frequency band as that of the physiological motion, it is extremely difficult to remove using simple filtering techniques. The consequence is the degradation of accuracy in the estimation of the physiological vital signs.

[1] "Relative Demodulation" is the author's published work in [57] and is presented in chapter 3 and chapter 7 of the Thesis.

In an attempt to address the multi-targets cancellation problem, a technique referred to as Generalized Likelihood Ratio Test (GLRT), based on a model of the heartbeat was proposed to firstly distinguish between the presence of 2, 1, or 0 subjects using a single-antenna Doppler radar system. Using multiple antennas will also result in the detection of up to 2N-1 subjects. The use of a single antenna method is based on the subject's heartbeat signature in the frequency domain, and the use of the multiple antennas method is based on the angle of signal arrival. The results demonstrated the theoretical concept, however the accuracy and reliability were not consistent when this method is used [89].

Multiple transceivers system had been reported to cancel the noise caused by random body movements. Additionally, the use of differential front-end Doppler radar operating at two different frequencies, with dual helical antennas, had also been reported to improve the performance in cancelling motion artefacts [90].

An alternative approach to quantify the physical characteristics of the subjects (such as orientations, body size, body mass index, sleeping positions, body responses to illuminating waves) had also been explored through the vital signs cross section approach [71, 91]. This approach considers the similarity between the conventional radar cross section affected by target geometry to the orientations and material composition. Regardless of the motions of the respiratory rate or heart rate, the vital sign cross section remains unchanged. This is a key element in human cardiopulmonary activity and can be used to distinguish the front and side torso of the measuring subject. The indicated body position can also be linked to the use of multi-targets cancellation and random body movements.

Arctangent demodulation and complex signal demodulation method using Bessel's functions and dual-radar systems had been reported to address the random body movements and DC offsets issues. The complex signal demodulation is simpler in implementation, robust in DC offsets elimination, and is more favorable for random body movement cancellation. However, the arctangent demodulation has the advantage of eliminating the harmonic and intermodulation interference at high frequencies using

high gain antennas. The common challenge faced by these methods is the present of even order harmonics in the baseband signal [7, 87, 92].

The Empirical Mode Decomposition (EMD) noted in the literatures as an effective method for analyzing non-stationary and non-linear signals. Its application for non-contact Doppler radar system in separating and removing motions artefacts was also proposed. As documented in the literatures, EMD can be used for breaking down the radar signal output into its Intrinsic Mode Functions (IMFs). The removal of the motions artefacts interferences is achieved by selecting the proper IMFs. However, the proposed EMD application has its limitation in handling the interferences that occurred at frequencies very close to the heart rate. EMD is also limited in removing interferences of the same type from the background objects [93].

A separation of mixed respiratory signals between two individuals, using dual-radar system and applying Blind Source Separation (BSS) signal processing technique had also been proposed. The method was confirmed using simulated and experimental results, however, the sample data was deemed to be too low to provide convincing evidence of the reported accuracy and reliability [94].

Chen et al. proposed a separation of mixed respiratory signals between two individuals using dual-radar system and Blind Source Separation (BSS). The method was validated against simulated and experimental results; however, the sample data was too low to provide convincing evidence regarding the accuracy and reliability of the method. [94].

The Cyclostationary approach for body movement cancellation using the Doppler radar system had previously been proposed and the theory is believe to be one of the most suitable methods for analyzing signals that have a cyclic pattern of statistical properties. The advantage of this approach is the robustness of the cyclostationary processing in an environment with high noise and interferences. The numerical results demonstrated that the vital signs can be extracted as cyclic frequencies, independent of signal to noise ratio (SNR) and without any filtering or phase unwrapping. Experimental results also illustrate that when applying cyclostationary theory to a complex radar signal, the respiratory and heart rates can accurately be estimated in an environment with high

noise volume, long ranges and weak signals. This includes high body movement artefacts without the need of phase unwrapping or demodulation [95].

A frequency domain signal processing method had been reported as being able to extract both respiratory and heart rates for single and multiple subjects [96]. For a single-subject, the signal processing method utilized a digital FIR filter with Kaiser Window functions to achieve a relatively smooth pass-band amplitude response and to increase the stop-band attenuation. For two-subjects, two-radars are used with natural gradient Blind Source Separation (BSS) algorithm to separate the mixed signals in real-time. The average respiratory rate error percentage ranges between 4.25–6.6% and the heart rate is approximately around 6.25%. The paper noted that the respiratory and heart rates can be successfully extracted from a single subject, and mixed signals can be separated with two subjects. However, the number of population samples is too low and could not effectively conclude the robustness, accuracy or reliability of the method.

1.6 Categories of Non-Contact Doppler Radar Signal Processing Techniques

To-date, signal processing techniques being investigated and reported in literatures for the non-contact Doppler radar can be categorized into the following four categories:

1. Time-Frequency Analysis – this methodology uses time-series and frequency domain as the basis of signals analysis.

2. Numerical Analysis – this methodology uses numerical techniques such as statistical, transformation and complex frequency as the basis of signals analysis.

3. Classification and Training – this methodology utilizes machine learning methodologies and algorithms as the basis of signals analysis and prediction.

4. Other Methodologies: these methodologies utilize experimental and mathematical modelling as the basis of signals analysis and estimation.

The subsequent sub-sections provide details on each of the identified categories.

1.6.1 Time-Frequency Analysis

Numerous works had been explored using the time-domain autocorrelation with peak detection, autocorrelation output with Fast Fourier Transform (FFT) [35, 77] and statistical analysis [36, 41, 79] to detect both respiratory and heart rate peaks. The time-domain peak detection method, with the addition of smoothing methods, such as the Newton relation, had been reported in the literatures as having achieved the detection of the variability of peaks interval, revealing information such as heart rate variability (HRV) for diagnosis and prognosis [36, 60, 97].

Frequency-domain analysis applying FFT or alternative Chirp Z-Transform (CZT) [42] with or without Fourier Spectral Subtraction (FSS) [98], had been proposed to identify the highest peak on the frequency-domain at a specific bandwidth targeting respiratory or heart rate. The highest peak at the frequency detected correlates to the rate of the targeted physiological measurement such as respiratory or heart rates. The ranges of the reported filter bandwidth frequencies for respiratory rate are from 0.1–0.5 Hz which is equivalent to 6–30 breaths per minute. The heart rate frequencies are from 0.8–2.0 Hz which is equivalent to 48–120 beats per minute [7, 35, 41, 56, 57, 76, 77, 79, 81, 85].

Another time-frequency domain analysis proposed was the application of Gabor transform, which is basically a Short Time Fourier Transform (STFT) component selection and Gabor expansion, to identify patterns in the time-frequency domain and to extract vital signs such as respiratory and heart rates. This approach differs from the conventional approach of phase observation in the baseband signal. The experimental results noted an accuracy of less than three beats per minute error in measuring heart rate with motion artefacts. However, identifying a best fit pattern for the vital signs in time-frequency domain, especially for respiratory, still poses a difficult challenge for this approach [99].

Additionally, it had also been reported in literatures that since there is a large difference in respiratory and heartbeat induced displacements, the simultaneous measures of the respiratory and heart rates will require a large dynamic range to cover the substantial difference in signal levels. The higher order harmonics of the respiratory rate near the heart rate may appear and can cause an error in the heart rate measurement. Complex signal demodulation without the need for DC offset calibration in the frequency-domain had also been proposed to eliminate the harmonics interference problem. Experimental results demonstrated that when the harmonics of the respiration signal is strong, the proposed harmonics cancellation method can reduce the average error from 15.9% to 3.2% [100].

There are studies which reported some commendable achievements, such as error of less than 0.5 breath per minute for respiratory rate and one beat per minute for heart rate [35, 36, 77]. In addition, the achieved accuracy of the Doppler radar in measuring physiological parameters, such as respiratory rate is 92% [56], heart rate is 88% [56, 76, 97] to 91% [57], and with the addition of harmonics interference, the average error can be reduced further to 3.2% [100]. However, conventional FFT may not always be able to reliably separate the rich sinusoidal components due to smearing and leakage problems, particularly from the limited data samples [90]. The number of samples under study is also often too low to conclusively verify and validate the accuracy, reliability, and robustness of the proposed methods.

1.6.2 Numerical Analysis

There are a number of discretized numerical signal processing algorithms reported for the physiological vital signs estimations [101]. The first and simplest approach reported is the Mean of Signals (MEAN) method, with the assumption of phase changes varying between 0–2π uniformly and the offset is stable in a single window. The second approach is the Least Squares (LS) method, where the offset is fixed in small duration and the selected data samples fitted on a circle (the circle is plotted on Lissajous curve). The third is the Hough Transformation (HOUGH) method, applicable for data samples that distributed inhomogeneously, for example, when the target has no motion and caused biased estimation. The fourth approach is the Particle Filter (PF) method, a kind

of Bayesian Filter, which features robust estimation of the state and less restriction on the filter design. The fifth approach is the Direct Phase Estimation, based on Vector Difference (DIFF) method to estimate the phase changes by calculating the angle differences in which the estimation of offsets is not required. The experimental results demonstrated that the phase estimation based on LS method, is the most preferable approach for respiratory measurements and with respect to accuracy and calculation time.

The Extended Kalman Filter (EKF) approach for both respiratory and heart rates estimation had also been proposed [102]. The proposed EKF is a non-linear extension of the earlier conventional Kalman Filter (KF) proposal. The EKF algorithm is base on defining a state space model of the quadrature I/Q signals in combination with EKF to simultaneously estimate the respiratory and heart rates using unified statistically approach. The experimental results illustrate an acceptable level of accuracy with an error of approximately 1.7 beats per minute for heart rate. However, there is still a lack of dynamic modelling for other sources of noise and the comparison against other current methodologies and techniques [88].

The use of the Wavelet Transform (WT) [103], Wavelet Filter [104], Wavelet Packet Decomposition (WPD) [56], Discrete Wavelet Transform (DWT) and Complex Wavelet Transform (CWT) with Morlet mother wavelet [38] had also been proposed in literatures for the respiratory and heart rate estimations. The advantage of the Wavelet analysis over conventional methods, such as FFT, is that Wavelet design to operate on non-stationary signals and retains time and frequency information, providing good frequency resolution at lower frequencies. The experimental results demonstrate that the wavelet frequency has an absence of harmonics, which is an advantage over the conventional FFT. Harmonics in conventional FFT can cause difficulty in detecting heart rates when the third and fourth harmonics of respiratory rate overlaps with the heart rate [103].

Another approach reported in literatures is the parametric and cyclic optimization approach referred to as the RELAX algorithm. RELAX is a spectral estimation and it is computationally efficient in comparison to many other spectral estimation algorithms.

However, it is still more computationally demanding than the conventional Periodogram. Both theoretical and experimental results have demonstrated success in mitigating the effects of smearing and leakage problems of the conventional Periodogram. The smearing and leakage problems are often due to limited data length of both respiratory and heart rates [105].

The Lomb-Scargle Periodogram had also been reported in literatures for respiratory rate estimation. An application of the Lomb-Scargle Periodogram as signal processing technique to identify respiratory rate in sleeping subjects had also been reported. When the Lomb-Scargle Periodogram is used, the corrupted signals, which are often cause by intermittent movements or motion artefacts, can be excluded by treating those portions as missing data segments. The results demonstrated that the Lomb-Scargle Periodogram had successfully used evenly sampled data, with periods of missing data, to achieve an average error of less than 0.4 breath per minute and standard deviation of 0.3 breath per minute for respiratory rate estimation [106].

1.6.3 Classification and Training

The Support Vector Machine (SVM) had been explored for the detection of aspiration and apnea events for those subjects in lying position [107]. The calculation of the SVM utilized the training sets of three portions and one test data portion with the assumption of near ideal low-disturbance environment. However, the results did not support the accuracy and reliability of the machine.

Sleep stages classification algorithm based on bodily movements and the variability of the respiratory changes had been proposed for the sleep/wake pattern recognition. The long-noted characteristic of the respiratory rate did appear to be steadier in both frequency and amplitude during the rapid-eye-movement (REM) stage compared to the wakefulness stage. The body movements also changed between sleep stages, with the proposed algorithm demonstrating an accuracy level of 69% for the awake state and 88% for the sleep stages. In general, there is good performance results demonstrated for this classification method in recognizing the five standard sleep stages (Stages I-IV and REM) [6] (sleep stages that are prior to AASM classification in 2007).

Additionally, a linear discriminants classifier based on bio-motions had also been proposed for sleep/wake pattern recognition. This method applied the initial training sets of six recordings to train the linear discriminants classifier in classifying sleep/wake states in sleeping subjects. The experimental results reported an overall per-subject accuracy of 78% [64].

Linear discriminants classifier-based detection algorithms using feature extraction, vector transformation and pattern recognition techniques had also been proposed to recognize Cheyne-Stokes respiration (CSR) and apnea-hypopnea index (AHI) events. The detection of CSR & AHI via non-contact Doppler radar is relatively new and very few attempts had been made. The experiments demonstrated promising result with correlation co-efficient of 0.87 with %CSR > 5.0 and 0.8 with AHI > 15.0. However tested samples were too low and require a larger study cohort to confirm the diagnostic value [66, 67].

1.6.4 Other Methodologies

The other methodologies category includes the DC reconstruction and calibration techniques that are proposed to extract the tidal volume measurement from the non-contact Doppler radar signal [62]. The experiments indicated that there is a linear relationship between lung volume and chest-wall displacement during unobstructed breathing. The relationship is then used to detect and estimate the lung volume or tidal volume measurement based on the output of the non-contact Doppler radar signal. The proposed DC reconstruction employs the integration of the AC-coupled signal and the calibration of the signal amplitude as a ratio against the spirometer sensors. The experimental results reported an average mean difference of 38.9 mL in seated subjects and 23.5 mL in supine subjects.

A pulmonary ventilation mathematical model and algorithm[2] that defines the relationship between the intrapulmonary pressure and the chest displacement had also been proposed [58]. The mathematical model and algorithm estimate the tidal volume from the non-contact Doppler radar I/Q signals from a set of 24 chronic heart failure

[2] Pulmonary ventilation mathematical model and algorithm is the author's published work in [58] and is presented in chapter 4 and chapter 7 of the Thesis.

(CHF) patients with median sleep duration of 7.76 h. The tidal volume estimation median accuracy achieved is 83.13%, with a median error of 57.32 milliliters.

These works demonstrated a potential application of non-contact continuous monitoring of intrapulmonary pressure and tidal volume during sleep in the home.

1.7 Ultra-Wide Band Doppler Radar

A simple architecture of ultra-wide band (UWB) system, as proposed in [69], requires only one antenna and a rather simple signal processing algorithms in frequency-domain (FFT analysis) to extract respiratory motions and to compensate for the body movements. The results demonstrated feasibility of concept however, it is deem not suitable for real-life applications. The reason for its unsuitability is due to the unrealistic hypothesis that respiration frequency is constant during body movement.

An alternative signal processing method for UWB radar using 2-D FFT and time–frequency analysis method S-Transform (ST) to detect and identify the subject's respiratory motions under strong clutter with high SNR had also been reported. Even though the results were promising, limitations such as using experimental data and low-sample population with stationary standing subjects, resulted in demonstrating feasibility of the method only [108].

Dual-pair sensors impulse UWB radar to track a single subject's respiratory motions had also been proposed. The signal processing technique is the Hidden Markov Model (HMM) based method, where the respiratory rate of the subject is estimated from the backscattered signals from the dual-pair receiver antennas. The results showed the estimated respiratory rate can be successfully extracted with an accuracy of 81% [109].

Another proposed detection algorithm, with three stages finite impulse response (FIR) filters in the fast-time domain and linear trend subtraction (LTS) algorithm, is also use for clutter suppression. The respiratory rate is estimated using improved harmogram matrix threshold-based detection method. Analysis of the results showed that

approximately 1.5 dB improvement of SNR and signal to clutter and noise (SNCR) in comparison with the algorithm proposed by Xu et al. [110].

Impulse UWB radar for both respiratory and heart rates detection for non-line-of-sight (NLOS) had also been reported. The proposed signal processing technique is derive from the Developed Adaptive Line Enhancer (DALE) technique. This technique processes the signals in discrete form with DALE FIR filter and the respiratory and the heart rates are estimated by finding the maximum peak. The results demonstrated that both respiratory and heart rates can be extracted using UWB, with the target subject located at non-line-of-sight, however, clutter, motions, and non-stationary complex scenarios still posed as a challenge [111].

A measurement method based on MUltiple SIgnal Classification (MUSIC) algorithm for through-wall life-signs detection had also been proposed. This method analyses the phase modulation, spatial smoothing de-correlation strategy that applied to the traditional algorithm for MUSIC, mandated to single out the spectral components of the received phase signal. The results indicated feasibility of the algorithm. However, performance is an area that will require further improvement [112].

Another signal processing methodology had been proposed to estimate sleep apnea detection and respiratory rate from a single-subject measurement [113]. The signal processing incorporates the suppressing of clutter, body movement and body orientation detection. The signal processing uses digitalized frequency domain technique with the estimation of respiratory rate determined from Lomb Periodogram algorithm. The removal of quasi-static clutter to enhance the breathing signal detection is achieve using a moving averaging filter. The body movements are removed using a threshold method, and motion is detected using the time delay that maximizes the received signal after a clutter removing algorithm is applied. The apnea periods detected after the clutter removal is define by the cessation of respiratory efforts. The results indicated that respiratory rates and apnea event detection can be successfully extracted. However, a major challenge for the practical application of night breathing monitoring system is the noise signal produced by the body motion, where it is difficult to estimate the breathing rate during motion periods.

1.8 Challenges and Future Research Directions

1.8.1 Current Achievements

Prior to identifying the challenges and future research directions, it is important to provide an overview of the current achievements of sleep monitoring using non-contact Doppler radar.

The current achievements are summarized in Table 1.8.1.1.

Physiological Parameters	**Achievements**	**Year & References**
Respiratory rate[3]	Up to 91.52% accuracy with error up to ±1.31 breaths per minute.	2010 – 2015 [9, 52-57]
Heart rate[3]	Up to 91.29% accuracy with error up to ±6.16 beats per minute.	2013 – 2015 [8, 9, 55-57]
Heart rate variability	Error between 3–11% for single antenna, and 1–6% for dual antenna.	2012 [60]
Pulse pressure	Preliminary observation was made on the correlation between the pulse pressure and cardiac motion.	2011 [61]
Intrapulmonary pressure[4]	Demonstrated as feasible through modelling and interrelated to the tidal volume estimation accuracy.	2016 [58]
Tidal volume[4]	Up to 83.13% accuracy with error up to 57.32 milliliters.	2013 – 2016 [58, 62, 63]
Sleep/wake	Up to 69% for awake state and 88% for sleep	2008 & 2011

[3] Part of respiratory rate and heart rate achievements are the author's published work in [57] and are presented in chapter 3 and chapter 7 of the Thesis.

[4] Intrapulmonary pressure and tidal volume achievement is the author's published work in [58] and is presented in chapter 4 and chapter 7 of the Thesis.

pattern	stages.	[6, 64]
Apnea-hypopnea index	Overall accuracy of 85.8% with 70% sensitivity and 89% specificity.	2009 – 2016 [21, 65, 66]
Cheyne-Stokes Respiration	Correlation coefficient of 0.87 with %CSR > 5 and 0.8 with AHI > 15.	2013 [67]
Body orientations[5]	Overall accuracy of 99.2%.	2017 [59]

Table 1.8.1.1 – Sleep Monitoring Using Non-Contact Doppler Radar Achievements

1.8.2 Challenges and Future Research Directions

There are numerous published examples in the literatures regarding non-contact assessments of respiratory and heart rates, however there has been limited attempts made for the non-contact assessment of heart rate variability. It is also important to emphasize that the tendencies of the reported achievements on the non-contact physiological vital signs estimations, is based on "stationary" and "direct-facing" subject measurements, which is not an ideal scenario for sleep monitoring. There is recognition that the assessment of non-contact heart rate and heart rate variability, with "non-stationary" and "non-direct facing" subject poses a greater challenge in the signal processing of the non-contact Doppler radar system [8, 9]. In conjunction with continuous improvements on the accuracy of non-contact physiological vital signs estimations, there are two important areas in the non-contact sleep monitoring space that future researches may want to consider:

1. Firstly, it is recommended that future research be broadened to include non-contact assessment of the heart rate and the heart rate variability, as well as, targeting sleep monitoring with "non-stationary" and "non-direct facing" subject measurements. Additionally, pulse pressure, intrapulmonary pressure, tidal volume, minute ventilation, air flow, oxygen saturation, and Cheyne-Stokes respirations estimations are also encourage to be explored extensively. The future achievements in these areas will significantly

[5] Body orientations prediction is the author's published work in [59] and is presented in chapter 7 of the Thesis.

contribute to the screening, diagnosing and monitoring of cardiovascular comorbidity in obstructive sleep apnea (OSA) patients. This will also lead to new opportunities and market potentials towards Cardiology in Sleep Disordered Breathing (SDB).

2. Secondly, it is recommended that future research be broadened to include the complex sleep environment, such as noises associated with unpredictable body movements, body orientations, the change in sleeping posture, multi-subjects' cancellation, undesired harmonics and intermodulation. The future achievements in these areas will significantly contribute to the practical realization and commercialization of non-contact sleep monitoring and diagnosing technology.

With the increasing prevalence of OSA and its comorbidities, particularly cardiovascular comorbidity, there are substantial market potentials for the realization of non-contact continuous sleep monitoring technology. The most current prevailing market potential is the non-contact remote monitoring and screening of OSA at home. The applications of the non-contact Doppler radar for sleep monitoring can widely be utilized in homes, hospitals, primary care sectors, nursing home facilities and sleep laboratories.

1.9 Conclusion

Chapter 1 presented a comprehensive review of the non-contact Doppler radar technology for monitoring different physiological parameters during sleep. The presented information, covering most aspects of the current research field, can be used as foundational knowledge. Along with the challenges identified, the recommended future research directions can help facilitate the practical realization and commercialization of the technology, especially for obstructive sleep apnea (OSA) screening and monitoring which can be used in everyday life. The work presented in Chapter 1 is published in [114].

CHAPTER 2

SLEEP DISORDERS

Thesis Contribution 1: Knowledge

INTRODUCTION

Chapter 2 presents a general brief overview of the sleep disorders and focuses on one particular type of sleep disorders, i.e., the obstructive sleep apnea (OSA). The aim of chapter 2 is to outline the basic fundamentals of sleep disorders, which will provide background knowledge to the research works presented in the subsequent chapters of the Thesis.

2.1 Sleep Disorders

2.1.1 Sleep Disorders – Classification

According to the International Classification of Sleep Disorders (ICSD) revised edition published in 2001, sleep disorders (SD) is categorized into four main categories [115]:

1. Dyssomnias – disorders that produce either difficulty initiating or maintaining sleep or excessive sleepiness.

2. Parasomnias – disorders of arousal, partial arousal and sleep-stage transition.

3. Sleep Disorders Associated with Mental, Neurologic, or Other Medical Disorders – disorders that are not primarily sleep disorders but are mental, neurologic, or other medical disorders that have either sleep disturbance or excessive sleepiness as a major feature of the disorder.

4. Proposed Sleep Disorders – disorders for which there is insufficient information available to confirm their acceptance as definitive sleep disorders.

2.1.2 Sleep Disordered Breathing – Definition

ICSD also categorized Dyssomnias into 3 subcategories:

1. Intrinsic Sleep Disorders – are primarily sleep disorders that either originate or develop within the body or arise from causes within the body.

2. Extrinsic Sleep Disorders – include those disorders that originate or develop from causes outside of the body.

3. Circadian Rhythm Sleep Disorders – is the misalignment between actual sleep pattern and the sleep pattern that is desire or regard as the societal norm.

The Intrinsic Sleep Orders, subcategory (1) of Dyssomnias, is divided into the following 12 subgroups:

1. Psychophysiologic Insomnia
2. Sleep State Misperception
3. Idiopathic Insomnia
4. Narcolepsy

5. Recurrent Hypersomnia
6. Idiopathic Hypersomnia
7. Posttraumatic Hypersomnia
8. Obstructive Sleep Apnea Syndrome
9. Central Sleep Apnea Syndrome
10. Central Alveolar Hypoventilation Syndrome
11. Periodic Limb Movement Disorder
12. Restless Legs Syndrome

The Sleep Disordered Breathing (SDB) is the general term use to describe any sleep related breathing abnormalities. As described above, SDB falls under the Dyssomnias category, Intrinsic Sleep Disorders subcategory and it describes number of disorders including Obstructive Sleep Apnea Syndrome (OSAS) and Central Sleep Apnea Syndrome (CSAS).

It is also important to recognize that Obstructive Sleep Apnea Syndrome (OSAS) is the most common type of sleep disorder breathing [116].

2.2 Obstructive Sleep Apnea

2.2.1 Epidemiology

The Obstructive Sleep Apnea (OSA) is a widely spread phenomenon and over the last 30 years, there had been numerous medical literatures that reported the prevalence of OSA over the world-wide populations. OSA is increasingly recognize as an important cause of medical morbidity and mortality [3] affecting at least 4% of adult males and 2% of adult females [117]. In a study published in 2013, the prevalence of OSA had increased especially in the Unites State of America (USA) to 10–17% for adult males and 3–9% for adult females [118].

There are a number of studies conducted using large samples to represent the general population. These studies had been published in countries such as United States, Australia, Italy, Israel, Spain, India, China (specifically Hong Kong), Korea and ethnicity group of Danish populations. The world-wide OSA prevalence statistics are summarized in Table 2.2.1.1.

Country / Ethnicity	**Samples**	**Prevalence**		**References**
		Men	**Women**	
United States	602	4.0 %	2.0 %	Young et al. 1993 [117]
	1741	3.9 %	1.2 %	Bixler et al. 2001 [119]
	1520	10–17%	3–9%	Peppard et al. 2013 [118]
Australia	294	3.0 %	–	Bearpark et al. 1995 [120]
Italy	365	–	7.7 %	Ferini-Strambi et al. 1999 [121]
Israel	1502	3.0 %	–	Lavie 1983 c*ited in* Provini et al. 2003 [122]
Spain	1360	2.2 %	0.8 %	Marin et al. 1997 [123]
India	250	7.5 %	–	Udwadia et al. 2004 [124]
Hong Kong	153	4.1 %	–	Ip et al. 2001 [125]
	106	–	2.1 %	Ip et al. 2004 [126]
Korea	457	4.5 %	3.2 %	Kim et al. 2004 [127]
Danish population	748	1.9 %	0.9 %	Jennum & Sjol 1992 [128]

Table 2.2.1.1 – OSA Prevalence Statistics World-Wide

2.2.2 Pathophysiology

The obstructive sleep apnea (OSA) pathophysiological mechanism relates to the upper airway obstruction during sleep. It is important to provide a brief overview of the human pharynx anatomy, gas exchange, cardiovascular function and the automatic nervous system activity.

The human pharynx in Fig. 2.2.2.1 is a complex structure composed of more than 20 muscles and the pharyngeal passage is divided into four sections: nasopharynx (from the nasal turbinates to the start of the soft palate), velopharynx (from the start of the soft palate to the tip of the uvula), oropharynx (from the tip of the uvula to the tip of the epiglottis), and hypopharynx or laryngopharynx (from the tip of the epiglottis to the level of the vocal cords). The pharyngeal passage is utilized for three critical functions of respiration (maintain gas exchange), swallowing (facilitate movement of liquids and solids from the pharynx to the esophagus), and phonation or speech [129] [130].

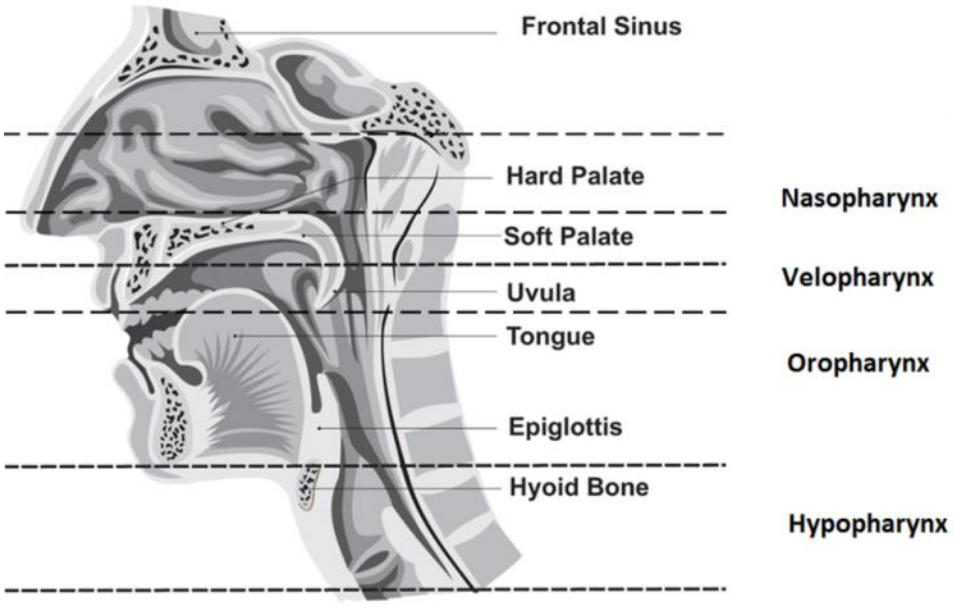

Figure 2.2.2.1 – Pharynx Anatomy

The risk of obstruction is interrelated to the geometric changes in the pharyngeal passage. When there is a relative increase in the intraluminal pressure during expiratory, the airway tends to enlarge, and vice versa, when there is a relative reduction in the intraluminal pressure during inspiratory, the airway tends to decrease in size. Particularly during sleep, if the intraluminal pressure is sufficiently negative it may facilitate a total collapse of the airway as illustrated in Fig. 2.2.2.2. In addition, when the muscles around the pharyngeal passage lose tone, there is an increased risk of airflow resistance during sleep and this can cause the upper airway to be obstructed. This in turn will create a predisposition to OSA [129] [130].

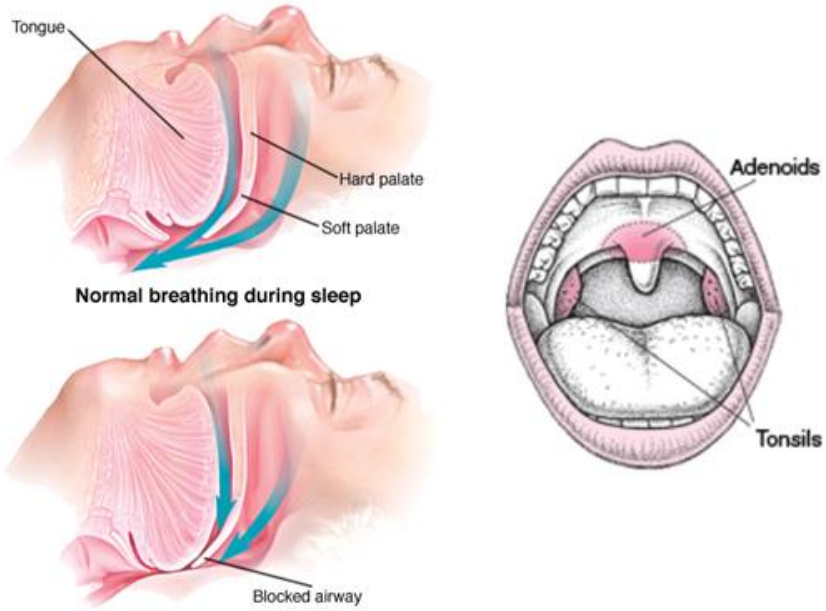

Figure 2.2.2.2 – Airway Obstruction During Sleep and Adenoids & Tonsil

There are number of anatomical abnormalities that can also lead to OSA including enlarged tonsils and adenoids, neck and jaw position, obesity, alcohol and some medications that can reduce the tone of the pharynx muscles [131] [130].

Gas exchange consequences often occur during an apnea event. When breathing ceases or when a person hyperventilates, the partial pressure of the oxygen in arterial blood (PaO_2) may decrease and the partial pressure of carbon dioxide in arterial blood ($PaCO_2$) may increase, causing changes in oxygen saturation (SaO_2) and impact the oxygen stores in the lung and carbon dioxide (CO_2) stores in the body. These will determine the degree of hypoxemia and hypercapnia that can occur following an apneic episode [132] [130].

Cardiovascular consequences from an apneic episode could result in hypoxemia and hypercapnia, leading to a change in the activity of the automatic nervous system. These changes to both the sympathetic and parasympathetic functions and will directly affect the cardiovascular function as illustrated in Fig. 2.2.2.3. Cardiac arrhythmias, bradycardia and tachycardia are reported as common symptoms for patients with OSA.

Importantly, the changes in cardiac rhythms may result in profound brady-arrhythmias or even asystole [130].

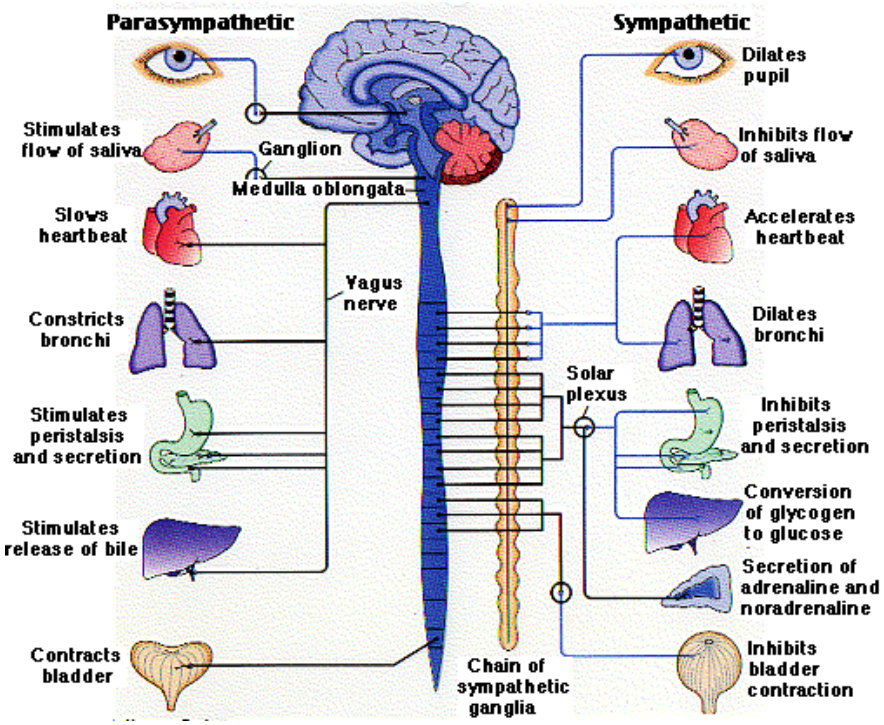

Figure 2.2.2.3 – Central Nervous System: Automatic Nervous System Activity

OSA is define as cessation of airflow due to the collapse of the upper airway for at least 10 seconds. Apnea Index (AI) is define as the number of apnea events per hour [133]. There are three types of apnea [134]:

1. Obstructive Apnea – this can occur when the respiratory effort is maintaining but ventilation decreases or disappears because of partial or total occlusion in the upper airway.

2. Central Apnea – this can occur when the respiratory effort is reduce resulting in reduced or absent ventilation.

3. Mixed Apnea – is an event that starts with the central apnea but ends with the obstructive apnea event.

Hypopnea is defined as a reduction in airflow by approximately 30% to 50% and often follows an arousal from sleep or a decrease in oxyhemoglobin saturation from 3% to 4%. Hypopnea Index (HI) is define as the number of hypopnea events per hour. These events are generally most prominent during the rapid-eye-movement (REM) sleep because of the hypotonia characteristics of the upper-airway muscles at this stage of sleep [133] [134] [135] [136].

Sleep apnea severity is assess based on the apnea-hypopnea index (AHI), which is the number of apnea and hypopnea events per hour of sleep [134]. According to the American Academy of Sleep Medicine [115] recommendations, the level of OSA is define using the AHI > 5 scoring system. Mild OSA will have AHI of 5 to 15, moderate OSA with AHI of 16 to 30, and severe OSA with AHI > 30.

The signs, symptoms and consequences of OSA as reported in the literatures include excessive daytime sleepiness due to abnormal sleep structure, tiredness with neuropsychological dysfunction, memory impairment, headache (especially during early hours of the day), abnormalities in gas exchange and cardiovascular function [133] [130]. These are a direct result of the derangements that occur due to the repetitive collapse of the upper airway, sleep fragmentation, hypoxemia, hypercapnia, marked swings in intrathoracic pressures, and the increase in sympathetic activity [137] [134].

2.2.3 Comorbidities

As cited in Valderas et al, 2011 [138], the term "comorbidity" was originally defined by Feinstein in 1970 as "*any distinct additional clinical entity that has existed or may occur during the clinical course of a patient who has the index disease under study*".

Research over the last 31 years, tracing back to the Wisconsin Study of 1988, indicates that OSA is an independent risk factor for a number of other disorders. OSA significantly increases the risk of many serious health condition and untreated OSA is significantly linked to the increased in morbidity and mortality [4].

In addition, the research publications over the last 20 years ranked the percentage of OSA comorbidities as follows:

1. 83% of patients with drug-resistance hypertension [139].
2. 77% of obesity [140].
3. 76% of congestive heart failure (CHF) [141].
4. 59% of pacemakers [142].
5. 49 % of atrial fibrillation (AF) [143].
6. 48% of type 2 diabetes mellitus [144].
7. 37% of all hypertensions (male subject only) [145].
8. 30% of coronary artery disease [146].

The graphical representation of the comorbidities statistics for patients with disorders who is also diagnose with OSA is included in Fig. 2.2.3.1.

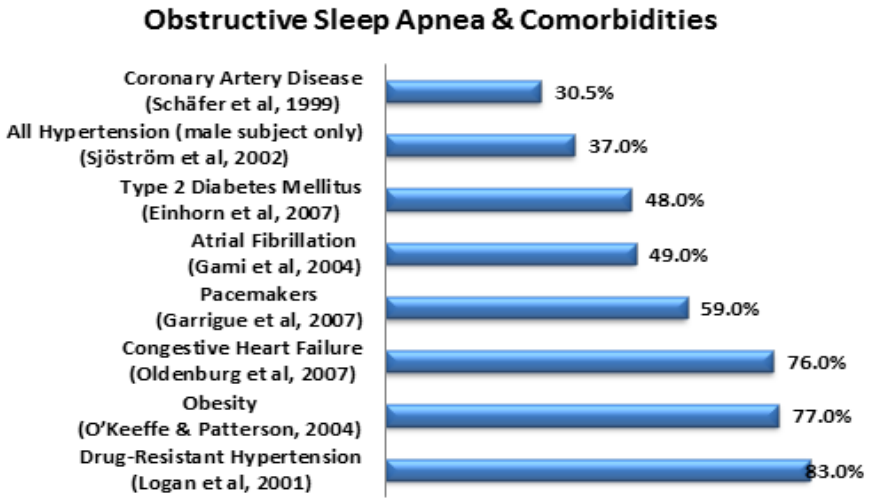

Figure 2.2.3.1 – Obstructive Sleep Apnea and Comorbidities Statistics

2.2.4 Obstructive Sleep Apnea & Cardiovascular Comorbidities

In the 1988 Wisconsin Study, an 18-year mortality follow-up study conducted on the population-based Wisconsin Sleep Cohort sample (n = 1,522), the results showed that people with untreated severe OSA (AHI ≥ 30), independent of sex, BMI, age, and other

potential confounders, had increased cardiovascular mortality of 5.2 times when compared to those with normal breathing during sleep. This study underscored the need for heightened clinical recognition and treatment of OSA [4].

As cited in Leung & Bradley, 2001 [147], according to the Sleep Heart Health Study, the first large-scale population-based study to examine the potential relationship between OSA and stroke in 6,424 subjects indicated that:

1. OSA modestly increased prevalence of stroke by 1.58 times (AHI > 11).

2. OSA was found to be an independent risk factor for coronary artery disease with an increased prevalence of 1.27 times (AHI > 11).

3. OSA and chronic heart failure (CHF) are associated with an increased prevalence of 2.38 times (AHI > 11) independent of other known risk factors.

It is also important to recognize that the treatment of severe and moderate OSA is associated with a 64% reduction in cardiovascular risk, independent of age, comorbidities and the pre-existing cardiovascular disease [5].

2.3 Conclusion

Chapter 2 presented an overview of sleep disorders and focuses on obstructive sleep apnea (OSA). The basic fundamentals of sleep disorders have been outlined and the background knowledge provided to assist in the understanding of the research works in the subsequent chapters of the Thesis.

CHAPTER 3

RELATIVE DEMODULATION

Thesis Contribution 2: Novel Theory 1

INTRODUCTION

Chapter 3 presents a novel real-time demodulation theory and technique for non-contact microwave Doppler radar system, named "Relative Demodulation". The name is given as an attribute to the application of "Relativity" concept in the demodulation of the subject's chest or abdomen periodic motions. In addition, a novel respiratory and heart rates estimation algorithm that utilizes the "Relative Demodulation" technique and the non-contact microwave Doppler radar is also presented.

3.1 Theory of Relative Demodulation

3.1.1 Continuous Time Domain

The non-contact Doppler radar system baseband quadrature outputs I and Q channels generally expressed as:

$$I(t) = V_I + A_I cos\left(\theta + \frac{4\pi x(t)}{\lambda} + \frac{4\pi y(t)}{\lambda} + \Delta\emptyset(t)\right) \quad (1)$$

$$Q(t) = V_Q + A_Q sin\left(\theta + \frac{4\pi x(t)}{\lambda} + \frac{4\pi y(t)}{\lambda} + \Delta\emptyset(t)\right) \quad (2)$$

$$\theta = \frac{4\pi d_0}{\lambda} + \theta_0 \quad (3)$$

$$\Delta\emptyset(t) = \emptyset(t) - \emptyset\left(t - \frac{2d_0}{c}\right) \quad (4)$$

Where:

- V_I & V_Q – the DC offsets of the channels.
- A_I & A_Q – the amplitude gains constants of the channels.
- θ_0 – the initial constant phase-shift of the system in radian.
- λ – the wave length, which equal to the speed of light divided by the radar operating frequency in Hertz.
- c – speed of light, i.e., 299,792,458 ms^{-1}.
- $\Delta\Phi$ – the phase noise of the system oscillation in radian.
- x(t) – function of respiratory that causes changes in the chest displacement in meter.
- y(t) – function of heart that causes changes in the chest displacement in meter.

For physiological vital signs monitoring, the subject's chest or abdomen distance is usually within 0.5–3.0 m, which can make the "$\Delta\phi(t)$" approaches zero, therefore, "$\Delta\phi(t)$" can be neglected.

In context of "Relative Demodulation", I and Q channels from this point onwards are to be referred to as "Observer I" and "Observer Q". The subject's chest or abdomen periodic motion is to be referred to as "Observation Target". The fundamental "Relative Demodulation" concept for non-contact Doppler bio-motion system is as follows:

- Both “Observer I” and “Observer Q” are moving at the same speed, however, at different phases.

- The instantaneous derivatives of the “Observer I” and “Observer Q” are “relative to” and “impacted by” the instantaneous derivatives of the “Observation Target”.

- At any given point in time, both “Observer I” and “Observer Q” observed the same “Observation Target” instantaneous derivatives with respect to the other “Observer”.

The “Relative Demodulation” concept diagram is present in Fig. 3.1.1.1.

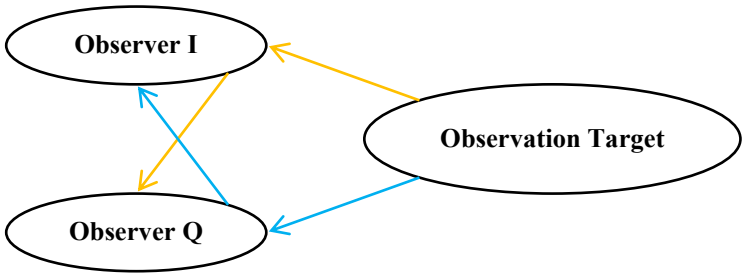

Figure 3.1.1.1 – Relative Demodulation Concept Diagram

The “Observation Target” instantaneous velocity as observed by “Observer I” with respect to “Observer Q” with unit “ms^{-1}” is defined as:

$$\frac{d}{dt}I(t) = -\frac{4\pi}{\lambda}\left(\frac{d}{dt}x(t) + \frac{d}{dt}y(t)\right)A_I sin\left(\theta_0 + \frac{4\pi}{\lambda}\left(d_0 + x(t) + y(t)\right)\right) \quad (5)$$

$$\frac{d}{dt}x(t) + \frac{d}{dt}y(t) = -\frac{\lambda}{4\pi}\left(\frac{A_Q I'(t)}{A_I\left(Q(t) - V_Q\right)}\right) \quad (ms^{-1}) \quad (6)$$

The “Observation Target” instantaneous velocity as observed by “Observer Q” with respect to “Observer I” with unit “ms^{-1}” is defined as:

$$\frac{d}{dt}Q(t) = \frac{4\pi}{\lambda}\left(\frac{d}{dt}x(t) + \frac{d}{dt}y(t)\right)A_Q cos\left(\theta_0 + \frac{4\pi}{\lambda}\big(d_0 + x(t) + y(t)\big)\right) \quad (7)$$

$$\frac{d}{dt}x(t) + \frac{d}{dt}y(t) = \frac{\lambda}{4\pi}\left(\frac{A_I Q'(t)}{A_Q(I(t) - V_I)}\right) \quad (ms^{-1}) \quad (8)$$

As shown in (6) and (8), both "Observer I" and "Observer Q" observed the same "Observation Target" instantaneous velocity. The null-points can be eliminated by averaging the observed instantaneous velocity of both "Observer I" and "Observer Q". Therefore, the resultant "Observation Target" instantaneous velocity "v(t)" with unit "ms^{-1}" is defined as:

$$v(t) = x'(t) + y'(t) = \frac{\lambda}{8\pi}\left(\frac{A_I Q'(t)}{A_Q(I(t) - V_I)} - \frac{A_Q I'(t)}{A_I\big(Q(t) - V_Q\big)}\right) \quad (ms^{-1}) \quad (9)$$

As shown in (9) the DC offsets of the channels eliminated by the subtraction of "V_I" and "V_Q". The constant phase-shift and clutters also eliminated by the first derivative.

Let "$h_r(t)$" be the respiratory band-pass filter (RBPF), which has the frequency bandwidth of normal respiratory rate range. The filter type and bandwidth will be discussed in details in section 3.2.3. By convoluting the RBPF with the resultant "Observation Target" instantaneous velocity, the "Observation Target" instantaneous respiratory velocity with unit "ms^{-1}" is defined as:

$$x'(t) = \big(h_r(t) * v(t)\big) \quad (ms^{-1}) \quad (10)$$

The "Observation Target" instantaneous respiratory displacement "x(t)" with unit "m" is obtain by integration and defined as:

$$x(t) = \int \big(h_r(t) * v(t)\big)dt \quad (m) \quad (11)$$

According to anatomy and physiology, respiration requires inspiration and expiration efforts, which contains both velocity and acceleration. The heart systole (contraction)

and diastole (relaxation) also contains both velocity and acceleration. The chest periodic displacements are cause by the velocity and acceleration of the inspiration-expiration and systole-diastole cycles in combination. Physics indicated that the third derivative, often referred to as "jerk" describes the changes of acceleration. Therefore, to describe the changes that the heart acceleration acted on the respiration acceleration, the resultant "Observation Target" instantaneous jerk has to be derived. Therefore, the resultant "Observation Target" instantaneous jerk with unit "ms^{-3}" is defined as:

$$x'''(t) + y'''(t) = \frac{\lambda}{8\pi}\left(\frac{Q'(t)}{I(t) - V} - \frac{I'(t)}{Q(t) - V}\right)'' \tag{12}$$

Let "$h_h(t)$" be the heart band-pass filter (HBPF), which has the frequency bandwidth of normal heart rate range. The filter type and bandwidth will be discussed in details in section 3.2.3. By convoluting the HBPF with the resultant "Observation Target" instantaneous jerk, the "Observation Target" instantaneous heart jerk with unit "ms^{-3}" is defined as:

$$y'''(t) = \big(h_h(t) * v''(t)\big) \quad (ms^{-3}) \tag{13}$$

The "Observation Target" instantaneous heart displacement with unit "m" can also be obtained by integration and defined as:

$$y(t) = \int \big(h_h(t) * v''(t)\big)dt \quad (m) \tag{14}$$

3.1.2 Discretized Time Domain

Backwards-difference numerical approximation has been selected for its simplicity in implementation to discretize the real-time "Relative Demodulation" derivatives.

$$v[n] = \frac{\lambda}{8\pi} f_s \left[\frac{A_I\big[Q[n] - Q[n-1]\big]}{A_Q[I[n] - V_I]} - \frac{A_Q\big[I[n] - I[n-1]\big]}{A_I\big[Q[n] - V_Q\big]}\right] \quad (ms^{-1}) \tag{15}$$

$$x'[n] = f_s\big[h_r[n] * v[n]\big] \quad (ms^{-1}) \tag{16}$$

$$x'''[n] + y'''[n] = {f_s}^2\big[v[n] - 2v[n-1] + v[n-2]\big] \quad (ms^{-3}) \tag{17}$$

$$y'''[n] = {f_s}^2\Big[h_h[n] * \big[v[n] - 2v[n-1] + v[n-2]\big]\Big] \quad (ms^{-3}) \tag{18}$$

Trapezoidal numerical integration approximation with unit spacing was selected for its simplicity in implementation to discretize the real-time "Relative Demodulation" displacements. The discretized real-time "Relative Demodulation" equations with "fs" as the analogue-to-digital (ADC) sample rate in Hertz are defined as:

$$x[n] = x[n-1] + \left[\frac{x'[n] + x'[n-1]}{2f_s}\right] \quad (m) \tag{19}$$

$$a_h[n] = a_h[n-1] + \left[\frac{y'''[n] + y'''[n-1]}{2f_s}\right] \quad (ms^{-2}) \tag{20}$$

$$v_h[n] = v_h[n-1] + \left[\frac{a_h[n] + a_h[n-1]}{2f_s}\right] \quad (ms^{-1}) \tag{21}$$

$$y[n] = y[n-1] + \left[\frac{v_h[n] + v_h[n-1]}{2f_s}\right] \quad (m) \tag{22}$$

Where:

- $a_h[n]$ – the "Observation Target" instantaneous heart acceleration.
- $v_h[n]$ – the "Observation Target" instantaneous heart velocity.

In real-world system implementation, a high-pass filter is required to be applied to the instantaneous velocity prior to deriving the instantaneous displacement. This is to eliminate the non-zero offsets or DC base wanders and to prevent DC accumulation in integration.

3.2 Respiratory and Heart Rates Estimation Algorithm

Section 3.2 introduces the novel inspiration and expiration detection, systole and diastole detection, and respiratory and heart rates estimation algorithms. The novelty of these algorithms include real-time, simple, fast, accurate, low computational, applicable for the embedded applications and it does not require advanced signal processing methods, such as, Wavelet Packet Decomposition (WPD), Fast Fourier Transform (FFT), Short Time Fourier Transform (STFT), local maxima detection or other nonlinear numerical techniques.

3.2.1 Algorithm Block Diagram

The block diagram of the respiratory and heart rates estimation algorithm is in Fig. 3.2.1.1.

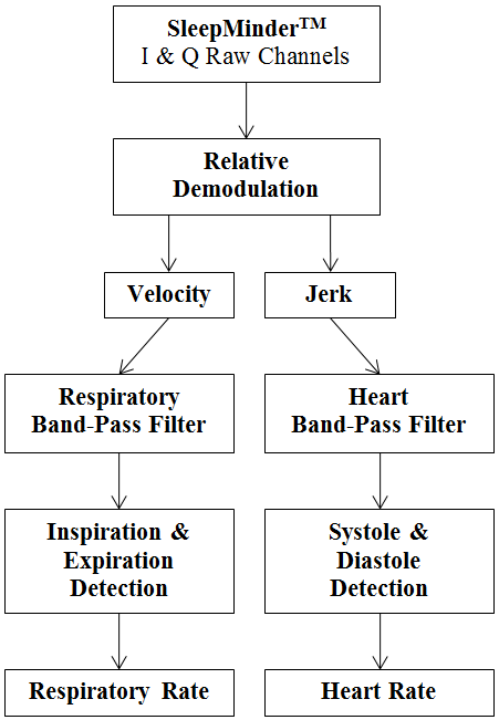

Figure 3.2.1.1 – Respiratory and Heart Rates Estimation Algorithm Block Diagram

3.2.2 DC Offsets and Amplitude Gain Constants

As documented in Appendix I, section A.I.I, the SleepMinder™ analogue-to-digital converter (ADC) voltage resolution is 0–3.2 V. The voltage mean value, which is the reference DC offset, is equal to 1.6 V. Therefore, "V_I" and "V_Q" are also approximately equal to 1.6 V. Due to the Intellectual Property (IP) agreement with ResMed Pty Ltd., the SleepMinder™ unpublished and undisclosed technical papers will not be referenced in the Thesis. However, information with respect to the amplitude gain constants can be included. As specified in the SleepMinder™ technical papers, the amplitude gain constants are approximately equaled for both channels "I" and "Q" and are typically 15–20 dB. Therefore, the amplitude gains constants "A_I" and "A_Q" are approximately equaled and their ratio "k" is also approximately equaled to 1.0.

3.2.3 Band-Pass Filter Type and Frequency Bandwidth

The Butterworth band-pass filter was chosen to be implemented both the respiratory band-pass filter (RBPF) and the heart band-pass filter (HBPF). The reason for choosing this type of filter is because the frequency response of the Butterworth filter is maximally flat (i.e. has no ripples) in the pass-band and it rolls off towards zero in the stop-band. In addition, the implementation of the Butterworth filter is much simpler and performs much faster compared to other finite impulse response (FIR) filters, which is more applicable for embedded applications.

The selected frequency bandwidth for RBPF is between 0.2–0.5 Hz corresponds to 12–30 breaths per minute for respiratory rate. The selected frequency bandwidth for HBPF is between 0.7–1.6 Hz corresponds to 42–96 beats per minute for heart rate. The Butterworth band-pass filter minimum order has been chosen to be at 6^{th} order with unity gain.

3.2.4 Inspiration and Expiration Detection Algorithm

The inspiration and expiration detection algorithm relied on the discretized "Observation Target" instantaneous respiratory velocity as specified in (16). Peaks and troughs detection using displacements may produce unreliable results due to the additions of heart displacements, body motions and noises. Relying on the peaks and troughs alone will not always guarantee that the inspiration and expiration are correctly detected, especially during periods of significant body movements. Using the velocity approach will give a better and reliable result with the property of zero-crossing when velocity changes direction, which should also correspond to inspiration and expiration. Inspirations are those zero-crossing with negative tangent and expirations are those zero-crossing with positive tangent. By incorporating a set of the detection rules, the inspiration and expiration can reliably be detected. The detection rule for inspiration "i[n]" and expiration "e[n]" is defined as:

$$i[n] = \begin{cases} 1 & , \quad x'[n] \leq 0 \ \wedge \ x'[n-1] > 0 \\ 0 & , \quad otherwise \end{cases} \tag{23}$$

$$e[n] = \begin{cases} 1 & , \quad x'[n] \geq 0 \ \wedge \ x'[n-1] < 0 \\ 0 & , \quad otherwise \end{cases} \tag{24}$$

The additional rules, acting as additional filtering, for inspiration and expiration detection are as follows:

1. The current detected inspiration/expiration index with value equal to 1, subtracting the previous detected inspiration/expiration index with value equal to 1, have to be greater than or equal to "$2f_s$", where "f_s" is the ADC sample rate in Hertz. This allows up to a maximum of 0.5 Hz, and corresponds to 30 breaths/min to be detected, any higher frequency will be ignored.

2. The current detected inspiration/expiration index with value equal to 1, subtracting the previous detected expiration/inspiration index with value equal to 1, have to be greater than or equal to "f_s".

3.2.5 Systole and Diastole Detection Algorithm

The key to the systole and diastole detection algorithm is the reliance on the discretized "Observation Target" instantaneous heart jerk as specified in (18). Using jerk will give a better and reliable result with the property of zero-crossing when jerk changes direction, this corresponds to the systole and diastole. Systoles are those zero-crossing with negative tangent and diastoles are those zero-crossing with positive tangent. By incorporating a set of detection rules, the systole and diastole can reliably be detected. The detection rule for systole "s[n]" and diastole "d[n]" is defined as:

$$s[n] = \begin{cases} 1 & , \quad y'''[n] \leq 0 \ \wedge \ y'''[n-1] > 0 \\ 0 & , \quad otherwise \end{cases} \tag{25}$$

$$d[n] = \begin{cases} 1 & , \quad y'''[n] \geq 0 \ \wedge \ y'''[n-1] < 0 \\ 0 & , \quad otherwise \end{cases} \tag{26}$$

The additional rules, acting as additional filtering, for the systole and diastole detection are as follows:

1. The current detected systole/diastole index with value equal to 1, subtracting the previous detected systole/diastole index with value equal to 1, have to be greater than or equal to "0.5 f_s", where "f_s" is the ADC sample rate in Hertz. This allows up to a maximum of 2 Hz, and corresponds to 120 beats/min to be detected, any higher frequency will be ignored.

2. The current detected systole/diastole index with value equal to 1, subtracting the previous detected diastole/systole index with value equal to 1, have to be greater than or equal to "0.25f_s".

3.2.6 Respiratory and Heart Rate Estimation Algorithm

The respiratory rate can easily be estimated from the averaged sum of the detected inspiration and expiration cycles per selected window-width.

The heart rate can easily be estimated from the averaged sum of the detected systole and diastole cycles per selected window-width.

The algorithms are flexible in window-width selection, however, for the research works presented in the Thesis, a fixed window-width of 60 seconds (2 epochs[6]) and a sliding fixed window-width of 30 seconds (1 epoch) are employed.

3.3 Conclusion

Chapter 3 contributes to the field of non-contact sleep monitoring by introducing "Relative Demodulation", a novel real-time demodulation theory and technique for the non-contact microwave Doppler radar system. The novelty of "Relative Demodulation" technique is that it pivots from conventional displacements analysis to introduce derivatives analysis. This technique is real-time, simple, fast, accurate, low computational, applicable for embedded applications and provides the following advantages:

1. Null-points automatic elimination.
2. Constant phase-shift and clutters automatic elimination.
3. DC offsets automatic elimination.
4. Real-time approximations of the instantaneous derivatives of the subject's chest or abdomen periodic motions.
5. Real-time approximations and separation of the instantaneous subject's respiratory and heart periodic displacements.

In addition, based on the real-time respiratory and heart displacements approximated by "Relative Demodulation", the subject's respiratory and heart rates can also be estimated. The real-life applications and results of "Relative Demodulation" in non-contact sleep monitoring is presented in Chapter 7, section 7.1 of the Thesis. The work presented in Chapter 3 is published in [57] and patented in [148-150].

[6] Epoch term in sleep is define as 30 seconds block interval. This definition is given by the American Academy of Sleep Medicine (AASM).

CHAPTER 4

PULMONARY VENTILATION MATHEMATICAL MODEL

Thesis Contribution 3: Novel Theory 2

INTRODUCTION

Chapter 4 presents a novel pulmonary ventilation mathematical model that defines the relationship between the intrapulmonary pressure and the chest displacement. In addition, a novel tidal volume estimation algorithm that utilizes the mathematical model and the non-contact microwave Doppler radar is also presented.

4.1 Pulmonary Ventilation Model

4.1.1 Theoretical Analysis and Modeling

The process of gas exchange in human body consists of three basic steps: pulmonary ventilation, external respiration and internal respiration. The focus of pulmonary ventilation is to derive a novel mathematical model that defines the relationship between

the intrapulmonary pressure and the chest displacement. The outcome of the derived relationship is the estimation of tidal volume based on the chest displacement. The model takes an engineering approach with the utilization of electronic elements to describe the time-varying differential relationships. The lungs are model as a container of certain volume that can hold a certain amount of pressurized gas, which can be described using capacitor "C". The resistance and elasticity in the respiratory system are describe using resistor "R" and inductor "L". The model presented in the Laplace's transform s-domain; this is for mathematical convenience in analyzing the time-varying differential parameters. The novel pulmonary ventilation model is in Fig. 4.1.1.1.

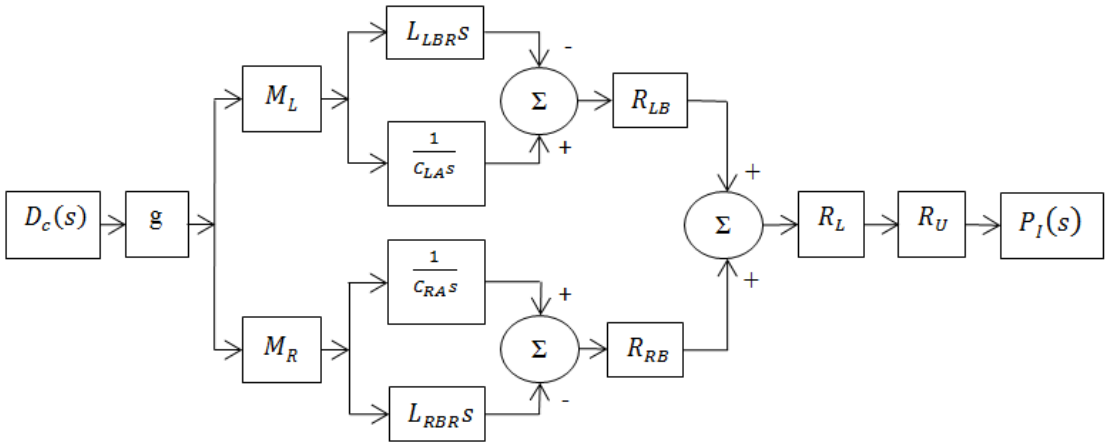

Figure 4.1.1.1 – Pulmonary Ventilation Model

The descriptions of the used symbols are as follows:

- $D_c(s)$ – chest displacement in meter (m).
- g – standard gravitational constant, i.e., 9.80665 ms^{-2}.
- M_L & M_R – left and right mass portion of the total subject's body mass in kilograms (kg) residing at the chest area.
- C_{LA} & C_{RA} – left and right lungs volume that can hold a certain amount of pressurized gas.
- L_{LBR} & L_{RBR} – left and right bronchiole and terminal bronchiole elasticity, which cause changes in resistance due to changes in gas pressure.
- R_{LB} & R_{RB} – left and right secondary and tertiary bronchus resistance.

- R_L – larynx and trachea resistance.
- R_U – upper respiratory system airway resistance, including the nose, pharynx & associated structures.
- PI(s) – intrapulmonary pressure.

From Fig. 4.1.1.1, the transfer function of the pulmonary ventilation model is defined as:

$$\frac{P_I(s)}{D_c(s)} = gR_LR_U\left(M_LR_{LB}\left(\frac{1 - L_{LBR}C_{LA}s^2}{C_{LA}s}\right) + M_RR_{RB}\left(\frac{1 - L_{RBR}C_{RA}s^2}{C_{RA}s}\right)\right) \quad (1)$$

The following assumptions applied to the pulmonary ventilation model as shown in Fig. 4.1.1.1:

- The left lung volume that can hold a certain amount of pressurized gas is approximately equal to the right lung volume, denoted by "C_A".

- The left bronchiole and terminal bronchiole elasticity are approximately equal to the right bronchiole and terminal bronchiole elasticity, denoted by "L_{BR}".

- The left secondary and tertiary bronchus resistance is approximately equal to the right secondary and tertiary bronchus resistance, denoted by "R_B".

Applying the specified assumptions simplifies (1) to:

$$\frac{P_I(s)}{D_c(s)} = -K\left(\frac{s^2 - f_{RR}}{s}\right) \quad where \quad \begin{matrix} K = g(M_L + M_R)L_{BR}R_BR_LR_U \\ f_{RR} = \frac{1}{L_{BR}C_A} \end{matrix} \quad (2)$$

The negative sign on the coefficient "K" in (2) indicates that when the lung volume increases due to the contraction of the diaphragm, which results in the increase of the chest displacement, the intrapulmonary pressure decreases for inspiration to occur, and vice versa for expiration. The bronchiole and terminal bronchiole elasticity "L_{BR}" in (2)

can be neglected for constant "K". This is because the changes in "L_{BR}" will impact the intrapulmonary pressure, which in turn is reflected through the reduction of the chest displacement magnitude "$D_c(s)$". The secondary and tertiary bronchus resistance "R_B", larynx and trachea resistance "R_L", upper respiratory system airway resistance, including the nose, pharynx and associated structures "R_U" in (2), can also be neglected for constant "K". The changes in these resistances also reflected through the reduction of the chest displacement magnitude "$D_c(s)$". The product of coefficients "L_{BR}" and "C_A" in (2) can be seen as a time constant (τ), which is the period of the pressure accumulation in the alveoli. The inverse of "τ", i.e. "f_{RR}", is, in fact, the frequency of breathing in Hertz. Therefore, "f_{RR}" is approximately equal to the respiratory rate (breaths per minute) divided by 60 seconds.

$$f_{RR} = \frac{Respiratory\ Rate}{60} \quad (Hz) \tag{3}$$

The "s^2" term in (2) indicates a second derivative, which in this case is the chest acceleration due to respiration efforts. The chest acceleration multiplied by a constant "K" indicates both Force (F) and Work (W) acted on the chest area. According to physics, W = mgh (Nm), where "m" is a mass in kilograms, "g" is the standard gravitational constant, and "h" is the height in meters, which in this case is the chest displacement "$D_c(s)$". The force (F) acted on the subject's chest is dependent on the mass portion of the total subject's body mass in kilograms residing at the chest area, i.e., "(M_L + M_R)" and gravity "g".

Interestingly, Quetelet stated in his book on page 66 that "*... the weight of developed persons, of different heights, is nearly as the square of the stature.*" and "*... a transverse section, giving both the breadth and thickness, is just proportioned to the height of the individual*" [151]. Therefore, it is reasonable to assume that the mass portion of the total subject's body mass in kilograms residing at the chest area, i.e., "(M_L + M_R)" can be estimated using the Quetelet's Index. In 1842, the relationship between the body's weight and height was known as Quetelet's Index, however, in 1972, it was renamed to Body Mass Index (BMI). Therefore, the constant "K" in (2) can be redefined in relation to the subject's actual body mass "M" in kilograms, actual height "H" in meters, and "g" as the standard gravitational constant, i.e., 9.80665 ms^{-2}:

$$K = g\left(M_{pL} + M_{pR}\right) = g\frac{M}{H^2} = gBMI \quad (kgm^{-1}s^{-2}) \tag{4}$$

To determine the units for the transfer function in (2), all units need to be combined. The gravity and the chest acceleration unit is ms^{-2}, the BMI unit is kgm^{-2}, and the denominator "s" unit is s^{-1}. The combination of units is $kgms^{-2}m^{-2}s^{-1}$, which equal to $Nm^{-2}s^{-1}$. Pressure is measure in SI unit of Pascal (Pa), equals to 1 Nm^{-2}. Therefore, the unit for the transfer function in (2) is Pascal per second (Pas^{-1}). The relationship between the intrapulmonary pressure "P_I" and the chest displacement "d_c" can now be defined as:

$$\frac{d}{dt}P_I(t) = -gBMI\left(\frac{d^2}{dt^2}d_c(t) - f_{RR}d_c(t)\right) \quad (Pas^{-1}) \tag{5}$$

For the discrete-time implementation of the pulmonary ventilation model, the matched Z-transform method, i.e., $z = e^{sTs}$, was chosen for the conversion of s-domain relationships to z-domain, where "T_s" is the sampling time in second and "f_s" is the sampling rate in Hertz:

$$\frac{P_I(s)}{D_c(s)} = -K\left(\frac{s^2 - f_{RR}}{s}\right) = -K\left(\frac{1}{s}\right)\left(s - \sqrt{f_{RR}}\right)\left(s + \sqrt{f_{RR}}\right) \tag{6}$$

$$\frac{P_I(z)}{D_C(z)} = -gBMI\left(\frac{z}{z-1}\right)\left(\frac{\left(z - e^{T_s\sqrt{f_{RR}}}\right)}{z}\right)\left(\frac{\left(z - e^{-T_s\sqrt{f_{RR}}}\right)}{z}\right) \tag{7}$$

$$\frac{P_I(z)}{D_C(z)} = -gBMI\left(\frac{z^2 - \left(e^{T_s\sqrt{f_{RR}}} + e^{-T_s\sqrt{f_{RR}}}\right)z + \left(e^{T_s\sqrt{f_{RR}}}e^{-T_s\sqrt{f_{RR}}}\right)}{z(z-1)}\right) \tag{8}$$

$$\frac{P_I(z)}{D_c(z)} = -gBMI\left(\frac{1 - k_z z^{-1} + z^{-2}}{1 - z^{-1}}\right) \quad where \quad k_z = 2\cosh\left(T_s\sqrt{f_{RR}}\right) \tag{9}$$

The discrete-time instantaneous rate of change of the intrapulmonary pressure is defined as:

$$\Delta P_I[n] = -gBMIf_s^2\left[d_c[n] - k_z[n]d_c[n-1] + d_c[n-2]\right] \quad (Pas^{-1}) \qquad (10)$$

$$k_z[n] = 2\cosh\left[T_s\sqrt{\frac{respiratory\ rate[n]}{60}}\right] \qquad (11)$$

Where the square of "f_s" in (10) is the amplitude gain constant when differentiate in discrete-time.

Trapezoidal numerical integration over 3 sample points (due to chest acceleration) yields the discrete-time instantaneous intrapulmonary pressure:

$$P_I[n] = P_I[n-1] - gBMIf_s\begin{bmatrix}(d_c[n])\\(-[k_z[n]-1]d_c[n-1])\\\left(\left[1-k_z[n-1]\right]d_c[n-2]\right)\\(d_c[n-3])\end{bmatrix} \quad (Pa) \qquad (12)$$

Applying Boyle's law relationship between pressure and volume in a closed system, the discrete-time instantaneous tidal volume (V_t) in milliliters, i.e., tidal value at a particular instance not the tidal volume per breath is defined as:

$$V_t[n] = \begin{Bmatrix}V_{TLC}\left[\frac{P_I[n-1]}{P_I[n]} - 1\right] & , & P_I[n] \neq 0\\ 0 & , & P_I[n] = 0\end{Bmatrix} \quad (mL) \qquad (13)$$

Noting that the initial lung volume is unknown (and is not required to be known), thus, the estimated volume will have the reference line at 0. This is the reason for subtracting value of 1 in (13).

"V_{TLC}" is the subject's total lung capacity (TLC) in milliliters. Adopting the power law prediction parameters for respiratory variables in mammals by Stahl [152] and the height-weight covariance by Livingston and Lee [153], "V_{TLC}" can be expressed in form of "allometric" formula, where "Wt" is the subject's predicted ideal body mass in kilograms and "Ht" is the subject's actual height in centimeters:

$$V_{TLC} = 53.5Wt^{1.06} \quad (mL) \quad where \quad Wt = \left(\frac{Ht}{33.34}\right)^{0.3922^{-1}} \quad (kg) \qquad (14)$$

The functional residual capacity (FRC) is unknown, and it is not required to be known, therefore, the discrete-time instantaneous tidal volume (V_t) will have a reference line at 0. This is also the reason for subtracting the value of 1 in (13).

To compensate for any noises and/or unwanted body movements, the subject's predicted tidal volume (V_{pt}) in milliliters must be calculated and used as the artefacts rejection criteria. According to Stahl [152], Livingston and Lee [153], "V_{pt}" can be expressed in form of "allometric" formula, where "Wt" and "Ht" as described above in relation to (11):

$$V_{pt} = 7.69Wt^{1.04} \quad (mL) \quad where \quad Wt = \left(\frac{Ht}{33.34}\right)^{0.3922^{-1}} \quad (kg) \qquad (15)$$

Therefore, the discrete-time instantaneous tidal volume with the inclusion of artefact rejection criteria (V_t*) in milliliters is defined as:

$$V_t^*[n] = \begin{Bmatrix} V_t[n] & , & |V_t[n]| \leq V_{pt} \\ V_t^*[n-1] & , & |V_t[n]| > V_{pt} \end{Bmatrix} \quad (mL) \qquad (16)$$

4.2 Tidal Volume Estimation Algorithm

4.2.1 Algorithm Block Diagram

A block diagram of the novel tidal volume estimation algorithm is in Fig. 4.2.1.1:

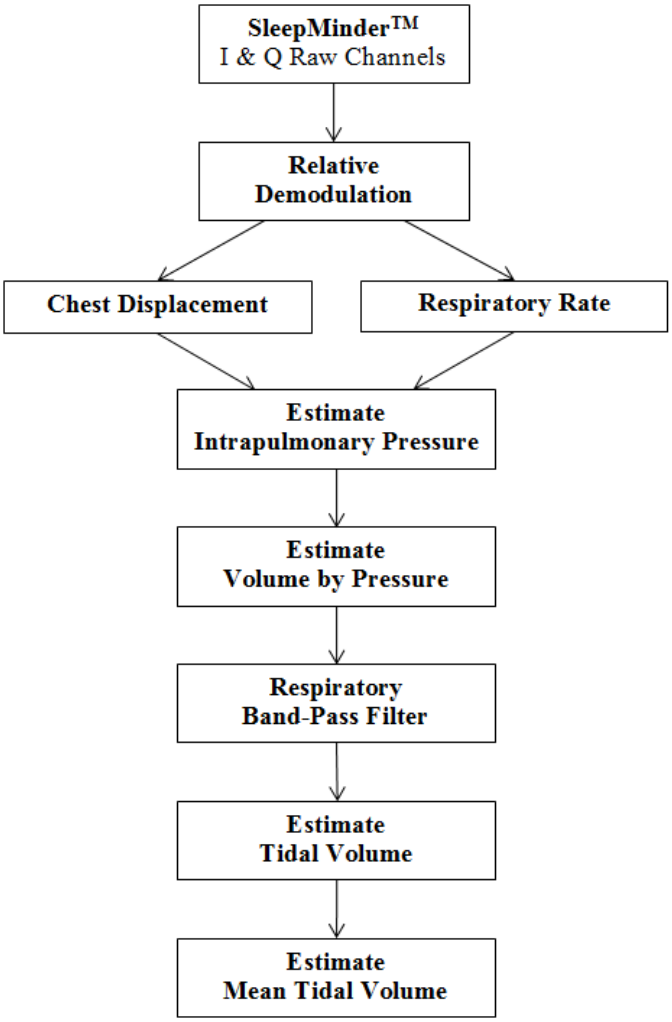

Figure 4.2.1.1 – Tidal Volume Estimation Algorithm

The "Relative Demodulation" technique presented in Chapter 3 is utilize to obtain the real-time chest displacement and respiratory rate.

The "Estimate Intrapulmonary Pressure" (EIP) implements the equation "P_I" as stated in (12) section 4.1.1. The "Estimate Volume by Pressure" (EVBP) implements the equation "V_t^*" as stated in (16) section 4.1.1.

The Butterworth band-pass filter had been chosen to implement the "Respiratory Band-Pass Filter" (RBPF). The reason for choosing this type of filter is the simplicity in implementation and faster performance when compared to other FIR filters. The selected frequency bandwidth for RBPF is 0.2–0.5 Hz which corresponds to 12–30 breaths per minute.

The "Estimate Tidal Volume" (ETV) identifies the peak locations of the estimated instantaneous "V_t^*" waveform. One tidal cycle is determine by the current and previous identified peak of "V_t^*". The maximum and minimum values are then identify per cycle. The tidal volume is then estimated as the difference between the maximum and the minimum values of "V_t^*" over a cycle. The value of "V_{pt}" is also apply as a conditional rule, i.e., if the current estimated tidal volume is greater than "V_{pt}", then the current estimated tidal is equal to the previous estimated tidal volume.

The "Estimate Mean Tidal Volume" (EMTV) calculates the mean value of the tidal volume per selected window-width. For the research works presented in the Thesis, a fixed window-width of 60 seconds (2 epochs) and a sliding window-width of 30 seconds (1 epoch) are employ.

4.3 Conclusion

Chapter 4 contributes to the field of non-contact sleep monitoring by introducing a novel pulmonary ventilation mathematical model that enables the capability of tidal volume estimation using the non-contact microwave Doppler radar. The novelty of the pulmonary ventilation mathematical model is that it defines the relationship between the intrapulmonary pressure and the chest displacement. The tidal volume can also be estimated via the mathematical model.

It is also important to emphasize that the pulmonary ventilation mathematical model is derive from the understanding of anatomy and physiology, it is not simply an application of regressions between the chest displacement and intrapulmonary pressure or tidal volume values.

The real-life applications and results of "Pulmonary Ventilation Mathematical Model" in non-contact sleep monitoring is presented in Chapter 7, section 7.2 of the Thesis.

The work presented in Chapter 4 is published in [58] and patented in [148, 150, 154].

CHAPTER 5

EXTERNAL VENTILATION MATHEMATICAL MODEL

Thesis Contribution 4: Novel Theory 3

INTRODUCTION

Chapter 5 presents a novel mathematical model that quantitatively defines the relationships between the arterial oxygen saturation (SaO_2), the arterial partial pressure of oxygen (PaO2) and the arterial partial pressure of carbon dioxide ($PaCO_2$). In addition, a novel non-contact algorithm that utilizes the mathematical model, multilayer perceptron (MLP) artificial neural network (ANN) and the non-contact microwave Doppler radar to translate the human periodic chest displacements caused by respiratory efforts into peripheral capillary oxygen saturation (SpO_2) measurements is also presented.

5.1 Oxygen-Hemoglobin Dissociation Model

Section 5.1 presents a novel oxygen-hemoglobin dissociation mathematical model that quantitatively defines the relationships between the arterial oxygen saturation (SaO_2),

the arterial partial pressure of oxygen (PaO_2), and the arterial partial pressure of carbon dioxide ($PaCO_2$). A generalized SaO_2 equation is also presented.

5.1.1 Theoretical Analysis and Modeling

The oxygen-hemoglobin dissociation curve (ODC), as shown in Fig. 5.1.1.1, is a replicate of Christian Harald Lauritz Peter Emil Bohr's original laboratory data published in 1904 [155]. ODC is an important tool in clinical medicine to understand how blood carries and releases oxygen. ODC indicates the relationship between the oxygen-hemoglobin percentage of saturation (SO_2), the partial pressure of oxygen (PO_2) and the partial pressure of carbon dioxide (PCO_2). This relationship is known as the "hemoglobin affinity for oxygen", i.e., how readily hemoglobin acquires and releases oxygen molecules into the fluid that surrounds it [156, 157].

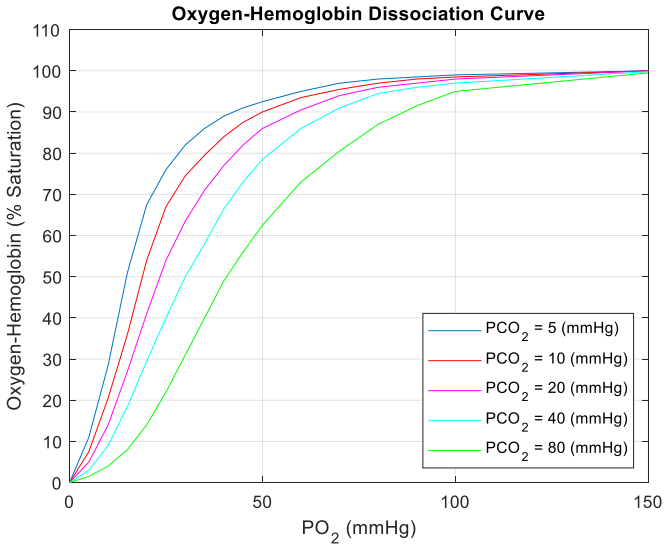

Figure 5.1.1.1 – Bohr's Oxygen-Hemoglobin Dissociation Curve (ODC)

The hemoglobin affinity for oxygen is also affected by the blood pH (potential of Hydrogen), body temperature and the concentration in the red cells of 2,3-bisphosphoglycerate (2,3-BPG) [156, 157]. However, these factors are not consider in the mathematical model. The principle aim of the model is to quantitatively defines the physiological relationships between SaO_2, PaO_2 and $PaCO_2$, excluding pathophysiological factors.

Simulated step responses of generic overdamped second-order transfer functions with 5 simulated ζ and ω_n values are presented in Fig. 5.1.1.2. The purpose of presenting these simulation curves is to highlight the visual similarities between the step responses and the ODC as in Fig. 5.1.1.1.

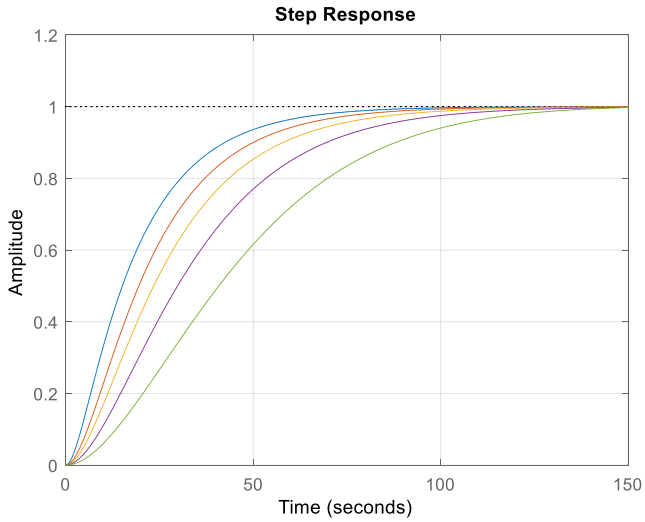

Figure 5.1.1.2 – Simulated Step Responses of Second-Order Transfer Functions

As can be seen in Fig. 5.1.1.1 and Fig. 5.1.1.2, with the associations of x-axis "*PO_2 (mmgH)*" in Fig. 5.1.1.1 to "*Time (seconds)*" in Fig. 5.1.1.2 and y-axis "*SO_2 (%)*" in Fig. 5.1.1.1 to "*Amplitude*" in Fig. 5.1.1.2, the responses of ODC are analogous to that of step responses in overdamped second-order transfer functions. A second-order is a reasonable choice in system modeling to balance between accuracy and complexity. Higher orders increase complexity and does not result in a commensurate increase in benefits.

Therefore, for this observed visual similarities, a second-order transfer function with a unit step response in Laplace's s-domain were chosen to represent the ODC as shown in Fig. 5.1.1.1. The Laplace's s-domain was chosen for the mathematical convenience purpose. The transfer function is defined as:

$$\frac{SaO_2(s)}{PaO_2(s)} = K\left(\frac{1}{s}\right)\left(\frac{{\omega_n}^2}{s^2 + 2\zeta\omega_n + {\omega_n}^2}\right) \quad (1)$$

The descriptions of the symbols used in (1) are:

1. SaO_2 – The arterial oxygen saturation. The unit for SaO_2 is %. SO_2 is equivalent to SaO_2 in the context of arterial blood.

2. PaO_2 – The arterial partial pressure of oxygen. The unit for PaO_2 is mmHg. PO_2 is equivalent to PaO_2 in the context of arterial blood, assuming alveolar–arterial O_2 gradient equal to 0 mmHg.

3. K – The gain constant that determine the size of steady-state response. The gain constant (K) is equal to 100.

4. ζ – The damping ratio which determines how much the model oscillates as the response decays toward steady state. ζ is dimensionless.

5. ω_n – The natural frequency which determine how fast the model oscillates during any transient response. The unit for ω_n is $rads^{-1}$.

Heuristic method of "trial-and-error" is performed to empirically estimate the two unknown values of ζ and ω_n. The aim is to simulate the model to produce responses that closely matches the ODC as shown in Fig. 5.1.1.1. The estimates of ζ and ω_n are shown in Table 5.1.1.1. $PaCO_2$ unit is mmHg and is equivalent to PCO_2 in the context of arterial blood.

$PaCO_2$ (mmHg)	**zeta**	**W_n ($rads^{-1}$)**
5	1.3850	0.1382
10	1.1592	0.0942
20	1.0934	0.0754
40	1.0076	0.0565
80	0.9055	0.0390

Table 5.1.1.1 – Empirical Estimates of Zeta and W_n

Based on the estimates shown in Table 5.1.1.1, a natural log linear regression analysis for ω_n versus $PaCO_2$ is performed. The line of best fit equation with Pearson correlation coefficient of determination "r^2" of 0.9908 is defined as:

$$ln(\omega_n) = -0.4486\, ln(PaCO_2) - 1.2714 \quad (2)$$

Therefore, the continuous time-domain solution for $\omega_n(t)$ relationship to $PaCO_2(t)$ is defined as:

$$\omega_n(t) = 0.28\, PaCO_2(t)^{-0.45} \quad (rads^{-1}) \quad (3)$$

Based on the estimates shown in Table 5.1.1.1, a linear regression analysis for ζ versus ω_n is performed. The line of best fit equation with Pearson correlation coefficient of determination "r^2" of 0.9966 is defined as:

$$\zeta = 4.6599\omega_n + 0.7333 \quad (4)$$

Therefore, the continuous time-domain solution for $\zeta(t)$ relationship to $PaCO_2(t)$ is defined as:

$$\zeta(t) = 1.31\, PaCO_2(t)^{-0.45} + 0.73 \quad (5)$$

Equation (5) indicates that both $\zeta(t)$ and $PaCO_2(t)$ must be greater than zero. Therefore, to solve the transfer function stated in (1), three cases are require to be considered, i.e., $\zeta > 1$, $\zeta = 1$, and $0 < \zeta < 1$.

5.1.2 Case 1 – Overdamped Solution ($\zeta > 1$)

The transfer function stated in (1) for overdamped criteria can be re-written as:

$$\frac{SaO_2(s)}{PaO_2(s)} = K\left(\frac{1}{s}\right)\left(\frac{\alpha\beta}{(s+\alpha)(s+\beta)}\right) \quad (6)$$

Where:

$$\alpha = \omega_n\left(-\zeta + \sqrt{\zeta^2 - 1}\right) \quad (rads^{-1}) \tag{7}$$

$$\beta = \omega_n\left(-\zeta - \sqrt{\zeta^2 - 1}\right) \quad (rads^{-1}) \tag{8}$$

Perform inverse Laplace transform using partial fraction expansion, the time-domain solution for $SaO_2(t)$ is defined as:

$$SaO_2(t) = K\left(1 - \frac{f_{\alpha\beta}(t)}{\beta(t) - \alpha(t)}\right) \quad (\%) \tag{9}$$

Where:

$$f_{\alpha\beta}(t) = \beta(t)e^{\alpha(t)PaO_2(t)} - \alpha(t)e^{\beta(t)PaO_2(t)} \tag{10}$$

5.1.3 Case 2 – Critically Damped Solution ($\zeta = 1$)

The transfer function stated in (1) for critically damped criteria can be re-written as:

$$\frac{SaO_2(s)}{PaO_2(s)} = K\left(\frac{1}{s}\right)\left(\frac{\omega_n}{s + \omega_n}\right)^2 \tag{11}$$

Perform inverse Laplace transform using partial fraction expansion, the time-domain solution for $SaO_2(t)$ is defined as:

$$SaO_2(t) = K\left(1 - e^{-\omega_n(t)PaO_2(t)}f_{\omega_n}(t)\right) \quad (\%) \tag{12}$$

Where:

$$f_{\omega_n}(t) = 1 + \omega_n(t)PaO_2(t) \tag{13}$$

5.1.4 Case 3 – Underdamped Solution ($0 < \zeta < 1$)

Perform inverse Laplace transform using partial fraction expansion for the transfer function stated in (1), the time-domain solution for $SaO_2(t)$ is defined as:

$$SaO_2(t) = K\left(1 - A(t)e^{-\gamma(t)PaO_2(t)}f_{sin}(t)\right) \quad (\%) \tag{14}$$

Where:

$$A(t) = \frac{\omega_n(t)}{\omega_{sin}(t)} \tag{15}$$

$$\gamma(t) = \zeta(t)\omega_n(t) \quad (rads^{-1}) \tag{16}$$

$$f_{sin}(t) = sin\left(\omega_{sin}(t)PaO_2(t) + \phi(t)\right) \tag{17}$$

$$\omega_{sin}(t) = \omega_n(t)\sqrt{1 - \zeta(t)^2} \quad (rads^{-1}) \tag{18}$$

$$\phi(t) = cos^{-1}\zeta(t) \quad (rads^{-1}) \tag{19}$$

5.1.5 Generalized SaO_2 Equation

Therefore, the mathematical model of the oxygen-hemoglobin dissociation that quantitatively defines the relationships between SaO_2 to the activation functions of amplitude (f_A), $PaCO_2$ (f_{PaCO2}) and PaO_2 (f_{PaO2}) is defined as:

$$SaO_2(t) = K\left(1 - f_A(t)e^{-f_{PaCO_2}(t)PaO_2(t)}f_{PaO_2}(t)\right) \quad (\%) \tag{20}$$

The activation functions are defined as:

$$f_A(t) = \begin{Bmatrix} \left(\beta(t) - \alpha(t)\right)^{-1} & , & \zeta(t) > 1 \\ 1 & , & \zeta(t) = 1 \\ A(t) & , & 0 < \zeta(t) < 1 \end{Bmatrix} \quad (21)$$

$$f_{PaCO_2}(t) = \begin{Bmatrix} 0 & , & \zeta(t) > 1 \\ \omega_n(t) & , & \zeta(t) = 1 \\ \gamma(t) & , & 0 < \zeta(t) < 1 \end{Bmatrix} \quad (22)$$

$$f_{PaO_2}(t) = \begin{Bmatrix} f_{\alpha\beta}(t) & , & \zeta(t) > 1 \\ f_{\omega_n}(t) & , & \zeta(t) = 1 \\ f_{sin}(t) & , & 0 < \zeta(t) < 1 \end{Bmatrix} \quad (23)$$

Based on the relationships between ζ(t) and $PaCO_2$(t) in (5), the ζ(t) criteria in (21), (22) and (23) can be expressed in terms of $PaCO_2$(t) criteria as follows:

$$\begin{array}{rcll} \zeta(t) > 1 & \approx & 0 < PaCO_2(t) < 34.56 & (mmHg) \\ \zeta(t) = 1 & \approx & PaCO_2(t) \cong 34.56 & (mmHg) \\ 0 < \zeta(t) < 1 & \approx & PaCO_2(t) > 34.56 & (mmHg) \end{array} \quad (24)$$

Any short-term rise in $PaCO_2$ above 40 mmHg due to decrease ventilation results in respiratory acidosis. Any short-term decrease in ventilation that lowers $PaCO_2$ below 35 mmHg results in respiratory alkalosis [156]. The activation functions in (21), (22) and (23) are design to be activated according to the respiratory alkalosis, adequate ventilation and respiratory acidosis conditions.

5.2 Relationships of the Alveolar Partial Pressures

Section 5.2 integrates published research findings and established relationships of the alveolar partial pressures, as specified in [152, 153, 156-158], to present the novel sets of alveolar parameters equations that are the inputs to the mathematical model presented in section 5.1.1. The principle aim is to estimate the actual time-domain "$PaCO_2$(t)" and

"$PaO_2(t)$". The alveolar ventilation "$V_A(t)$" and carbon dioxide production "$V_{CO2}(t)$" are also require to be estimated as it is require in the "$PaCO_2(t)$" estimation. The methodologies are detailed in the subsequent sub-sections of section 5.2.

5.2.1 Alveolar Ventilation Relationship to Subject's Height

According to Hart [158], the subject's predicted "anatomic" respiratory dead-space volume "V_D" in milliliters relationship to the subject's actual height "Ht" in centimeters can be estimated as:

$$V_D = 7.585Ht^{2.363} \times 10^{-4} \quad (mL) \tag{25}$$

Combining Stahl [152], Livingston and Lee [153] published research findings, the subject's predicted tidal volume "V_T" in milliliters can be estimated as:

$$V_T = 7.038Ht^{2.652} \times 10^{-4} \quad (mL) \tag{26}$$

Therefore, the "anatomic" respiratory dead-space ratio "R_D" is defined as:

$$R_D = \frac{V_D}{V_T} = 1.078Ht^{-0.289} \tag{27}$$

In the context of the mathematical model of the oxygen-hemoglobin dissociation, the "physiological" respiratory dead-space volume is assume to be negligible. Therefore, the actual real-time alveolar ventilation "$V_A(t)$" in liters per minute relationship to the subject's actual height is defined as:

$$\dot{V}_A(t) = (1 - 1.078Ht^{-0.289})\dot{V}_E(t) \quad (Lm^{-1}) \tag{28}$$

Where: $V_E(t)$ is the subject's actual minute ventilation in liters per minute (Lm^{-1}).

5.2.2 Carbon Dioxide Production Relationships to Subject's Heart Rate and Respiratory Quotient

According to Stahl [152], the subject's predicted oxygen consumption "V_{O2}" in milliliters per minute, cardiac output "CO" in milliliters per minute and heart rate "HR" in beats per minute relationships to the subject's actual body mass in kilograms "Wt" can be estimated as:

$$V_{O_2} = 11.6Wt^{0.76} \quad (mLmin^{-1}) \tag{29}$$

$$CO = 187Wt^{0.81} \quad (mLmin^{-1}) \tag{30}$$

$$HR = 241Wt^{-0.25} \quad (bpm) \tag{31}$$

By dividing (30) by (31), the subject's predicted stroke volume "SV" in milliliters per beat is defined as:

$$SV = \frac{CO}{HR} = 0.776Wt^{1.06} \quad \left(\frac{ml}{beat}\right) \tag{32}$$

Fick's principle [156] indicates that the oxygen consumption "V_{O2}" is the product of cardiac output "CO" and arteriovenous oxygen difference "$C_{aO2} – C_{vO2}$". Therefore, V_{O2} can be expressed as:

$$\dot{V}_{O_2} = CO\left(C_{aO_2} - C_{vO_2}\right) \quad (mLmin^{-1}) \tag{33}$$

By dividing (29) by (30) and rearranging (33), the subject's predicted "$C_{aO2} – C_{vO2}$" is defined as:

$$C_{aO_2} - C_{vO_2} = \frac{\dot{V}_{O_2}}{CO} = 0.062Wt^{-0.05} \quad \left(\frac{mL}{100mL}\right) \tag{34}$$

The respiratory quotient (RQ) is defined as:

$$RQ = \frac{\dot{V}_{CO_2}}{\dot{V}_{O_2}} \tag{35}$$

RQ is approximately equal to 1.0 for the subject receiving an intravenous glucose solution. RQ is approximately equal to 0.7 for the subject with hypoglycemic or diabetic and relying on fatty acid metabolism. RQ is approximately equal to 0.8 for the subject with mixes of fuels, i.e., fat and glucose [156, 157].

By combining (32), (33), (34), (35) and replacing the subject's predicted HR in (32) with the actual heart rate (HR(t)), the actual $V_{CO2}(t)$ in milliliters per minute relationships to the subject's actual weight in kg, heart rate and respiratory quotient is defined as:

$$V_{CO_2}(t) = 0.048Wt^{1.01} \times HR(t) \times RQ \quad (mLmin^{-1}) \tag{36}$$

5.2.3 Arterial Partial Pressure of Carbon Dioxide Relationships to Alveolar Ventilation and Carbon Dioxide Production

One of the important physiological relationship between $PaCO_2$ and V_A is that dead-space does not participate in the gas exchange process; all of the expired carbon dioxide comes from the alveolar gas. The amount of V_{CO2} excreted by the lungs equals to V_A times the fraction of alveolar carbon dioxide "$FACO_2$". Since $PaCO_2$ = $FACO_2$ times the total alveolar gas pressure [156, 157]. Therefore, $PaCO_2$ in mmHg relationships to the alveolar ventilation and carbon dioxide production is defined as:

$$PaCO_2(t) = \frac{K_c V_{CO_2}(t)}{\dot{V}_A(t)} = \frac{0.041Wt^{1.01} \times HR(t) \times RQ}{(1 - 1.078Ht^{-0.289})\dot{V}_E(t)} \quad (mmHg) \tag{37}$$

Where: "K_C" is a constant that equates dissimilar units for V_{CO2} ($mLmin^{-1}$) and V_A ($Lmin^{-1}$) to $PaCO_2$ pressure unit (mmHg), as well as the conversion of $FACO_2$ to $PaCO_2$. The constant "K_C" is equal to 0.863 [156, 157].

To compensate for any unwanted fluctuations caused by noises and other means of disturbances, the criteria of $PaCO_2(t)$ must be within the range of a minimum of 0 mmHg to a maximum of 125 mmHg. The reason for applying this range is that physiologically $PaCO_2(t)$ must be greater than 0 mmHg and $PaO_2(t)$ approaches 0 mmHg when $PaCO_2(t)$ approaches 125 mmHg. Therefore, $PaCO_2{}^*(t)$, i.e., with the inclusion of artefact rejection criteria is defined as:

$$PaCO_2{}^*(t) = \begin{cases} PaCO_2(t) & , \quad 0 \leq PaCO_2(t) \leq 125 \\ PaCO_2{}^*(t_{-1}) & , \quad otherwise \end{cases} \tag{38}$$

The expression 't_{-1}' refers to the value at the previous instance of time.

5.2.4 Arterial Partial Pressure of Oxygen Relationship to Arterial Partial Pressure Carbon Dioxide

It is by passive diffusion down a partial pressure gradient that pulmonary capillary blood is oxygenated. According to the established alveolar gas equation (AGE) [156, 157], PaO_2 in mmHg relationship to $PaCO_2$ in mmHg is defined as:

$$PaO_2(t) = PiO_2 - PaCO_2{}^*(t)\left(\frac{1 - FiO_2(1 - RQ)}{RQ}\right) \quad (mmHg) \tag{39}$$

Where:

$$PiO_2 = FiO_2\left(P_{atm} - P_{H_2O}\right) \tag{40}$$

The descriptions of the symbols used in (39) and (40) are:

1. FiO_2 – Fractional content of inspired oxygen of air. Natural air includes 20.95% of oxygen, which is equivalent to FiO_2 of 0.2095. Oxygen-enriched air has greater than 20.95% to 100% of oxygen. However, FiO_2 is typically maintain below 0.5 even with mechanical ventilation to prevent oxygen toxicity [159].

2. P_{atm} – Barometric or atmospheric pressure. P_{atm} is approximately equal to 760 mmHg at sea level. However, P_{atm} can varies depending on geographical locations and altitudes [156, 157].

3. P_{H20} – Vapor pressure of water in the alveoli. P_{H20} is fully saturated at body temperature of 37°C and is approximately equal to 47 mmHg. However, P_{H20} can varies depending on body temperatures [156, 157].

To compensate for any unwanted fluctuations caused by noises and other means of disturbances, the criteria of $PaO_2(t)$ must be within the range of a minimum of 0 mmHg to a maximum of 150 mmHg. The reason for applying this range is that physiologically $PaO_2(t)$ must be greater than 0 mmHg and oxygen-hemoglobin is fully saturated, i.e., 100% when $PaO_2(t)$ approaches 150 mmHg. Therefore, PaO_2*(t), i.e., with the inclusion of artefact rejection criteria is defined as:

$$PaO_2{}^*(t) = \begin{Bmatrix} PaO_2(t) & , & 0 \leq PaO_2(t) \leq 150 \\ PaO_2{}^*(t_{-1}) & , & otherwise \end{Bmatrix} \quad (41)$$

5.3 Non-Contact Prediction of Oxygen Saturation Algorithm

The challenges to the processing of the non-contact Doppler radar signals are clutters, DC offsets, phase-nulling, motions artefacts and electromagnetic interferences. Another major challenge in sleep monitoring application is the noise associated with unpredictable body movements, body orientations, changes in sleeping posture, multi-subjects' cancellation, undesired harmonics and intermodulation.

Therefore, section 5.3 presents a novel non-contact algorithm that utilizes the mathematical model, MLP neural network, and patented microwave Doppler radar to translate the human periodic chest displacements caused by respiratory efforts into SpO_2 measurements. SpO_2 refers to peripheral capillary oxygen saturation measured from

pulse oximeter, whilst SaO_2 refers to arterial oxygen saturation measured from arterial blood gas (ABG) analysis. The target output used to train the MLP artificial neural network is obtain from PSG SpO_2 measured from a pulse oximeter. This is the reason why the non-contact oxygen saturation prediction algorithm uses the term SpO_2 instead of SaO_2.

The purpose of utilizing patented sensor system is that the issues of motions artefacts, electromagnetic interferences, multi-subjects' cancellation, undesired harmonics and intermodulation have been addressed by the sensor's design, which is detailed in Appendix I, section A.I.I.

The motivation for utilizing MLP artificial neural network in conjunction with the mathematical model is to enable the capability to train and compensate for the noises associated with the complex sleep environment, such as, motions artefacts, unpredictable body movements, body orientations, and changes in sleeping posture. The inclusion of MLP artificial neural network increases the accuracy and robustness of the SpO_2 predictions.

5.3.1 Algorithm Block Diagram

The block diagram of the non-contact prediction of SpO_2 algorithm is in Fig. 5.3.1.1.

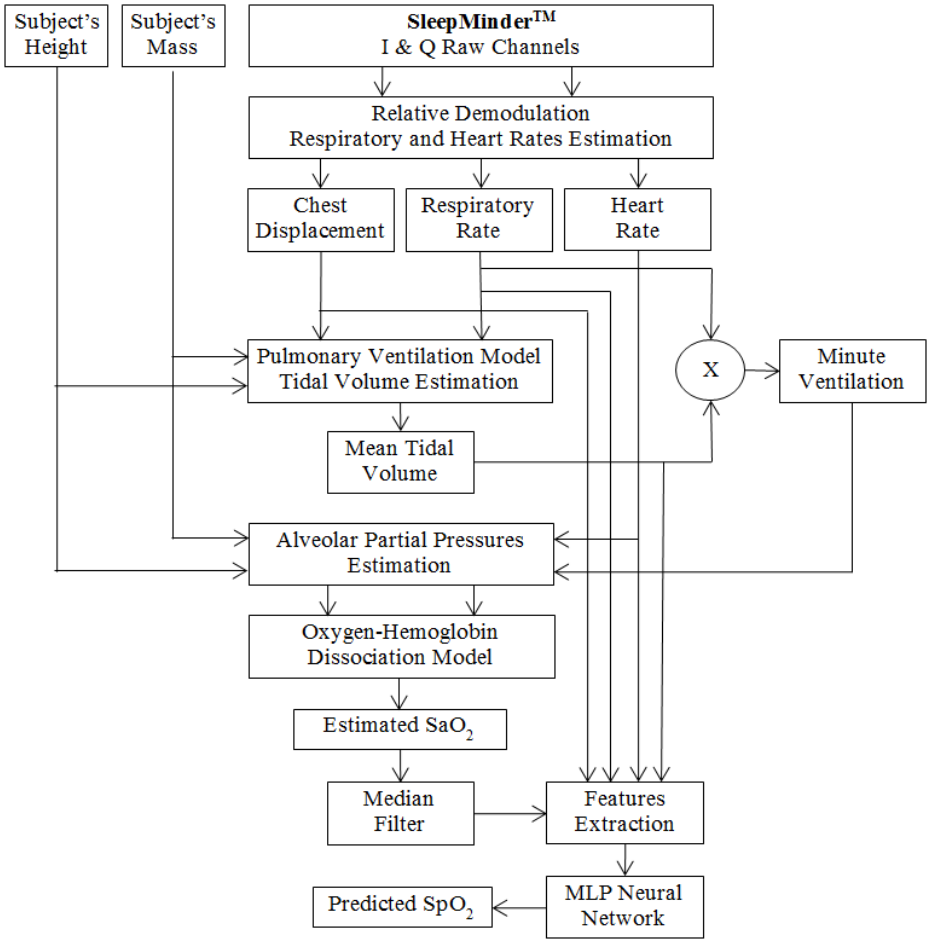

Figure 5.3.1.1 – Non-Contact Prediction of SpO_2 Algorithm Block Diagram

The "Relative Demodulation" technique and "Respiratory and Heart Rate Estimation" algorithm presented in Chapter 3 are utilize to obtain the absolute chest displacements in meters, respiratory rates in breaths per minute, and heart rates in beats per minute (bpm). This technique was chosen over conventional "Arctangent Demodulation" because the demodulated chest displacements are absolute, addressed clutters, DC offsets, phase-nulling and less sensitive to quadrature orthogonal issues. In addition, the estimations of respiratory and heart rates are also accurate.

The "Pulmonary Ventilation Model" and "Tidal Volume Estimation" algorithm presented in Chapter 4 are also utilize to obtain the mean tidal volume in milliliters (mL). The mean tidal volume is not a mean value across the entire duration; it is the mean value within a fixed window-width of 60 seconds (2 epochs) and a sliding window-width of 30 seconds (1 epoch). This technique was chosen as it gives the ability

to convert the absolute chest displacements, which obtained from the "Relative Demodulation" technique, to tidal volume via mathematical model derived from anatomy and physiology instead of simply applying regressions between the chest displacement and tidal volume values.

The "Minute Ventilation" ($V_E(t)$) is estimated by the multiplication of the respiratory rate and mean tidal volume. The $V_E(t)$ is then converted to liters per minute.

The "Alveolar Partial Pressures Estimation" and "Oxygen-Hemoglobin Dissociation Model" (OHDM) implements the equations stated in section 5.1 and 5.2. The following assumptions was applied to OHDM:

1. RQ – The patients' mean age is 69.05 years with overweight BMI of 28.01. People who are overweight or have obesity will have additional pressure on their body's ability to use insulin to properly control blood sugar levels. Therefore, diabetes is more likely to be developed. It is assume that the patients are most likely to be diabetic and RQ is approximately equal to 0.7.

2. FiO_2 – The CHF patients are admitted in the sleep laboratory for OSA diagnoses and neither oxygen-enriched air nor positive airway pressure therapy are prescribed during the entire duration of the sleep test. Therefore, it is assume that the patients consumed natural air and FiO_2 is approximately equal to 0.2095.

3. P_{atm} – It is assume that the atmospheric pressure is approximately equal to 760 mmHg at sea level.

4. P_{H20} – There are neither evidences nor records to indicate that the CHF patients experienced hypothermia or hyperthermia during the entire duration of the sleep test. It is assume that the patient's body temperature is normal at 37°C and P_{H20} is approximately equal to 47 mmHg.

A “Median Filter” with a fixed window-width of 60 seconds (2 epochs) and a sliding window-width of 30 seconds (1 epoch) is apply to smooth the estimated SaO_2 values.

5.3.2 Feature Extraction Process

There are 5 chosen inputs to the feature extraction process, which are the chest displacement, respiratory rate, heart rate, mean tidal volume and estimated SaO_2 from the mathematical model. The feature extraction process extract features as per fixed window-width of 60 seconds (2 epochs) and a sliding window-width of 30 seconds (1 epoch) for the entire length of the input signal. The terminology “epoch” is refer to the interval of 30 seconds in the sleep analysis defined by the American Academy of Sleep Medicine (AASM). This is the standardized block of analysis in OSA diagnosis recommended by AASM, and the feature extraction window is an adherence to the epoch standard. Table 5.3.2.1 indicate the chosen 8 time-domain statistical features as per window, where “x” is the selected signal at the selected window. The statistical methods for obtaining the features are mean, variance (var), standard deviation (std) and median-absolute-deviation (mad).

mean(x)	mean(x^2)	var(x)	var(x^2)
std(x)	std(x^2)	mad(x)	mad(x^2)

Table 5.3.2.1 – Time-Domain Statistical Features

The feature extraction process produces a total of 40 features, which is the product of 5 input signals and 8 time-domain statistical features. The total 40 features are then re-scale to the range of -1.0 to 1.0.

5.3.3 SpO_2 Multilayer Perceptron Artificial Neural Network Architecture

The MLP artificial neural network architecture for SpO_2 prediction is presented in Fig. 5.3.3.1. The MLP artificial neural network is a simple fully connected with hyperbolic

tangent sigmoid (tansig) as activation function for the hidden layers and identity (linear) as activation function for the output layer. The MLP artificial neural network contains 3 layers, in which 2 layers are hidden layers and 1 output layer. The output layer contains regression values for SpO_2.

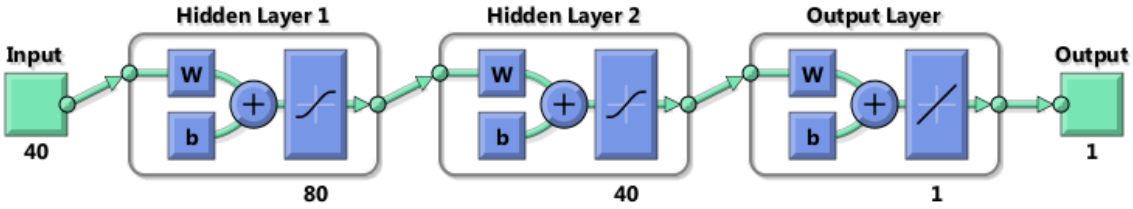

Figure 5.3.3.1 – SpO_2 MLP Artificial Neural Network Architecture

The summary of SpO_2 MLP artificial neural network hyperparameters are shown in Table 5.3.3.1.

	Hidden Layer 1	***Hidden Layer 2***	***Output Layer***
Number of Neuron	80	40	1
Activation Function	Hyperbolic Tangent Sigmoid		Identity

Table 5.3.3.1 – SpO_2 MLP Artificial Neural Network Architecture Characteristics

The common training characteristics of the artificial neural network are summarized in Appendix III, Table A.III.1.

5.4 Conclusion

Chapter 5 contributes to the field of non-contact sleep monitoring by introducing a novel oxygen-hemoglobin dissociation mathematical model that quantitatively defines the relationships between SaO_2, PaO_2 and $PaCO_2$. The novelty of the mathematical model is that it enables the capability to estimate oxygen saturation using the non-contact microwave Doppler radar.

However, to increase the accuracy and robustness in the complex sleep environment, a novel non-contact algorithm that utilizes the mathematical model, MLP artificial neural network and microwave Doppler radar is also introduce to translate the human periodic chest displacements caused by respiratory efforts into peripheral capillary oxygen saturation (SpO_2) measurements.

It is also important to emphasize that the oxygen-hemoglobin dissociation mathematical model is theoretically generic and not restricted to non-contact applications.

The real-life applications and results of “External Ventilation Mathematical Model” in non-contact sleep monitoring is presented in Chapter 7, section 7.3 of the Thesis.

The work presented in Chapter 5 is published in [160] and patented in [161].

CHAPTER 6

3-DIMENSIONAL FEATURE REPRESENTATION AND EXTRACTION TECHNIQUE

Thesis Contribution 5: Novel Theory 4

INTRODUCTION

Deep artificial neural networks, i.e., with multiple layers, usually require significant amount of training data to achieve good performance and generalization. However, acquiring significant amount of training data is always a challenge. Hand-crafted and/or algorithm-based feature extraction often requires certain degree of expert domain knowledge. In addition, feature engineering process does not achieve data transformation, augmentation, normalization, scaling and feature extraction in a single process.

Therefore, chapter 6 presents a novel 3-dimensional feature representation and extraction technique, consisting of two methods, Spatial Dimensions Transform (SDT) and Spatial Dimensions Decomposition (SDD). SDT and SDD when combined can

achieve data transformation, augmentation, normalization, scaling and feature extraction in a single process.

6.1 Spatial Dimensions Transform

Section 6.1 presents the theory and methodologies of Spatial Dimensions Transform (SDT) and inverse Spatial Dimensions Transform (iSDT). The principle aim of SDT is to transpose any given function, scalar values (minimum 2 values) or vector onto 3-dimensional Cartesian coordinates. The SDT rules and methodologies are detailed in subsections 6.1.1 and 6.1.2. The iSDT methodology is detailed in subsection 6.1.3.

6.1.1 SDT Rules

1. For any given function, scalar values (minimum 2 values) or vector, denoted as function "f(t)", at any two instances, denoted as "$f(t_{n-1})$" and "$f(t_n)$", is define as the transpose window, denoted as "T_w".

2. As per "T_w", a straight line is connected between the magnitudes of "$f(t_{n-1})$" and "$f(t_n)$", and referred to as the hypotenuse of a right-angle triangle or simply a line segment.

3. As per "T_w", the angle between the magnitude-axis and instance-axis "t" is denote as "$\theta(t_n)$".

4. As per "T_w", the magnitude of "$f(t_n)$" at "t_n", is define as the spatial magnitude and denoted as "$A(t_n)$". The aim is to preserve the data integrity of the given function, scalar values (minimum 2 values) or vector.

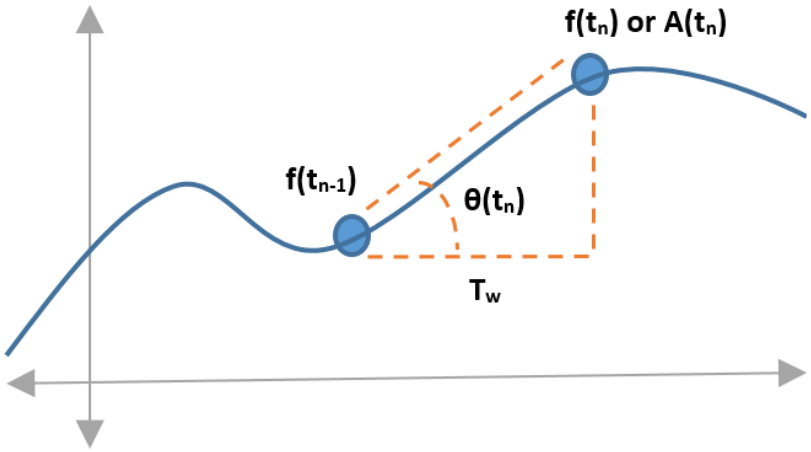

Figure 6.1.1.1 – Spatial Dimensions Transform Theory Graphical Representation

6.1.2 SDT Methodology

The angle "θ" (theta) between the magnitude-axis and instance-axis is defined as:

$$\theta(t_n) = \tan^{-1}\left(\frac{f(t_n) - f(t_{n-1})}{t_n - t_{n-1}}\right) \quad (rads^{-1}) \tag{1}$$

Therefore, in general, the vector "θ" is defined as:

$$\theta = \tan^{-1}\left(\frac{d}{dt}f(t)\right) \quad (rads^{-1}) \tag{2}$$

Let's introduce "φ" (phi) as an amplification factor for the rate of change of "$f(t_n)$", where "φ" is any real number:

$$\theta = \tan^{-1}\left(\varphi\frac{d}{dt}f(t)\right) \quad (rads^{-1}) \tag{3}$$

The spatial magnitude vector is defined as:

$$A = f(t) \tag{4}$$

Let the directional cosines of the spatial vector relative to the “x-coordinate” be alpha (α), “y-coordinate” be beta (β) and “z-coordinate” be gamma (γ) as shown in Fig. 6.1.2.1.

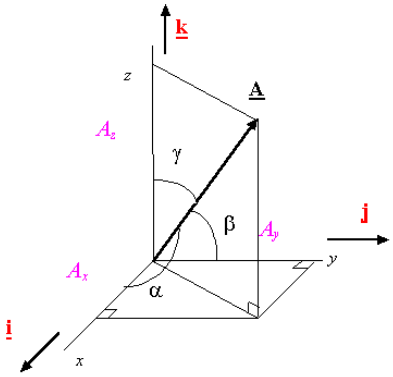

Figure 6.1.2.1 – Spatial Dimensions Directional Cosines

Therefore, the directional cosines are:

$$\cos(\alpha) = \frac{A_x}{A} \tag{5}$$

$$\cos(\beta) = \frac{A_y}{A} \tag{6}$$

$$\cos(\gamma) = \frac{A_z}{A} \tag{7}$$

The constraint of the directional cosines is defined as:

$$\cos^2(\alpha) + \cos^2(\beta) + \cos^2(\gamma) = 1 \tag{8}$$

The unit vector “u” along the vector “A” is defined as:

$$u = \cos(\alpha)\, i + \cos(\beta)\, j + \cos(\gamma)\, k \tag{9}$$

$$u = \frac{A_x}{A} i + \frac{A_y}{A} j + \frac{A_z}{A} k \tag{10}$$

Let's transpose the angle "θ" onto 3-dimensional Cartesian coordinates relative to vector "A" as shown in Fig. 6.1.2.2.

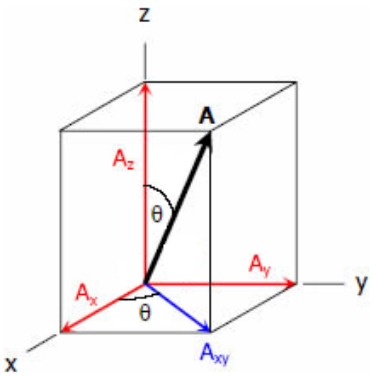

Figure 6.1.2.2 – Spatial Dimensions Theta Transposition

The magnitudes of the coordinates are:

$$A_{xy} = A \cos\theta \tag{11}$$

$$A_x = A_{xy} \cos\theta \tag{12}$$

$$A_y = A_{xy} \sin\theta \tag{13}$$

$$A_y = A_{xy} \sin\theta \tag{14}$$

Therefore, the unit vector "u" along the vector "A" relationship to "θ" is defined as:

$$u = \cos^2\theta\, i + \sin\theta \cos\theta\, j + \sin\theta\, k \tag{15}$$

Using Trigonometry to represent the unit vector "u" relationship to $\varphi \frac{\mathrm{d}}{\mathrm{dt}} \mathrm{f(t)}$ as follows:

$$\sin\theta = \sin\left(\tan^{-1}\left(\varphi\frac{d}{dt}f(t)\right)\right) = \frac{\varphi\frac{d}{dt}f(t)}{\sqrt{\left(\varphi\frac{d}{dt}f(t)\right)^2+1}} \tag{16}$$

$$\cos\theta = \cos\left(\tan^{-1}\left(\varphi\frac{d}{dt}f(t)\right)\right) = \frac{1}{\sqrt{\left(\varphi\frac{d}{dt}f(t)\right)^2+1}} \tag{17}$$

$$u = \frac{1}{\left(\varphi\frac{d}{dt}f(t)\right)^2+1}i + \frac{\varphi\frac{d}{dt}f(t)}{\left(\varphi\frac{d}{dt}f(t)\right)^2+1}j + \frac{\varphi\frac{d}{dt}f(t)}{\sqrt{\left(\varphi\frac{d}{dt}f(t)\right)^2+1}}k \tag{18}$$

Therefore, the Unit Spatial Dimensions Transform (USDT) matrix is defined as:

$$U = \begin{bmatrix} \frac{1}{\left(\varphi\frac{d}{dt}f(t)\right)^2+1} & \frac{\varphi\frac{d}{dt}f(t)}{\left(\varphi\frac{d}{dt}f(t)\right)^2+1} & \frac{\varphi\frac{d}{dt}f(t)}{\sqrt{\left(\varphi\frac{d}{dt}f(t)\right)^2+1}} \end{bmatrix} \tag{19}$$

To determine the ranges of the “i”, “j” and “k” coordinates, limits approaches ±∞, 0, and 1 are apply as follows:

$$\lim_{\varphi\frac{d}{dt}f(t)\to\pm\infty} U = [0 \quad 0 \quad \pm 1] \tag{20}$$

$$\lim_{\varphi\frac{d}{dt}f(t)\to 0} U = [1 \quad 0 \quad 0] \tag{21}$$

$$\lim_{\varphi\frac{d}{dt}f(t)\to\pm 1} U = \left[\frac{1}{2} \quad \pm\frac{1}{2} \quad \pm\frac{1}{\sqrt{2}}\right] \tag{22}$$

Therefore, the “i”, “j” and “k” coordinates ranges are:

$$0 \leq i\ coordinate \leq 1 \tag{23}$$

$$-\frac{1}{2} \leq j\ coordinate \leq \frac{1}{2} \tag{24}$$

$$-1 \leq k\ coordinate \leq 1 \tag{25}$$

Let's investigate the effects of the amplification factor "φ":

$$\lim_{\varphi \to \pm\infty} U = [0 \quad 0 \quad \pm 1] \tag{26}$$

$$\lim_{\varphi \to 0} U = [1 \quad 0 \quad 0] \tag{27}$$

$$\lim_{\varphi \to \pm 1} U = \left[\frac{1}{\left(\frac{d}{dt} f(t)\right)^2 + 1} \quad \frac{\pm \frac{d}{dt} f(t)}{\left(\frac{d}{dt} f(t)\right)^2 + 1} \quad \frac{\pm \frac{d}{dt} f(t)}{\sqrt{\left(\frac{d}{dt} f(t)\right)^2 + 1}} \right] \tag{28}$$

The effects of the amplification factor "φ" can be summarized as follows:

- "φ" = 0 – saturate the transformation state.
- "φ" = 1 – unscaled transformation state, where the rate of change of "f(t)" is not amplify.
- "φ" = –1 – unscaled transformation state, however, for "j" and "k" coordinates, the rate of change is inverse.
- "φ" positive increase – decreases in "i" coordinate and increases in "j" and "k" coordinates. This will amplify the effects of small changes and saturate large changes.
- "φ" negative decrease – decreases in "i" coordinate and inversely increases

in “j” and “k” coordinates. This will inversely amplify the effects of small changes and saturate large changes.

Therefore, the value of “φ” is introduced to enhance and control the small changes in data and saturate large changes to minimize the effects of noises. In practice, the value of “φ” is an arbitrary number and can be selected via trial and error mechanism.

It is important to emphasize that USDT automatically transform, normalize and scale the data to the range between negative 1.0 to positive 1.0. The transformation of the data is achieve by the removal of offsets using derivatives and the modulations of the amplification factor. The normalization and scaling of the data is achieve by the derivatives in unit vector dimensions.

To enforce the directional cosines constraint as defined in (8), USDT is square and defined as:

$$U^2 = \left[\frac{1}{\left(\left(\varphi \frac{d}{dt} f(t)\right)^2 + 1\right)^2} \quad \frac{\left(\varphi \frac{d}{dt} f(t)\right)^2}{\left(\left(\varphi \frac{d}{dt} f(t)\right)^2 + 1\right)^2} \quad \frac{\left(\varphi \frac{d}{dt} f(t)\right)^2}{\left(\varphi \frac{d}{dt} f(t)\right)^2 + 1} \right] \tag{29}$$

$$0 \leq U^2 \leq 1 \tag{30}$$

The key feature of U^2 is that the sum of its “i”, “j” and “k” coordinates is equal to 1.0. Therefore, the data is consistently transform, normalize and scale to the range between 0.0 and 1.0, which is well suited for artificial neural networks (ANN) inputs.

The SDT matrix denoted as “S”, which preserves the data integrity of the function, scalar values (minimum 2 values) or vector is:

$$S = A \odot U \tag{31}$$

$$S = f(t) \odot \left[\frac{1}{\left(\varphi \frac{d}{dt} f(t)\right)^2 + 1} \quad \frac{\varphi \frac{d}{dt} f(t)}{\left(\varphi \frac{d}{dt} f(t)\right)^2 + 1} \quad \frac{\varphi \frac{d}{dt} f(t)}{\sqrt{\left(\varphi \frac{d}{dt} f(t)\right)^2 + 1}} \right] \tag{32}$$

To visualize the SDT for a time-series signal, a simulation of a sinewave and transposed using SDT is shown in Fig. 6.1.2.3.

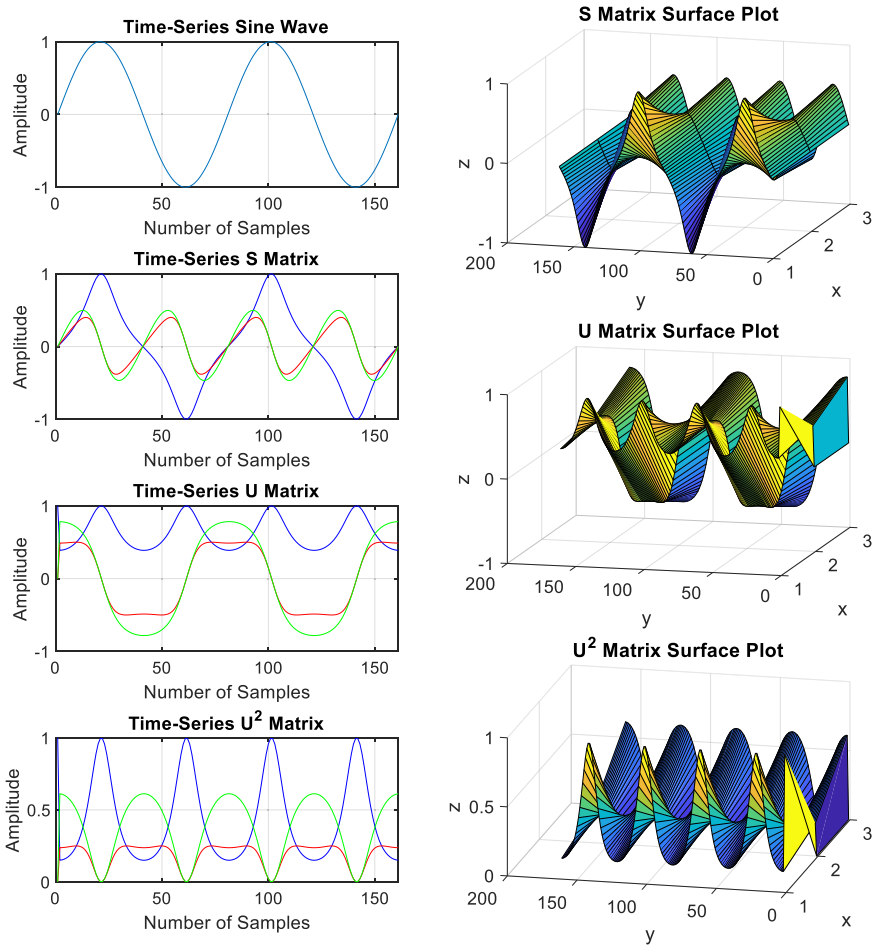

Figure 6.1.2.3 – Spatial Dimensions Transform of Simulated Time-Series Signal

Figure 6.1.2.3 plotted in time-series the values of the "i" (blue), "j" (red) and "k" (green) coordinates for the matrix "U" and "U^2". The "x" (blue), "y" (red) and "z" (green) coordinates for the matrix "S". The 3D surface plots of "S", "U" and "U^2" also plotted in Fig. 6.1.2.3.

As shown in Fig. 6.1.2.3, SDT represent the data as vectors on 3-dimensional Cartesian coordinates. Each of the coordinates is one representation of the data and can be selected as an augmented data.

To visualize the SDT for an image data, a public domain image of the Sydney Opera House, which released under Creative Commons CC0 by Pixabay, is downloaded and transposed using SDT. The image is shown in Fig. 6.1.2.4.

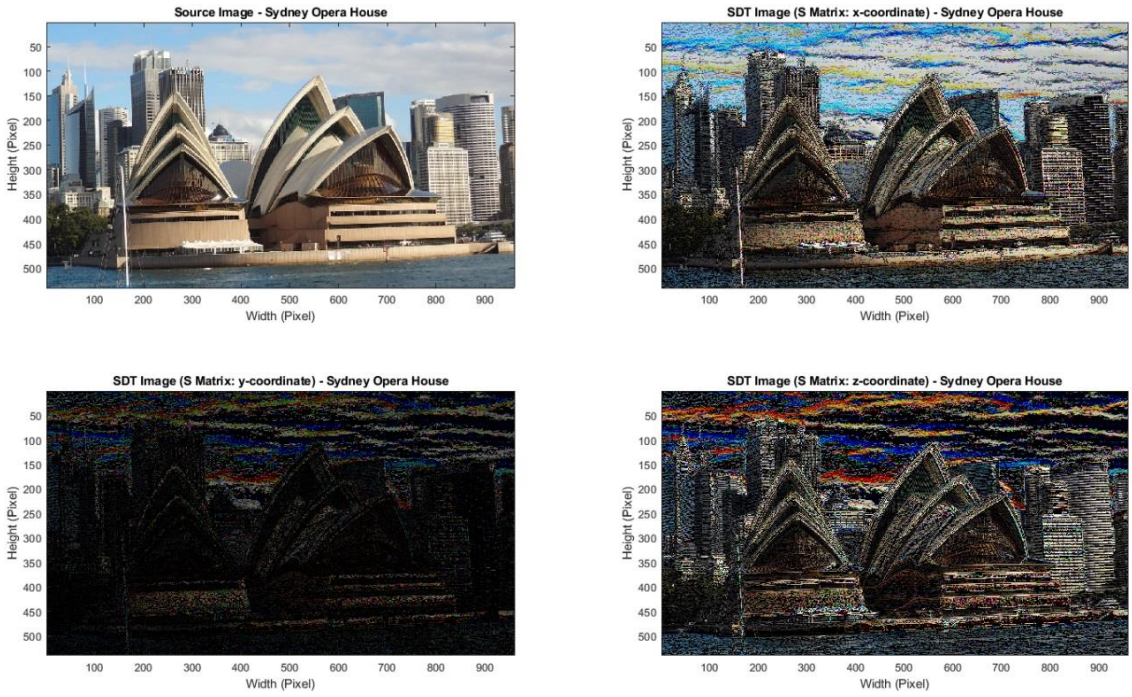

Figure 6.1.2.4 – Spatial Dimensions Transform of An Image

As shown in Fig. 6.1.2.4, SDT transposed the original image into 3 separate images, which are the “x-dimension”, “y-dimension” and “z-dimension” representations. It can be observed that the rate of change in the image contrast, brightness, color intensity and edges are highlighted on different scales. SDT, when it is applied to the image data, besides the data augmentation and features extraction capabilities, can also deliver the benefit of edge detection.

6.1.3 Inverse SDT

A transform method cannot be completed if the methodology to inverse the transformed matrix to recover the original data is not defined. Therefore, section 6.1.3 presents the inverse process of the SDT named inverse Spatial Dimensions Transform (iSDT). This technique can be used to recover the original data when only SDT matrix is provided. The iSDT is defined as:

$$\text{iSDT}(t) = \frac{1}{\varphi}\int \frac{\sin\theta\cos\theta}{\cos^2\theta}d\theta + c_0 \tag{33}$$

$$\text{iSDT}(t) = \frac{1}{\varphi}\int \frac{\sin\left(\tan^{-1}\left(\varphi\frac{d}{dt}f(t)\right)\right)}{\cos\left(\tan^{-1}\left(\varphi\frac{d}{dt}f(t)\right)\right)}dt + c_0 \tag{34}$$

$$\text{iSDT}(t) = \begin{Bmatrix}\frac{1}{\varphi}\int \frac{U_j(t)}{U_i(t)}dt & , & U_i(t) \neq 0 \\ 0 & , & U_i(t) = 0\end{Bmatrix} + c_0 \tag{35}$$

Where: "c_0" is a constant of the initial value.

6.2 Spatial Dimensions Decomposition

Section 6.2 presents the methodologies in data transformation, augmentation, normalization, scaling and feature extraction, named Spatial Dimensions Decomposition (SDD). The principle aim of SDD is to decompose any given function, scalar values (minimum 2 values) or vector into flattened matrix consisting of multi-coordinates columns according to the decomposition level. The SDD methodology, decomposition tree and algorithm are detailed in subsections 6.2.1, 6.2.2 and 6.2.3. The SDD approaches on data transformation, augmentation and feature extraction are detailed in subsections 6.2.4, 6.2.5 and 6.2.6.

6.2.1 SDD Methodology

SDD is an iterative SDT according to the decomposition level. The number of flattened multi-coordinates columns "C" according to the decomposition level is:

$$C = \sum_{d=1}^{D} 3^d \tag{36}$$

Where: "C" is the number of flattened multi-coordinates columns and "D" is the decomposition level.

6.2.2 SDD Decomposition Tree

The visualization of the SDD decomposition tree is shown in Fig. 6.2.2.1.

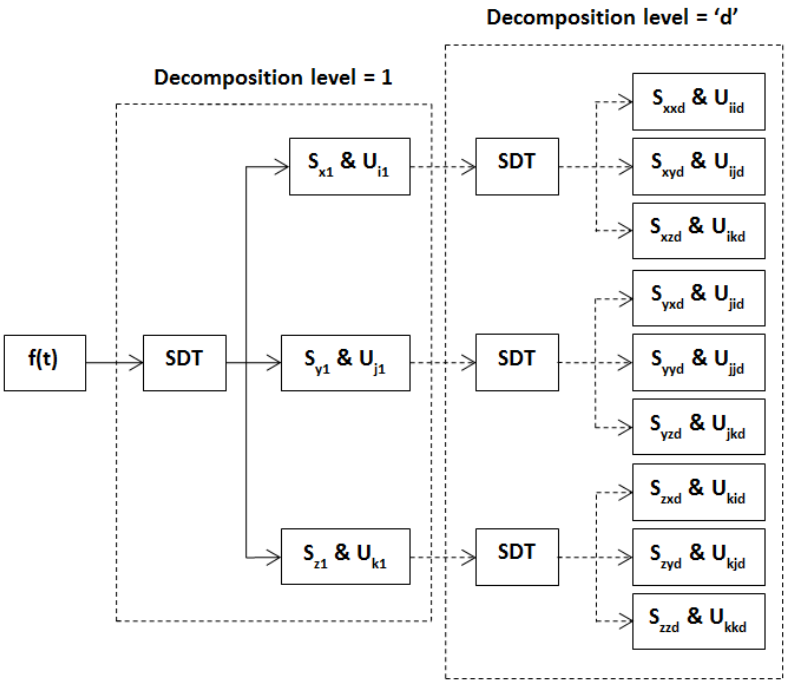

Figure 6.2.2.1 – Spatial Dimensions Decomposition Tree

6.2.3 SDD Algorithm

```
[S_temp, U_temp, U^2_temp] = SDT _function(f);
S(:, 1:3) = S_temp;
U(:, 1:3) = U_temp;
U^2(:, 1:3) = U^2_temp;
pointer = 1;
start_column = 4;
for i = 2 : decompose_level
   iteration = 3^i / 3;
   for j = 1 : iteration
      [f] = S(:, pointer);
      end_column = start_column + 2;
      [S_temp, U_temp, U^2_temp] = SDT_function (f);
      S(:, start_column:end_column) = S_temp;
      U(:, start_column:end_column) = U_temp;
      U^2(:, start_column:end_column) = U^2_temp;
      pointer = pointer + 1;
      start_column = start_column + 3;
   end
end
```

6.2.4 SDD Approach on Data Transformation

SDT and SDD are design to automatically transform, normalize and scale the data in a single process. SDD can be used as multi-dimensional data transformation for any given function, scalar values (minimum 2 values) or vector. The term “data” also encapsulate variations of data types, such as, image, text, dynamic time-series or speech signals.

6.2.5 SDD Approach on Data Augmentation

The decomposed flattened multi-coordinates columns produced by SDD represent the data in multi 3-dimensional coordinates. Each of the flattened coordinates is by itself an augmented representation of the data. In addition, the iSDT of each of the decompose level is also an augmented representation of the data.

6.2.6 SDD Approach on Feature Extraction

There are many features that can be extracted from SDD depending on the application.

In the context of simplicity, section 6.2.6 only presents the basic features extraction methods as an initial guide.

SDT and SDD are generic, however, section 6.2.6 only focuses on supervised learning applications, which is either "classification" or "regression" applications.

1. Classification Features – For classification application, to reduce the variations in each of the SDD flattened multi-coordinates columns; a basic statistical features are applied. The basic statistical features extract features as per window-based, with a fixed window-width, denoted as "W_f", and a sliding window-width, denoted as "W_s", for the entire length of each of the flattened multi-coordinates columns.

2. Regression Features – For regression application, the features in the most simplistic form are the SDD flattened multi-coordinates columns according to the decomposition level. The higher the decomposition level, the higher numbers of features are obtained. In addition, iSDT can be used to augment the data, and follow by a transformation using SDT. In either case, basic statistical features then apply similar to the classification features approach as described above.

3. Statistical Features – The basic statistical methods for obtaining the features are: "mean", "standard deviation" and "variance".

   The number of statistical features, denoted as "F_{stat}" is:

$$F_{stat} = mC = m\sum_{d=1}^{D} 3^d \tag{37}$$

   Where: "m" is the number of statistical methods.

6.3 Conclusion

Chapter 6 contributes to the field of non-contact sleep monitoring by introducing a novel 3-dimensional feature representation and extraction technique, consisting of two methods named Spatial Dimensions Transform (SDT) and Spatial Dimensions Decomposition (SDD). SDT and SDD when combined can achieve data transformation, augmentation, normalization, scaling, and feature extraction in a single process. The novelty of SDT and SDD is that feature engineering process is not required. The pre-processing of signals, DC-offsets removal, signals filtering, expert domain knowledge, wavelet decomposition and/or time-frequency domain analysis are not required in the process of extracting the features.

The real-life applications and results of "SDT and SDD" in non-contact sleep monitoring is presented in Chapter 7, section 7.3 and 7.4 of the Thesis.

The work presented in Chapter 6 is patented in [162, 163].

CHAPTER 7

NOVEL REAL-LIFE APPLICATIONS AND RESULTS OF NON-CONTACT SLEEP MONITORING

Thesis Contribution 6:

Novel Real-Life Applications and Results

INTRODUCTION

Chapter 7 is a response to the demands for non-contact sleep monitoring systems. The demands arise due to the limitations of the polysomnography (PSG) system, the importance of early screening for obstructive sleep apnea (OSA), the need for long-term continuous monitoring and the concern with respect to patient discomfort when using current devices. In this chapter, real-life applications and the results of the non-contact sleep monitoring using the microwave Doppler radar in the complex sleep environment, including "non-stationary" and "non-direct facing" subject's measurements are presented. The contribution of chapter 7 is the novel high accuracy non-contact estimations/predictions of the following sleep monitoring parameters:

1. Respiratory rate.
2. Heart rate.
3. Tidal volume.
4. Body orientations, i.e., “Prone”, “Upright”, “Supine”, “Right” and “Left” sleep orientations.
5. Oxygen saturation.

The importance of continuous monitoring of the above vital signs and sleep orientations are due to the following reasons:

- Respiratory Rate – Respiratory parameters have been widely used in psychophysiology to index the effects of stress and emotions [164] [165]. Psychological distress generally leads to increases in respiration rate, minute volume and a shift from abdominal to thoracic breathing. In extreme cases this may lead to a lowering of carbon dioxide partial pressure (pCO_2) values with concomitant symptoms of the hyperventilation syndrome [166].

  In addition, sleep causes certain impairment in breathing for normal people and exaggerates instability in breathing pattern. The rapid-eye-movement (REM) sleep stage has specific effects on breathing with variability in breathing pattern [167].

- Heart Rate – Heart rate (HR) among other vital signs, such as, respiration rate, blood oxygen saturation and blood pressure, is one of the most commonly measured and monitored health indicator. The HR is considered the primary vital sign information needed from patients in both emergency and clinical situations [168] [169]. The HR data is related to the analysis of the circadian rhythm (in sleep), temperature regulation, cardiac sympathetic nervous activity and synchronization with respiration rate [169]. It is also important to recognize that increased autonomic nervous system (ANS) activity during the REM sleep may increase the risk of ventricular arrhythmia or exacerbate underlying pathology [167].

- Tidal Volume – Sleep in general and especially in the REM often decreases the tidal volume and ventilation. The effects are exaggerated significantly in patients with OSA and respiratory disease [167].

- Body Orientations – Sleep body orientations reveal the relationships to OSA, insomnia, and periodic limb movement disorder (PLMD). Analyzing the body orientations during sleep will also help determine the sleep quality and irregular sleeping patterns.

- Oxygen saturation – Continuous monitoring of oxygen saturation level is crucial because it provides important information about the severity of the respiratory dysfunction.

7.1 Non-Contact Respiratory and Heart Rates Estimation

The aim of section 7.1 is to present two novel real-life applications, "non-stationary" and "non-direct facing", including the results of the non-contact respiratory and heart rates estimation using the microwave Doppler radar in the complex sleep environment.

The first application utilizes an automated estimation algorithm, comprising of signals separation, reconstruction, demodulation, respiratory and heart rates estimation to estimate the respiratory and heart rates during sleep.

The second application utilizes the "Relative Demodulation" and "Respiratory and Heart Rates Estimation Algorithm" theory and technique presented in Chapter 3 to estimate the respiratory and heart rates during sleep.

A comparison of the respiratory and heart rates estimation accuracy between the two applications and results is also presented.

7.1.1 Patients' Dataset for Respiratory and Heart Rates Estimation

A sample of twenty chronic heart failure (CHF) patients, selected from the patients' database as documented in Appendix II, section A.II.IV, were utilized for the verification of the respiratory and heart rates estimation accuracy for both applications. Refer to Appendix II, section A.II.IV, for further details on the dataset.

7.1.2 Respiratory and Heart Rates Estimations using Automated Estimation Algorithm

Subsection 7.1.2 presents a novel automated estimation algorithm that estimates the respiratory and heart rates for CHF patients in the complex sleep environment. The automated estimation algorithm is design based on the arrangement of three key components:

- Signals Separation & Reconstruction (SSR).
- Signals Demodulation (SD).
- Respiratory and Heart Rates Estimation (RHE).

The automated estimation algorithm is presented in a block diagram as shown in Fig. 7.1.2.1. The "Detrend" and "Wavelet Packet Decomposition" are sub-components of SSR component. The "Gram-Schmidt Orthogonalization", "Arctangent Demodulation", "Motion Scaling" and "Butterworth Filters" are sub-components of SD component. The two final rates estimation blocks are the sub-components of the RHE component.

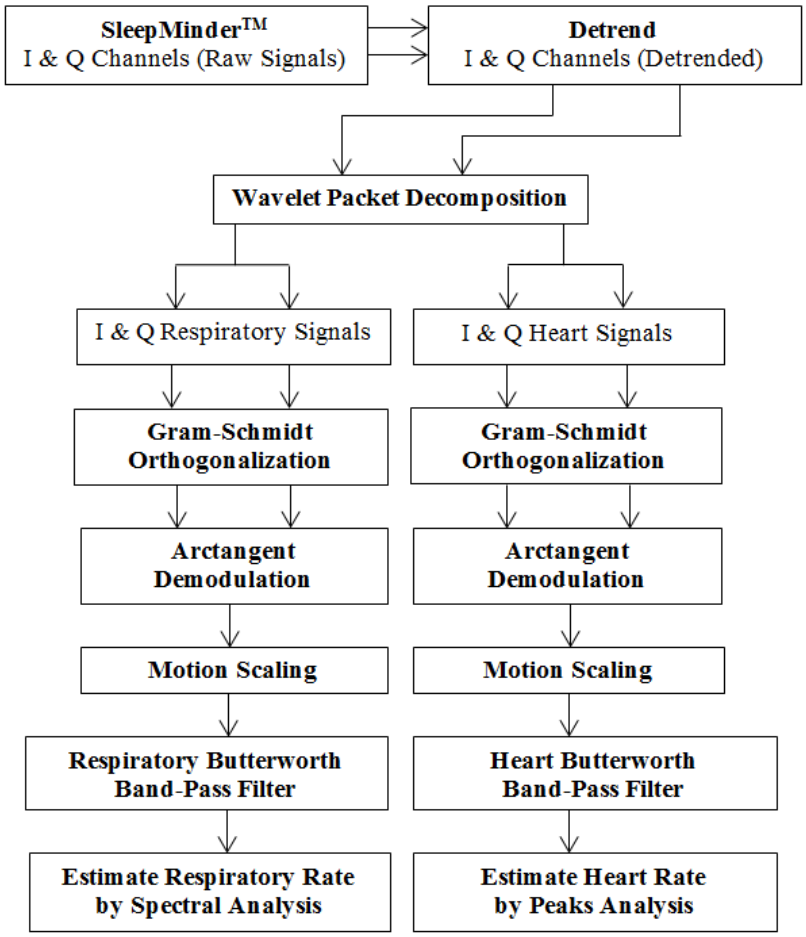

Figure 7.1.2.1 – Automated Estimation Algorithm Block Diagram

7.1.2.1 Signal Separation & Reconstruction Component

Wavelet analysis is a powerful and popular tool used in the analysis of the non-stationary signals. The Wavelet Packet Decomposition (WPD) was chosen instead of the Discrete Wavelet Transform (DWT) because both the "approximations" and "details" coefficients are required to separate the respiratory and heart signals. To determine the choice of the wavelet filter and order, a "trial-and-error" approach was adopted to compare the performance of some known wavelet families, such as, Haar, Daubechies, Symlets and Coiflets. The performance results indicated that the Symlet wavelet with filter order of 4 provides the most optimum accuracy level and a balance of computational time.

Prior to decomposing the signals, DC offsets were removed by applying the Detrend method, which subtracts the mean from the signals. Based on the SleepMinder™ (SM)

sample rate, both I and Q channels are decomposed to 4th level with both "approximations" and "details" coefficients decomposed. From the decomposed "approximations" and "details" coefficients, the frequency band of interest for respiratory signal is 0–5 Hz, which corresponds to the 0–30 breaths per minute and the heart signal is 0.5–2.0 Hz, which corresponds to the 30–120 beats per minute. The decomposed I and Q respiratory signals are then reconstructed at the 4th level using the "approximations" coefficients. The decomposed I and Q heart signals are then reconstructed from the sum of both 3rd and 4th level using the "details" coefficients.

7.1.2.2 Signal Demodulation Component

In the Doppler radar system, the most important limitation when measuring periodic motions such as respiratory and heart rates is the presence of null-points. The arctangent demodulation method is a solution that combines the in-phase and quadrature baseband signals into single channel to eliminate null-points.

Prior to the demodulation, the Gram-Schmidt procedure was employed to correct both respiratory and heart signals imbalances. The arctangent demodulation is then performed to extract the phase-modulated signals. The extracted phase-modulated is then multiplied with a motion scaling factor to obtain the respiratory and heart motions. The motion scaling factor is (λ / 4π), where λ = 299,792,458 ms^{-1} / 5.8 x 10^{6} Hz.

A Butterworth 6th order band pass filter (BPF) with frequency bandwidth of 0.2–0.5 Hz corresponds to 12–30 breaths/min is applied to the respiratory motions to eliminate clutters, heart motions, movements and noises.

A Butterworth 6th order BPF with frequency bandwidth of 0.7–1.6 Hz corresponds to 42–96 beats/min is applied to the heart motions to eliminate respiratory motions, movements and noises.

7.1.2.3 Respiratory and Heart Rates Estimation Component

The estimation of the respiratory and heart rates employs two analysis methods. The respiratory rate estimation uses spectral analysis, which employs Short Time Fourier Transform (STFT) with a fixed window width of 60 seconds (2 epochs) and a sliding fixed window width of 30 seconds (1 epoch). The terminology "epoch" is refer to the interval of 30 seconds in the sleep analysis defined by the American Academy of Sleep Medicine (AASM). This is the standardized block of analysis in OSA diagnosis recommended by AASM, and the selected window is an adherence to the epoch standard. For each fixed window width, Fast Fourier Transform (FFT) is performed and the spectrum magnitudes are smoothed by applying cubic Savitzky-Golay filter. The smoothed magnitude peaks are then identified and sorted in descending order.

The respiratory rate is then calculated from the associated frequency of the first sorted peak, multiplied by 60 seconds to obtain the breaths per minute. The heart rate estimation uses time-domain peaks analysis with the same window and sliding window width as used in spectral analysis. For each fixed window width, local maxima are identified and the heart rate is then calculated from the sum of the number of identified local maxima to obtain the beats per minute.

7.1.2.4 Performance Measures

In order to compare the outputs of the algorithm with the gold-standard PSG recordings, the PSG respiratory inductive plethysmography (RIP) thorax sample at 32Hz and electrocardiogram (ECG) sample at 256Hz signals were selected. However, since the sample rate of the PSG signals differs from the SM sample rate, the RIP thorax signal is down-sampled to the SM sample rate and the SM extracted heart motions is up-sampled to the ECG sample rate. The respiratory rate estimation of the down-sampled RIP thorax is performed via Detrend, WPD, respiratory Butterworth 6^{th} order BPF and spectral analysis. This ensures similar mechanism is applied to both SM and PSG respiratory rate estimations for accurate comparison. The ECG heart rate estimation utilized a reliable real-time QRS detection algorithm by Pan-Tompkins [170] to extract the R-wave peaks. The ECG heart rate is then calculated from the number of identified R-peaks within the

fixed window as used by SM peaks analysis to obtain the beats per minute. This ensures reliable and accurate comparison.

Equation (1) is used to find the mean accuracy percentage for a single patient with "N" equal to the total number of estimated data points:

$$\overline{x} = \frac{100}{N}\sum_{n=1}^{N}\left\{\begin{matrix}\frac{SM[n]}{PSG[n]} & , \quad SM[n] \leq PSG[n] \\ \frac{2PSG[n] - SM[n]}{PSG[n]} & , \quad SM[n] > PSG[n]\end{matrix}\right\} \tag{1}$$

Equation (2) is used to find the mean error for a single patient and compares between the SM estimated rate and the PSG estimated rate:

$$e = \frac{1}{N}\sum_{n=1}^{N}|PSG[n] - SM[n]| \tag{2}$$

7.1.2.5 Results and Discussions

One patient (from a sample size of twenty patients) was selected to demonstrate the accuracy of the automated estimation algorithm and this is shown in Fig. 7.1.2.2. The SM estimated respiratory and heart rates tracked exceptionally well with the PSG RIP thorax and ECG estimated respiratory and heart rates for the whole duration of the sleep recording of 6 hours 23 minutes and 19.1875 seconds (367,987 samples at 16Hz). The spikes are in those periods which correspond to the significant body movements and the differences in the x-axis are due to the down-sampled and up-sampled data.

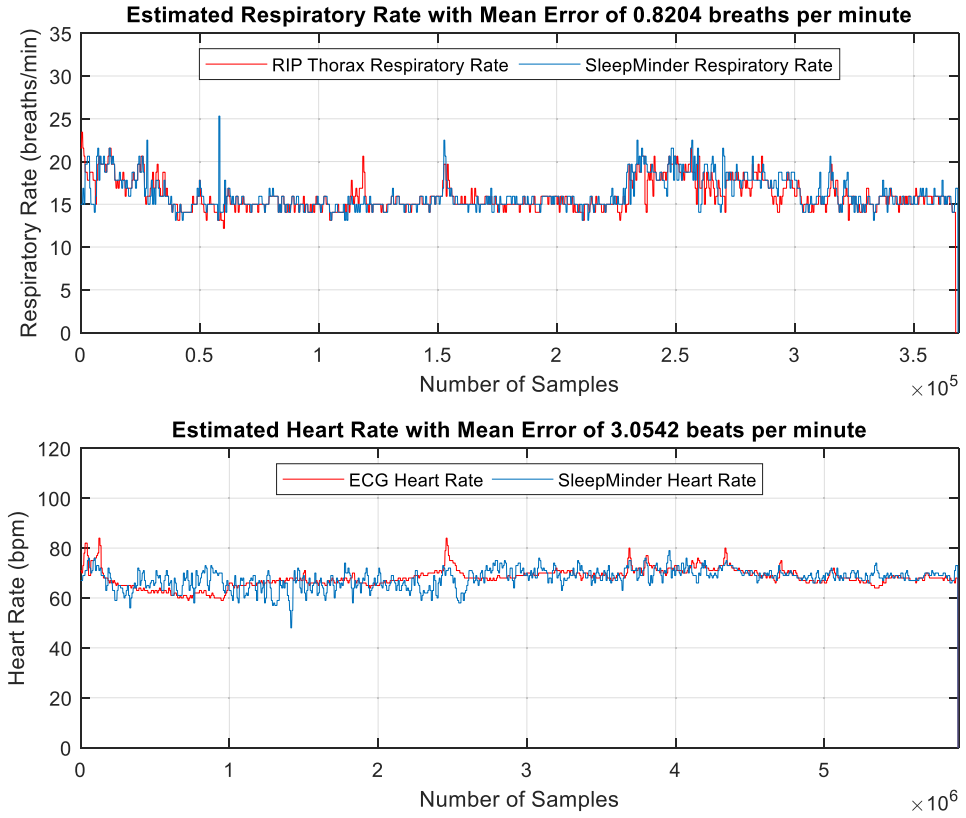

Figure 7.1.2.2 – SleepMinder™ versus PSG Estimated Respiratory and Heart Rates

The performance measures were obtained for all twenty patients and are shown in Fig. 7.1.2.3 and Fig. 7.1.2.4. Across all the twenty patients' recordings, the respiratory rate estimation median accuracy achieved is 92.68% with a median error of ±1.22 breaths per minute. The heart rate estimation median accuracy achieved is 88.26% with a median error of ±7.85 beats per minute.

The outliers on the statistical analysis box whisker plot, for the respiratory rate estimation correspond to those patients whose PSG and SM data contain significant body movements, noises and signals dropouts during the sleep recording. The main challenge that affects the accuracy of the heart rate estimation is a condition referred to as "bradycardia" or "tachycardia" which affect the body movements during sleep. Predefined signal decomposition, demodulation and static filtering have not been able to adapt in this case. CHF patients in particular, or sleep subjects in general, pose a greater challenge in the non-contact signal processing of heart rate estimation.

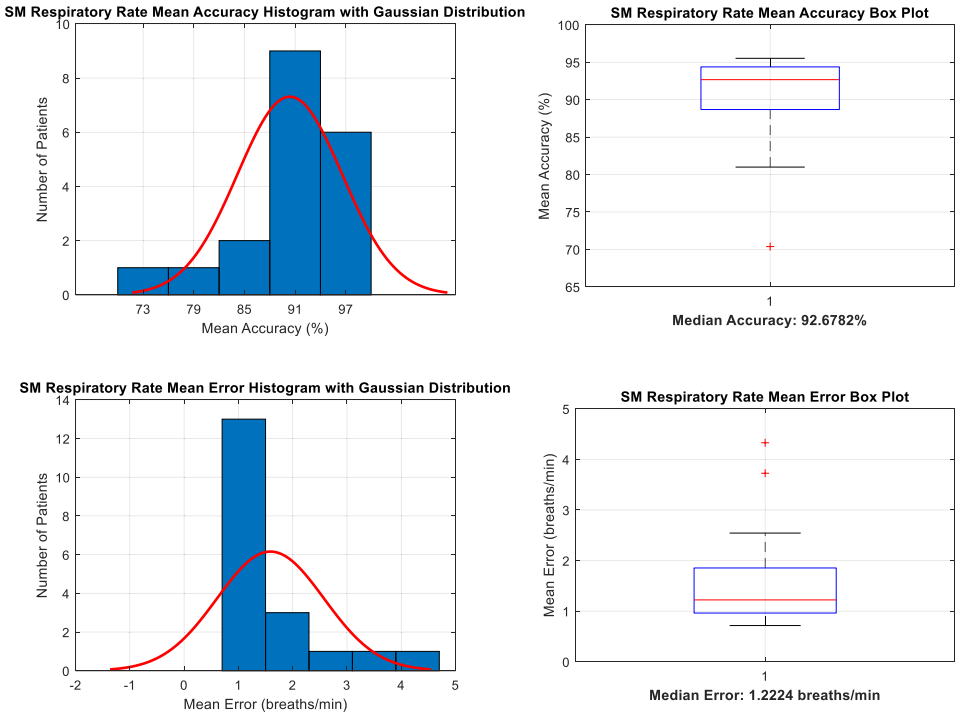

Figure 7.1.2.3 – SleepMinder™ Estimated Respiratory Rate Mean Accuracy and Error

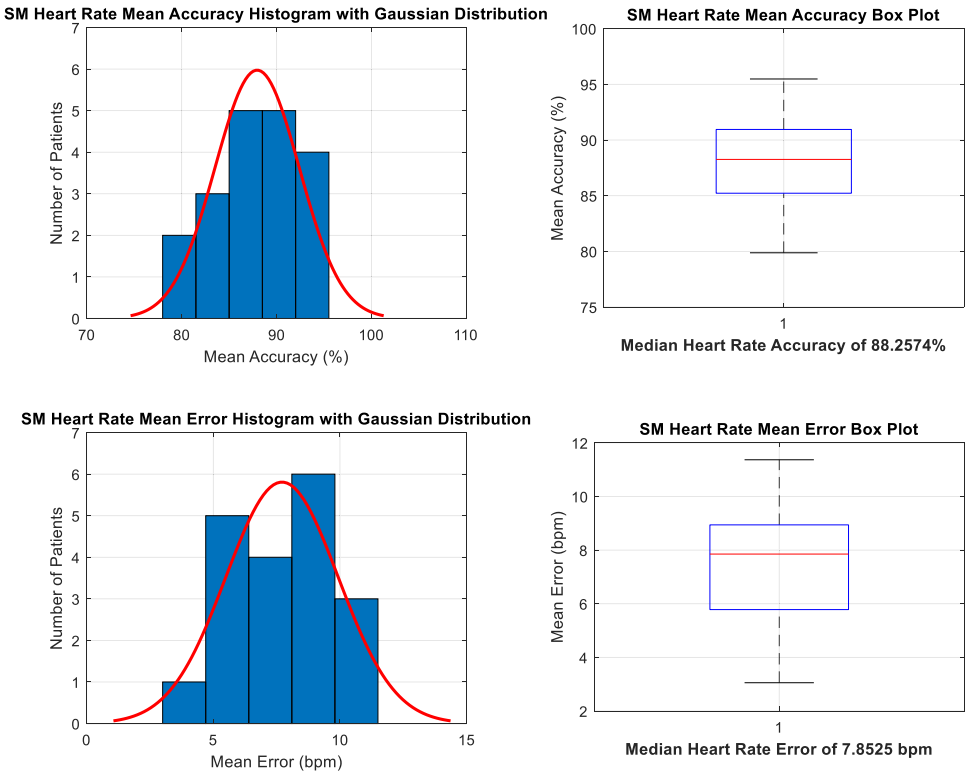

Figure 7.1.2.4 – SleepMinder™ Estimated Heart Rate Mean Accuracy and Error

7.1.2.6 Conclusion

Subsection 7.1.2 demonstrates the proven methodology of using an automated estimation algorithm and the non-contact microwave Doppler radar, to estimate both respiratory and heart rates in the complex sleep environment with good accuracy rate.

The respiratory rate estimation median accuracy achieved is 92.68% with median error of ±1.22 breaths per minute. The heart rate estimation median accuracy achieved is 88.26% with median error of ±7.85 beats per minute. A potential application is the non-contact continuous sleep and circadian rhythm monitoring which can be used at home.

7.1.3 Respiratory and Heart Rates Estimations using Relative Demodulation and Respiratory and Heart Rates Estimation Algorithm

Section 7.1.3 presents the results of the application of the "Relative Demodulation" and "Respiratory and Heart Rates Estimation" algorithm presented in Chapter 3. A detailed discussion on the results is also provided.

7.1.3.1 Results and Discussions

In order to compare the outputs of the algorithms with the gold-standard PSG recordings, the PSG RIP thorax sample at 32Hz and ECG sample at 256Hz signals were selected. However, since the sample rate of the PSG signals differs from the SM sample rate, the RIP thorax signal is down-sampled to SM sample rate and the SM demodulated heart jerk is up-sampled to ECG sample rate.

The respiratory rate estimation for the down-sampled RIP Thorax is performed via RBPF, inspiration and expiration detection, and respiration rate estimation algorithms. This ensures similar mechanisms are applied to both SM and PSG respiratory rate estimations for accurate comparison.

The ECG heart rate estimation utilized a reliable real-time QRS detection algorithm by Pan-Tompkins [170] to extract the R-wave peaks. The ECG heart rate is then calculated from the number of identified R-peaks as per selected window-width. This ensures reliable and accurate reference for heart rate comparison.

One patient (from a sample size of twenty patients) was selected to demonstrate the accuracy of the real-time "Relative Demodulation" technique and estimation algorithm, which is shown in Fig. 7.1.3.1 and Fig. 7.1.3.2.

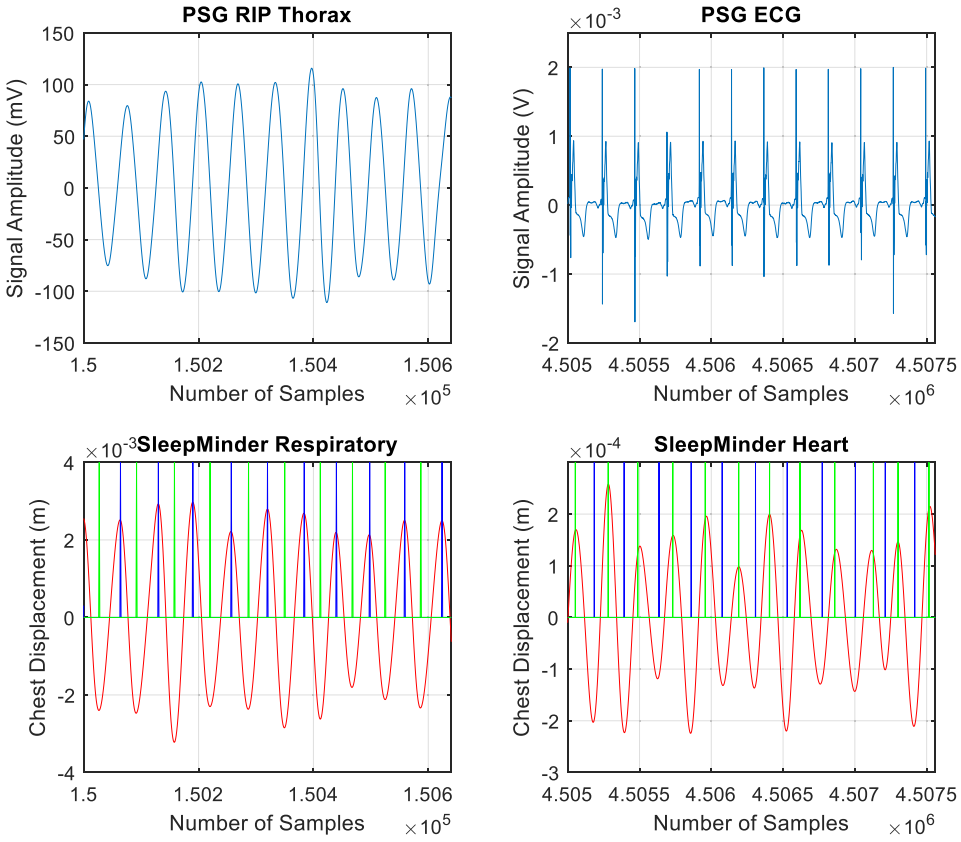

Figure 7.1.3.1 – SleepMinder™ Demodulated Respiratory and Heart Displacements

Fig. 7.1.3.1, the top and bottom left hand side graphs with a data segment of 60 seconds shows that the respiratory displacement has accurately demodulated compared to the PSG RIP Thorax (resampled and filtered) respiratory signal. The inspirations and expirations also accurately detected. The time delay is due to the filtering effects and numerical approximations.

Fig. 7.1.3.1, the top and bottom right hand side graphs with a data segment of 10 seconds shows that the heart displacement (resampled) has accurately demodulated compared to the PSG ECG signal. The systoles (troughs) and diastoles (peaks) also accurately detected. The time delay is due to the filtering effects and numerical approximations.

Fig. 7.1.3.2 shows that the SM estimated respiratory and heart rates track exceptionally well with the PSG RIP Thorax and ECG estimated respiratory and heart rates for the entire duration of the sleep recording of 6 hours 23 minutes and 19.1875 seconds (367,987 samples at 16Hz). The differences in the x-axis are due to the down-sampled and up-sampled data.

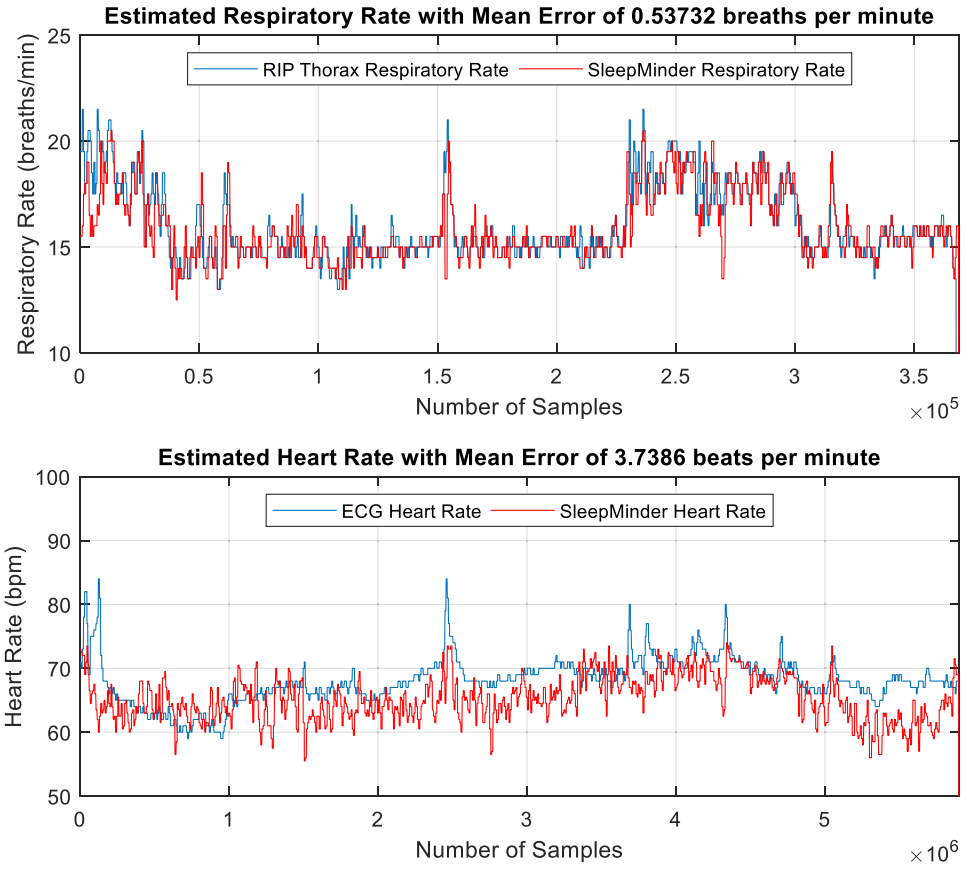

Figure 7.1.3.2 – SleepMinder™ versus PSG Estimated Respiratory and Heart Rates

The performance measures were obtained for all twenty patients and are shown in Fig. 7.1.3.3 and Fig. 7.1.3.4. Across the twenty patients' recordings, the respiratory rate estimation median accuracy achieved is 91.53% with median error of ±1.30 breaths/min. The heart rate estimation median accuracy achieved is 91.28% with median error of ±6.20 beats/min.

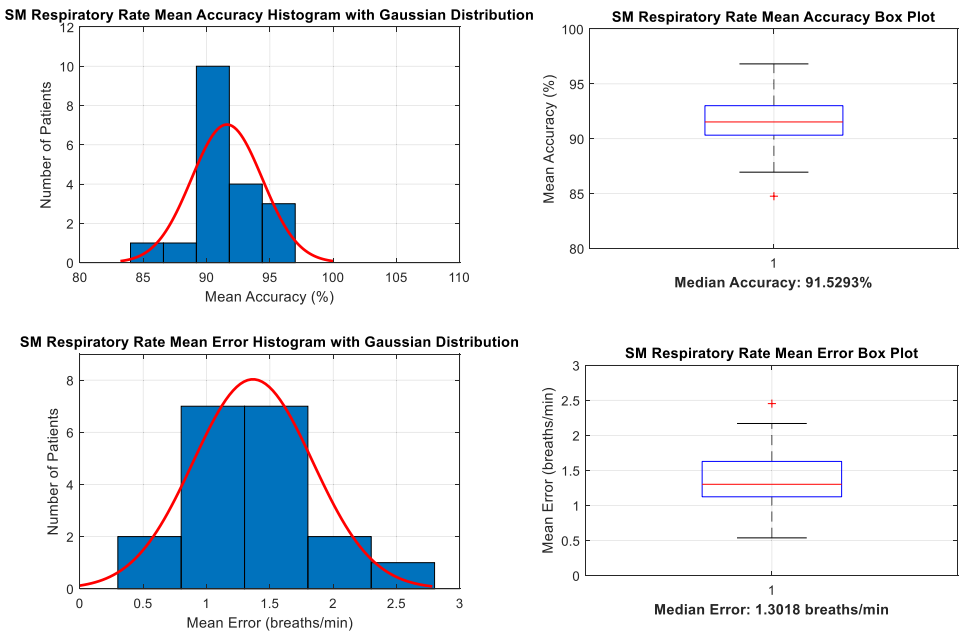

Figure 7.1.3.3 – SleepMinder™ Estimated Respiratory Rate Mean Accuracy and Error

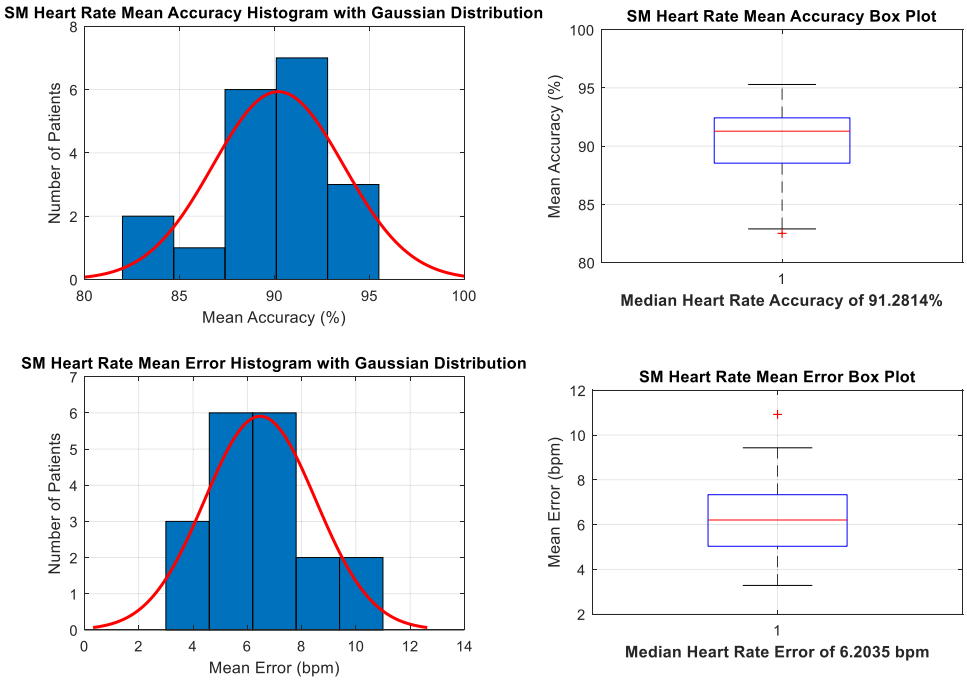

Figure 7.1.3.4 – SleepMinder™ Estimated Heart Rate Mean Accuracy and Error

7.1.3.2 Conclusion

Subsection 7.1.3 demonstrates the proven methodology using the "Relative Demodulation", "Respiratory and Heart Rates Estimation Algorithm" and the non-contact microwave Doppler radar to estimate both respiratory and heart rates. This is done in real-time, in the complex sleep environment and with good accuracy rate.

The respiratory rate estimation median accuracy achieved is 91.53% with median error of ±1.30 breaths/min. The heart rate estimation median accuracy achieved is 91.28% with median error of ±6.20 beats/min. A potential application is the non-contact continuous sleep and circadian rhythm monitoring which can be done at home.

7.1.4 Remarks

Section 7.1 demonstrates the proven methodology of the "non-stationary" and "non-direct facing" respiratory and heart rates estimations using the non-contact microwave

Doppler radar in the complex sleep environment. The two approaches presented has good accuracy results. An accuracy comparison between the respiratory and heart rates estimation presented in section 7.1.2 and 7.1.3 is shown in Table 7.1.4.1.

	Automated Estimation Algorithm (section 7.1.2)	***Relative Demodulation Respiratory and Heart Rates Estimation Algorithm (section 7.1.3)***	***Accuracy Comparison Relative Demodulation as Reference***
Respiratory Rate	92.68% ±1.22 breaths/min	91.53% ±1.30 breaths/min	Decrease accuracy by 1.15% Increase error by 0.08 breaths/min
Heart Rate	88.26% ±7.85 beats/min	91.28% ±6.20 beats/min	Increase accuracy by 3.02% Decrease error by 1.65 beats/min

Table 7.1.4.1 – Respiratory and Heart Rates Accuracy Comparison

As shown in Table 7.1.4.1, the "Relative Demodulation" approach in section 7.1.3 outperforms the "Automated Estimation Algorithm" in section 7.1.2 with respect to heart rate estimation accuracy and error. However, there is an insignificant decrease in the respiratory rate accuracy and error. The key benefits of the "Relative Demodulation" approach is that it is real-time, simple, fast, accurate, low computational and applicable for embedded system. On the other hand, the "Automated Estimation Algorithm" utilizes the wavelet packet decomposition (WPD) and the arctangent demodulation but it is post-processing.

In conclusion, the two novel approach presented can be utilized for the non-contact respiratory and heart rates monitoring during sleep. However, if real-time capability is the priority, then the "Relative Demodulation" method is the preferred approach.

7.2 Non-Contact Tidal Volume Estimation

The aim of section 7.2 is to present the "non-stationary" and "non-direct facing" real-life application and the results of the non-contact tidal volume estimation using the microwave Doppler radar in the complex sleep environment. The application utilizes "Pulmonary Ventilation Mathematical Model" and "Tidal Volume Estimation Algorithm" presented in Chapter 4 to estimate the tidal volume during sleep.

7.2.1 Patients' Dataset for Tidal Volume Estimation

A sample of twenty CHF patients, selected from the patients' database as documented in Appendix II, section A.II.V, Table V.1, were utilized for the verification of the tidal volume estimation application. Refer to Appendix II, section A.II.V, Table V.1, for further details on the dataset.

7.2.2 Tidal Volume Estimations using Pulmonary Ventilation Model and Tidal Volume Estimation Algorithm

Section 7.2.2 presents the results of the application of pulmonary ventilation model and tidal volume estimation algorithm presented in chapter 4. A detailed discussion on the results is also provided.

7.2.2.1 Results and Discussions

In order to compare the output of the algorithm with the gold-standard PSG recordings, the PSG pressure signal from the cannula pressure sensor sample at 8Hz was selected as the reference signal. However, since the sample rate of the PSG pressure differs from the SleepMinder^{TM} (SM) sample rate, the PSG pressure signal was first up-sampled to the SM sample rate.

The tidal volume estimation for the up-sampled pressure signal was performed via EVBP, RBPF, ETV, and EMTV as described in section 4.2.1 Fig. 4.2.1.1. This ensures that identical mechanisms are applied to both SM and PSG estimations for accurate comparison.

Equation (1) is use to find the mean accuracy percentage for single patient, with "N" equal to the total number of estimated data points:

$$\overline{x} = \frac{100}{N}\sum_{n=1}^{N}\begin{Bmatrix} \frac{SM[n]}{PSG[n]} & , \quad SM[n] \leq PSG[n] \\ \frac{2PSG[n] - SM[n]}{PSG[n]} & , \quad SM[n] > PSG[n] \end{Bmatrix} \tag{1}$$

Equation (2) is use to find the mean error for single patient, comparing the SM estimated rate and PSG estimated rate:

$$e = \frac{1}{N}\sum_{n=1}^{N}|PSG[n] - SM[n]| \tag{2}$$

The accuracy percentages, as well as the errors per patient, were calculated by comparing each sample, the estimated mean tidal volume value from the SM to the PSG for the entire sleep recording duration. The resultant median accuracy percentage and error values were then obtained over the patient's entire recording duration. The final median accuracy percentage and error over the entire sample population, i.e., the twenty CHF patients, were obtained via statistical analysis as shown in Fig. 7.2.2.1.

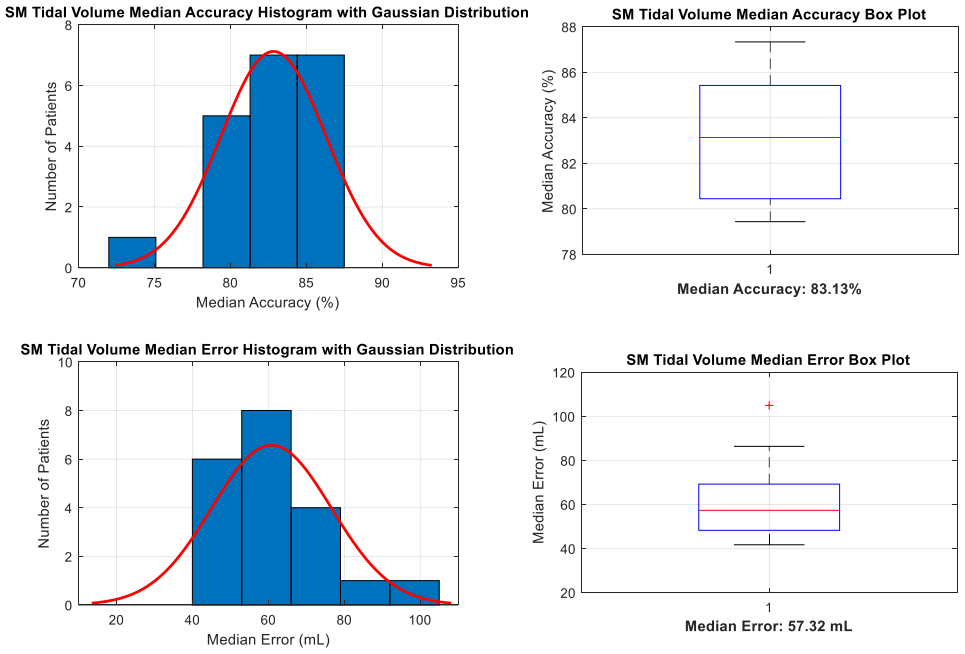

Figure 7.2.2.1 – SleepMinder™ Estimated Tidal Volume Median Accuracy and Error

The performance measures were obtained for all twenty CHF patients and are shown in Fig. 7.2.2.1. Across all twenty CHF patients' recordings with mean recorded sleep duration of 7 hours, 45 minutes and 36 seconds (446,976 samples at 16Hz), the tidal volume estimation median accuracy achieved is 83.13% with a median error of 57.32 milliliters.

The accuracy of the tidal volume estimation is impacted by the real-time chest displacement magnitude and the respiratory rate. However, these are hard to measure in the complex sleep environment because of the unpredictable body movements, body orientation, and interferences. The undesired harmonics, body movements and body orientation in the complex sleep environment are the main challenges in the non-contact signal processing.

7.2.2.2 Conclusion

Subsection 7.2.2 demonstrates the proven methodology using pulmonary ventilation mathematical model, tidal volume estimation algorithm, and the non-contact microwave

Doppler radar to estimate tidal volume in the complex sleep environment with good accuracy level.

Across all twenty CHF patients' recordings with a total sleep duration of 155 hours, 6 minutes and 36 seconds, a mean sleep duration of 7 hours, 45 minutes and 36 seconds, and more than 17 million sample points, the tidal volume estimation median accuracy achieved is 83.13% with a median error of 57.32 milliliters. A potential application is the non-contact continuous monitoring of tidal volume during sleep in the home.

It is important to emphasize that the pulmonary ventilation mathematical model is not restricted to the non-contact applications, it is a novel mathematical model that can also be applied to the PSG systems or to home sleep test devices.

7.3 Non-Contact Body Orientations Prediction

The aim of section 7.3 is to firstly present two "non-stationary" and "non-direct facing" real-life applications and the results of the non-contact nocturnal body orientations prediction using the microwave Doppler radar in the complex sleep environment.

The first application utilizes the wavelet packet decomposition (WPD) as a feature extraction mechanism and a deep artificial neural network. It is implemented using the multilayer perceptron (MLP) architecture to predict the body orientations during sleep.

The second application utilizes the Spatial Dimensions Transform (SDT) and the Spatial Dimensions Decomposition (SDD), as presented in Chapter 6, as a 3-dimensional feature extraction mechanism and multilayer perceptron (MLP) artificial neural network to predict the body orientations during sleep.

A comparison of the body orientations predictions, the performance and the accuracy level between the two applications including the results is also presented.

The aim of section 7.3 is also to illustrate the application of the SDT and SDD when combined with artificial neural network (ANN). This can be applied to solve real-life complex challenge such as “non-stationary”, “non-direct facing” and non-contact prediction of nocturnal body orientations in the complex sleep environment.

7.3.1 Patients’ Dataset Partitions for Body Orientations Prediction

A sample of twenty-four CHF patients, selected from the patients’ database as documented in Appendix II, section A.II.VI, were utilized for the “Training”, “Validation” and “Test” of the body orientations prediction for both applications. Refer to Appendix II, section A.II.VI, for further details on the dataset.

7.3.2 Body Orientations Prediction using Wavelet Packet Decomposition and Deep Neural Network

7.3.2.1 Wavelet Packet Decomposition Process

Body orientations prediction during sleep is a challenging task in non-contact sleep monitoring due to the unpredictable body orientations and positions of a patient during sleep. There is multiple interplay of signal frequencies that are superimposed especially for non-contact sleep monitoring system that uses microwave Doppler radar. The frequencies spectrum consists of multi factors, such as, slow body movements, fast or sudden turn of body orientation, respiratory and heart motions. The complexity increases when patient have other related disorders, such as, restless leg syndrome (RLS) that causes undesired motions in the frequencies spectrum.

In able to predict a patient’s body orientations during sleep, Wavelet Packet Decomposition (WPD) is chosen to separate the wavelets at different frequencies that correspond to physical phenomena, such as, slow/fast body movements, respiratory and heart motions. The reason for utilizing WPD is that the wavelet packet method localized both in time and frequency, and well-suited for non-linear signal analysis.

A block diagram illustrating the process of wavelets extraction from the raw I and Q channels is shown in Fig. 7.3.2.1.

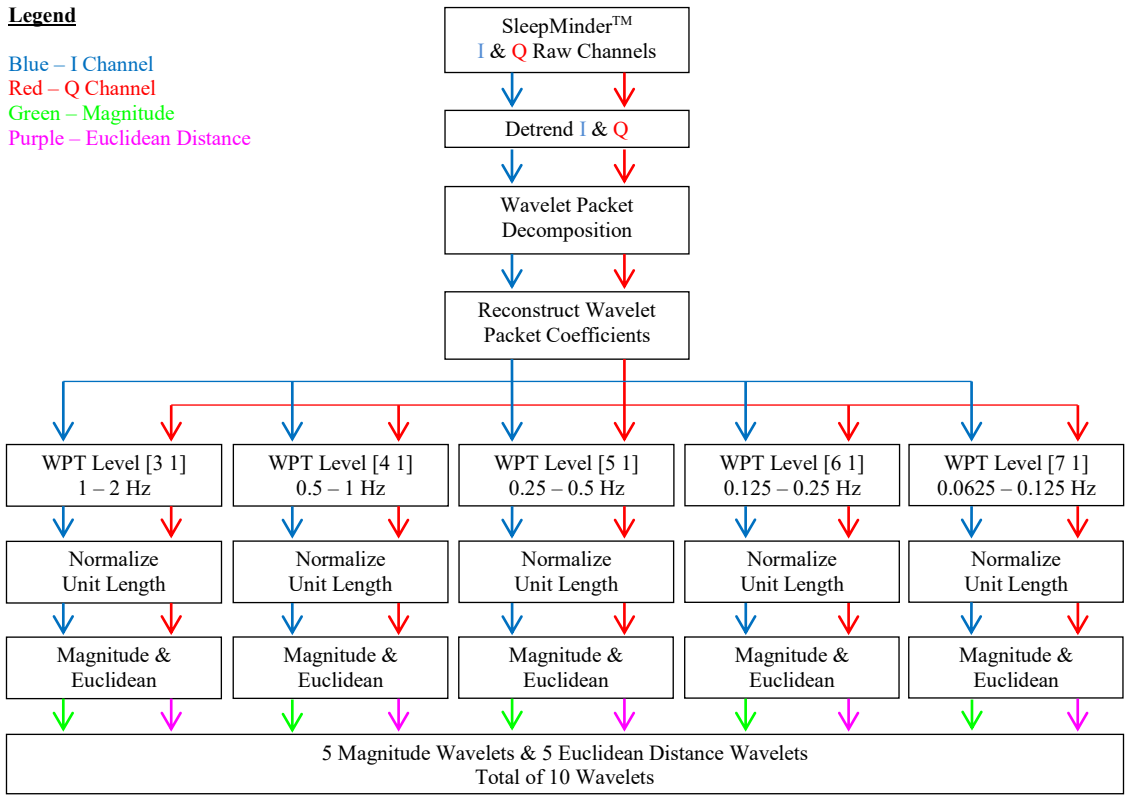

Figure 7.3.2.1 – Wavelets Extraction Process Block Diagram

Prior to applying the wavelet packet decomposition (WPD), the signal was filtered and the DC offsets were removed by subtracting the mean from the raw I and Q channels. The detrended I and Q channels were decomposed to 7^{th} level with both the "approximations" and "details" coefficients decomposed. The mother wavelet for the WPD is the "Symlet" wavelet with 4^{th} order filter. The reason for choosing the "Symlet" wavelet is for its performance and accuracy as detailed in section 7.1.2.1 and the author's published work in [56].

The categories of frequency bandwidth are:

- Slow body movements – The Doppler signatures are reflected at frequencies between greater than 0Hz and 0.25Hz.

- Respiratory chest movements – The Doppler signatures are reflected at frequencies between 0.25Hz and 0.5Hz, which correspond to 7.5–30 breaths per minute.

- Heart chest movements – The Doppler signatures are reflected at frequencies between 0.5Hz and 1.0Hz, which correspond to 30–120 heart beats per minute.

- Fast body movements – The Doppler signatures are reflected at frequencies between 1.0Hz and 2.0Hz.

Therefore, only the "details" coefficients are of interest. The decomposed "details" coefficients were reconstructed at the wavelet packet tree (WPT) levels as indicated in Fig. 7.3.2.1. The reconstructed wavelets were normalized to unit length.

To combine the normalized I and Q wavelets, the magnitude of I & Q and the Euclidean distance of I & Q are calculated for each of the normalized I & Q wavelets. This produces a total of 10 unique wavelets, which contains 5 unique magnitude wavelets and 5 unique Euclidean distance wavelets.

7.3.2.2 Feature Extraction Process

This process extract features as per wavelet, with a fixed window-width of 60 seconds (2 epochs) and a sliding window-width of 30 seconds (1 epoch) for the entire length of the wavelet. There are two types of features extracted as per window, one being the time-domain statistical features and the other is the frequency-domain features.

Table 7.3.2.1 illustrates the 11 time-domain statistical features as per window, where "x" is the selected signal at the selected window. The statistical methods for obtaining the features include mean, variance, median-absolute-deviation (mad), standard deviation, natural logarithm of mean and geometric mean.

mean(x)	mean(x^2)	ln(mean(x))	ln(mean(x^2))
var(x)	var(x^2)	std(x)	std(x^2)
mad(x)	mad(x^2)	geomean(x^2)	

Table 7.3.2.1 – Time-Domain Statistical Features

Table 7.3.2.2 demonstrates the methods for obtaining the frequency-domain features as per window. The Fast Fourier transform (FFT) was performed on the selected window. The absolute magnitudes of the frequency components and the derivative of the absolute magnitudes were calculated. The sum of the absolute magnitudes and the sum of the derivative of the absolute magnitudes was obtained as features.

The power spectral density (PSD) was performed on the selected window. The PSD magnitudes and the derivative of the PSD magnitudes were calculated. The sum of the PSD magnitudes and the sum of the derivative of the PSD magnitudes was obtained as features.

sum(abs_mag)	sum(psd)
sum(diff_abs_mag)	sum(diff_psd)

Table 7.3.2.2 – Frequency-Domain Features

The features extraction process produced a total of 150 features, which is the product of 10 wavelets and the sum of 11 time-domain statistical features and 4 frequency-domain features. The total 150 features were then re-scaled to the range of -1.0 to 1.0.

7.3.2.3 Deep Artificial Neural Network Architecture

The deep artificial neural network architecture for body orientations prediction is presented in Fig. 7.3.2.2. The deep artificial neural network architecture is implemented using fully connected multilayer perceptron (MLP) with logistic sigmoid activation for the hidden layers and Softmax activation for the output layer. The deep artificial neural network contains 5 layers, of which 4 layers are hidden layers and 1 output layer. The

output layer contains 5 binary classes, “Prone”, “Upright”, “Supine”, “Right”, and “Left” body orientations.

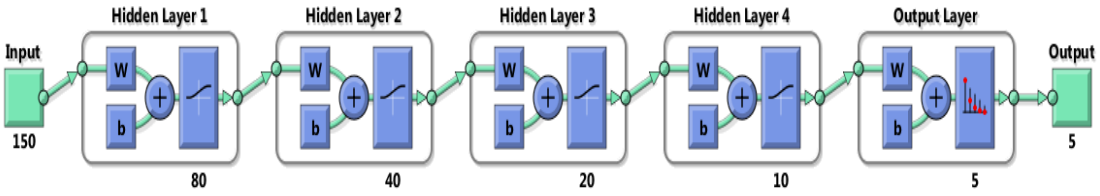

Figure 7.3.2.2 – Deep Artificial Neural Network Architecture For Body Orientations Prediction

A summary of the deep neural network architecture characteristics is shown in Table 7.3.2.4. The number of neurons per layer selected is equal to half of the total number of neurons in the previous layer. The goal is to reduce the non-linear high-dimensional features as propagated through each of the network layer. The total sum of neuron across all the hidden layers is 150.

	Hidden Layer 1	***Hidden Layer 2***	***Hidden Layer 3***	***Hidden Layer 4***	***Output Layer***
Number of Neuron	80	40	20	10	5
Activation Function	Logistic Sigmoid	Logistic Sigmoid	Logistic Sigmoid	Logistic Sigmoid	Softmax

Table 7.3.2.3 – Deep Artificial Neural Network Architecture Characteristics

7.3.2.4 Deep Artificial Neural Network Training Characteristics

Common training characteristics of the artificial neural network are summarized in Appendix III, Table A.III.1.

7.3.2.5 Results and Discussions

The deep artificial neural network is trained with a maximum validation fail criteria of 6 epochs, i.e., the training will stop after a maximum of 6 consecutive epochs of "Validation" errors compared to "Training" errors. Based on the maximum validation fail criteria, the network stopped at 32,941 epochs. The epoch, prior to the first validation fail criteria is recorded at 32,935 and this is referred to as the "best validation" epoch. The network's weights are obtained at the "best validation" epoch.

The training performance of the deep artificial neural network is presented in Fig. 7.3.2.3. As shown in Fig. 7.3.2.3, all errors with respect to "Training", "Validation" and "Test" decreases and approaches zero as the training progress. This indicates that the input features are predictable, the dataset size is adequate to prevent under-fitting, the network is well regularized to prevent over-fitting and the network has successfully learned the features characteristics. It is important to emphasize that the "Test" dataset is used for independent monitoring purpose only and does not participate in training performance criteria.

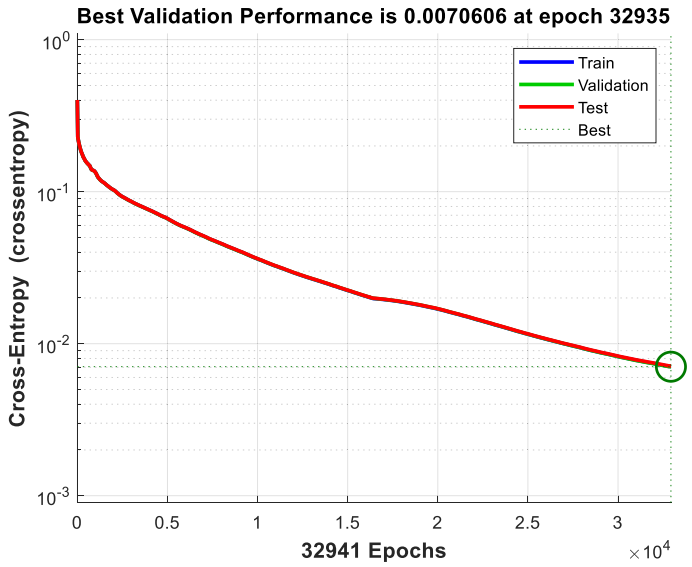

Figure 7.3.2.3 – Deep Artificial Neural Network Training Performance

The results of the body orientations prediction are presented in Fig. 7.3.2.4 as Confusion Matrix. As shown in Fig. 7.3.2.4, the "Training", "Validation" and "Test" accuracy achieved a coherence and highly correct classification rate of 99.2% for the 5 binary classes of body orientations. The misclassification also cohered to a negligible rate of 0.8%. Figure 7.3.2.4 class label "1" corresponds to "Prone", "2" corresponds to "Upright", "3" corresponds to "Supine", "4" corresponds to "Right" and "5" corresponds to "Left" body orientations.

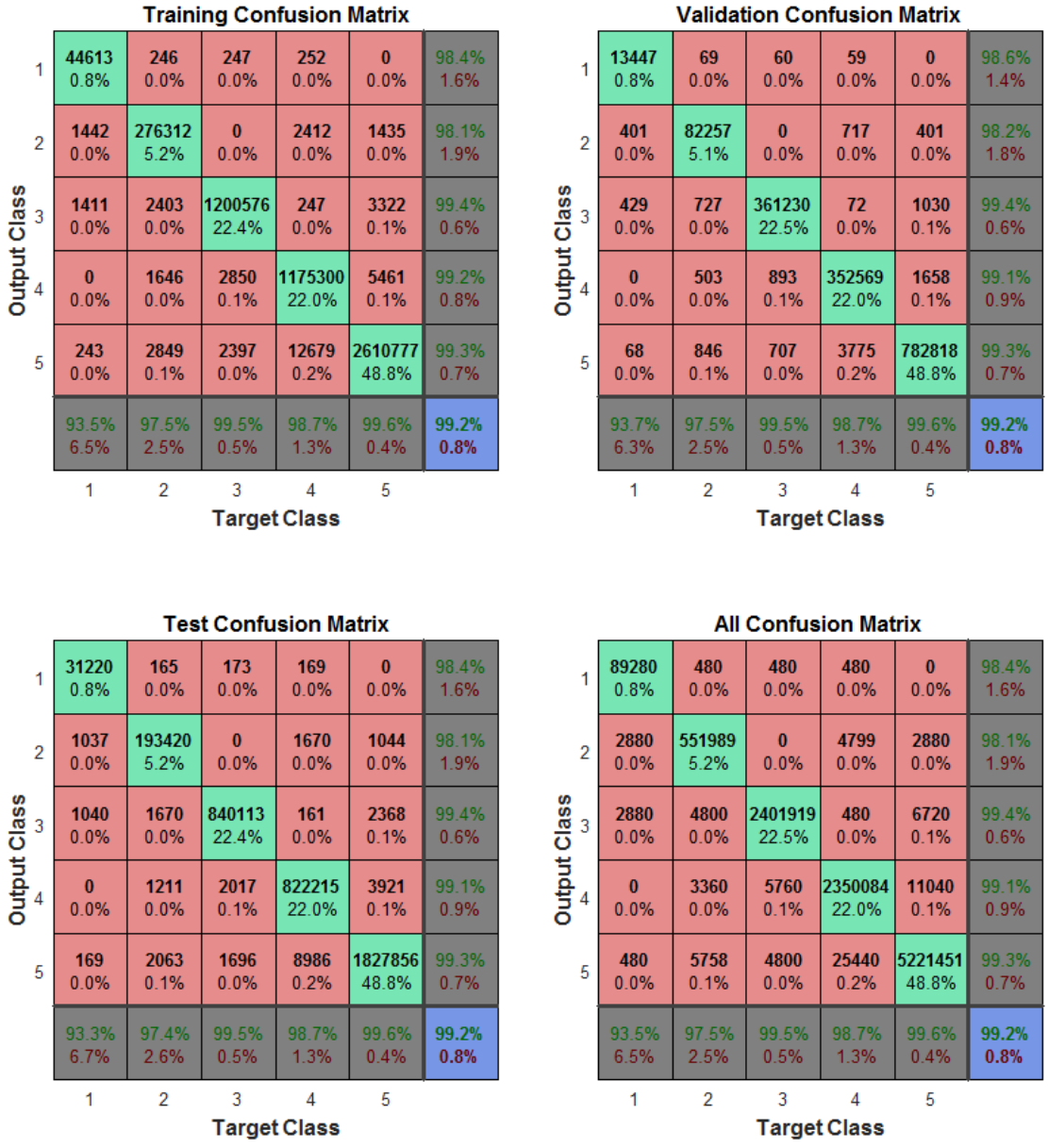

Figure 7.3.2.4 – Deep Artificial Neural Network Confusion Matrix

Figure 7.3.2.5 presents the body orientations prediction for the "Test" dataset. As shown in Fig. 7.3.2.5, the non-contact prediction of the nocturnal body orientations, using the deep artificial neural network accurately predicts the correct body orientations compared to the reference body orientations recorded by the PSG system. The accuracy achieved is 99.2% for a total sleep duration of 65 hours. This result proves the feasibility of nocturnal body orientations prediction using the deep artificial neural network and the non-contact microwave Doppler radar for CHF patients in the complex sleep environment.

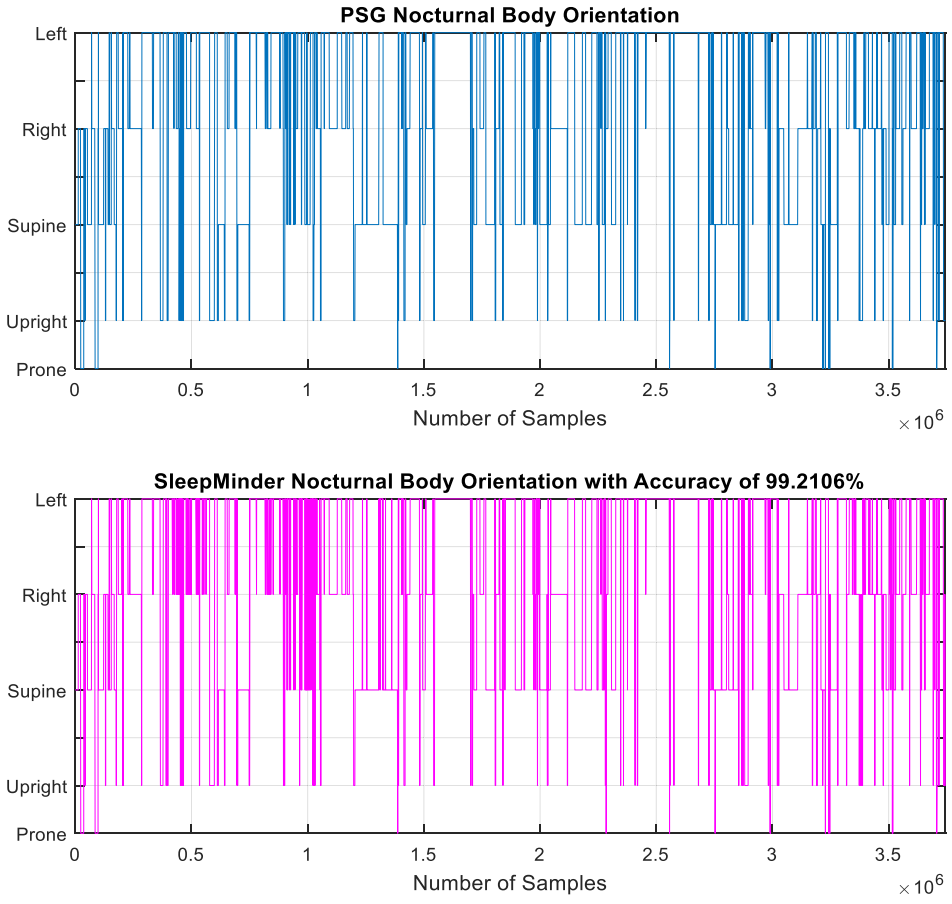

Figure 7.3.2.5 – Nocturnal Body Orientations Prediction For "Test" Dataset

Figure 7.3.2.6 presents the non-contact prediction of the nocturnal body orientations for a CHF patient. As shown in Fig. 7.3.2.6, the non-contact body orientations prediction is

exceptionally accurate compared to the reference body orientations recorded by the PSG system.

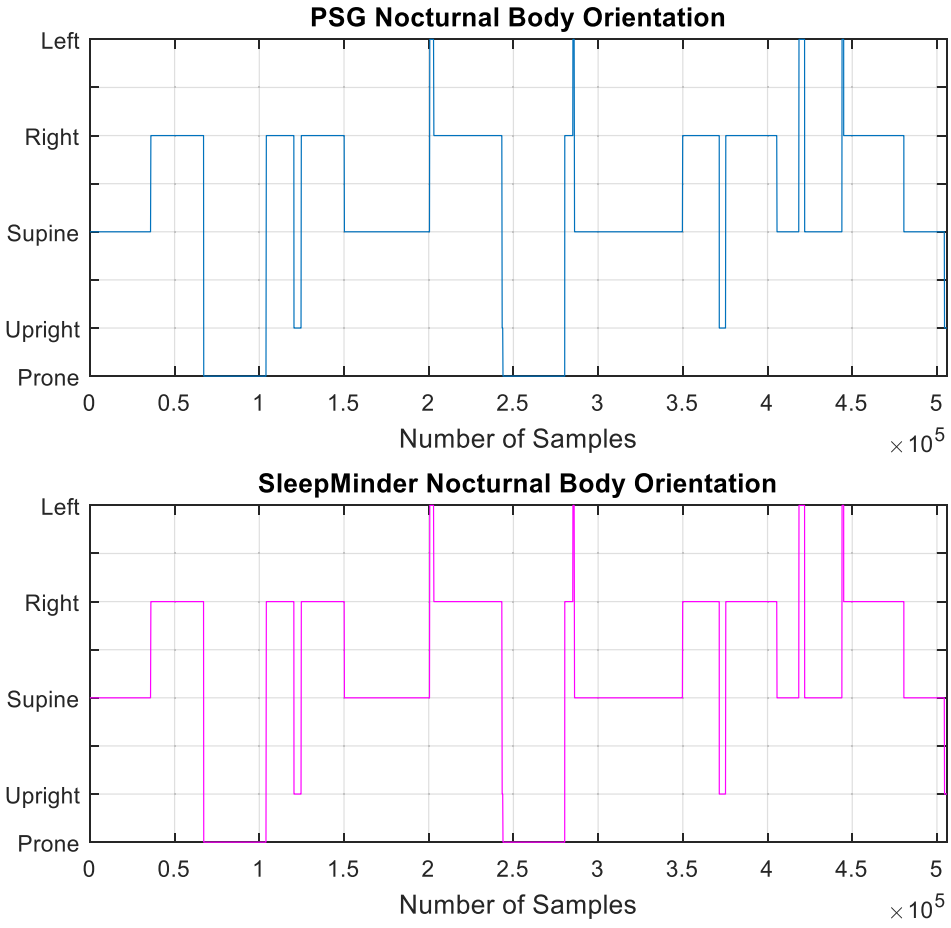

Figure 7.3.2.6 – Nocturnal Body Orientations Prediction for a CHF Patient

Figure 7.3.2.7 is a time-series illustration of the features for a CHF patient. A total of 150 features were plotted against the patients' entire sleep duration samples to assist in the visualization of the corresponding body orientations. However, the features do not correspond to any meaningful phenomenon. The features are therefore only applicable to the machine learning applications and are incomprehensible to human logic.

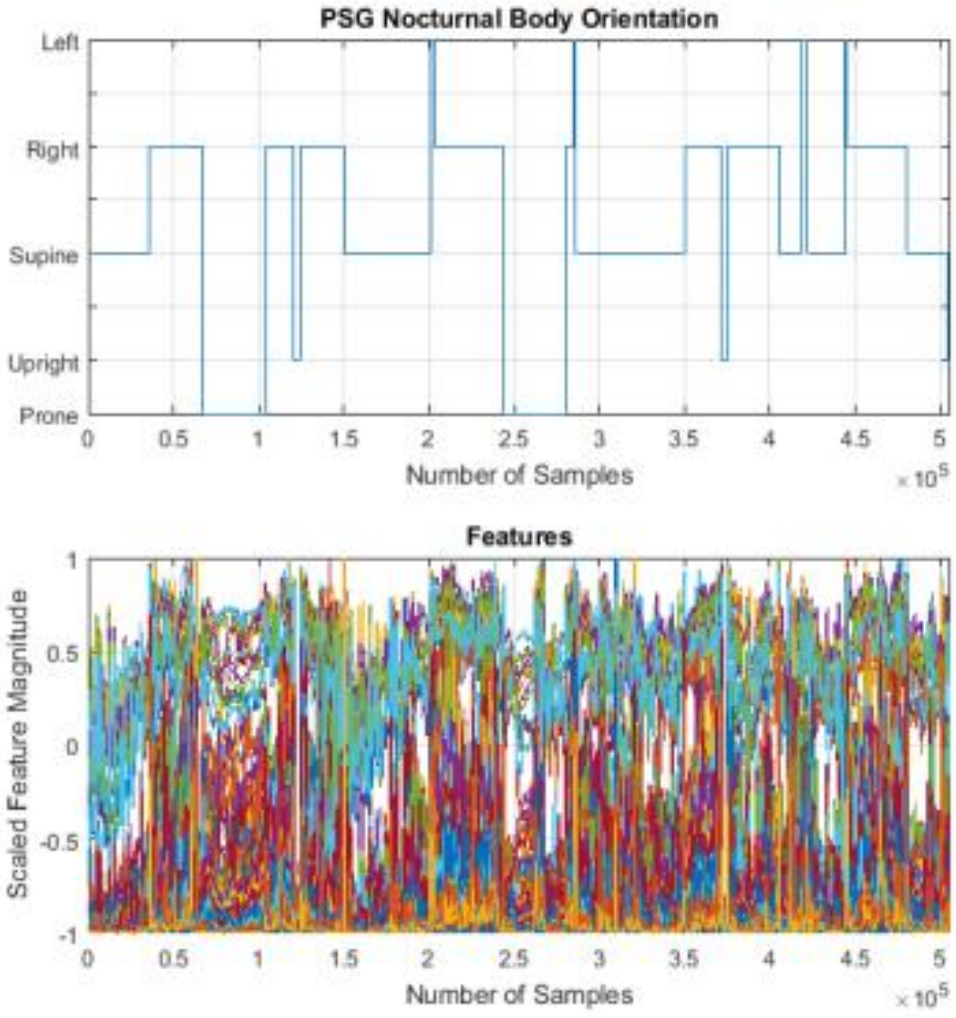

Figure 7.3.2.7 – Time-series Illustration Of The Features For A CHF Patient

7.3.2.6 Conclusion

Subsection 7.3.2 demonstrates the proven methodology of the non-contact microwave Doppler radar prediction of nocturnal body orientations using wavelet packet decomposition (WPD) and deep artificial neural network for CHF patients in the complex sleep environment. The achievement is a highly correct classification rate of 99.2% for the 5 classes of "Prone", "Upright", "Supine", "Right", and "Left" body orientations. The misclassification is at a negligible rate of 0.8%.

7.3.3 Body Orientations Prediction using SDT, SDD and Multilayer Perceptron

7.3.3.1 Feature Extraction using SDT and SDD

SDT and SDD, presented in Chapter 6, are employed as data transformation, augmentation, normalization, scaling and feature extraction for body orientations. I and Q raw channels are the inputs to the SDT and SDD.

For the body orientations classification application, the SDD decomposition level "D" is 3 and "φ" (phi) is 1. The fixed window-width "W_f" is 60 seconds (2 sleep epochs) and the sliding window-width "W_s" is 30 seconds (1 sleep epoch). This means that the classification MLP artificial neural network has a resolution of 30 seconds with an initial delay of 60 seconds. The total number of extracted features is 234, which uses the standard statistical features.

7.3.3.2 Multilayer Perceptron Artificial Neural Network Architecture

The multilayer perceptron (MLP) artificial neural network architecture is similar to the deep artificial neural network architecture presented in section 7.3.2.3, however, the MLP is modified with less neurons and hidden layers. The aim is to compare the MLP training performance and accuracy level when the SDT and SDD are employed.

The MLP artificial neural network architecture for body orientations is presented in Fig. 7.3.3.1. The network architecture is fully connected with the logistic sigmoid as activation function for the hidden layers and Softmax as activation function for the output layer.

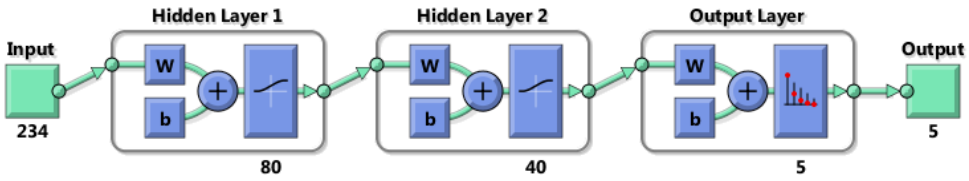

Figure 7.3.3.1 – Body Orientations MLP Artificial Neural Network Architecture

The MLP artificial neural network contains 3 layers, 2 are hidden layers and 1 output layer. The output layer contains 5 binary classes, “Prone”, “Upright”, “Supine”, “Right” and “Left”. A summary of the body orientations MLP artificial neural network hyperparameters are shown in Table 7.3.3.1.

	Hidden Layer 1	***Hidden Layer 2***	***Output Layer***
Number of Neuron	80	40	5
Activation Function	Logistic Sigmoid		Softmax

Table 7.3.3.1 – MLP Artificial Neural Network Architecture Characteristics

7.3.3.3 Multilayer Perceptron Artificial Neural Network Training Characteristics

Common training characteristics of the artificial neural network are summarized in Appendix III, Table A.III.1.

7.3.3.4 Results and Discussions

In accordance with the maximum validation fail criteria, the body orientations MLP artificial neural network stopped at 22,284 epochs. The epoch, prior to the first validation fail criteria is recorded at 22,278 and this is referred to as the “best validation” epoch. The network’s weights are obtained at the “best validation” epoch. The training performance is presented in Fig. 7.3.3.2.

The results of the body orientations prediction are presented in Fig. 7.3.3.3 as Confusion Matrix. As shown in Fig. 7.3.3.3, the “Training”, “Validation” and independent “Test” accuracy achieved an exceptionally high correct classification rate of 99.9% for 5 binary classes of body orientations. The misclassification is at a negligible rate of 0.1%. Figure 7.3.3.3 class label “1” corresponds to “Prone”, “2” corresponds to “Upright”, “3” corresponds to “Supine”, “4” corresponds to “Right” and “5” corresponds to “Left” body orientations.

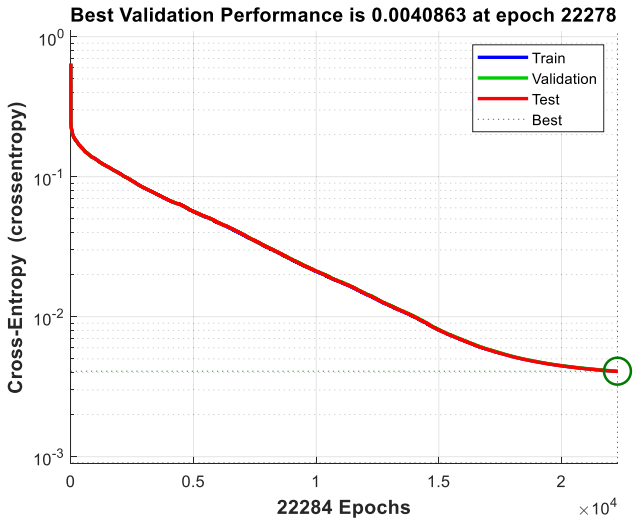

Figure 7.3.3.2 – Body Orientations MLP Artificial Neural Network Training Performance

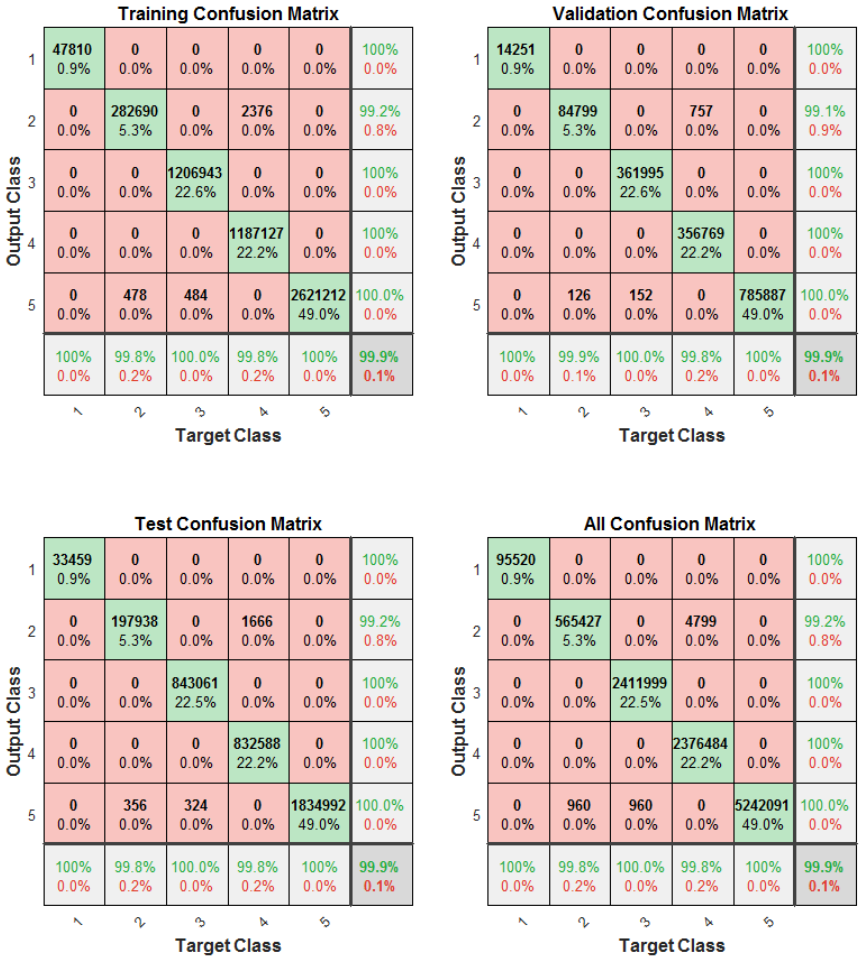

Figure 7.3.3.3 – Body Orientations MLP Artificial Neural Network Confusion Matrix

Figure 7.3.3.4 presents the body orientations prediction for the independent "Test" dataset with a total sleep duration of 65 hours. As shown in Fig. 7.3.3.4, the non-contact prediction of the nocturnal body orientations, using the SDT, SDD and MLP artificial neural network accurately predicts the correct body orientations compared to the reference body orientations recorded by the PSG system. The independent "Test" achieved an impressive 99.94% accuracy rate for a total sleep duration of 65 hours.

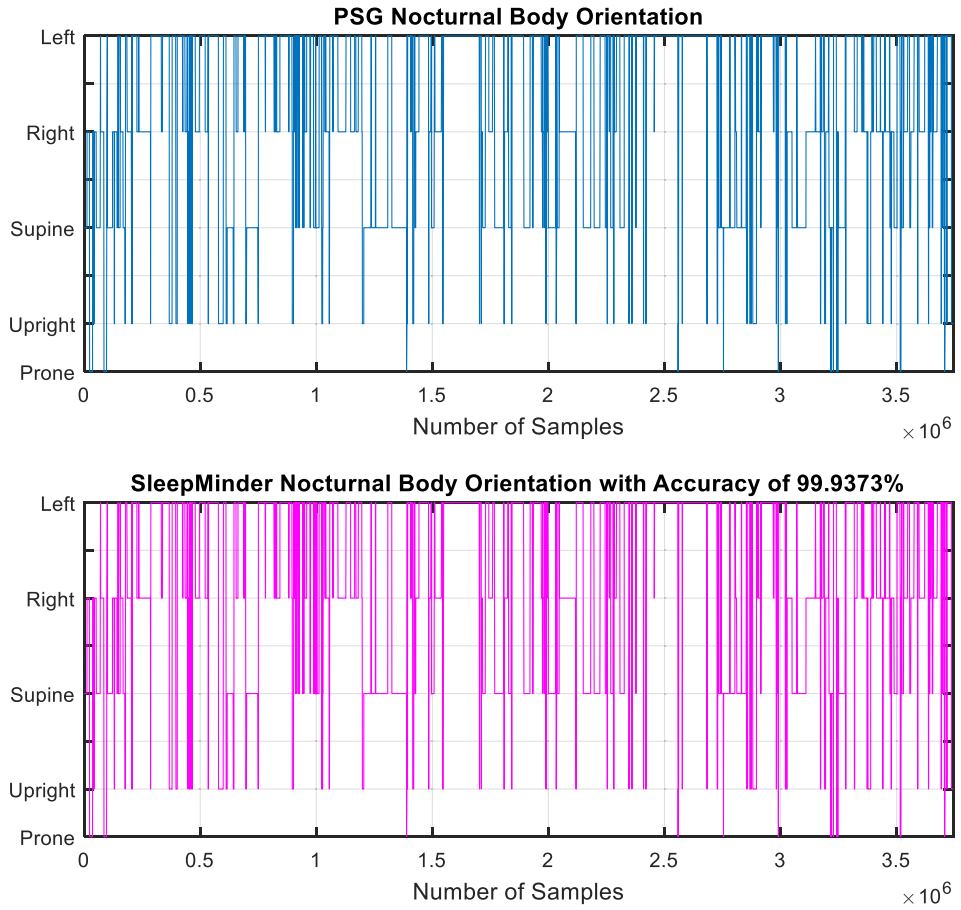

Figure 7.3.3.4 – Nocturnal Body Orientations Prediction For "Test" Dataset

Figure 7.3.3.5 presents the non-contact prediction of nocturnal body orientations for a CHF patient. As shown in Fig. 7.3.3.5, the non-contact body orientations prediction is exceptionally accurate compared to the reference body orientations recorded by the PSG system.

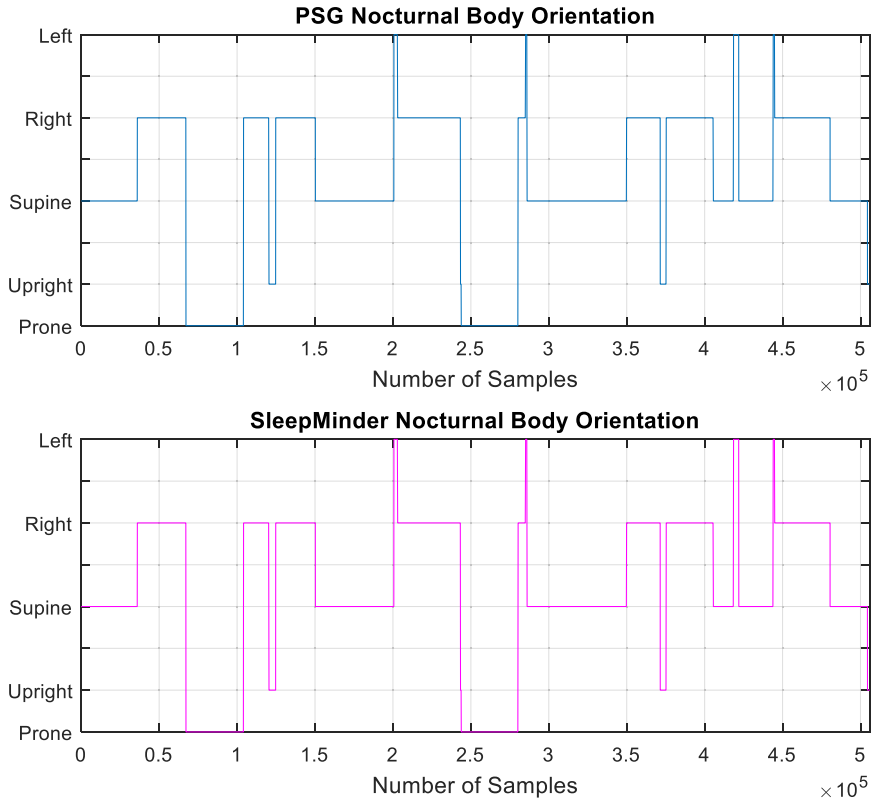

Figure 7.3.3.5 – Nocturnal Body Orientations Prediction For A CHF Patient

7.3.3.5 Conclusion

Subsection 7.3.3 demonstrates the proven methodology of the non-contact microwave Doppler radar prediction of nocturnal body orientations using SDT, SDD and MLP artificial neural network for CHF patients in the complex sleep environment. The achievement is at a high correct classification rate of 99.9% for 5 classes of "Prone", "Upright", "Supine", "Right", and "Left" body orientations. The misclassification is at a negligible rate of 0.1%.

7.3.4 Remarks

Section 7.3 demonstrates the proven methodology of the "non-stationary" and "non-direct facing" body orientations prediction using the non-contact microwave Doppler

radar in the complex sleep environment. The two approach presented has demonstrated good accuracy results.

A comparison of the artificial neural network architectures, the training performance and the accuracy level between the application of the SDT and SDD in section 7.3.3 and the application in section 7.3.2 is detailed in Table 7.3.3.2. As shown in Table 7.3.3.2, the application of the SDT and SDD with respect to data transformation, augmentation, normalization, scaling, and feature extraction, has resulted in the artificial neural network architecture, the training performance and the accuracy level being significantly improved and optimized. This result demonstrates the superiority of the SDT and SDD compared to section 7.3.2 on identical application of the non-contact nocturnal body orientations prediction.

It is also important to emphasize that the SDT and SDD, presented in Chapter 6, can deliver the capability of the automatic feature extraction without the associated cost of the feature engineering process.

	Section 7.3.2.5 Results	***Section 7.3.3.4 Results***	***Optimization (%) SDT and SDD as Reference***
Total Number of Hidden Neurons	120	150	20% decrease
Number of Hidden Layers	2	4	50% decrease
Total Training Epochs	22284	32941	32.36% faster
Best Validation Epoch	22278	32935	32.36% faster
Correct Classification (%)	99.9	99.2	0.7% more accurate
Misclassification (%)	0.1	0.8	0.7% reduction in misclassification.

Table 7.3.4.1 – Body Orientations Prediction Performance and Accuracy Comparison

In conclusion, the two novel approach presented can be utilized for the "non-stationary", "non-direct facing" and non-contact body orientations monitoring during

sleep. However, if self-extracting features is the priority, then SDT and SDD is the preferred approach.

7.4 Non-Contact Oxygen Saturation Prediction

The aim of section 7.4 is to firstly present two “non-stationary” and “non-direct facing” real-life applications and the results of the non-contact oxygen saturation prediction using the Doppler radar in the complex sleep environment.

The first application utilizes the oxygen-hemoglobin dissociation mathematical model, the alveolar partial pressure equations and the non-contact algorithms presented in Chapter 5, to predict the patient’s oxygen saturation during sleep.

The second application utilizes the Spatial Dimensions Transform (SDT) and the Spatial Dimensions Decomposition (SDD), presented in Chapter 6, as a 3-dimensional feature extraction mechanism and multilayer perceptron (MLP) artificial neural network to predict the patient’s oxygen saturation during sleep.

A comparison of the oxygen saturation estimation, the performance and the accuracy level between the two applications including the results is also presented.

The aim of section 7.4 is also to illustrate the application of the SDT and SDD when combined with the artificial neural network (ANN). This can be applied to solve real-life complex challenge such as “non-stationary”, “non-direct facing” and non-contact estimation of the oxygen saturation in the complex sleep environment.

7.4.1 Patients' Database for Oxygen Saturation Estimation

7.4.1.1 Adjusted Patients' Database and Patients' Data Partitions for External Ventilation Mathematical Model

A sample of twenty CHF patients, selected from the patients' database as documented in Appendix II, section A.II.V, Table V.2, were utilized for the "Training", "Validation" and "Test" of the oxygen saturation prediction. Refer to Appendix II, section A.II.V, Table V.2, for further details on the dataset.

7.4.1.2 Adjusted Patients' Database and Patients' Data Partitions for SDD and SDT

A sample of twenty-one CHF patients, selected from the patients' database as documented in Appendix II, section A.II.VII, were utilized for the "Training", "Validation" and "Test" of the oxygen saturation prediction. Refer to Appendix II, section A.II.VII, for further details on the dataset.

7.4.2 Oxygen Saturation Estimation using External Ventilation Mathematical Model

Section 7.4.2 presents the results of the application of the oxygen-hemoglobin dissociation mathematical model, the alveolar partial pressure equations, and the non-contact prediction of oxygen saturation algorithm presented in Chapter 5. A detailed discussion on the results is also provided.

7.4.2.1 Results and Discussions

The verifications of the mathematical model and the non-contact SpO_2 prediction algorithm were performed in 2 stages.

Stage one of the verification is the comparison based on Bohr's PO_2 reference values ranging from 0–150 mmHg and PCO_2 reference values of 5, 10, 20, 40 and 80 mmHg. The mathematical model estimated the SaO_2 values for all PO_2 and PCO_2 reference values. The estimated SaO_2 values were then combined with Bohr's measured SO_2 values into a single two-column dataset. Bland-Altman analysis is then performed to compute the correlation and limits of agreement between the mathematical model estimated SaO_2 values and Bohr's measured SO_2 values for all PO_2 and PCO_2 reference values.

The Bland-Altman plot is presented in Fig. 7.4.2.1. As shown in Fig. 7.4.2.1, the correlation coefficient "r" is 0.9987 with error sum of squares (SSE) of 1.8 (% of oxygen saturation). These results indicate a very strong positive correlation between Bohr's measured SO_2 values and the model's estimated SaO_2 values. The mean error between the Bohr's measured SO_2 values and the model's estimated SaO_2 values is 0.015 (% of oxygen saturation), which is an insignificant mean error. The bias for 95% limits of agreement (LoA) is 3.7 (% of oxygen saturation) for SO_2 values ranging from 50% – 100% and negative 3.7 (% of oxygen saturation) for SO_2 values ranging from 0% – 50%. The third quartile (75^{th} percentile) of the bias is 1.1 (% of oxygen saturation), which is an insignificant margin error. Therefore, the oxygen-hemoglobin dissociation mathematical model is comparable to Bohr's oxygen-hemoglobin dissociation curve.

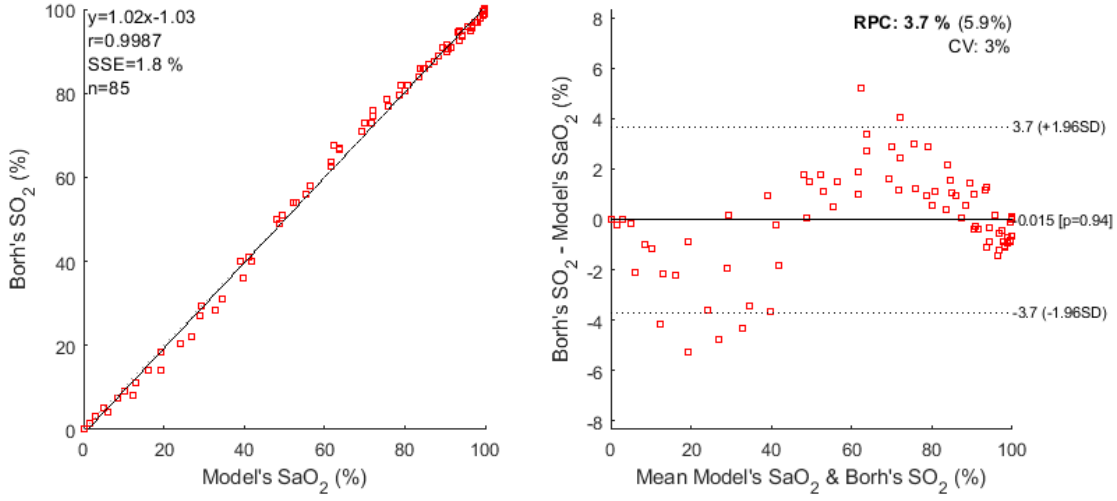

Figure 7.4.2.1 – Bland-Altman Plot of Bohr's Measured SO_2 and Model's SaO_2

A plot of both Bohr's laboratory recorded values and the model's estimated values for the oxygen-hemoglobin dissociation curve (ODC) are also presented in Fig. 7.4.2.2. As shown in Fig. 7.4.2.2, the model's curves successfully mapped to Bohr's laboratory recorded values. These results prove the accuracy of the mathematical model in representing Bohr's oxygen-hemoglobin dissociation curve as shown in chapter 5, section 5.1.1, Fig. 5.1.1.1.

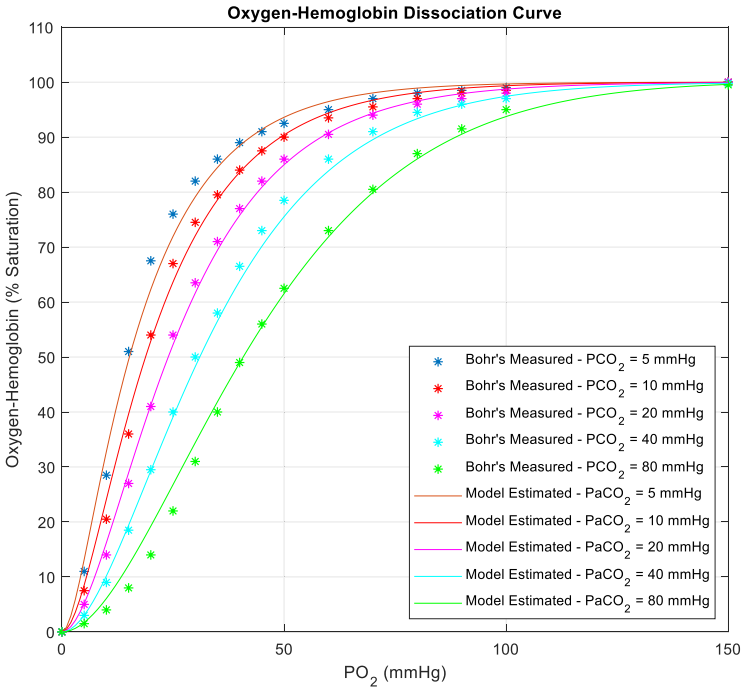

Figure 7.4.2.2 – Bohr and Model Oxygen-Hemoglobin Dissociation Curve

Stage two of the verification is the comparison between the SpO_2 prediction algorithm and the PSG recordings. The PSG SpO_2 measured from a pulse oximeter sample at 4Hz was selected as the reference (target output) signal. This is the reason for the non-contact oxygen saturation prediction algorithm to use the terminology of SpO_2 instead of SaO_2. Since the sample rate of the PSG SpO_2 differs from the SM sample rate, the PSG SpO_2 was first up-sampled to the SM sample rate. A "Median Filter" with a fixed window-width of 60 seconds (2 epochs) and a sliding window-width of 30 seconds (1 epoch) is then applied to smooth the PSG SpO_2.

The MLP artificial neural network for SpO_2 is trained with a maximum validation fail criteria of 6 epochs. The training will stop after the maximum validation fail criteria have been reached. The validation fail criterion is defined as "Validation" error

increases while the “Training” error decreases.

In accordance to the maximum validation fail criteria, the SpO_2 MLP artificial neural network stopped at 29897 epochs. The epoch prior to the first validation fail criteria is recorded at 29891. The network’s weights are obtained at the “best validation” epoch. The training performance is presented in Fig. 7.4.3.2.

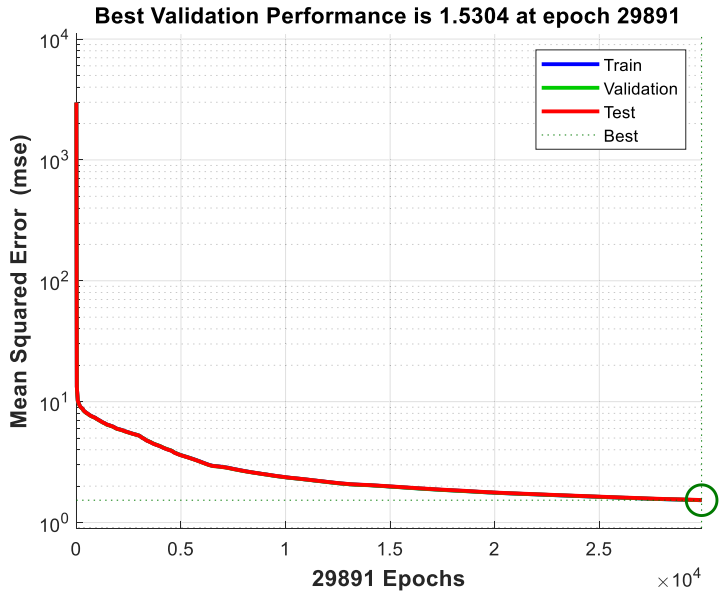

Figure 7.4.2.3 – SpO_2 MLP Artificial Neural Network Training Performance

The SpO_2 regression correlation “r” and mean squared error (MSE) is detailed in Table 7.4.2.3.

	Training	***Validation***	***Test***
Regression correlation “r”	0.93133	0.93098	0.93099
Mean squared error (MSE) ***(% oxygen saturation)***	1.5298	1.5310	1.5362

Table 7.4.2.1 – SpO_2 MLP Artificial Neural Network Mean Squared Error (MSE)

The SpO_2 “Training”, “Validation”, “Test” and “All” regression performance is presented in Fig. 7.4.2.4.

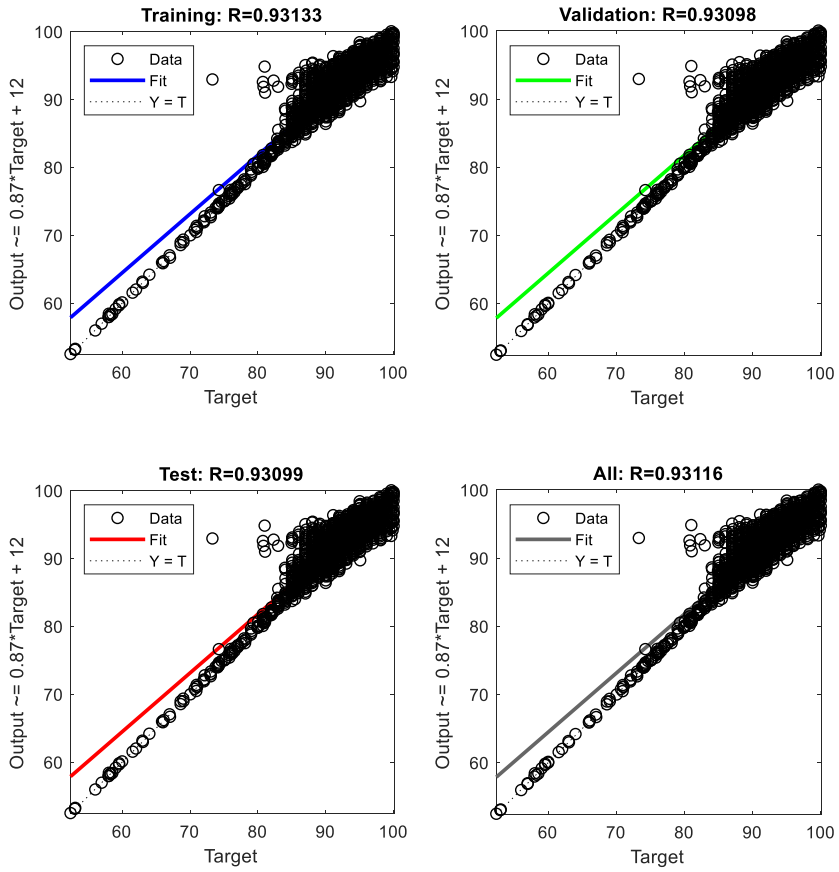

Figure 7.4.2.4 – SpO_2 MLP Artificial Neural Network Regression Performance

Figure 7.4.2.4 presents the SpO_2 predictions for the independent "*Test*" dataset with a total sleep duration of 54 hours, 15 minutes and 31.5 seconds. As shown in Fig. 7.4.2.4, the non-contact predictions of SpO_2 is able to track along the changes with reference to the PSG SpO_2. The mean accuracy percentage achieved is 99.06% compared to the reference PSG SpO_2 values.

The third plot in Fig. 7.4.2.4 is the zoomed window of 20 minutes and 49.8 seconds. This is to highlight the fluctuations between 55–100% of the SpO_2 during the night due to multiple apneic episodes and Cheyne-Stokes respirations (CSR). The fourth plot in Fig. 7.4.2.4 is the zoomed window of 20 minutes and 49.8 seconds to highlight a stable SpO_2 between 90–100% during the night. For the fluctuations as well as the stable scenarios, the SpO_2 prediction is able to track the changes accordingly. The tracking does result in some errors, however the overall performance still achieved a good accuracy level of 99.06%.

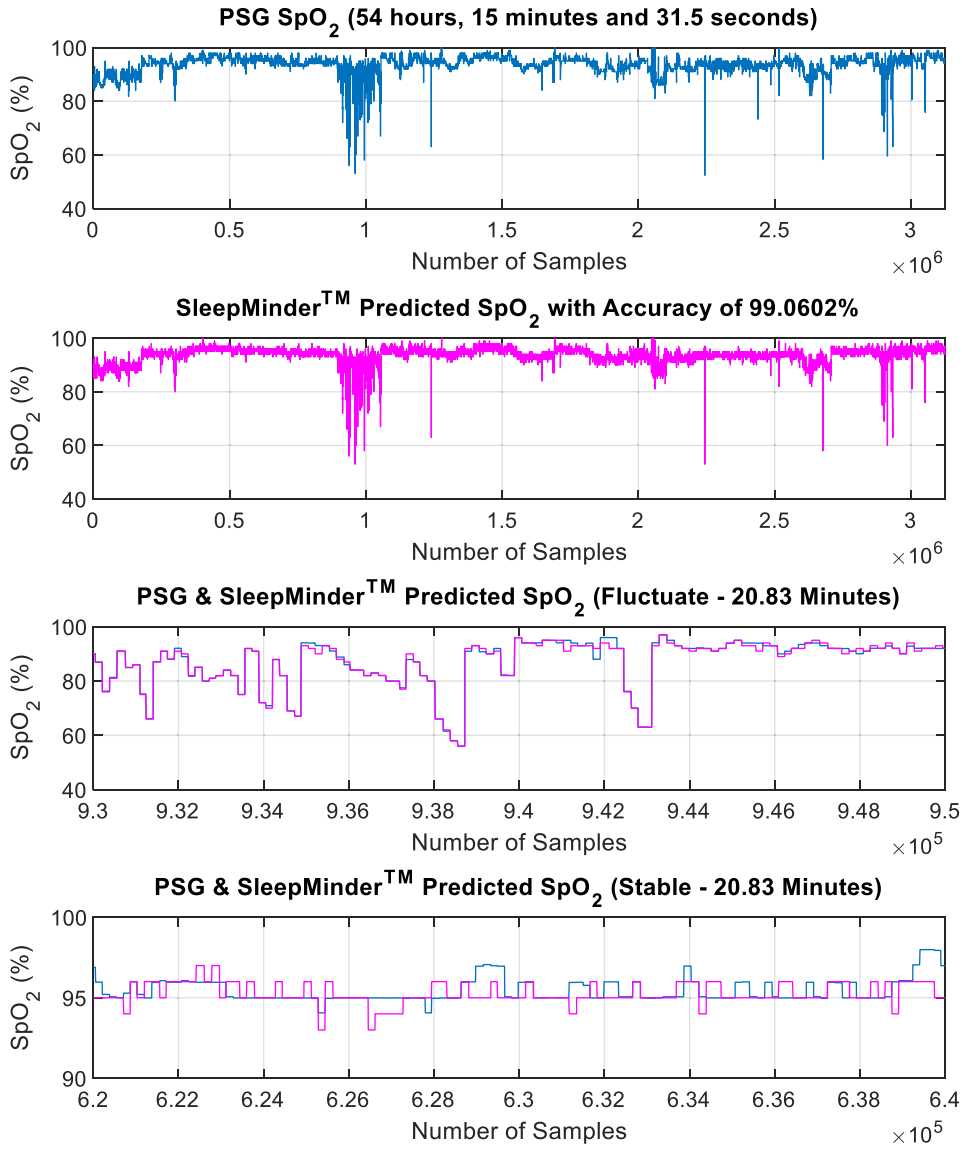

Figure 7.4.2.5 – Nocturnal SpO2 Prediction for "Test" Dataset

The Bland-Altman (B&A) plots are presented in Fig. 7.4.2.6 to Fig. 7.4.2.9 to analyze the 95% limits of agreement (LoA) between the SM predicted SpO_2 and the reference PSG SpO_2 measurements. The B&A plots and analyses demonstrated that the maximum differences between the SM predicted SpO_2 and the reference PSG SpO_2 measurements is 4 (% of oxygen saturation). The 95% limits of agreement, which is the same as the reproducibility coefficient (RPC) for "Training", "Validation" and "Test" is ±2.5 and overall is ±2.5 (% of oxygen saturation). An RPC of 2.5 (% of oxygen saturation) is still

an acceptable bias range as the fluctuations of oxygen saturation at this value does not consider to be clinical significant. The overall sum of squared errors (SSE) is 1.3 (% of oxygen saturation) and the coefficient of variation (CV), which is the standard deviations of the mean differences is 1.4 (% of oxygen saturation). The average mean error across "Training", "Validation" and "Test" is 0.0018 (% of oxygen saturation), which is an insignificant mean error. Therefore, it can be considered that the non-contact prediction of SpO_2 results are comparable to the pulse oximeter measurements.

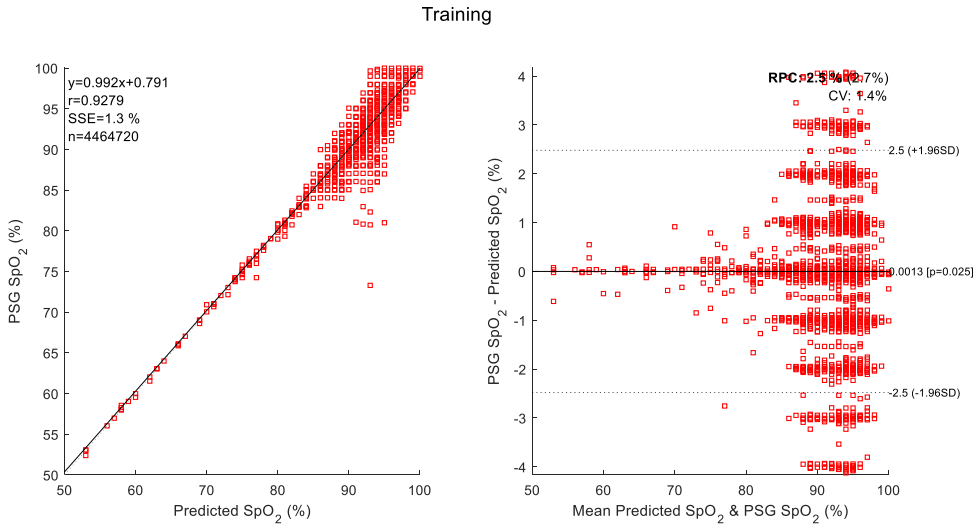

Figure 7.4.2.6 – Bland-Altman (B&A) Plot for "Training"

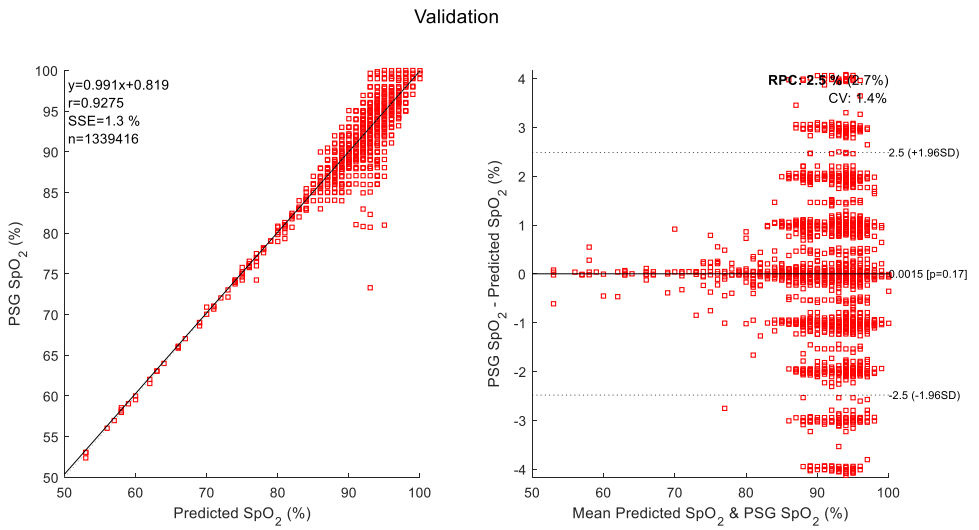

Figure 7.4.2.7 – Bland-Altman (B&A) Plot for "Validation"

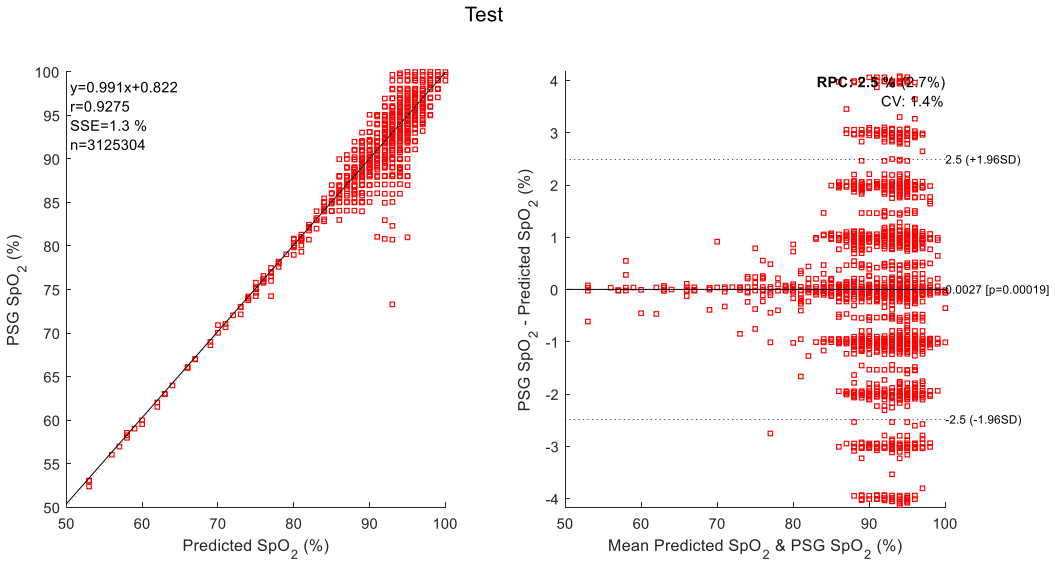

Figure 7.4.2.8– Bland-Altman (B&A) Plot for "Test"

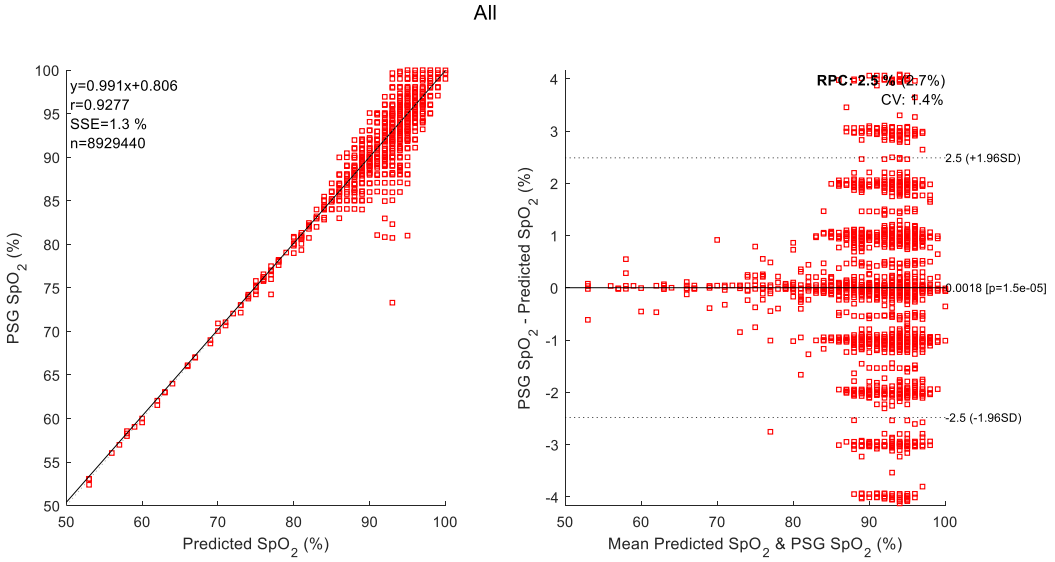

Figure 7.4.2.9 – Bland-Altman (B&A) Plot for "All"

The B&A plots highlighted that there are higher variations of differences in predicted SpO_2 between 85–100% and lower variations between 50–85%. This is due to the patients' conditions, such as multiple apneic episodes and CSR, which caused the desaturations to occur and resulted in fluctuations of SpO_2 measurements. Even though the non-contact predictions of the SpO_2 is still able to track along the fluctuations, the variations of the differences may need further improvements in the future.

Figure 7.4.2.10 and Fig. 7.4.2.11 presents the non-contact SpO_2 predictions with the estimated $PaCO_2$, PCO_2, V_A, CO and VCO_2 for a random OSA and CHF patient, within the "*Test*" dataset with sleep duration of 8 hours 47 minutes and 20.06 seconds. As shown in Fig. 7.4.2.10 and Fig. 7.4.2.11, the non-contact SpO_2 predictions achieved good accuracy level of 98.94% compared to the reference SpO_2 recorded by the PSG system.

Overall, the results demonstrate the proven methodology of the non-contact SpO_2 predictions, using the microwave Doppler radar in the complex sleep environment. The benefit of utilizing the mathematical model is the capability to apply non-contact monitoring of multiple parameters, such as, SpO_2, $PaCO_2$, PCO_2, V_A, CO and VCO_2.

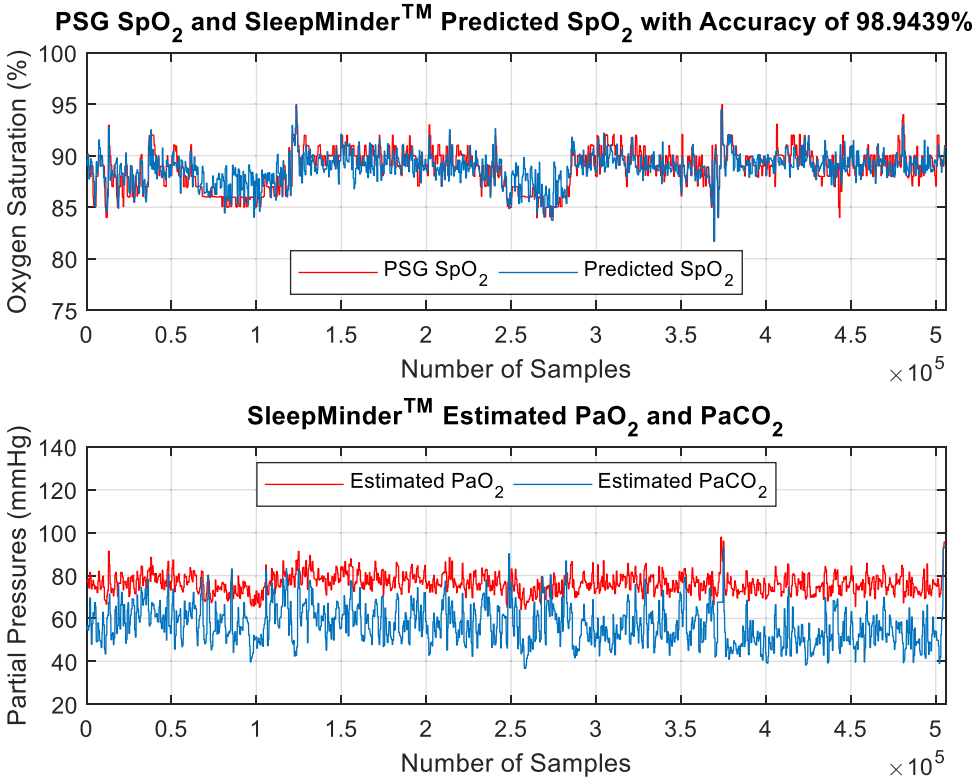

Figure 7.4.2.10 – SleepMinder™ Estimated SaO_2, PaO_2 and $PaCO_2$

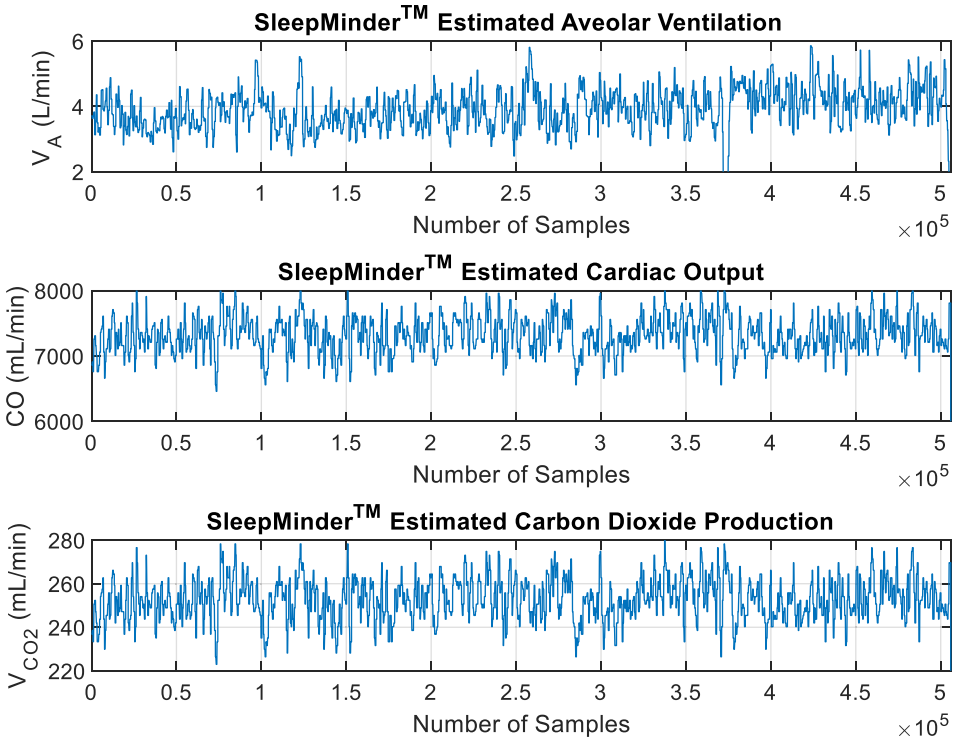

Figure 7.4.2.11 – SleepMinder™ Estimated V_A, CO and VCO_2

7.4.2.2 Conclusion

Subsection 7.4.2 demonstrates the proven methodology of using the oxygen-hemoglobin dissociation mathematical model, the alveolar partial pressure equations, the non-contact prediction of the oxygen saturation algorithm presented in Chapter 5, and the non-contact microwave Doppler radar to predict oxygen saturation in the complex sleep environment with a good accuracy level.

For the SpO_2 independent "Test" dataset with a total sleep duration of 54 hours, 15 minutes and 31.5 seconds, the SpO_2 correlation coefficient achieved is 0.93. The mean squared error (MSE) is 1.54 (% oxygen saturation) and the 95% limits of agreement is ±2.5 (% oxygen saturation). A potential application is a non-contact system that can continuously monitor the oxygen saturation level during sleep and can be used at home.

However, due to the non-contact predictions of the SpO_2 overall 95% limits of agreement of ±2.5 (% of oxygen saturation), it may not be applicable as a replacement

for the PSG pulse oximeter. This is due to the SpO_2 desaturation criteria of 2–5% in sleep diagnosis as specified by the American Academy of Sleep Medicine (AASM) [11]. Nevertheless, a potential application could be the non-contact early screening of oxygen saturation level during sleep, which can be used at home.

It is also important to emphasize that the mathematical model is theoretically generic and is not restricted to the non-contact applications. Even though the model and the non-contact algorithm was used to verify against the OSA and CHF patients' data, its applications is not constrained. The model and the non-contact algorithm can be applied against the general healthy populations or patients that have other health conditions.

7.4.3 Oxygen Saturation Estimation using SDT, SDD and Multilayer Perceptron

7.4.3.1 Feature Extraction using SDT and SDD

SDT and SDD, presented in Chapter 6, are employed as data transformation, augmentation, normalization, scaling and feature extraction for the SpO_2 prediction. I and Q raw channels are the inputs to the SDT and SDD.

For the SpO_2 regression application, the SDD decomposition level "D" is 3 and "φ" (phi) is 4. The SDD flattened multi-coordinates columns are extracted and followed by iSDT to obtain 78 augmented inputs signals. The augmented inputs are then transposed using SDT. The standard statistical features are then applied with a fixed window-width "W_f" of 30 seconds (1 sleep epoch) and the sliding window-width "W_s" of 2 seconds. This means that the regression MLP artificial neural network has a resolution of 2 seconds with an initial delay of 30 seconds. The total number of extracted features is 234.

All features are automatically normalized and scaled to 0 and 1 by the directional cosine constraint of U^2 matrix.

It is important to emphasize that the pre-processing of I and Q raw channels are not required. That is, neither the DC-offsets removal, signals filtering, expert domain knowledge, wavelet decomposition and/or time-frequency domain analysis are applicable in the process of extracting the features.

7.4.3.2 Multilayer Perceptron Artificial Neural Network Architecture

The MLP artificial neural network architecture for SpO_2 is presented in Fig. 7.4.3.1. The network architecture is fully connected with radial basis (exponential) as activation function for the hidden layers and identity (linear) as activation function for the output layer.

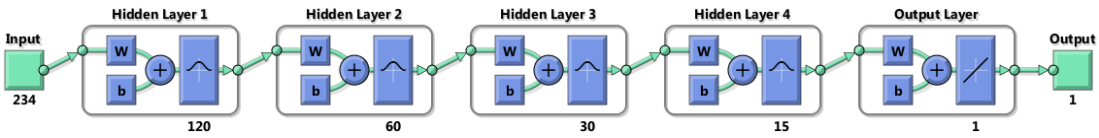

Figure 7.4.3.1 – SpO_2 MLP Artificial Neural Network Architecture

The MLP artificial neural network contains 5 layers, of which 4 layers are hidden layers and 1 output layer. The output layer contains regression values for SpO_2. A summary of the SpO_2 MLP artificial neural network hyperparameters is shown in Table 7.4.3.1.

	Hidden Layer 1	***Hidden Layer 2***	***Hidden Layer 3***	***Hidden Layer 4***	***Output Layer***
Number of Neuron	120	60	30	15	1
Activation Function	Radial Basis (e^{-n^2})				Identity

Table 7.4.3.1 – SpO_2 MLP Artificial Neural Network Architecture Characteristics

7.4.3.3 Multilayer Perceptron Artificial Neural Network Training Characteristics

The common training characteristics of the artificial neural network are summarized in Appendix III, Table A.III.1.

7.4.3.4 Results and Discussions

The MLP artificial neural network for SpO_2 is trained with a maximum validation fail criteria of 10 epochs. The training will stop after the maximum validation fail criteria have been reached. The validation fail criterion is defined as "Validation" error increases while "Training" error decreases.

In accordance to the maximum validation fail criteria, the SpO_2 MLP artificial neural network stopped at 19230 epochs. The epoch just prior to the first validation fail criteria is recorded at 19220. The network's weights are obtained at the "best validation" epoch. The training performance is presented in Fig. 7.4.3.2.

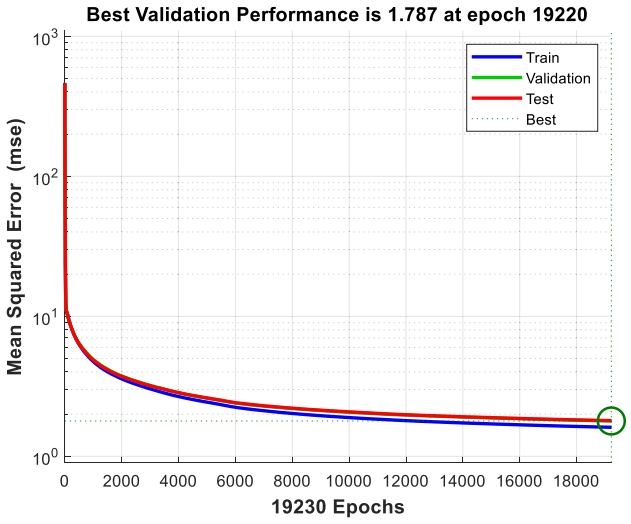

Figure 7.4.3.2 – SpO_2 MLP Artificial Neural Network Training Performance

The SpO_2 regression correlation "r" and mean squared error (MSE) is detailed in Table 7.4.3.2.

	Training	*Validation*	*Test*
Regression correlation "r"	0.9286	0.9198	0.9195
Mean squared error (MSE)	1.6103	1.7870	1.7971

Table 7.4.3.2 – SpO_2 MLP Artificial Neural Network Mean Squared Error (MSE)

The SpO_2 "Training", "Validation", "Test" and "All" regression performance is presented in Fig. 7.4.3.3.

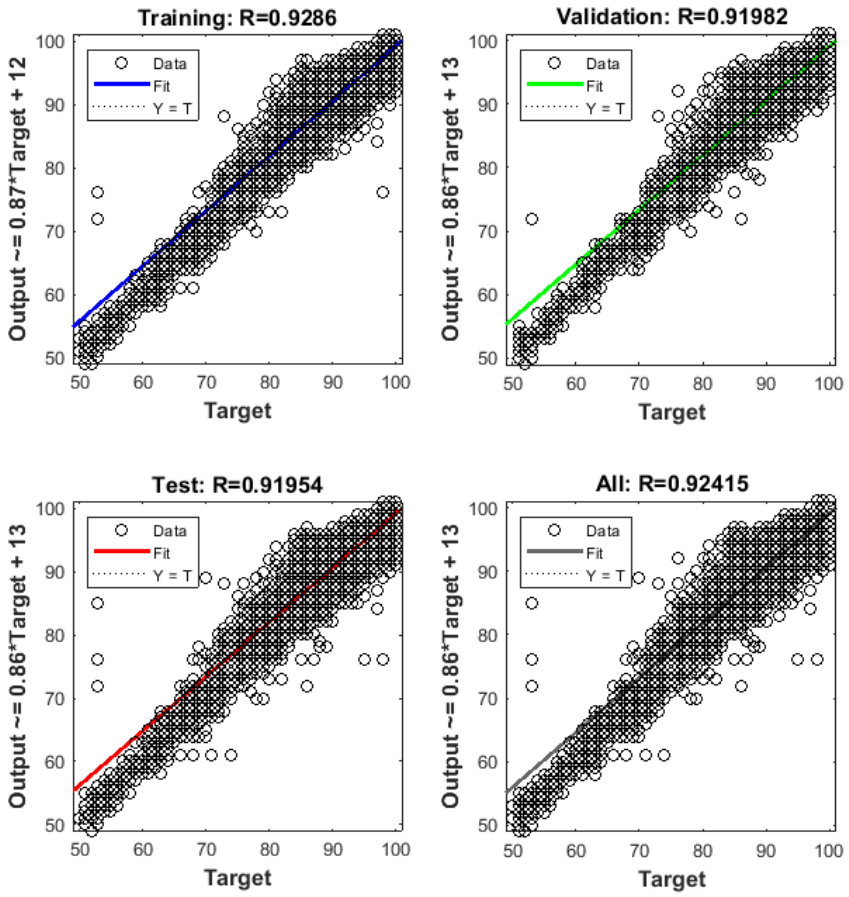

Figure 7.4.3.3 – SpO_2 MLP Artificial Neural Network Regression Performance

Figure 7.4.3.4 presents the SpO_2 prediction for the independent "Test" dataset with a total sleep duration of 56 hours 57 minutes and 46.5 seconds. As shown in Fig. 7.4.3.4, the non-contact prediction of the SpO_2 using SDT, SDD and MLP artificial neural

network is able to track along the changes with reference to the PSG SpO_2. The mean accuracy percentage achieved is 98.95% compared to the reference PSG SpO_2 values.

The third plot in Fig. 7.4.3.4 is the zoomed window of 10 minutes. This is to highlight the fluctuations between 75–100% of the SpO_2 during the night due to multiple apneic episodes and Cheyne-Stokes respirations (CSR). The fourth plot in Fig. 7.4.3.4 is the zoomed window of 10 minutes to highlight a more stable SpO_2 between 87–97% during the night.

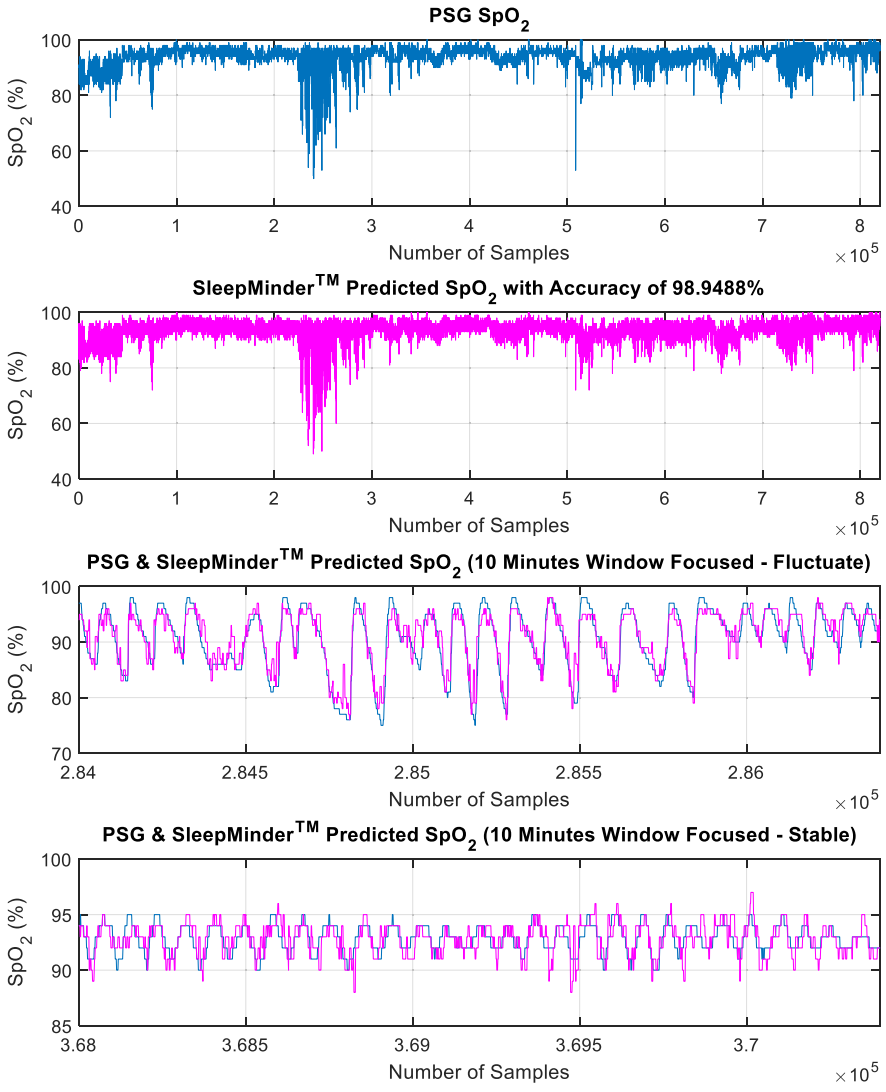

Figure 7.4.3.4 – Nocturnal SpO2 Prediction for "Test" Dataset

Under the high fluctuations as well as more stable scenarios, the SpO_2 and the non-contact SpO_2 predictions are able to track the changes accordingly. The tracking of the rapid changes does result in some errors as can be seen in Fig. 7.4.3.4. However, the overall performance still achieved a good accuracy level of 98.94%.

The Bland-Altman (B&A) plots are presented in Fig. 7.4.3.5 to Fig. 7.4.3.8 to analyze the 95% limits of agreement between the SM predicted SpO_2 and the reference PSG SpO_2 measurements. The B&A plots and analyses demonstrated that the maximum differences between the SM predicted SpO_2 and the reference PSG SpO_2 measurements is 5 (% of oxygen saturation). The 95% limits of agreement, which is the same as the reproducibility coefficient (RPC) for "Training" is ±2.6, "Validation" & "Test" is ±2.7 and overall is ±2.6 (% of oxygen saturation). An RPC of 2.6 (% of oxygen saturation) is still an acceptable bias range as the fluctuations of oxygen saturation at this value does not consider to be clinical significant. The overall sum of squared errors (SSE) is 1.3 (% of oxygen saturation) and the coefficient of variation (CV), which is the standard deviations of the mean differences is 1.4 (% of oxygen saturation). The average mean error across "Training", "Validation" and "Test" is 0.0008 (% of oxygen saturation), which is an insignificant mean error. Therefore, it can be considered that the non-contact prediction of SpO_2 results are comparable to the pulse oximeter measurements.

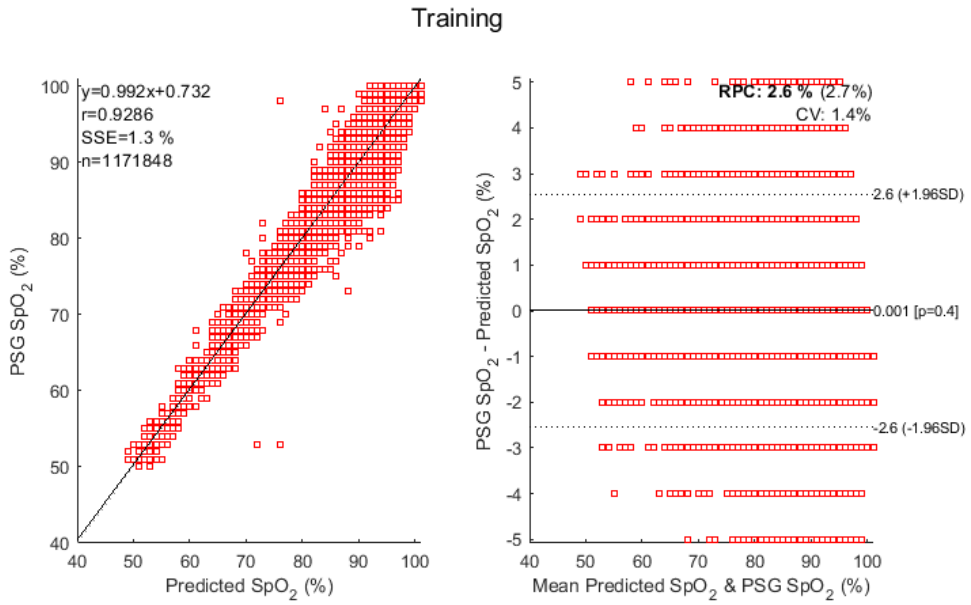

Figure 7.4.3.5 – Bland-Altman (B&A) Plot for "Training"

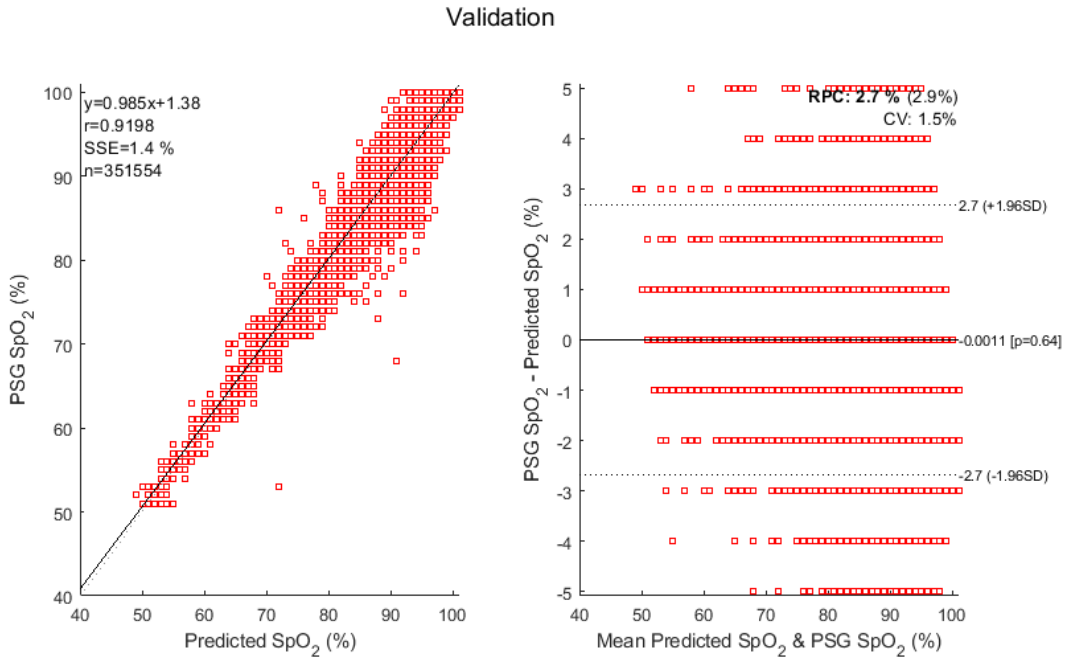

Figure 7.4.3.6 – Bland-Altman (B&A) Plot for "Validation"

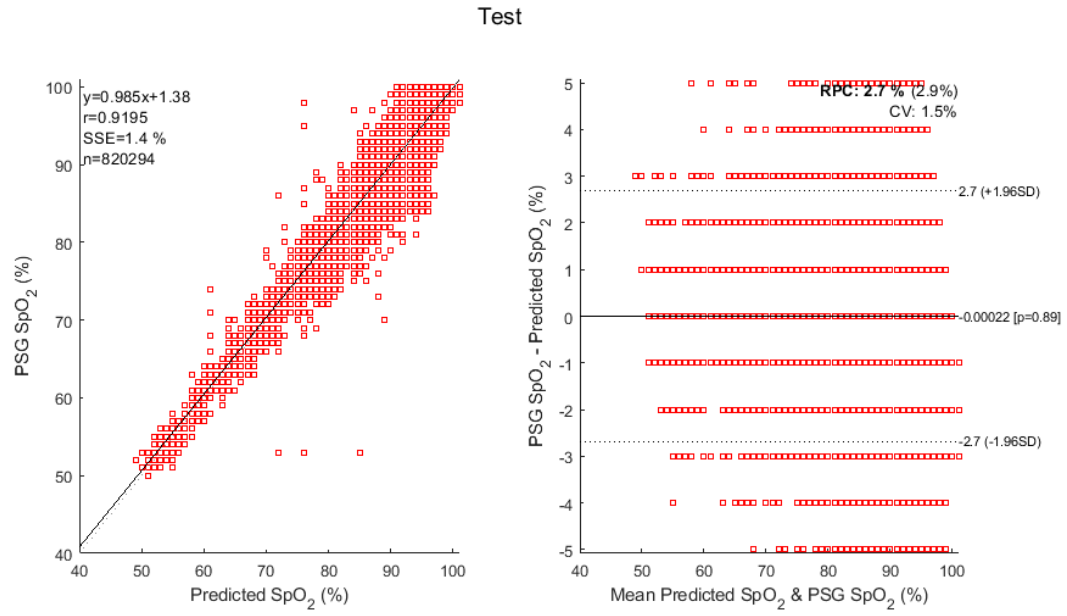

Figure 7.4.3.7– Bland-Altman (B&A) Plot for "Test"

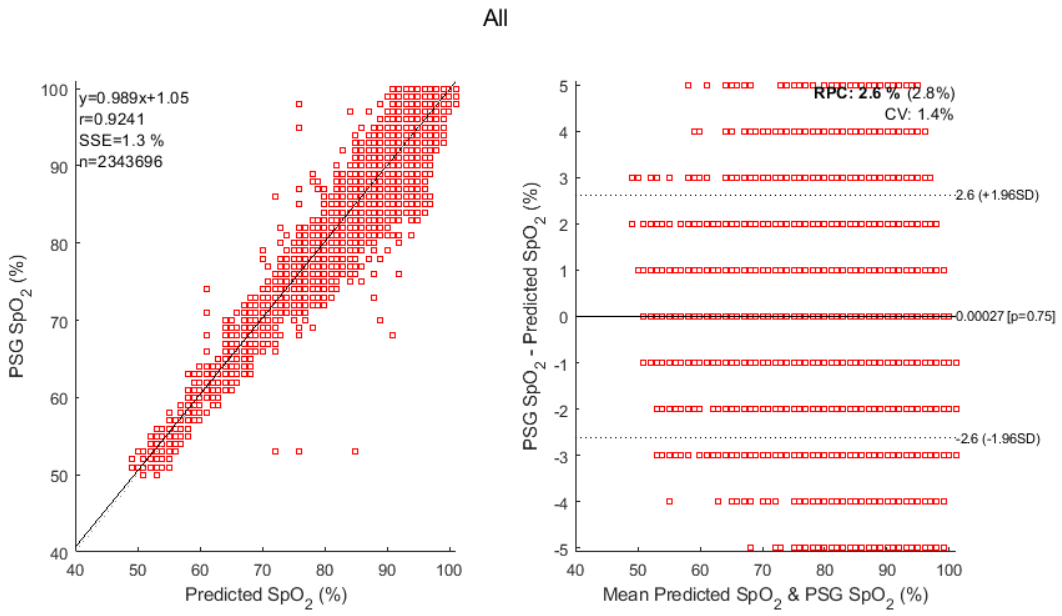

Figure 7.4.3.8 – Bland-Altman (B&A) Plot for "All"

The B&A plots also highlighted that there are higher variations of differences in SpO_2 between 70–100% and lower variations between 50–70%. This is due to the patients' conditions, such as multiple apneic episodes and CSR, which caused the desaturations to occur and resulted in fluctuations of SpO_2 measurements. This means that even though the non-contact prediction of the SpO_2 is still able to track along the fluctuations, the variations of the differences may need further improvements in the future.

Figure 7.4.3.9 presents the non-contact prediction of the nocturnal SpO_2 for a CHF patient with a sleep duration of 7 hours 38 minutes and 20 seconds. As shown in Fig. 7.4.3.9, the non-contact SpO_2 prediction achieved a good accuracy level when compared to the reference SpO_2 recorded by the PSG system.

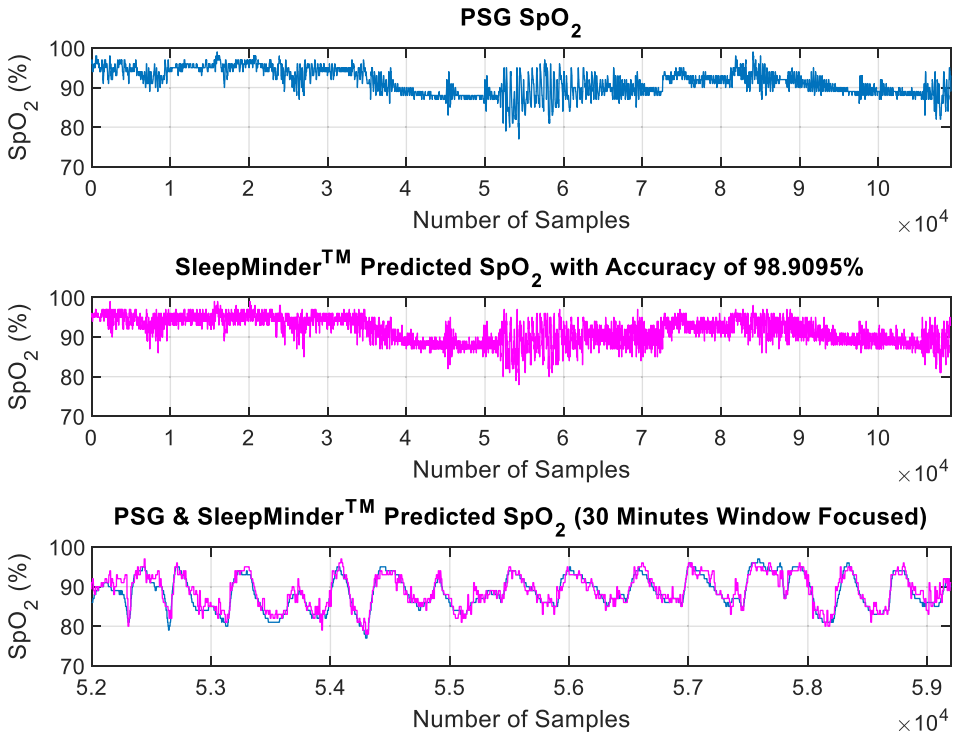

Figure 7.4.3.9 – Nocturnal SpO_2 Prediction for a CHF Patient

Overall, the results demonstrate the proven methodology of the SpO_2 predictions using the non-contact microwave Doppler radar in the complex sleep environment. It is also important to emphasize that the SDT and SDD can deliver the capability of the automatic feature extraction without the associated cost of the feature engineering process.

7.4.3.5 Conclusion

Subsection 7.4.3 demonstrates the proven methodology of using the SDT, SDD, MLP artificial neural network, and the non-contact microwave Doppler radar to estimate the oxygen saturation in the complex sleep environment with a good accuracy level.

For the SpO_2 independent "Test" with a total sleep duration of 56 hours, 57 minutes and 46.5 seconds, the SpO_2 correlation coefficient achieved is 0.92. The mean squared error (MSE) is 1.80 (% oxygen saturation) and the 95% limits of agreement is ±2.7 (%

oxygen saturation). A potential application is a non-contact system that can continuously monitor the oxygen saturation level during sleep and can be used at home.

However, due to the non-contact predictions of the SpO_2 overall 95% limits of agreement of ±2.7 (% of oxygen saturation), it may not be applicable as a replacement for the PSG pulse oximeter. This is due to the SpO_2 desaturation criteria of 2–5% in sleep diagnosis as specified by the American Academy of Sleep Medicine (AASM) [11]. Nevertheless, a potential application could be the non-contact early screening of oxygen saturation level during sleep, which can be used at home.

7.4.4 Remarks

Section 7.4 demonstrates the proven methodology of the "non-stationary" and "non-direct facing" SpO_2 prediction, using the non-contact microwave Doppler radar in the complex sleep environment. The two applications presented has demonstrated good accuracy results.

A comparison of the performance and accuracy between the application of external ventilation mathematical model in section 7.4.2, and the SDT & SDD in section 7.4.3 is detailed in Table 7.4.4.1. As shown in Table 7.4.4.1, the application of the SDT and SDD with respect to data transformation, augmentation, normalization, scaling, and feature extraction, has insignificant performance and accuracy variations. This result demonstrates the capability of the SDT and SDD compared to the application of the non-contact SpO_2 prediction outlined in section 7.4.2.

	Section 7.4.2.1 Results	***Section 7.4.3.4 Results***	***Performance Comparison SDT and SDD as Reference***
Correlation Coefficient "r"	0.93	0.92	Decrease correlation coefficient by 0.01
Mean Squared Error (MSE)	1.54	1.80	Increase MSE by 0.26

95% limits of agreement	±2.5	±2.7	Increase 95% limits of agreement by 0.2

Table 7.4.4.1 – SpO_2 Prediction Performance and Accuracy Comparison

The nature of using the artificial neural network model with an automatic feature extraction approach is that the features cannot always be explainable and or correspond to the natural or physical phenomena. In contrast, the mathematical modeling approach offers explainable processes and results that may correspond to the natural or physical phenomena. However, this approach requires build-in assumptions and constraints, which may lead to complex data variations in the data boundaries and may result in increased complexity and impact the accuracy level.

In conclusion, the two novel approach presented can be utilized for the non-contact oxygen saturation monitoring during sleep. However, if the accuracy level and the self-extracting features are determined to be more important than the explainable features and processes, then the SDT and SDD is the preferred approach.

7.5 Conclusion

Chapter 7 contributes to the field of non-contact sleep monitoring by presenting the real-life non-contact sleep monitoring applications and the results, along with the contributions presented in Chapters 3, 4, 5 and 6. The novel non-contact sleep monitoring real-life applications and the results that the Thesis contributes to the field of non-contact sleep monitoring include:

1. Respiratory rate – achieved 91.53% accuracy level with median error of ±1.30 breaths/min.

2. Heart rate – achieved 91.28% with median error of ±6.20 beats/min.

3. Tidal volume – achieved 83.13% accuracy level with a median error of 57.32 milliliters.

4. Body orientations – achieved high correct classification rate of 99.9%. The misclassification is at a negligible rate of 0.1%.

5. Oxygen saturation – achieved correlation coefficient of 0.92 and the 95% limits of agreement is ±2.7 (% oxygen saturation).

A potential application is the non-contact sleep early screening and/or continuous monitoring of the respiratory and heart rates, tidal volume, body orientations, and saturation oxygen level during sleep. This can be used in homes, hospitals, primary care sectors, nursing home facilities and/or sleep laboratories.

CHAPTER 8

SUMMARY, FUTURE RESEARCH, and CONCLUSION

INTRODUCTION

The Thesis is a response to the demands for the non-contact sleep monitoring systems. The demands arise due to the limitations of the PSG system, the importance of early screening for OSA, the need for long-term continuous monitoring and the concern with respect to patient discomfort when using the gold-standard PSG system.

The contributions of the Thesis are the novel theories, real-life applications and the results of the non-contact sleep monitoring using the non-contact microwave Doppler radar, including the “non-stationary” and “non-direct facing” subjects’ measurements in the complex sleep environment.

Chapter 8 provides the summary of the Thesis contributions, recommendations for the future research directions and conclude the work presented in the Thesis.

8.1 Thesis Summary

The highlights of the novel theories and applications that the Thesis contributes to the field of non-contact sleep monitoring are:

1. **Relative Demodulation** – A novel real-time demodulation theory and technique for the non-contact microwave Doppler radar system is propose in Chapter 3. In addition, a novel respiratory and heart rates estimation algorithm, using the non-contact microwave Doppler radar is also proposed. The novelty of "Relative Demodulation" technique is that it pivots from conventional displacements analysis to introduce derivatives analysis. This technique offers real-time, simple, fast, accurate, low computational and applicable for embedded applications. "Relative Demodulation" technique is verified against the real-life sleep monitoring application with 20 chronic heart failure (CHF) and diagnosed obstructive sleep apnea (OSA) patients for the respiratory and heart rates estimations during sleep. The respiratory rate estimation median accuracy achieved is 91.53% with median error of ±1.30 breaths/min. The heart rate estimation median accuracy achieved is 91.28% with median error of ±6.20 beats/min. The "Relative Demodulation" technique accuracy and performance is also compared against an automated estimation algorithm. The results indicated that the performance is comparable, however, the "Relative Demodulation" distinctive feature is the real-time estimation capability with high accuracy.

2. **Pulmonary Ventilation Mathematical Model** – A novel pulmonary ventilation mathematical model that defines the relationship between the intrapulmonary pressure and the chest displacement is propose in Chapter 4. In addition, a novel tidal volume estimation algorithm, using the non-contact microwave Doppler radar is also proposed. The novelty of the pulmonary ventilation mathematical model is that it defines the relationship between the intrapulmonary pressure and the chest displacement. The tidal volume can then be estimated via the mathematical model. It is also important to emphasize that the pulmonary ventilation mathematical model

is derive from the understanding of anatomy and physiology, it is not simply an application of regressions between the chest displacement and intrapulmonary pressure or tidal volume values. The propose pulmonary ventilation mathematical model is verified against the real-life sleep monitoring application with 20 CHF and diagnosed OSA patients for the tidal volume estimation during sleep. The tidal volume estimation median accuracy achieved is 83.13% with a median error of 57.32 milliliters. It is important to emphasize that the pulmonary ventilation mathematical model is not restricted to the non-contact applications, it is a novel mathematical model that can also be applied to the PSG systems or to home sleep test devices.

3. **External Ventilation Mathematical Model** – A novel external ventilation mathematical model that quantitatively defines the relationships between the arterial oxygen saturation (SaO_2), the arterial partial pressure of oxygen (PaO_2) and the arterial partial pressure of carbon dioxide ($PaCO_2$) is propose in Chapter 5. In addition, a novel non-contact algorithm that utilizes the propose mathematical model, multilayer perceptron (MLP) artificial neural network (ANN), and the non-contact microwave Doppler radar, to translate the human periodic chest displacements caused by respiratory efforts into peripheral capillary oxygen saturation (SpO_2) measurements is also proposed. The novelty of the external ventilation mathematical model is that it enables the capability to estimate oxygen saturation using the non-contact microwave Doppler radar. The propose model and MLP ANN is verified against the real-life sleep monitoring application with 20 CHF and diagnosed OSA patients for the SpO_2 estimation during sleep. The SpO_2 correlation coefficient achieved is 0.93. The mean squared error (MSE) is 1.54 (% oxygen saturation) and the 95% limits of agreement is ±2.5 (% oxygen saturation). It is also important to emphasize that the external ventilation mathematical model is theoretically generic and not restricted to non-contact applications.

4. **3-Dimensional Feature Representation and Extraction Technique** – A novel 3-dimensional feature representation and extraction technique, consisting of two methods, Spatial Dimensions Transform (SDT) and Spatial Dimensions Decomposition (SDD) is propose in Chapter 6. SDT and SDD when combined can achieve data transformation, augmentation, normalization, scaling, and feature extraction in a single process. The novelty of SDT and SDD is that feature engineering process is not required in the process of extracting the features. The propose SDT and SDD is applied as automatic feature extraction and representation, in conjunction with MLP ANN for both classification and regression applications to classify the sleep body orientations and predict SpO_2 during sleep. The propose methodology is verified against the real-life sleep monitoring application with 24 CHF and diagnosed OSA patients for sleep body orientations classifications and 21 patients for SpO_2 predictions during sleep. Sleep body orientations achieved a high correct classification rate of 99.9% for 5 classes of "Prone", "Upright", "Supine", "Right", and "Left" body orientations. The SpO_2 correlation coefficient achieved is 0.92. The mean squared error (MSE) is 1.80 (% oxygen saturation) and the 95% limits of agreement is ±2.7 (% oxygen saturation).

The propose novel theories and techniques are verified through real-life applications in the complex sleep environment, including "non-stationary" and "non-direct facing" subjects' measurements. The high accuracy and performance verification results in Chapter 7 indicate the feasibility, integrity and reliability of the novel theories and techniques in the non-contact sleep monitoring applications.

It is also important to emphasize that the Thesis pioneer the real-time monitoring of the respiratory and heart rates, the interval-based monitoring of the tidal volume and SpO_2, and the classification of sleep body orientations in real-life, complex, "non-stationary" and "non-direct facing" sleep environment using microwave Doppler radar.

8.2 Recommendations for Future Research

In relation to the theories and applications presents in the Thesis, there are two specific research opportunities that could advance the field of non-contact sleep monitoring. The recommendations for future research directions as per opportunity are outlined as follows:

1. Moving towards to non-contact Cardiology in Sleep Disordered Breathing (SDB):

    a. Extend the research utilizing "Relative Demodulation" technique, which provide the absolute chest displacements, respiratory and heart rates, to estimate the heart rate variability (HRV) during sleep.

    b. Extend the research utilizing "Pulmonary Ventilation Mathematical Model" with different types of neural networks to increase the accuracy and reliability of the tidal volume, as well as, the estimation of the pulse pressure, minute ventilation and air flow/volume during sleep.

    c. Extend the research utilizing "External Ventilation Mathematical Model", "3-Dimensional Feature Representation and Extraction" techniques, and different types of neural networks to extend the classifications of Cheyne-Stokes respirations, sleep/wake stages, apnea-hypopnea index (AHI), apnea index (AI), hypopnea index (HI), snore index, and/or hypercapnia (also known as carbon dioxide (CO_2) retention).

    The area of focus should be in the disturbance management due to the complex nature existed in the sleep environment. The continual research achievements in these areas will enable the possibilities of screening, diagnosing and monitoring of cardiovascular comorbidity in OSA patients.

2. Moving towards to practical realization and commercialization:

    a. Extend the research for the theories and techniques presented in the Thesis to wider patients' populations and groups, ranging from healthy to critical care patients. There are also opportunities to leverage multi-techniques in combination to complement the accuracy and performance. The goal is to achieve generalization for the non-contact sleep monitoring system. The focus should be in the adaption of the theories and techniques to "big data" and general populations, while maintaining or increasing the accuracy and performance of the system.

The continual research achievements in these areas will enable the possibilities of practical realization and commercialization of the non-contact sleep monitoring and diagnosing technology.

8.3 Conclusion

The Thesis contributes to the field of the non-contact sleep monitoring by developing novel physiological mathematical models, 3-dimensional feature representation and extraction technique, and artificial neural network applications, to enable non-contact continuous monitoring of physiological vital signs and sleep body orientations in the complex sleep environment.

The novel theories and applications introduced in the Thesis addresses real-life challenges for the "non-stationary" and "non-direct facing" measurements issues, and provide solutions to enable non-contact sleep monitoring. The achievements and contributions of the Thesis include:

Sleep Monitoring Parameters	***Achieve Performance and Accuracy***
Respiratory Rate	91.53% accuracy with median error of ±1.30 breaths/min.
Heart Rate	91.28% with median error of ±6.20 beats/min.
Tidal Volume	83.13% accuracy with a median error of 57.32 milliliters.
Body Orientations	High correct classification rate of 99.9%. The misclassification is at a negligible rate of 0.1%.
Saturation Oxygen	Correlation coefficient of 0.92 and the 95% limits of agreement is ±2.7 (% oxygen saturation).

A potential application is the non-contact sleep early screening and/or continuous monitoring of the respiratory and heart rates, tidal volume, body orientations, and saturation oxygen in the home. More importantly, the non-contact sleep monitoring system eliminates the need for body-contact sensors, which in turn addresses the PSG limitations, such as limited mobility, irritations, distress and discomforts to patients during the monitoring process.

The novel theories and applications presents in the Thesis will open up possibilities and opportunities for the practical realization of the non-contact sleep monitoring technology that can be used in everyday life, including in homes, hospitals, primary care sectors, nursing home facilities and/or sleep laboratories.

The optimistic future research directions are the applications of screening and monitoring of cardiovascular comorbidity in OSA patients. This will also lead to new opportunities and market potentials for Cardiology in Sleep Disordered Breathing (SDB).

APPENDIX I

A.I Biosensor

A.I.I SleepMinder™

The SleepMinder™ (SM) is a ResMed Asia Pacific Ltd. patented (WO/2013/177621) [171] novel sensor technology for contactless and convenient measurement of sleep and breathing in the home. SleepMinder™ was originally developed by BiancaMed Ltd. (Dublin, Ireland) and acquired by ResMed Inc. (San Diego, USA) in 2011.

SM is a dual pulsed-wave (PW) Doppler system designed to transmit two short pulses of radio frequency energy at 5.8 GHz, each pulse is approximately 5 ns long, emits an average power less than 1 mW, and is capable of measuring movements at a distance between 0.5–3.0 m, nominally.

The core architecture of SM is that it generates pairs of pulses with the first pulse as the transmit pulse and the second pulse as the mixer pulse. The first pulse reflects nearby objects to create an echo pulse that is received back to the sensor. By multiplying the echo pulse with the mixer pulse inside the receiver, a continuous output signal proportionate to any phase shift of the echo pulse is generated [64, 171, 172]. Even though SM transmits PW, its novel circuitry design generates continuous output signals and corresponds to the continuous-wave (CW) Doppler radar system, which is a unique feature of SleepMinder™.

SM sensor also employed quadrature detection technique to overcome a well-known limitation in radio frequency sensing referred to as the range-correlation effect (or phase-nulling), which leads to two estimates of the movements signals, called I and Q channels. The DC value of I and Q channels will depend on the local static environment. In the case of two people lying on the bed, a combination of the

sophisticated sensor design, called “Range Gating”, and the intelligent on board signal processing, will result in measuring only the motions of the person nearest to the sensor [64, 65, 171, 172].

The outputs I and Q channels are internally pre-filtered by an active analogue low-pass filters at 1.6Hz, and sampled at 64Hz with 12 bits resolution and with 0–3.2 V voltage resolution. The 64Hz samples are then averaged over 4 samples, producing two 16Hz channels and saved to the SM flash SD memory card in a proprietary binary format.

Images of the SleepMinder™ and the innovative re-design S+ by ResMed Asia Pacific Ltd. are shown below in Fig. I.1 and Fig. I.2.

Figure I.1 – SleepMinder™ by BiancaMed

Figure I.2 – S+ by ResMed

APPENDIX II

A.II Patients' Database

A.II.I Total Patients

The patients' database was obtained under the "ResMed IP Agreement" and the "Student Placement Agreement" between ResMed Asia Pacific Ltd. (Bella Vista, NSW 2153, Australia) and the University of Technology Sydney (UTS) (Ultimo, NSW 2007, Australia). The agreements were signed by the author, the principle supervisor from UTS, the Director of Research and Innovation Office from UTS, and the Vice President of Technology and Applied Research from ResMed Asia Pacific Ltd.

The patients' database consists of:

- thirty chronic heart failure (CHF) patients sleep recordings.
- two females out of 30 CHF patients.
- twenty-seven males out of 30 CHF patients.
- one undisclosed gender out of 30 CHF patients.

The patients were diagnosed with chronic heart failure (CHF) of Class II & III New York Heart Association (NYHA) classification. The patients were sequentially admitted in the Royal Brompton Centre for Sleep, London, UK, between 26-Sep-2011 and 21-Nov-2012 for the diagnosis of sleep apnea, disordered sleep, or both. The patients had the clinic's ethics approval and written consent obtained, and underwent full polysomnography (PSG) analysis with manually scored by sleep experts.

ResMed Asia Pacific Ltd. patented SleepMinder^{TM} sensor (WO/2013/177621) [171] was installed in the sleep laboratory and its bio-motions signals were recorded simultaneously with the PSG signals. SleepMinder^{TM} was installed in the sleep

laboratory and its bio-signals were recorded simultaneously with the PSG signals. The SleepMinder™ was positioned facing the patient and in line with the chest, at a distance of 0.5 m, and an elevation of 0.5 m from the edge of the bed. An illustration of the SleepMinder™ setup in a sleep laboratory or at home is shown in Fig. I.1.

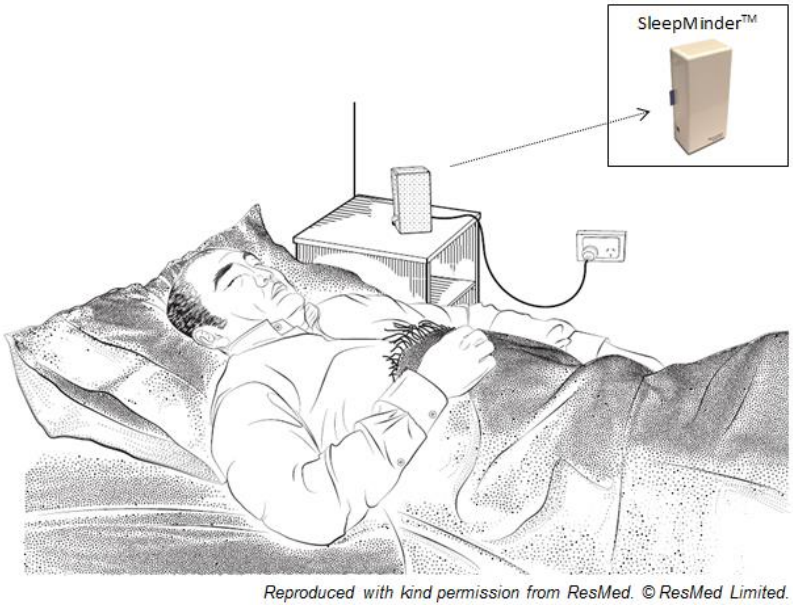

Figure I.1 – SleepMinder™ Setup in a Sleep Laboratory or at Home

A.II.II Patients Exclusions

The following patients' recordings were excluded due to the following reasons:

1. Three deidentified patients with patients' IDs of "LONPSG01", "LONPSG06" and "LONPSG08" were identified as missing the recorded PSG's European data format (EDF) files. Therefore, these patients' records are deemed invalid and excluded from the patients' database.

2. Three deidentified patients with patients' IDs of "LONPSG14", "LONPSG24" and "LONPSG25" do have the PSG signals recorded, however, the recorded signals are very short in duration, this is due to the operator's errors during the data collection process. Therefore, it is deemed unusable and excluded from the patients' database.

The patients' demographics and recorded sleep duration is presented in Table II.1.

Patient ID	***Age (yr)***	***Height (m)***	***Weight (kg)***	***BMI***	***Gender (Male / Female) (M/F)***	***NYHA Class***	***Recorded Sleep Duration (hr)***
LONPSG01	*Invalid patient record. Refer to section A.II.II point 1.*						
LONPSG02	66	1.67	98.0	35	M	II	8.79
LONPSG03	81	1.67	73.0	26	M	II	9.61
LONPSG04	74	1.74	76.8	25	M	II	10.30
LONPSG05	89	1.57	65.6	27	F	III	8.53
LONPSG06	*Invalid patient record. Refer to section A.II.II point 1.*						
LONPSG07	73	1.72	60.8	21	M	II	7.24
LONPSG08	*Invalid patient record. Refer to section A.II.II point 1.*						
LONPSG09	72	1.65	85.0	31	M	II	7.90
LONPSG10	66	1.75	89.5	29	M	II	7.37
LONPSG11	81	1.75	95.9	31	M	II	9.18
LONPSG12	74	1.72	83.9	28	M	III	7.66

LONPSG13	84	1.67	70.0	25	M	II	7.91
LONPSG14	*Invalid patient record. Refer to A.II.II point 2.*						
LONPSG15	74	1.72	83.9	28	M	III	6.86
LONPSG16	72	1.77	79.0	25	M	II	6.39
LONPSG17	57	1.70	95.4	33	F	II	7.36
LONPSG18	33	1.72	74.3	25	M	II	6.74
LONPSG19	46	1.80	157.0	48	M	II	8.22
LONPSG20	72	1.77	103.1	33	M	II	6.87
LONPSG21	74	1.60	59.0	23	M	III	8.37
LONPSG22	74	1.72	84.8	29	M	III	7.04
LONPSG23	48	1.67	84.0	30	M	III	7.59
LONPSG24	*Invalid patient record. Refer to A.II.II point 2.*						
LONPSG25	*Invalid patient record. Refer to A.II.II point 2.*						
LONPSG26	73	1.72	77.3	26	M	III	7.47
LONPSG27	55	1.88	102.0	29	M	II	7.28

LONPSG28	*UD*	*UD*	*UD*	*UD*	*UD*	*UD*	7.49
LONPSG29	55	1.88	102	29	M	II	6.01
LONPSG30	80	*UD*	*UD*	*UD*	M	II	7.65

Table II.1 – Patients' Demographics and Recorded Sleep Duration

Note:

- "UD" – undisclosed information according to patient's consent.
- "NYHA" – New York Heart Association classification system for patients with cardiac diseases.
- NYHA Class II – patients that have cardiac disease resulting in slight limitation of physical activity. They are comfortable at rest. Ordinary physical activity results in fatigue, palpitation, dyspnea or anginal pain.
- NYHA Class III – patients that have cardiac disease resulting in marked limitation of physical activity. They are comfortable at rest. Less than ordinary physical activity causes fatigue, palpitation, dyspnea or anginal pain.

A.II.III Selected Patients' Database

The selected patients' database for the work presented in the Thesis include:

- twenty-four chronic heart failure (CHF) patients sleep recordings.
- two females out of 24 CHF patients.
- twenty-one males out of 24 CHF patients.

- one undisclosed gender out of 24 CHF patients.

The summary of the selected patients' data is presented in Table III.1.

Total Sample Length (16 Hz)	***Total Recorded Sleep Duration (hr)***	***Mean Recorded Sleep Duration (hr)***	***Mean Age (yr)***	***Mean Height (m)***	***Mean Weight (kg)***	***Mean BMI***
10,786,680	187.27	7.80	68.39	1.72	86.38	28.99

Table III.1 – Selected Patients' Database Summary

A.II.IV Adjusted Patients' Database for Respiratory and Heart Rates Estimations

There were additional patients' data records which have also been excluded from the selected patients' database as stated in subsection A.II.III due to the following reasons:

1. Three deidentified patients with patients' IDs of "LONPSG05", "LONPSG09" and "LONPSG28" demonstrated tachycardia condition, which is outside the SleepMinder^{TM} internal motions frequency range due to device internal filter bandwidth. Therefore, these patients were excluded from the selected patients' database.

2. One deidentified patient with patient's ID of "LONPSG23" demonstrated bradycardia condition, which is outside the SleepMinder^{TM} internal motions frequency range due to device internal filter bandwidth. Therefore, the patient was excluded from the selected patients' database.

The adjusted patients' database for the respiratory and heart rates estimations presented in the Thesis include:

- twenty chronic heart failure (CHF) patients sleep recordings.
- one female out of twenty CHF patients.
- nineteen males out of twenty CHF patients.

A summary of the selected patients' data is presented in Table IV.1.

Total Sample Length (16 Hz)	***Total Recorded Sleep Duration (hr)***	***Mean Recorded Sleep Duration (hr)***	***Mean Age (yr)***	***Mean Height (m)***	***Mean Weight (kg)***	***Mean BMI***
8,927,700	154.99	7.75	68.20	1.74	87.67	28.94

Table IV.1 – Adjusted Patients' Database Summary for Respiratory and Heart Rates

A.II.V Adjusted Patients' Database for Tidal Volume and Oxygen Saturation Estimations by External Ventilation Mathematical Models

There were additional patients' data records which have also been excluded from the selected patients' database as stated in section A.II.III due to the following reasons:

1. Two deidentified patients with patients' IDs of "LONPSG28" and "LONPSG30" does not contains the patients' weight and height information. The mathematical models required these information for the calculations, therefore, these patients have been excluded from the selected patients' database.

2. One deidentified patient with patient's ID of "LONPSG10" does not have the reference PSG Pressure signal recorded. This is the required signal for the verification of the mathematical models. Therefore, the patient has been excluded from the selected patients' database.

3. One deidentified patient with patient's ID of "LONPSG19" contains multiple dropouts (periods of no data) in SleepMinder^{TM} signals due to the operator's errors during the data collection process. It is not recommended to be included as these errors may cause incorrect or skewness in the results. Therefore, this patient has been excluded from the selected patients' database.

The adjusted patients' database for the respiratory and heart rates estimations presented in the Thesis is:

- twenty chronic heart failure (CHF) patients sleep recordings.
- two females out of twenty CHF patients.
- eighteen males out of twenty CHF patients.

The summary of the selected patients' data is presented in Table V.1.

Total Sample Length (16 Hz)	***Total Recorded Sleep Duration (hr)***	***Mean Recorded Sleep Duration (hr)***	***Mean Age (yr)***	***Mean Height (m)***	***Mean Weight (kg)***	***Mean BMI***
8,981,668	155.93	7.80	69.05	1.72	82.69	28.01

Table V.1 – Adjusted Patients' Database Summary for Tidal Volume & Oxygen Saturation by Mathematical Models

A summary of the selected patients' data partitions for the "Training", "Validation" and "Test" of the oxygen saturation prediction using external ventilation mathematical model is presented in Table V.2.

Sample Rate at 16 Hz	***Dataset (100%)***	***Training (50%)***	***Validation (15%)***	***Test (35%)***
Sample Count	8,929,440	4,464,720	1,339,416	3,125,304
Sleep Hour	155.03	77.51	23.25	54.26

Table V.2 – Selected Patients' Database Partitions for Saturation Oxygen

A.II.VI Patients' Database Partitions for Body Orientations Prediction

Predicting body orientations does not impact by cardiac conditions, such as, tachycardia or bradycardia and/or the availability of patients' weight and height information. Patients exclusions was not necessary as the reference PSG body orientations signals are all available and valid in the recordings. Therefore the total twenty four CHF patients from the selected patients' database stated in section A.II.III are randomly concatenated into a single dataset with a total sleep duration of 185.7 hours. The concatenated dataset is then randomly partitioned into 3 datasets of "Training", "Validation" and "Test". The dataset partition categories are summarized in Table A.VI.1.

Sample Rate at 16 Hz		***Dataset (100%)***	***Training (50%)***	***Validation (15%)***	***Test (35%)***
Sample Count	*Total*	10698240	5349120	1604736	3744384
	Prone	95520	47709	14345	33466
	Upright	566387	283456	84402	198529
	Supine	2412959	1206070	362890	843999
	Right	2381283	1190890	357192	833201
	Left	5242091	2620995	785907	1835189

Sleep Duration (hr)	*Total*	185.7	92.9	27.9	65.0
	Prone	1.7	0.8	0.2	0.6
	Upright	9.8	4.9	1.5	3.4
	Supine	41.9	20.9	6.3	14.7
	Right	41.3	20.7	6.2	14.5
	Left	91.0	45.5	13.6	31.9
Percentage of Total Sample (%)	*Prone*	0.9	0.9	0.9	0.9
	Upright	5.3	5.3	5.3	5.3
	Supine	22.5	22.5	22.5	22.5
	Right	22.3	22.3	22.3	22.3
	Left	49.0	49.0	49.0	49.0

Table VI.1 – Selected Patients' Database Partitions for Body Orientations

A.II.VII Patients' Database Partitions for Oxygen Saturation Prediction by SDT and SDD

Only twenty one out of the twenty four CHF patients from the selected patients' database stated in section A.II.III are selected for the oxygen saturation (SpO_2) prediction application. The reasons for excluding three patients are:

1. One deidentified patient with patient's ID of "LONPSG28" does not have the reference PSG SpO_2 signal recorded. This is the required signal to verify the SpO_2 prediction. Therefore, this patient has been excluded from the selected patients' database.

2. Two deidentified patients with patients' IDs of "LONPSG17" and "LONPSG19" have multiple PSG SpO_2 signal dropouts during the nights. This is due to the patients' movements during sleep which caused the pulse oximeter fingertip connection to be disengaged. Therefore, these patients have been excluded from the selected patients' database.

The 16 Hz SM data is down sampled to the PSG SpO_2 sample rate at 4 Hz. The patients' data are randomly concatenated and partitioned into 3 datasets of "Training", "Validation" and independent "Test". The dataset partitions are summarized in Table VII.1.

Sample Rate at 4 Hz	***Dataset (100%)***	***Training (50%)***	***Validation (15%)***	***Test (35%)***
Sample Count	2,343,696	1,171,848	351,554	820,294
Sleep Hour	162.76	81.38	24.41	56.96

Table VII.1 – Selected Patients' Database Partitions for Saturation Oxygen

APPENDIX III

A.III Common Neural Network Training Characteristics

A.III.I Hyperparameters

The common training characteristics of the artificial neural network used in the Thesis are summarized in Table III.1.

Derivative Function	***Network Initialization***	***Performance Function***	***Training Function***
Static derivative function (*chain rule*)	Layer-by-layer: Nguyen-Widrow initialization function	Cross Entropy Regularization: 0.001 Normalization: none	Scaled Conjugate Gradient σ: 0.005 λ: 0.0005

Table I.1 – Artificial Neural Network Training Characteristics

REFERENCES

[1] T. Young, M. Palta, J. Dempsey, J. Skatrud, S. Webber, and S. Badr, "The Occurrence of Sleep-Disordered Breathing Among Middle-Aged Adults," *The New England Journal of Medicine,* vol. 328, no. 17, pp. 1230-1235, 1993.

[2] G. Amabile, F. Pauri, and F. Fattapposta, "Neurological Correlations in Neurological Breathing Disorders," *Surgery for Snoring and Obstructive Sleep Apnea Syndrome*, M. Fabiani, ed., pp. 39-46, The Netherlands: Kugler Publications, 2003.

[3] N. M. Punjabi, "The Epidemiology of Adult Obstructive Sleep Apnea," *Proceedings of the American Thoracic Society,* vol. 5, no. 2, pp. 136-143, 2008.

[4] T. Young, Finn, L., Peppard, P.E., Szklo-Coxe, M., Austin, D., Nieto, F.J., Stubbs, R. & Hla, K.M., "Sleep Disordered Breathing and Mortality: Eighteen-Year Follow-up of the Wisconsin Sleep Cohort," *Sleep,* vol. 31, no. 8, pp. 1071-1078, 2008.

[5] N. J. Buchner, Sanner, B.M., Borgel, J. & Rump, C.L., "Continuous Positive Airway Pressure Treatment of Mild to Moderate Obstructive Sleep Apnea Reduces Cardiovascular Risk," *American Journal of Respiratory and Critical Care Medicine,* vol. 176, no. 12, pp. 1274-1280, 2007.

[6] P. D. Chazal, E. O'Hare, N. Fox, and C. Heneghan, "Assessment of Sleep/Wake Patterns Using a Non-Contact Biomotion Sensor," in 30th Annual International IEEE EMBS Conference, Vancouver, British Columbia, Canada, 2008, pp. 514-517.

[7] D. Y. C. Lie, R. Ichapurapu, S. Jain, J. Lopez, R. E. Banister, T. Nguyen, and J. Griswold, "A 2.4GHz Non-Contact Biosensor System for Continuous Monitoring of Vital-Signs," *Telemedicine Techniques and Applications*, 9, G. Graschew, ed., InTech, 2011, pp. 211-238.

[8] M. Kagawa, K. Ueki, H. Tojima, and T. Matsui, "Noncontact Screening System with Two Microwave Radars for the Diagnosis of Sleep Apnea-Hypopnea Syndrome," in 35th Annual International Conference of the IEEE EMBS, Osaka, Japan, 2013, pp. 2052-2055.

[9] M. Kagawa, Y. Yoshida, M. Kubota, A. Kurita, and T. Matsui, "An overnight vital signs monitoring system for elderly people using dual microwave radars." pp. 590-593.

[10] P. E. Peppard, T. Young, J. H. Barnet, M. Palta, E. W. Hagen, and K. M. Hla, "Increased Prevalence of Sleep-Disordered Breathing in Adults," *American Journal of Epidemiology,* vol. 177, no. 9, pp. 1006-1014, 14 April, 2013, 2013.

[11] American Academy of Sleep Medicine, *International Classification of Sleep Disorders, Revised: Diagnostic and Coding Manual*, Chicago, Illinois, USA: American Academy of Sleep Medicine, 2001.

[12] R. S. T. Leung, and T. D. Bradley, "Sleep Apnea and Cardiovascular Disease," *American Journal of Respiratory and Critical Care Medicine,* vol. 164, no. 12, pp. 2147–2165, 2001.

[13] R. P. Pedrosa, L. F. Drager, C. C. Gonzaga, M. G. Sousa, L. K. G. De Paula, A. C. S. Amaro, C. Amodeo, L. A. Bortolotto, E. M. Krieger, T. D. Bradley, and G. Lorenzi-Filho, "Obstructive Sleep Apnea: The Most Common Secondary Cause of Hypertension Associated With Resistant Hypertension," *Hypertension,* vol. 58, no. 5, pp. 811-817, 2011.

[14] R. S. Aronsohn, H. Whitmore, E. V. Cauter, and E. Tasali, "Impact of Untreated Obstructive Sleep Apnea on Glucose Control in Type 2 Diabetes," *American journal of respiratory and critical care medicine,* vol. 181, no. 5, pp. 507-513, 2010.

[15] S. Seicean, K. P. Strohl, A. Seicean, C. Gibby, and T. H. Marwick, "Sleep Disordered Breathing as a Risk of Cardiac Events in Subjects With Diabetes Mellitus and Normal Exercise Echocardiographic Findings," *The American Journal of Cardiology,* vol. 111, no. 8, pp. 1214-1220, 2013.

[16] F. J. Nieto, P. E. Peppard, T. Young, L. Finn, K. M. Hla, and R. Farré, "Sleep-disordered Breathing and Cancer Mortality: Results from the Wisconsin Sleep Cohort Study," *American Journal of Respiratory and Critical Care Medicine,* vol. 186, no. 2, pp. 190-194, 2012.

[17] T. Young, J. Skatrud, and P. E. Peppard, "Risk Factors for Obstructive Sleep Apnea in Adults," *Journal of American Medical Association,* vol. 291, no. 16, pp. 2013-2016, April 28, 2004, 2004.

[18] Y. J. Suzuki, V. Jain, A.-M. Park, and R. M. Day, “Oxidative stress and oxidant signaling in obstructive sleep apnea and associated cardiovascular diseases,” *Free Radical Biology & Medicine,* vol. 40, no. 10, pp. 1683–1692, 2006.

[19] H. P. Attarian, and A. N. Sabri, “When to suspect obstructive sleep apnea syndrome. Symptoms may be subtle, but treatment is straightforward ” *Postgraduate Medicine,* vol. 111, no. 3, pp. 70-76, March, 2002, 2002.

[20] L. Ren, L. Kong, F. Foroughian, H. Wang, P. Theilmann, and A. E. Fathy, “Comparison Study of Noncontact Vital Signs Detection Using a Doppler Stepped-Frequency Continuous-Wave Radar and Camera-Based Imaging Photoplethysmography,” *IEEE Transactions on Microwave Theory and Techniques,* vol. 65, no. 9, pp. 3519-3529, 2017.

[21] H. O. Savage, R. N. Khushaba, A. Zaffaroni, M. Colefax, S. Farrugia, K. Schindhelm, H. Teschler, G. Weinreich, H. Grueger, M. Neddermann, C. Heneghan, A. Simonds, and M. R. Cowie, “Development and validation of a novel non-contact monitor of nocturnal respiration for identifying sleep-disordered breathing in patients with heart failure,” *ESC Heart Failure*, pp. 1-8, 2016.

[22] H. Wang, J.-H. Cheng, J.-C. Kao, and T.-W. Huang, “Review on Microwave/Millimeter-wave Systems for Vital Sign Detection,” in Wireless Sensors and Sensor Networks (WiSNet), 2014 IEEE Topical Conference, Newport Beach, CA, USA, 2014, pp. 19-21.

[23] T. Hall, D. Y. C. Lie, T. Q. Nguyen, J. C. Mayeda, P. E. Lie, J. Lopez, and R. E. Banister, “Non-Contact Sensor for Long-Term Continuous Vital Signs Monitoring: A Review on Intelligent Phased-Array Doppler Sensor Design,” *Sensors,* vol. 17, no. 11, 2017.

[24] C.-T. Lin, M. Prasad, C.-H. Chung, D. Puthal, H. El-Sayed, S. Sankar, Y.-K. Wang, J. Singh, and A. K. Sangaiah, “IoT-Based Wireless Polysomnography Intelligent System for Sleep Monitoring,” *IEEE Access,* vol. 6, pp. 405-414, 2018.

[25] D. C. Yacchirema, D. Sarabia-Jacome, C. E. Palau, and M. Esteve, “A Smart System for Sleep Monitoring by Integrating IoT With Big Data Analytics,” *IEEE Access,* vol. 6, pp. 35988-36001, 2018.

[26] G. Matar, J.-M. Lina, J. Carrier, and G. Kaddoum, “Unobtrusive Sleep Monitoring Using Cardiac, Breathing and Movements Activities: An Exhaustive Review,” *IEEE Access,* vol. 6, pp. 45129-45152, 2018.

[27] I. Sadek, E. Seet, J. Biswas, B. Abdulrazak, and M. Mokhtari, “Nonintrusive Vital Signs Monitoring for Sleep Apnea Patients: A Preliminary Study,” *IEEE Access,* vol. 6, pp. 2506-2514, 2018.

[28] M. I. Skolnik, "An Introduction To Radar," *Radar Handbook*, pp. 1.1 - 1.21, San Francisco: McGraw-Hill, Inc., 1990.

[29] W. K. Saunders, "CW and FM Radar," *Radar Handbook*, pp. 14.1 - 14.23, San Francisco: McGraw-Hill, Inc., 1990.

[30] I. M. Coman, “Christian Andreas Doppler -- the man and his legacy,” *European Journal of Echocardiography,* vol. 6, no. 1, pp. 7-10, 2005.

[31] “Detection & Ranging: Radar in the Twentieth Century,” *IEEE Aerospace and Electronic Systems Magazine,* vol. 15, no. 10, pp. 27-44, 2000.

[32] R. J. Serafin, "Meteorological Radar," *Radar Handbook*, pp. 23.1 - 23.33, San Francisco: McGraw-Hill, Inc., 1990.

[33] C. Li, V. Lubecke, O. Boric-Lubecke, and J. Lin, “A Review on Recent Advances in Doppler Radar Sensors for Noncontact Healthcare Monitoring,” *IEEE Transactions on Microwave Theory and Techniques,* vol. 61, no. 5, pp. 2046-2060, May, 2013, 2013.

[34] L. Scalise, "Non Contact Heart Monitoring," *Advances in Electrocardiograms - Methods and Analysis*, 4, R. Millis, ed., InTech, 2012, pp. 81-106.

[35] R. Ichapurapu, S. Jain, M. U. Kakade, D. Y. C. Lie, and R. E. Banister, “A 2.4GHz Non-Contact Biosensor System for Continuous Vital-Signs Monitoring on a Single PCB,” in ASIC, 2009. ASICON '09. IEEE 8th International Conference, Changsha, Hunan, 2009, pp. 925-928.

[36] O. Boric-Lubecke, V. Lubecke, I. Mostafanezhad, B.-K. Park, W. Massagram, and B. Jokanovic, “Doppler Radar Architectures and Signal Processing for Heart Rate Extraction,” *Mikrotalasna revija,* vol. 15, no. 2, pp. 12-17, 2009.

[37] H. Avagyan, A. Hakhoumian, H. Hayrapetyan, N. Pogosyan, and T. Zakaryan, “Portable Non-Contact Microwave Doppler Radar for Respiration and Heartbeat Sensing,” *Armenian Journal of Physics,* vol. 5, no. 1, pp. 8-14, 13 April, 2012, 2012.

[38] O. A. Postolache, P. S. Girão, and G. Postolache, “Comparative analysis of two systems for unobtrusive heart signal acquisition and characterization,” in 35th Annual International Conference of the IEEE EMBS, Osaka, Japan, 2013, pp. 7021-7024.

[39] G. Wang, J.-M. Munoz-Ferreras, C. Gu, C. Li, and R. Gomez-Garcia, “Linear-Frequency-Modulated Continuous-Wave Radar for Vital-Sign Monitoring,” in Wireless Sensors and Sensor Networks (WiSNet), Newport Beach, CA, USA, 2014, pp. 37-39.

[40] Y. Wang, Q. Liu, and A. E. Fathy, “CW and Pulse–Doppler Radar Processing Based on FPGA for Human Sensing Applications,” *IEEE Transaction on Geoscience and Remote Sensing,* vol. 51, no. 5, pp. 3097-3107, 2013.

[41] Y. S. Lee, P. N. Pathirana, T. Caelli, and S. Li, “Further Applications of Doppler Radar for Non-contact Respiratory Assessment,” in 35th Annual International Conference of the IEEE EMBS, Osaka, Japan, 2013, pp. 3833-3836.

[42] D. Girbau, A. Lázaro, Á. Ramos, and R. Villarino, “Remote Sensing of Vital Signs Using a Doppler Radar and Diversity to Overcome Null Detection,” *IEEE SENSORS Journal,* vol. 12, no. 3, pp. 512-518, March, 2012, 2012.

[43] Author ed.^eds., “A 2.4GHz Non-Contact Biosensor System for Continuous Monitoring of Vital-Signs,” *Telemedicine Techniques and Applications*, Rijeka, Croatia: InTech, 2011, p.^pp. Pages.

[44] R. Ichapurapu, Jain, S., Kakade, M.U., Lie, D.Y.C. & Banister, R.E., “A 2.4GHz Non-Contact Biosensor System for Continuous Vital-Signs Monitoring on a Single PCB,” in IEEE 8th International Conference on ASIC (ASICON09), Changsha, China,, 2009, pp. 925-928.

[45] B. Lohman, Boric-Lubecke, O., Lubecke, V.M., Ong, P.W. & Sondhi, M.M., "A Digital Signal Processor for Doppler Radar Sensing of Vital Signs."

[46] J. Han, Kim, J.G. & Hong, S., “A Compact Ka-Band Doppler Radar Sensor for Remote Human Vital Signal Detection,” *Journal of Electromagnetic Engineering and Science,* vol. 12, no. 4, pp. 234-239, 2012.

[47] O. Boric-Lubecke, Lubecke, V.M., Mostafanezhad, I., Park, B.K., Massagram, W. & Jokanovic, B., “Doppler Radar Architectures and Signal Processing for Heart Rate Extraction,” *Mikrotalasna revija,* vol. 15, no. 2, pp. 12-17, 2009.

[48] Y. S. Yee, Pathirana, P.N, Caelli, T. & Li, S., "Further Applications of Doppler Radar for Non-contact Respiratory Assessment," in 35th Annual International Conference of the IEEE EMBS, Osaka, Japan, 2013, pp. 3833-3836.

[49] D. Girbau, Lázaro, A., Ramos, Á. & Villarino, R., "Remote Sensing of Vital Signs Using a Doppler Radar and Diversity to Overcome Null Detection," *IEEE Sensors Journal,* vol. 12, no. 3, pp. 512-518, 2012.

[50] C. Gu, Li, C., Lin, J., Long, J., Huangfu, J. & Ran, L., "Instrument-Based Noncontact Doppler Radar Vital Sign Detection System Using Heterodyne Digital Quadrature Demodulation Architecture," *IEEE Transactions on Instrumentation and Measurement,* vol. 59, no. 6, pp. 1580-1588, 2010.

[51] K. Mostov, E. Liptsen, and R. Boutchko, "Medical applications of shortwave FM radar: remote monitoring of cardiac and respiratory motion," *Medical Physics,* vol. 37, no. 3, pp. 1332–1338, March, 2010, 2010.

[52] R. B. Shouldice, C. Heneghan, G. Petres, A. Zaffaroni, P. Boyle, W. T. McNicholas, and P. D. Chazal, "Real Time Breathing Rate Estimation from a Non Contact Biosensor," in 32nd Annual International Conference of the IEEE EMBS, Buenos Aires, Argentina, 2010, pp. 630-633.

[53] V. Vasu, C. Heneghan, S. Sezer, and T. Arumugam, "Contact-free Estimation of Respiration Rates during Sleep," in The 22nd IET Irish Signals and Systems Conference, ISSC 2011, Dublin, Ireland, 2011.

[54] T. Ballal, R. B. Shouldice, C. Heneghan, and A. Zhu, "Breathing Rate Estimation from a Non-Contact Biosensor Using an Adaptive IIR Notch Filter," in Biomedical Wireless Technologies, Networks, and Sensing Systems (BioWireleSS 2012), Santa Clara, CA, 2012, pp. 5-8.

[55] A. Singh, M. Baboli, X. Gao, E. Yavari, B. Padasdao, B. Soll, O. Boric-Lubecke, and V. Lubecke, "Considerations for Integration of a Physiological Radar Monitoring System with Gold Standard Clinical Sleep Monitoring Systems," in 35th Annual International Conference of the IEEE EMBS, Osaka, Japan, 2013, pp. 2120-2123.

[56] V. P. Tran, and A. A. Al-Jumaily, "Non-Contact Dual Pulse Doppler System based Respiratory and Heart Rates Estimation for CHF Patients," in 37th Annual International Conference of the IEEE Engineering in Medicine and Biology Society, MiCo - Milano Conference Center - Milan, Italy, 2015, pp. 4202-4205.

[57] V. P. Tran, and A. A. Al-Jumaily, “Non-Contact Dual Pulse Doppler System Based Real-Time Relative Demodulation and Respiratory & Heart Rates Estimations for Chronic Heart Failure Patients,” *Procedia Computer Science,* vol. 76, no. 2015, pp. 47–52, 2015.

[58] V. P. Tran, and A. A. Al-Jumaily, “Non-Contact Real-Time Estimation of Intrapulmonary Pressure and Tidal Volume for Chronic Heart Failure Patients,” in 38th Annual International Conference of the IEEE Engineering in Medicine and Biology Society, Orlando, Florida USA, 2016, pp. 3564-3567.

[59] V. P. Tran, and A. A. Al-Jumaily, “Non-Contact Doppler Radar Based Prediction of Nocturnal Body Orientations Using Deep Neural Network for Chronic Heart Failure Patients,” in 2017 International Conference on Electrical and Computing Technologies and Applications (ICECTA), American University of Ras Al Khaimah, Ras Al Khaimah, United Arab Emirates (UAE), 2017.

[60] D. Obeid, G. Zaharia, S. Sadek, and G. El Zein, “Microwave Doppler Radar for Heartbeat Detection Vs Electrocardiogram,” *Microwave and Optical Technology Letters,* vol. 54, no. 11, pp. 2610-2617, 2012.

[61] A. Singh, V. Lubecke, and O. Boric-Lubecke, “Pulse Pressure Monitoring Through Non-Contact Cardiac Motion Detection Using 2.45 GHz Microwave Doppler Radar,” in 33rd Annual International Conference of the IEEE EMBS, Boston, Massachusetts USA, 2011, pp. 4336-4339.

[62] W. Massagram, N. Hafner, V. Lubecke, and O. Boric-Lubecke, “Tidal Volume Measurement Through Non-Contact Doppler Radar With DC Reconstruction,” *IEEE Sensors Journal,* vol. 13, no. 9, pp. 3397-3404, 2013.

[63] Y. S. Lee, P. N. Pathirana, C. L. Steinfort, and T. Caelli, “Non-Contact Measurement of Respiratory Function and Deduction of Tidal Volume,” in 36th Annual International Conference of the IEEE Engineering in Medicine and Biology Society, Chicago, Illinois, USA, 2014, pp. 594-597.

[64] P. D. Chazal, N. Fox, E. O’Hare, C. Heneghan, A. Zaffaroni, P. Boyle, S. Smith, C. O’Connell, and W. T. McNicholas, “Sleep⁄wake measurement using a non-contact biomotion sensor,” *Journal of Sleep Research,* vol. 20, pp. 356–366, 22 June, 2010, 2011.

[65] A. Zaffaroni, P. D. Chazal, C. Heneghan, P. Boyle, P. Ronayne, and W. T. McNicholas, “SleepMinder: An Innovative Contact-Free Device for the

Estimation of the Apnoea-Hypopnoea Index," in 31st Annual International Conference of the IEEE EMBS, Minneapolis, Minnesota, USA, 2009, pp. 7091-7094.

[66] H. O. Savage, R. Khushaba, P. Bateman, S. Farrugia, K. Schindhelm, A. K. Simonds, and M. R. Cowie, "A Novel Non-Contact Device That Identifies and Categorises Sleep Disordered Breathing in Patients with Chronic Heart Failure," *Heart,* vol. 99, no. 2, 2013.

[67] H. O. Savage, R. Khushaba, P. Bateman, S. Farrugia, K. Schindhelm, A. K. Simonds, and M. R. Cowie, "Cheyne Stokes respiration in patients with heart failure detected by a novel non-contact monitor of nocturnal respiration," *European Journal of Heart Failure Supplements,* vol. 15, no. 12, 2013.

[68] Y. Li, R. Pal, and C. Li, "Non-contact Multi-Radar Smart Probing of Body Orientation based on Micro-Doppler Signatures." pp. 598-601.

[69] M. Baldi, F. Appignani, B. Zanaj, and F. Chiaraluce, "Body Movement Compensation in UWB Radars for Respiration Monitoring," in 2012 IEEE First AESS European Conference on Satellite Telecommunications (ESTEL), Rome, 2012, pp. 1-6.

[70] J. Sachs, M. Helbig, R. Herrmann, M. Kmec, K. Schilling, and E. Zaikov, "Remote vital sign detection for rescue, security, and medical care by ultra-wideband pseudo-noise radar," *Ad Hoc Networks,* vol. 13, pp. 42–53, 25 July, 2012, 2012.

[71] J. E. Kiriazi, O. Boric-Lubecke, and V. Lubecke, "Considerations in Measuring Vital Signs Cross Section with Doppler Radar," in Radio and Wireless Symposium (RWS 2011), Phoenix, AZ, USA, 2011, pp. 426-429.

[72] B.-K. Park, O. Boric-Lubecke, and V. M. Lubecke, "Arctangent Demodulation With DC Offset Compensation in Quadrature Doppler Radar Receiver Systems," *IEEE Transactions on Microwave Theory and Techniques,* vol. 55, no. 5, pp. 1073-1079, May, 2007, 2007.

[73] P.-H. Wu, J.-K. Jau, C.-J. Li, T.-S. Horng, and P. Hsu, "Phase- and Self-Injection-Locked Radar for Detecting Vital Signs with Efficient Elimination of DC Offsets and Null Points," *IEEE Transactions on Microwave Theory and Techniques,* vol. 61, no. 1, pp. 685-695, January, 2013, 2013.

[74] M. Steffen, and S. Leonhardt, “Non-Contact Monitoring of Heart and Lung Activity by Magnetic Induction Measurement,” *Acta Polytechnica,* vol. 48, no. 3, pp. 71-78, 2008.

[75] Ø. Aardal, Y. Paichard, S. Brovoll, T. Berger, T. S. Lande, and S.-E. Hamran, “Physical Working Principles of Medical Radar,” *IEEE Transactions on Biomedical Engineering,* vol. 60, no. 4, pp. 1142-1149, April, 2013, 2013.

[76] V. Vasu, N. Fox, T. Brabetz, M. Wren, C. Heneghan, and S. Sezer, “Detection of Cardiac Activity using a 5.8 GHz Radio Frequency Sensor,” in 31st Annual International Conference of the IEEE EMBS, Minneapolis, Minnesota, USA, 2009, pp. 4682-4686.

[77] R. Ichapurapu, S. Jain, G. John, T. Monday, D. Y. C. Lie, R. Banister, and J. Griswold, “A 2.4GHz Non-Contact Biosensor System for Continuous Vital-Signs Monitoring,” in Wireless and Microwave Technology Conference, 2009, Clearwater, FL, 2009, pp. 1-3.

[78] R. Fletcher, and J. Han, “Low-Cost Differential Front-End for Doppler Radar Vital Sign Monitoring,” in 2009 IEEE MTT-S International Microwave Symposium Digest, Boston, MA, 2009, pp. 1325-1328.

[79] G. Lu, F. Yang, Y. Tian, X. Jing, and J. Wang, “Contact-free Measurement of Heart Rate Variability via a Microwave Sensor,” *Sensors,* vol. 9, pp. 9572-9581, 2009.

[80] V. Das, A. Boothby, R. Hwang, T. Nguyen, J. Lopez, and D. Y. C. Lie, “Antenna Evaluation of a Non-Contact Vital Signs Sensor for Continuous Heart and Respiration Rate Monitoring,” in Biomedical Wireless Technologies, Networks, and Sensing Systems (BioWireleSS 2012), Santa Clara, CA, 2012, pp. 13-16.

[81] J. Han, J.-G. Kim, and S. Hong, “A Compact Ka-Band Doppler Radar Sensor for Remote Human Vital Signal Detection,” *Journal of Electromagnetic Engineering and Science,* vol. 12, no. 4, pp. 234-239, December, 2012, 2012.

[82] A. Boothby, V. Das, J. Lopez, J. Tsay, T. Nguyen, R. E. Banister, and D. Y. C. Lie, “Accurate and Continuous Non-Contact Vital Signs Monitoring Using Phased Array Antennas in a Clutter-Free Anechoic Chamber,” in 35th Annual International Conference of the IEEE EMBS, Osaka, Japan, 2013, pp. 2862-2865.

[83] R. R. Fletcher, and S. Kulkarni, “Wearable Doppler radar with integrated antenna for patient vital sign monitoring,” in Radio and Wireless Symposium (RWS 2010), New Orleans, LA, USA, 2010, pp. 276-279.

[84] M. A. Othman, M. Sinnappa, H. Azman, M. Z. Abidin Abd Aziz, M. M. Ismail, M. N. Hussein, H. A. Sulaiman, M. H. Misran, M. A. Meor Said, R. A. Ramlee, S. P. Jack, and B. H. Ahmad, “5.8 GHz Microwave Doppler Radar for Heartbeat Detection,” in 23th Conference Radioelektronika, Pardubice, Czech Republic, 2013, pp. 367-370.

[85] Y.-J. An, Y.-P. Hong, B.-J. Jang, and J.-G. Yook, “Comparative Study of 2.4 GHz and 10 GHz Vital Signal Sensing Doppler Radars,” in Proceedings of the 40th European Microwave Conference, Paris, France, 2010, pp. 501-504.

[86] X. Gao, A. Singh, E. Yavari, V. Lubecke, and O. Boric-Lubecke, “Non-contact Displacement Estimation Using Doppler Radar,” in 34th Annual International Conference of the IEEE EMBS, San Diego, California USA, 2012, pp. 1602-1605.

[87] C. Li, and J. Lin, “Complex Signal Demodulation and Random Body Movement Cancellation Techniques for Non-contact Vital Sign Detection,” in Microwave Symposium Digest, 2008 IEEE MTT-S International, Atlanta, GA, 2008, pp. 567-570.

[88] M. S. Rahman, and K.-D. Kim, “Extended Kalman Filter for Rate Estimation in Doppler Radar Cardiopulmonary Monitoring System,” *International Journal of Bio-Science and Bio-Technology,* vol. 4, no. 4, pp. 95-106, December, 2012, 2012.

[89] Q. Zhou, J. Liu, A. Høst-Madsen, O. Boric-Lubecke, and V. Lubecke, "Detection of Multiple Heartbeats Using Doppler Radar." pp. 1160-1163.

[90] C. Li, and J. Lin, “Recent Advances in Doppler Radar Sensors for Pervasive Healthcare Monitoring,” in Proceedings of Asia-Pacific Microwave Conference 2010, Yokohama, Japan, 2010, pp. 283-290.

[91] J. E. Kiriazi, O. Boric-Lubecke, and V. M. Lubecke, “Radar Cross Section of Human Cardiopulmonary Activity for Recumbent Subject,” in 31st Annual International Conference of the IEEE EMBS, Minneapolis, Minnesota, USA, 2009, pp. 4808 -4811.

[92] C. Li, and J. Lin, “Random Body Movement Cancellation in Doppler Radar Vital Sign Detection,” *IEEE Transactions on Microwave Theory and Techniques,* vol. 56, no. 12, pp. 3143-3152, December, 2008, 2008.

[93] I. Mostafanezhad, O. Boric-Lubecke, V. Lubecke, and D. P. Mandic, “Application of Empirical Mode Decomposition in Removing Fidgeting Interference in Doppler Radar Life Signs Monitoring Devices,” in 31st Annual International Conference of the IEEE EMBS, Minneapolis, Minnesota, USA, 2009, pp. 340-343.

[94] Y. Chen, H. Tan, B. Hu, and Y. Li, "Doppler Radar Based Non-Contact Multi-Person Respiration Signals Separation." pp. 799-802.

[95] S. Kazemi, A. Ghorbani, H. Amindavar, and C. Li, “Cyclostationary approach to Doppler radar heart and respiration rates monitoring with body motion cancelation using Radar Doppler System,” *Biomedical Signal Processing and Control,* vol. 13, no. 2014, pp. 79–88, 2014.

[96] D. Qiao, T. He, B. Hu, and Y. Li, “Non-contact physiological signal detection using continuous wave Doppler radar,” *Bio-Medical Materials and Engineering,* vol. 24, pp. 993–1000, 2014.

[97] D. Obeid, S. Sadek, G. Zaharia, and G. El Zein, "Doppler Radar for Heartbeat Rate and Heart Rate Variability Extraction."

[98] E. Yavari, B. Padasdao, V. Lubecke, and O. Boric-Lubecke, “Packet Radar Spectrum Recovery for Physiological Signals,” in 35th Annual International Conference of the IEEE EMBS, Osaka, Japan, 2013, pp. 1760-1763.

[99] N. Birsan, D.-P. Munteanu, G. Iubu, and T. Niculescu, “Time-Frequency Analysis in Doppler Radar for Noncontact Cardiopulmonary Monitoring,” in Proceedings of the 3rd International Conference on E-Health and Bioengineering - EHB 2011, Iaşi, Romania, 2011, pp. 1-4.

[100] J. Tu, and J. Lin, “Respiration Harmonics Cancellation for Accurate Heart Rate Measurement in Non-contact Vital Sign Detection,” in Microwave Symposium Digest (IMS), 2013 IEEE MTT-S International, Seattle, WA, 2013, pp. 1-3.

[101] H. Noguchi, H. Kubo, T. Mori, T. Sato, and H. Sanada, “Signal Phase Estimation for Measurement of Respiration Waveform Using a Microwave Doppler Sensor,” in 35th Annual International Conference of the IEEE EMBS, Osaka, Japan, 2013, pp. 6740-6743.

[102] M. S. Rahman, B.-J. Jang, and K.-D. Kim, “A New Digital Signal Processor for Doppler Radar Cardiopulmonary Monitoring System,” in 5th International Conference on Electrical and Computer Engineering (ICECE 2008), Dhaka, Bangladesh, 2008, pp. 76-79.

[103] A. Tariq, and H. G. Shiraz, “Doppler Radar Vital Signs Monitoring using Wavelet Transform,” in 2010 Loughborough Antennas & Propagation Conference, Loughborough, UK, 2010, pp. 293-296.

[104] W. Hu, H. Zhang, Z. Zhao, Y. Wang, and X. Wang, “Real-time remote vital sign detection using a portable Doppler sensor system,” in IEEE Sensors Applications Symposium (SAS), Queenstown, 2014, pp. 89 - 93.

[105] C. Li, J. Ling, J. Li, and J. Lin, “Accurate Doppler Radar Noncontact Vital Sign Detection Using the RELAX Algorithm,” *IEEE Transactions on Instrumentation and Measurement,* vol. 59, no. 3, pp. 687-695, March, 2010, 2010.

[106] V. Vasu, N. Fox, C. Heneghan, and S. Sezer, “Using the Lomb Periodogram for Non-Contact Estimation of Respiration Rates,” in 32nd Annual International Conference of the IEEE EMBS, Buenos Aires, Argentina, 2010, pp. 2407-2410.

[107] S. Inui, K. Okusa, K. Maeno, and T. Kanakura, "Recognizing Aspiration Presence using Model Parameter Classification from Microwave Doppler Signals."

[108] J. Li, Z. Zeng, J. Sun, and F. Liu, “Through-Wall Detection of Human Being’s Movement by UWB Radar,” *IEEE Geoscience and Remote Sensing Letters,* vol. 9, no. 6, pp. 1079-1083, November, 2012, 2012.

[109] Y. Nijsure, W. P. Tay, E. Gunawan, F. Wen, Z. Yang, Y. L. Guan, and A. P. Chua, “An Impulse Radio Ultrawideband System for Contactless Noninvasive Respiratory Monitoring,” *IEEE Transactions on Biomedical Engineering,* vol. 60, no. 6, pp. 1509-1517, 2013.

[110] X. Li, D. Qiao, Y. Li, and H. Dai, “A Novel Through-Wall Respiration Detection Algorithm Using UWB Radar,” in 35th Annual International Conference of the IEEE EMBS, Osaka, Japan, 2013, pp. 1013-1016.

[111] W. Z. Li, Z. Li, H. Lv, G. H. Lu, Y. Zhang, X. J. Jing, S. Li, and J. Q. Wang, “A new method for non-line-of-sight vital sign monitoring based on developed

adaptive line enhancer using low centre frequency UWB radar," *Progress In Electromagnetics Research,* vol. 133, pp. 535-554, 2013.

[112] M. Ascione, A. Buonanno, M. D'Urso, L. Angrisani, and R. S. LoMoriello, "A New Measurement Method Based on Music Algorithm for Through-the-Wall Detection of Life Signs," *IEEE Transactions on Instrumentation and Measurement,* vol. 62, no. 1, pp. 13-26, January, 2013, 2013.

[113] A. Lazaro, D. Girbau, and R. Villarino, "Techniques for Clutter Suppression in the Presence of Body Movements during the Detection of Respiratory Activity through UWB Radars," *Sensors,* vol. 14, no. 2, pp. 2595-2618, 7 February, 2014, 2014.

[114] V. P. Tran, A. A. Al-Jumaily, and S. M. S. Islam, "Doppler Radar-Based Non-Contact Health Monitoring for Obstructive Sleep Apnea Diagnosis: A Comprehensive Review," *Big Data and Cognitive Computing,* vol. 3, no. 3, pp. 1-21, 2019.

[115] "International classification of sleep disorders, revised: Diagnostic and coding manual," American Academy of Sleep Medicine, 2011.

[116] T. Penzel, Glos, M., Schöbel, C., Lal, S. & Fietze I., "Estimating Sleep disordered Breathing Based on Heart Rate Analysis." pp. 6517-6574.

[117] T. Young, Palta, M., Dempsey, J., Skatrud, J., Webber, S. & Badr, S., "The Occurrence of Sleep-Disordered Breathing Among Middle-Aged Adults," *The New England Journal of Medicine,* vol. 328, no. 17, pp. 1230-1235, 1993.

[118] P. E. Peppard, Young, T., Barnet, J.H., Palta, M., Hagen, E.W. & Hla, K.M., "Increased Prevalence of Sleep-Disordered Breathing in Adults " *American Journal of Epidemiology,* vol. 177, no. 9, pp. 1006-1014, 2013.

[119] E. O. Bixler, Vgontzas, A.N., Lin, H.M., Have, T.T., Rein, J., Vela-Bueno, A. & Kales, A., "Prevalence of Sleep-disordered Breathing in Women," *American Journal of Respiratory and Critical Care Medicine,* vol. 163, no. 3, pp. 608-613, 2001.

[120] H. Bearpark, Elliott, L., Grunstein, R., Cullen, S., Schneider, H., Althaus, W. & Sullivan, C., "Snoring and sleep apnea. A population study in Australian men," *American Journal of Respiratory and Critical Care Medicine,* vol. 151, no. 5, pp. 1459-1465, 1995.

[121] L. Ferini-Strambi, Zucconi, M., Castronovo, V., Garancini, P., Oldani, A. & Smirne, S., "Snoring & Sleep Apnea: A Population Study in Italian Women," *Sleep,* vol. 22, no. 7, pp. 859-864, 1999.

[122] Author ed.^eds., "Epidemiology," *Surgery for Snoring and Obstructive Sleep Apnea Syndrome*, The Netherlands: Kugler Publications, 2003, p.^pp. Pages.

[123] J. M. Marin, Gascon, J.M., Carrizo, S. & Gispert, J., "Prevalence of Sleep Apnoea Syndrome in the Spanish Adult Population," *International Journal of Epidemiology,* vol. 26, no. 2, pp. 381-386, 1997.

[124] Z. F. Udwadia, Doshi, A.V., Lonkar, S.G. & Singh, C.I., "Prevalence of Sleep-disordered Breathing and Sleep Apnea in Middle-aged Urban Indian Men," *American Journal of Respiratory and Critical Care Medicine,* vol. 169, no. 2, pp. 168-173, 2004.

[125] M. S. M. Ip, Lam, B., Lauder, I.J., Tsang, K.W.T, Chung, K, Mok, Y & Lam, W.K., "A Community Study of Sleep-Disordered Breathing in Middle-aged Chinese Men in Hong Kong," *Chest,* vol. 119, no. 1, pp. 62-69, 2001.

[126] M. S. M. Ip, Lam, B., Tsang, L.C.H, Lauder, I.J, Ip, T.Y. & Lam, W.K, "A Community Study of Sleep-Disordered Breathing in Middle-Aged Chinese Women in Hong Kong," *Chest,* vol. 125, no. 1, pp. 127-134, 2004.

[127] J. K. Kim, In, K.H., Kim, J.H., You, S.H., Kang, K.H., Shim, J.J., Lee, S.Y., Lee, J.B., Lee, S.G., Park, C. & Shin, C., "Prevalence of Sleep-disordered Breathing in Middle-aged Korean Men and Women," *American Journal of Respiratory and Critical Care Medicine,* vol. 170, no. 10, pp. 1108-1113, 2004.

[128] P. S. Jennum, A., "Epidemiology of snoring and obstructive sleep apnoea in a Danish population, age 30–60," *Journal of Sleep Research,* vol. 1, no. 4, pp. 240–244, 1992.

[129] S. P. Patil, Schneider, H., Schwartz, A.R. & Smith, P.L., "Adult Obstructive Sleep Apnea Pathophysiology and Diagnosis," *Chest,* vol. 132, no. 1, pp. 325-337, 2007.

[130] Author ed.^eds., "Pathophysiology of Obstructive Sleep Apnea Syndrome," *Surgery for Snoring and Obstructive Sleep Apnea Syndrome*, The Netherlands: Kugler Publications, 2003, p.^pp. Pages.

[131] A. N. Vgontzasa, Bixlera, E.O. & Chrousos, G.P., "Sleep apnea is a manifestation of the metabolic syndrome," *Sleep Medicine Reviews,* vol. 9, pp. 211–224, 2005.

[132] Author ed.^eds., "Obstructive Sleep Apnea and Central Sleep Apnea: Epidemiology, Pathophysiology, and Risk Factors," *ACCP Sleep Medicine Board Review*, 4th ed., Northbrook, USA: Chest, 2009, p.^pp. Pages.

[133] Author ed.^eds., "Neurological Correlations in Neurological Breathing Disorders," *Surgery for Snoring and Obstructive Sleep Apnea Syndrome*, The Netherlands: Kugler Publications, 2003, p.^pp. Pages.

[134] J. C. M. Lam, Sharma, S.K. & Lam, B., "Obstructive sleep apnoea: Definitions, epidemiology & natural history," *Indian Journal of Medical Research,,* vol. 131, pp. 165-170, 2009.

[135] P. J. R. Trollo, R.M., "Obstructive Sleep Apnea," *Current Concepts,* vol. 334, no. 2, pp. 99-104, 1996.

[136] J. R. Stradling, "Obstructive sleep apnoea: definitions, epidemiology, and natural history," *Thorax,* vol. 50, pp. 683-689, 1995.

[137] L. J. Epstein, Kristo, D., Strollo, P.J., Friedman, N., Malhotra, A., Patil, S.P., Ramar, K., Rogers, R., Schwab, R.J., Weaver, E.M. & Weinstein, M.D., "Clinical Guideline for the Evaluation, Management and Long-term Care of Obstructive Sleep Apnea in Adults," *Journal of Clinical Sleep Medicine,* vol. 5, no. 3, pp. 263-276, 2009.

[138] J. M. Valderas, Mercer, S.W., & Fortin, M., "Research on patients with multiple health conditions: different constructs, different views, one voice," *Journal of Comorbidity,* vol. 1, pp. 1-3, 2011.

[139] A. G. Logan, Perlikowski, S.M., Mente, A., Tisler, A., Tkacova, R., Niroumand, M., Leung, R.S.T. & Bradley, T.D., "High prevalence of unrecognized sleep apnoea in drug-resistant hypertension," *Journal of Hypertension,* vol. 19, no. 12, pp. 2271–2277, 2001.

[140] T. P. O'Keeffe, E.J., "Evidence Supporting Routine Polysomnography Before Bariatric Surgery," *Obesity Surgery,* vol. 14, pp. 23-26, 2004.

[141] O. Oldenburg, Lamp, B., Faber, L., Teschler, H., Horstkotte, D. & Töpfer, V., "Sleep-disordered breathing in patients with symptomatic heart failure A

contemporary study of prevalence in and characteristics of 700 patients," *European Journal of Heart Failure,* vol. 9, no. 3, pp. 251-257, 2007.

[142] S. Garrigue, Pépin, J.L., Defaye, P., Murgatroyd, F., Poezevara, Y., Clémenty, J. & Lévy, P., "High Prevalence of Sleep Apnea Syndrome in Patients With Long-Term Pacing: The European Multicenter Polysomnographic Study," *Circulation,* vol. 115, no. 25, pp. 1703-1709, 2007.

[143] A. S. Gami, Pressman, G., Caples, S.M., Kanagala, R., Gard, J.J., Davison, D.E., Malouf, J.F., Ammash, N.M., Friedman, P.A. & Somers, V.K., "Association of Atrial Fibrillation and Obstructive Sleep Apnea," *Circulation,* vol. 110, no. 3, pp. 364-367, 2004.

[144] D. Einhorn, Stewart, D.A., Erman, M.K., Gordon, N., Philis-Tsimikas, A. & Casal, E. , "Prevalence of Sleep Apnea in a Population of Adults with Type 2 Diabetes Mellitus," *Endocrine Practice,* vol. 13, no. 4, pp. 355-362, 2007.

[145] C. Sjöström, Lindberg, E., Elmasry, A., Hägg, A., Svärdsudd, K. & Janson, C., "Prevalence of sleep apnoea and snoring in hypertensive men: a population based study," *Thorax,* vol. 57, pp. 602-607, 2002.

[146] H. Schäfer, Koehler, U., Ewig, S., Hasper, E., Tasci, S. & Lüderitz, B., "Obstructive Sleep Apnea as a Risk Marker in Coronary Artery Disease," *Cardiology,* vol. 92, pp. 79-84, 1999.

[147] R. S. T. B. Leung, T.D., "Sleep Apnea and Cardiovascular Disease," *American Journal of Respiratory and Critical Care Medicine,* vol. 164, no. 12, pp. 2147–2165, 2001.

[148] V. P. Tran, and A. A. Al-Jumaily, *(WO2016205891) Diagnosis and Monitoring of Cardio-Respiratory Disorders*, W. I. P. Organization, 2016.

[149] V. P. Tran, and A. A. Al-Jumaily, *Heart and respiratory rate estimation from non-contact sensor data*, A.-I. Australia, 2015.

[150] V. P. Tran, and A. A. Al-Jumaily, *(US20180153427) Diagnosis and Monitoring of Cardio-Respiratory Disorders*, United States of America, W. I. P. Organization, 2018.

[151] A. Quetelet, *A treatise on man and the development of his faculties*, Edinburgh, Scotland: William and Roberts Chambers, 1842.

[152] W. R. Stahl, "Scaling of respiratory variables in mammals," *Journal of Applied Physiology,* vol. 22, no. 3, pp. 453-460, 1967.

[153] E. H. Livingston, and S. Lee, “Body surface area prediction in normal-weight and obese patients,” *American Journal of Physiology - Endocrinology and Metabolism,* vol. 281, no. 3, pp. E586–E591, 2001.

[154] V. P. Tran, and A. A. Al-Jumaily, *Estimation of pulmonary ventilation quantities based on non-contact sensor data*, A.-I. Australia, 2016.

[155] C. H. L. P. E. Bohr, K. A. Haseelbalch, and S. A. S. Krogh, “Ueber einen in biologischer Beziehung wichtigen Einfluss, den die Kohlensäurespannung des Blutes auf dessen Sauerstoffbindung übt,” *Skandinavisches Archiv Für Physiologie,* vol. 16, no. 2, pp. 402-412, July, 1904, 1904.

[156] K. E. Barrett, H. L. Brooks, S. Boitano, and S. M. Barman, *Ganong's Review of Medical Physiology*, 23rd ed., USA: McGraw-Hill, 2010.

[157] S. E. Weinberger, B. A. Cockrill, and J. Mandel, *Principles of Pulmonary Medicine*, 5th ed., Philadelphia, USA: Elsevier, 2008.

[158] M. C. Hart, M. M. Orzalesi, and C. D. Cook, “Relation betwen anatomic respiratory dead space and body size and lung volume,” *Journal of Applied Physiology,* vol. 18, no. 3, pp. 519-522, May, 1963, 1963.

[159] H. Bitterman, “Bench-to-bedside review: Oxygen as a drug,” *Critical Care,* vol. 13, no. 1, pp. 205-212, 24 February 2009, 2009.

[160] V. P. Tran, and A. A. Al-Jumaily, “A Novel Oxygen-Hemoglobin Model for Non-Contact Sleep Monitoring of Oxygen Saturation,” *IEEE Sensors Journal,* vol. 19, no. 24, pp. 12325-12332, 15 Dec 2019, 2019.

[161] V. P. Tran, and A. A. Al-Jumaily, *Non-contact monitoring of nocturnal oxygen saturation in the arterial blood*, A.-I. Australia, 2016.

[162] V. P. Tran, and A. A. Al-Jumaily, *(WO2019079855) Detection and Monitoring of Body Orientation*, W. I. P. Organization, 2019.

[163] V. P. Tran, and A. A. Al-Jumaily, *Non-contact monitoring of nocturnal body position*, Australia, A.-I. Australia, 2018.

[164] P. Grossman, “Respiration, stress and cardiovascular function,” *Psychophysiology,* vol. 20, no. 3, pp. 284-300, 1983.

[165] C. J. E. Wientjes, “Respiration in psychophysiology: measurement issues and applications,” *Biological Psychology,* vol. 34, no. 2, pp. 179-203, 1992.

[166] G. P. Hibbert, D., “Hyperventilation: is it a cause of panic attacks? ,” *British Journal of Psychiatry,* vol. 155, pp. 805-809, 1989.

[167] S. S. Choudhary, and S. R. Choudhary, “Sleep effects on breathing and respiratory diseases,” *Lung India,* vol. 26, no. 4, pp. 117–122, 2009.

[168] G. W. Jenkins, Kemnitz, C.P. & Tortora, G.J., *Anatomy and Physiology – From Science to Life*, 2nd ed., USA: John Wiley & Sons, Inc., 2010.

[169] Author ed.^eds., “Non Contact Heart Monitoring,” *Advances in Electrocardiograms - Methods and Analysis*, Rijeka, Croatia: InTech, 2012, p.^pp. Pages.

[170] J. Pan, and W. J. Tompkins, “A Real-Time QRS Detection Algorithm,” *IEEE Transactions on Biomedical Engineering,* vol. BME-32, no. 3, pp. 230-236, March 1985, 1985.

[171] K. H. Schindhelm, S. P. Farrugia, M. W. Colefax, F. Javed, R. Khushaba, C. Heneghan, C. Philip De, A. Zaffaroni, N. Fox, P. Celka, E. O'Hare, and S. J. Redmond, *(WO2013177621) Method and Apparatus for Monitoring Cardio-Pulmonary Health*, World Intellectual Property Organization, 2013.

[172] C. Heneghan, M. Wren, and T. Brabetz, *Development of a range-gated sensor for sleep monitoring compliant with Japanese regulatory requirements (white paper)*, p.^pp. 1-24, Dublin, Ireland: BiancaMed, 2008.